

UNIVERSITY
OF OSLO

Snorre Braathen Kjeldby

**Polymorph transformations,
nanoparticles, and luminescence
in ion-implanted gallium oxide**

Thesis submitted for the degree of Philosophiae Doctor

Department of Physics
The Faculty of Mathematics and Natural Sciences



2024

© Snorre Braathen Kjeldby, 2024

*Series of dissertations submitted to the
Faculty of Mathematics and Natural Sciences, University of Oslo
No. 2793*

ISSN 1501-7710

All rights reserved. No part of this publication may be
reproduced or transmitted, in any form or by any means, without permission.

Cover: UiO.

Print production: Graphic center, University of Oslo.

*Betre byrði
du ber'kje i bakken
enn mannavit mykje.
- Håvamål*

Sammendrag

Galliumseskvioksid, Ga_2O_3 , er en halvleder med ultrabredt båndgap som er lovende for bruk i kraftelektronikk, solblinde UV fotodetektorer, som et gjennomsiktig elektrisk ledende materiale, og som gjennomsiktig vertsmateriale for emittere av synlig og infrarødt lys. I tillegg til den stabile monokline fasen, $\beta\text{-Ga}_2\text{O}_3$, har Ga_2O_3 flere ulike krystallstrukturer med samme kjemiske sammensetning.

I ioneimplantasjon dannes en stråle av ioner med høy kinetisk energi, og denne rettes mot overflaten av en prøve. Teknikken muliggjør kontrollert tilsetning av dopanter eller andre urenheter til prøven, med høy grad av kontroll over både konsentrasjonen og den romlige fordelingen til de implanterte ionene. Derfor er ioneimplantasjon i utbredt bruk i prosessering av halvledere, og i fabrikasjon av halvlederkomponenter, siden teknikken kan brukes til kontrollert justering av prøvens egenskaper. Utover den teknologiske relevansen, innebærer ioneimplantasjon interaksjoner mellom materialer og partikler med høy energi, og en fullstendig forståelse disse interaksjonene er av vitenskapelig interesse.

Nylig har forskning vist at høydoseimplantasjon i monoklin Ga_2O_3 resulterer i en faseovergang til en annen polymorf i det implanterte laget nær prøvens overflate. Denne effekten står i skarp kontrast til amorfiseringen av det implanterte laget, som observeres i de fleste tilfeller for tilstrekkelig høye implantasjonsdoser. Polymorfoverganger induert av interaksjoner med høyenergipartikler er ikke fullt ut beskrevet eller forstått i den vitenskapelige litteraturen. Siden effekten er observert i Ga_2O_3 , som forventes å ha teknologisk relevans, er en forståelse av effekten viktig for halvledervitenskapen. En slik forståelse er særlig viktig for å muliggjøre teknologisk anvendelse av Ga_2O_3 . Implantasjonsinduserte polymorfoverganger er rapportert få ganger i litteraturen. Allikevel ser ikke effekten ut til å være unik for Ga_2O_3 . Dermed kan en dypere forståelse av effekten også være fordelaktig for utvikling av andre materialer der lignende effekter har blitt observert.

Selv om flere aspekter ved den implantasjonsinduserte polymorfovergangen i Ga_2O_3 ikke er fullstendig beskrevet, har ny forskning klargjort et antall viktige aspekter. Denne avhandlingen omhandler i hovedsak undersøkelser av denne polymorfovergangen, inkludert dens avhengighet av kjemien til de implanterte ionene, orienteringen til $\beta\text{-Ga}_2\text{O}_3$ prøven under implantasjon, den termiske stabiliteten til det polymorftransformerte laget, utvetydig krystallografisk identifisering av det polymorftransformerte laget, og effekten av polymorftransformasjonen på utvalgte materialeegenskaper.

Tilgjengelig data viser at polymorfovergangen forekommer uavhengig av kjemien til de implanterte ionene og orientering av prøven. Det første poenget er av særlig viktighet, da det viser at transformasjonen drives av implantasjonsprosessen i seg selv heller enn kjemien til de implanterte ionene. Gjennom detaljert strukturell karakterisering ble det vist at polymorfovergangen resulterer i den kubiske defekte spinelpolymorfen til Ga_2O_3 , altså $\gamma\text{-Ga}_2\text{O}_3$. Det transformerte laget kan omdannes tilbake til $\beta\text{-Ga}_2\text{O}_3$ gjennom varmebehandling. Den detaljerte strukturelle utviklingen til prøven under denne tilbake-transformasjonen ble også undersøkt og beskrevet. For implantasjon av Si og Ge ble det demonstrert at nanopartikler av sekundære faser i Ga_2O_3 kunne dannes ved høydoseimplantasjon fulgt av varmebehandling ved høye temperaturer. Disse prosessene ga SiO_2 og Ge nanopartikler, avhengig av hvilke ioner som ble implantert. Tverrsnittsmålinger av katodeluminesens avdekket kun mindre endringer i luminesensen fra det transformerte laget sammenlignet med den karakteristiske luminesensen til $\beta\text{-Ga}_2\text{O}_3$ i bølgelengdeområdene for synlig og ultraviolet lys. Imidlertid viste disse målingene at varmebehandling i oksygenrik atmosfære ga opphopning av Cr-urenheter på prøvens overflate, som resulterte i sterk rød luminesens fra området nær overflaten av prøven. Kontrollert introduksjon av defekter i det samme området via ioneimplantasjon økte Cr-konsentrasjonen nær overflata ytterligere etter varmebehandling.

Denne avhandlingen utgjør et betydelig bidrag til en dypere forståelse av polymorfoverganger i materialer indusert av ioneimplantasjon. Selv om de siste årene har gitt betydelig framgang i dette feltet, gjenstår flere åpne spørsmål. Siden den nyligste litteraturen også har avdekket nye uventede egenskaper til det transformerte laget, spesielt dets bemerkelsesverdige motstand mot skade fra videre ioneimplantasjon, mener forfatteren at dette feltet fremdeles er av betydelig vitenskapelig og teknologisk interesse.

Abstract

Gallium sesquioxide, Ga_2O_3 , is an emerging ultra wide band gap semiconductor, which is promising for applications in power electronics, for solar-blind UV photodetectors, as a transparent conductive material, and as an optically transparent host for species with emission in the visible range of the electromagnetic spectrum. In addition to the stable monoclinic phase, $\beta\text{-Ga}_2\text{O}_3$, Ga_2O_3 displays rich polymorphism, i.e. different crystal structures sharing the same chemical composition.

In ion implantation, high kinetic energy ions of a selected species are directed onto the surface of a sample. The technique enables introduction of dopant and impurity species in semiconductors with excellent control over the concentration and the spatial distribution of the implanted species. Ion implantation is therefore ubiquitous in semiconductor processing and device manufacturing, as it allows localized and controlled tuning of sample properties. In addition to its obvious technological relevance, ion implantation involves interactions of a material with high-energy particles, a full understanding of which is of scientific interest.

Recent research has demonstrated that high-fluence ion implantation in monoclinic Ga_2O_3 results in a polymorph transformation around the implanted region of the sample. The observed polymorph transformation is in striking contrast to amorphization of the sample, which is typically observed for sufficiently high implantation fluences. Polymorph transformations induced by interactions with high-energy particles are not well understood, and a deeper understanding of such effects is of importance for semiconductor science. Moreover, a full understanding of the effects of ion implantation in Ga_2O_3 is important to facilitate technological application of this important emerging semiconductor. Although implantation-induced polymorph transformations are rarely observed, the existing literature suggests that the effect is not *unique* to Ga_2O_3 , and a deeper understanding of the effect may therefore prove advantageous to development of other materials in which the effect is observed.

Although the understanding of polymorph transformation in Ga_2O_3 remains incomplete, recent research has elucidated several key aspects. The majority of the work presented herein is dedicated to investigations of this effect, such as its dependence on the implanted species, the crystallographic orientation of the initial monoclinic $\beta\text{-Ga}_2\text{O}_3$ sample, the thermal stability of the polymorph-transformed layer, unambiguous crystallographic identification of the transformed layer, and the effect of the polymorph transformation on the luminescence properties of the material.

The data collected in this work reveals that the polymorph transformation occurs independently of the implanted species and the orientation of the sample. The former observation is of particular importance, since it reveals that the transformation is triggered by intrinsic effects of the ion implantation rather than the chemistry of the implanted ions. Through detailed structural characterization, it was revealed that the polymorph transformation yields the cubic defective spinel polymorph of Ga_2O_3 , namely $\gamma\text{-Ga}_2\text{O}_3$. The transformed layers can be returned to monoclinic $\beta\text{-Ga}_2\text{O}_3$ through post-implantation annealing. The detailed structural evolution during this back-transformation was also investigated. For implantation of Si and Ge, it was demonstrated that nanoparticles of secondary phases in Ga_2O_3 can be formed by high-fluence implantation followed by high-temperature annealing. This yielded SiO_2 and Ge nanoparticles respectively. A cross-sectional cathodoluminescence study revealed only minor changes to the luminescence in the implanted layer compared to the characteristic luminescence of $\beta\text{-Ga}_2\text{O}_3$ in the UV and visible spectral ranges. However, these measurements also revealed that high-temperature annealing in oxygen rich atmosphere results in accumulation of Cr-impurities near the sample surface, which yielded strong luminescence in the red spectral range. Controlled introduction of defects via ion implantation increased the Cr-concentrations near the sample surface after annealing.

This thesis represents a significant contribution to the developing understanding of polymorph transformations in materials induced by ion implantation. Although substantial progress has been made in this field in the last few years, several important questions remain open. As the most recent research has also revealed further unforeseen properties of the transformed layer, namely its remarkable resistance to further damage induced by ion irradiation, this topic remains of substantial scientific and technological importance in the author's opinion.

Acknowledgements

I have been fortunate to write my PhD at the university of Oslo, surrounded by kind and talented people, both in the semiconductor physics group and in the structure physics group. I have learned a lot from you all, and I have cherished your company at the lunch table, at the ping pong table, in Friday meetings, while taking quizzes, over beers, at bouldering sessions, at inside and outside running sessions, in meetings, and in the lab. Thank you all for greatly appreciating my puns, and for making the days much better than they otherwise would have been!

I am grateful to my supervisors Lasse Vines and Øystein Prytz for the opportunity to undertake this journey, for all our productive discussions, and for their guidance. As a part of the FUNCTION project, I thank all its members for contributing with their individual expertise. Thank you all for a fruitful collaboration. In particular, the research presented in this thesis would not have been possible without a close collaboration with Javier García-Fernández and also with Phuong Dan Nguyen. I am very grateful to you both for your contributions. I am also grateful to all of my other colleagues who have contributed to the work presented herein. The permanent staff in both research groups have been important in enabling this research. Thank you for maintaining the infrastructure that we depend on to do science. I am particularly grateful to Viktor Mihaly Bobal in this regard.

To all of my friends: you have been invaluable over the last few years. Thank you for all the good times we have had, thank you for listening to my worries, and for having the patience to let me occasionally babble about my research. Special thanks go out to my family, who have always supported me and continue to do so. Finally, I could not have finished this journey without Kristine Andreassen, my partner and the origin of the coordinate system of my life. I could not have asked for a better companion on this journey, and I am so grateful for all the help and support you have given me. At the ending of this chapter, I look forward to starting another one with you.

List of included papers

Paper I

S. B. Kjeldby, A. Azarov, P. D. Nguyen, V. Venkatachalapathy, R. Mikšová, A. Macková, A. Kuznetsov, Ø. Prytz and L. Vines, "Radiation-induced defect accumulation and annealing in Si-implanted gallium oxide", *Journal of Applied Physics* **131**, 125701 (2022)

DOI: <https://doi.org/10.1063/5.0083858>.

Paper II

J. García-Fernández, S. B. Kjeldby, P. D. Nguyen, O. B. Karlsen, L. Vines and Ø. Prytz, "Formation of γ -Ga₂O₃ by ion implantation: Polymorphic phase transformation of β -Ga₂O₃", *Applied Physics Letters* **121**, 191601 (2022)

DOI: <https://doi.org/10.1063/5.0120103>.

Paper III

J. García-Fernández, S. B. Kjeldby, L. J. Zeng, A. Azarov, A. Pokle, P. D. Nguyen, E. Olsson, L. Vines, A. Yu Kuznetsov, Ø. Prytz, "In-situ atomic-resolution study of transformations in double polymorph γ/β -Ga₂O₃ structures", Accepted in: *Materials Advances* (2024).

Paper IV

S. B. Kjeldby, J. García-Fernández, A. Galeckas, I.J.T. Jensen, Ø. Prytz and L. Vines, "Cross-sectional cathodoluminescence measurements of Cr-luminescence in implanted and annealed gallium oxide", Submitted to: *Journal of Applied Physics* (2024).

Paper V

S. B. Kjeldby, P. D. Nguyen, J. García-Fernández, K. Haug, A. Galeckas, I. J. T. Jensen, A. Thøgersen, L. Vines and Ø. Prytz, "Optical properties of ZnFe₂O₄ nanoparticles and Fe-decorated inversion domain boundaries in ZnO", *Nanoscale Advances* **5**, 2102 (2023)

DOI: <https://doi.org/10.1039/D2NA00849A>.

Author contributions to included papers

Paper I

Conceptualization and idea of research, planning of research, selecting implantation and annealing parameters, preparing samples, performing XRD measurements, analysis and discussion of XRD results, analysis and discussion of RBS/c results with contributions from coauthors, selection of sample preparation for (S)TEM and SIMS measurements, analysis and discussion of (S)TEM and EDS data with input from coauthors, analysis and discussion of SIMS data with input from coauthors, discussion, writing manuscript with input from coauthors.

Paper II

Conceptualization and idea of research, planning of research, choice of implantation parameters, choice of implanted species, preparation of implanted samples, contributions to analysis and discussion, contributions to manuscript writing (especially paragraph concerning polymorph transformations in other materials and paragraph discussing structural similarity between β - and γ -Ga₂O₃), finding approximate conservation of anion sublattice during transformation through inspection of published crystal structures (see supplementary information of article) and contributing to formulation of this argument in the main text of the article and supplementary, proof-reading.

Paper III

Conceptualization and idea of research, choice of implantation parameters for Si-implanted samples, preparation of Si-implanted samples (not including preparation of lamella for TEM and STEM), input to analysis of (S)TEM results, input to discussion, input to manuscript drafts, proof-reading.

Paper IV

Conceptualization and idea of research, choice of sample processing parameters, preparation of implanted and/or annealed samples, design and choice of CL measurement methodology, performing CL measurements, analysis and discussion of SIMS data with input from coauthors, analysis and discussion of luminescence data (CL and PL), discussion, writing manuscript with input from coauthors.

Paper V

Conceptualization and idea of research, performing XRD measurements, analysis of XRD data, analysis of (S)TEM and EDS data with contributions from coauthors, analysis of optical absorption data (DRS) with input from coauthors, analysis of low-loss EELS data with input from coauthors, CL measurements, analysis of CL measurements, SEM-EDS measurements and analysis (supplementary), contributions to XPS discussion, analysis and discussion with input from coauthors, writing manuscript with input from coauthors.

Related publications not included in this thesis

1. M. E. Bathen, G. M. Selnesaunet, M. J. Enga, S. B. Kjeldby, J. Müting, L. Vines and U. Grossner, "Charge State Control over Point Defects in SiC Devices", *Defect and Diffusion Forum* **425**, 35 (2023).
2. K. Milenko, S. S. Fuglerud, S. B. Kjeldby, R. Ellingsen, A. Aksnes, D. R. Hjelme, "Micro-lensed optical fibers for a surface-enhanced Raman scattering sensing probe", *Optics Letters* **43**, 6029 (2018).
3. S. B. Kjeldby, O. M. Evenstad, S. P. Cooil, J. W. Wells, "Probing dimensionality using a simplified 4-probe method", *Journal of Physics: Condensed Matter* **29**, 394008 (2017).

Contents

Sammendrag	iii
Abstract	v
Acknowledgements	vii
List of included papers	ix
Related publications not included in this thesis	xiii
Contents	xvi
1 Introduction	1
2 Wide and ultra wide band gap semiconductors	5
2.1 Polymorphism	9
2.2 Gallium oxide	9
2.2.1 Polymorph transformation in ion-irradiated β -Ga ₂ O ₃ . .	12
2.2.2 Polymorph transformation from irradiation in other ma- terials	15
2.2.3 Defects	16
2.2.4 Luminescence	16
2.3 Zinc oxide, zinc ferrite and Fe-decorated inversion domain bound- aries	19
2.3.1 Zinc oxide	19
2.3.2 Inversion domain boundaries in zinc oxide	19
2.3.3 Zinc ferrite	20
3 Sample fabrication and characterization	23
3.1 Sample processing	23
3.1.1 Ion implantation	23
3.2 Characterization methods	28
3.2.1 X-ray diffraction	28
3.2.2 Optical absorption and diffuse reflectance measurements	30
3.2.3 Scanning electron microscopy	31
3.2.4 Cathodoluminescence	32
3.2.5 Transmission electron microscopy and scanning transmis- sion electron microscopy	35

3.2.6	Electron energy-loss spectroscopy	37
3.2.7	Secondary-ion mass spectrometry	38
3.2.8	Rutherford backscattering spectrometry	40
3.2.9	Photoelectron spectroscopy	41
4	Results	43
4.1	Initial investigations of the polymorphic transformation in ion-implanted β -Ga ₂ O ₃	44
4.2	Structural identification of the polymorph-transformed layer . .	46
4.3	In situ characterization of back-transformation of the implanted layer	48
4.4	Luminescence from ion-implanted and annealed β -Ga ₂ O ₃	50
4.5	Formation of Ge-rich nanoparticles in ion-implanted β -Ga ₂ O ₃ .	52
4.6	Optical properties of ZnO containing ZnFe ₂ O ₄ nanoparticles or Fe-decorated IDBs	55
5	Concluding remarks	59
5.1	Suggestions for further work	60
	Bibliography	62
	Papers	71
	Paper I	73
	Paper II	85
	Paper III	95
	Paper IV	111
	Paper V	137

Chapter 1

Introduction

The technological adoption of novel materials is a major marker for technological development. In this context, the successful fabrication of semiconductor devices is undoubtedly one of the principal advances of the last century. Semiconductor devices have, for example, enabled storage and exchange of information at unprecedented scales, yielded vast increases in computing power and enabled extraction of electrical energy from new sources. In a word, semiconductor technology and physics underpin the modern technological world.

Despite the success of semiconductor science and technology, the field is still developing. Significant improvements in the fundamental understanding of semiconductors should still be expected, and may yield important improvements in the performance of devices. Silicon is used in the majority of semiconductor applications, even where the physical properties of silicon limit device performance. As a first example, the photovoltaic conversion rate of solar cells using only silicon for the absorbing layer are limited to around 30 % by the single-junction Shockley-Queisser limit [1]. By integrating additional absorbing layers, i.e. incorporating semiconductors other than silicon, the efficiency can be improved drastically, which is currently motivating research into semiconductors with wider band gaps, specifically around 1.7 eV [2].

Wide band gap semiconductors, defined as having a band gap greater than 2 eV, also provide improved performance in power switching. Here, the ability of these materials to sustain large electric fields before suffering electrical breakdown are important [3]. The figures of merit used to assess the suitability of materials for such applications also favor materials with wide band gaps. Gallium nitride and silicon carbide, with band gaps of 3.4 and 3.3 eV respectively [4], have therefore started to be adopted in power switching devices in recent years [5]. Semiconductors with band gaps greater than 3.4 eV are referred to as ultra wide band gap semiconductors. The development of ultra wide band gap semiconductors for power electronics applications is also receiving substantial research interest [4, 6]. In sensing applications, ultra wide band gap semiconductors provide sensitivity to ultraviolet light while remaining insensitive to interference from visible and infrared light. Fabrication of such solar blind sensors is of significant technological interest for fields such as secure communications, medical imaging, chemical and biological analysis, ozone

hole monitoring, flame detection etc. [7]. Furthermore, since ultra wide band gap semiconductors do not absorb light in the visible spectral range, they can be used as hosts for species emitting in the visible and infrared ranges, e.g. Cr [8, 9], Er, Eu [10], etc. Moreover, they can be used as transparent conductive materials for contacts in various optoelectronic applications [11, 12].

Beyond technological motivations, the study of wide and ultra wide band gap semiconductors is scientifically important since these materials are found at the edge of current semiconductor physics. These materials are distinguished from insulators, which also have wide band gaps, by their ability to be made highly conductive through introduction of electrically active dopants. In a sense, wide band gap semiconductors therefore exist at the intersection between traditional semiconductors and insulators. Research into wide and ultra wide band gap semiconductors therefore extends the limits of semiconductor science, providing new insights into the behavior of semiconductors. As there is ample motivation to study these materials both from the technological and the scientific point of view, it appears likely that research in coming years will continue to extend the field of semiconductor physics to materials with ever larger band gaps.

Among the ultra wide band gap semiconductors, gallium sesquioxide, Ga_2O_3 , is currently under extensive scientific research. Its technological applications include power electronic devices, solar-blind UV photodetectors, and uses as a transparent conductive oxide or a transparent host for species emitting in the visible range of the electromagnetic spectrum. In addition to its wide band gap of 4.4-4.9 eV [13, 14, 15], Ga_2O_3 is readily n-type dopable. From a scientific point of view, this material is also noteworthy for its rich polymorphism [16]. Furthermore, advances in crystal growth in recent years have made large wafers of high-quality gallium oxide available at relatively low costs, through melt-growth of bulk samples [6]. For technological applications, low fabrication costs are important from an economic point of view.

Selective tuning of electrical properties is essential in semiconductor physics and technology. This is most frequently achieved by selective introduction of appropriate electrically active dopants, which can be achieved through ion implantation. This fabrication method is ubiquitous, as it gives excellent control over both the concentration and the spatial distribution of dopants. During implantation, ions of the desired dopant species with high kinetic energy are directed onto a sample. In the sample, the ions lose energy through interactions with nuclei and electrons. This causes the ions to come to rest with a depth distribution which can be calculated from the known experimental parameters. However, the interactions of the high kinetic energy ions with the sample nuclei produces collision cascades in which sample nuclei are displaced from their equilibrium positions. Hence, ion implantation produces defects in crystalline samples.

When a high concentration of dopant species is introduced by ion implantation, high defect concentrations accumulate in the implanted region of the sample. In most semiconductors, including silicon, the accumulation of defects ultimately causes initially crystalline samples to become amorphous in the im-

planted layer. This process makes intuitive sense; the implantation-induced defects lead to increased disorder, which finally leads to a loss of the crystal structure entirely. However, in a few materials, including gallium oxide, a different process has been observed. Rather than causing amorphization, high fluence implantation in monoclinic β -Ga₂O₃ causes a change in the crystal structure in the implanted layer. Specifically, a transformation to the cubic defective spinel polymorph γ -Ga₂O₃ is observed [17, 18]. Although the existing literature suggests that such effects are not unique to gallium oxide, the observation of such effects is nonetheless rare. Over the last few years, this polymorph transformation in gallium oxide has therefore attracted extensive research interest. As ion implantation is important in semiconductor device fabrication, developing the understanding of ion implantation in gallium oxide is important in enabling emerging technological applications of this material.

The implantation-induced β -to- γ polymorph transformation in gallium oxide is the main focus of this thesis. The transformation has proven to be robust to variation in several important experimental parameters, such as the orientation of the initial β -Ga₂O₃ sample and the implanted species. The latter is significant, as it implies that the chemistry of the implanted ion is not essential for the transformation, which appears instead to be driven by the defects induced by ion implantation. Thus, the available data suggest that this transformation results from the ion-induced disorder, and an understanding of the observed effect is of general interest for materials science.

Recent literature results provide additional motivation to study the β -to- γ polymorph transformation. In 2023, Azarov *et al.* demonstrated that once ion implantation has transformed β -Ga₂O₃ to γ -Ga₂O₃, the resulting γ -Ga₂O₃ is remarkably resistant to further structural damage from ion implantation [19]. Radiation-tolerant materials are important for devices operating in harsh radiation conditions, e.g. aerospace applications. Hence, there is strong motivation for continued investigation of implantation-induced polymorphic transformations, several aspects of which remain poorly understood.

The work presented herein focuses predominantly on the effects of ion implantation in gallium oxide, specifically on the polymorphic transformation introduced above. This thesis contributes to the understanding of this process. Several aspects of the crystal structure of ion-implanted β -Ga₂O₃ are discussed and elucidated, including the transformation of β -Ga₂O₃ to γ -Ga₂O₃ induced by implantation, and the subsequent back-transformation of γ -Ga₂O₃ to β -Ga₂O₃ during post-implantation annealing. The possibility to use high-fluence ion implantation and post-implantation annealing to form nanoparticles embedded in gallium oxide is demonstrated for the cases of Si- and Ge-implantation. The effect of the polymorph transformation on the luminescence of ion-implanted samples is investigated using cross-sectional cathodoluminescence. Finally, the structural and functional properties of ZnO containing high Fe-concentrations is investigated, complementing previous characterization of similar structures in the literature, where the investigation of their impact on functional properties was largely missing.

Chapter 2

Wide and ultra wide band gap semiconductors

The work presented in this thesis concerns wide and ultra wide band gap semiconductors, in particular the oxides Ga_2O_3 and ZnO . In this chapter, relevant general properties of semiconductors are first introduced, followed by a treatment of the relevant background for wide and ultra wide band gap semiconductors, before finally progressing to the properties of the relevant materials for this thesis.

When initially separate atoms are brought into close spatial proximity, materials are formed by bonding between the constituent atoms. The position of the atoms in the material are determined by minimization of the free energy of the system, and is dependent on the temperature, pressure and chemical composition [20]. Materials may either be crystalline or amorphous. In crystalline materials, the structure is fully determined by periodic spatial repetition of a small unit of atoms, the unit cell, and crystals display long-range order [21]. Amorphous materials, in contrast, lack long-range order. Crystalline materials, also referred to as crystals, are of primary interest for this thesis.

During formation of a material, the discrete electron energy levels of the constituent atoms give rise to bands of permissible electron energies [22, p. 86-110]. The Fermi level ϵ_F corresponds to the energy where an electronic state has a probability of 50% to be occupied by an electron. The position of the Fermi level with respect to the bands has profound effects on material properties. In semiconductors, ϵ_F lies in the gap between bands, with the valence band lying directly below the Fermi level and the conduction band lying directly above the Fermi level. At low temperatures, all states in the valence band are filled, while all states in the conduction band are empty [21, p.187-218]. As a consequence, significant amounts of energy are required to move electrons into a band with empty states in which they can conduct electricity if an electric field is applied. Therefore, undoped semiconductors are poor electrical conductors compared to metals, where ϵ_F lies within a band, and thermal energy can excite electrons into empty states, enabling high electrical conductivity. For semiconductors, the term band gap is used both for the energetic range between the top of the valence band and the bottom of the conduction band and for the width of this

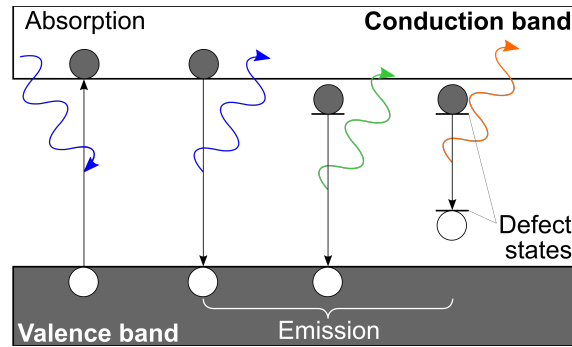


Figure 2.1: Absorption generating an electron hole pair (far left) which can recombine radiatively from the band edges (second from the left) or via defects (third and fourth from the left).

energy range. E_g denotes the energetic width of the band gap.

Ideal crystals are fully described by periodic spatial repetition of the unit cell. However, the entropic term of the free energy of the system favors formation of defects, points where the crystal structure differs from that of a perfect crystal [21, p. 583-595]. All real crystals therefore contain defects, although the defect concentrations vary significantly between materials and depends on the synthesis route. The simplest defects are point defects, which represent divergence from the perfect crystal structure at a single point. Vacancies, interstitials and substitutions are examples of point defects. Other defects include aggregations of point defects, e.g. two adjacent vacancies, and extended defects such as stacking faults, antiphase boundaries, inversion domain boundaries etc. Extrinsic defects involve atomic species which are not present in the perfect crystal, while intrinsic defects involve only the species that are present in the perfect crystal. Dopants are a type of defect with particular importance that introduce energy levels within the band gap, ideally close to either the conduction band or the valence band. Dopants can be used to increase the electrical conductivity of samples by providing free charge carriers. P-type dopants introduce energy levels close to the valence band which are vacant at 0 K. N-type dopants introduce energy levels close to the conduction band which are filled at 0 K [22, p. 104-105].

The band gap has important consequences for the interactions of semiconductors with light. In the ultraviolet and visible ranges of the electromagnetic spectrum, optical absorption in semiconductors is mediated by absorption of a photon by an electron, which excites the electron into a higher energy state. In undoped semiconductors, the highest occupied electronic states are located at the valence band edge, and the lowest unoccupied states are located at the conduction band edge. Therefore, only photons with energies larger than E_g can be absorbed by the semiconductor [22, p. 142-144].

When an electron is excited across the band gap in the manner described above, an empty electronic state appears in the valence band, which is referred to as a hole. The hole in the valence band and the electron in the conduction band are free to migrate. Over short time scales, both the electron and the

hole relax to the edge of their respective bands. The semiconductor can then relax back to the ground state through relaxation of the electron in the conduction band into the empty state in the valence band represented by the hole. The recombination can occur either directly across the band gap, or via defects in the material. In either case, recombination requires release of the energy difference between the excited state and the ground state. If the recombination involves emission of a photon, it is radiative. Otherwise, it is non-radiative. The light emitted from the sample due to radiative recombination is referred to as luminescence, and is utilized in experimental techniques such as photoluminescence and cathodoluminescence spectroscopy [22, p. 142-146]. A schematic representation of absorption and luminescence is shown in Figure 2.1.

Generally, there is a dispersion of the valence and conduction bands as a function of the wave vector k of the electron. The energy of electronic states near the valence band maximum (VBM) and the conduction band minimum (CBM) are often approximated to have a quadratic dependence on k , resulting in parabolic band edges [21]. Figure 2.2 shows two notable cases. In the first case, Figure 2.2(a), the valence band maximum and the conduction band minimum occur at different wave vectors k , i.e. $k_{VBM} \neq k_{CBM}$. In this case, the band gap is indirect. In the second case, Figure 2.2(b), the band extrema occur at the same wave vector, i.e. $k_{VBM} = k_{CBM}$. The band gap is then direct [22, p. 90-92]. Since the wave vector of photons is negligible in the relevant energy range, transitions involving absorption or emission of photons are approximately vertical in Figure 2.2, and phonons are required to mediate transitions between the band edges in indirect band gap semiconductors [21, p. 189-190]. In direct band gap semiconductors, phonons are not required to mediate transitions between the band edges.

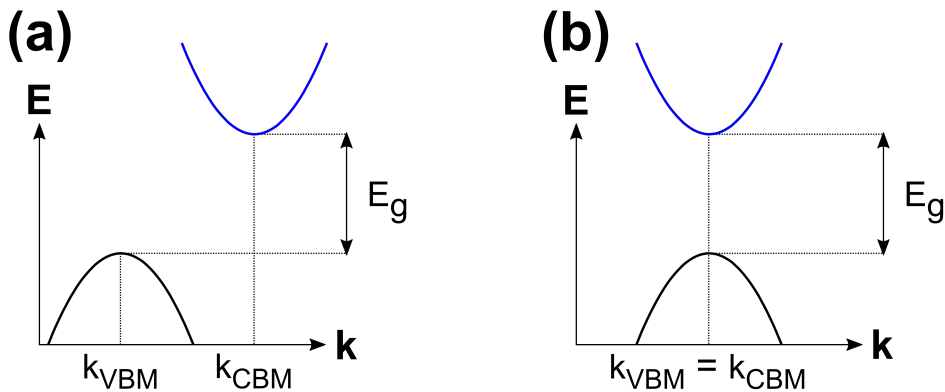


Figure 2.2: Relative position of valence band and conduction band edges for indirect band gap semiconductors (a) and direct band gap semiconductors (b), assuming approximately parabolic dispersions around the two band edges.

The width of the band gap is of critical importance for many semiconductor properties. Semiconductors with $E_g > 2$ eV are referred to as wide band gap semiconductors, and those with band gaps larger than those of GaN and SiC, corresponding to $E_g > 3.4$ eV, are referred to as ultra wide band gap semiconductors [4]. Ultra wide band gap semiconductors blur the conventional separa-

tion between semiconductors, typically assumed to have relatively narrow band gaps, and insulators, which have relatively broad band gaps. Thus, this class of materials constitute the current edge of semiconductor physics, and exhibit unique properties that can help solve important contemporary technological challenges. Despite the promising properties of ultra wide band gap semiconductors, most of these materials remain relatively undeveloped compared to conventional semiconductors. Both the understanding of basic material properties and the influence of commonplace processing techniques requires further research to enable future developments.

As was already mentioned in the introduction, there are several technological areas where ultra wide band gap materials could provide important improvements in performance. First, the band gap is strongly correlated with the critical electric field ϵ_{crit} , the maximum electric field a semiconductor can sustain before electrical failure occurs. Specifically, it has been reported that the correlation is well described by $\epsilon_{crit} \propto E_g^{1.83}$ [23]. Therefore, a modest increase in E_g provides comparatively large increases in ϵ_{crit} , which is beneficial in power electronics as it enables minimization of devices, thereby reducing conduction losses [5]. Baliga's figure of merit, which estimates the performance of semiconductors in power switching device applications [24, 25] is also high for many wide and ultra wide band gap materials compared to silicon, which has been the primary material used in power electronics [4, 6]. Since ultra wide band gap materials only absorb photons in the ultraviolet range of the electromagnetic spectrum, optical sensors based on these materials can provide selective sensitivity to ultraviolet light, while avoiding interference from longer-wavelength photons. This can be used to make solar-blind UV photodetectors in the wavelength range between 200 and 280 nm, where absorption in the ozone layer suppresses interference from solar radiation [7]. Solar-blind UV photodetectors attract interest for various applications including secure communications, flame detection, ozone hole monitoring, chemical and biological analysis, UV astronomy etc. [7]. The combination of optical transparency and electrical conductivity makes ultra wide band gap semiconductors suitable for use as transparent conducting materials (TCMs), which can be used to form optically transparent electrical contacts [12, 26]. The optical transparency also makes these semiconductors suitable for use as hosts for luminescence centers with optical emission in the visible and infrared [8, 9]. Luminescence centers denotes sites in the material, e.g. extrinsic defects, that can emit light through radiative recombination.

In ultra wide band gap semiconductors, n-type doping, i.e. introduction of electronic states close to the conduction band minimum, tends to be readily achieved, while p-type doping is often challenging. A notable exception is diamond, where p-type doping is comparatively easy, and n-type doping has been difficult [27]. Notable materials such as ZnO, In₂O₃, and Ga₂O₃ have relatively flat valence bands. This corresponds to large effective hole masses, which limits the mobility of holes at the valence band maximum and therefore the achievable p-type conductivity of the semiconductor [12, 28]. In oxides, the low-lying valence band which is typically mainly composed of O 2p-derived

orbitals can also make it difficult to introduce shallow acceptors [12, 28, 29]. Additionally, in several ultra wide band gap oxides, it is energetically favorable for a hole at the valence band maximum to localize on oxygen ions in the crystal lattice. This spontaneous localization gives a further decrease in the mobility of holes. Finally, in many ultra wide band gap oxides, p-type doping is rendered difficult by formation of compensating intrinsic defects [30, 31]. In combination, these challenges tend to render p-type doping of ultra wide band gap semiconductors challenging. Although ambipolar doping, i.e. the ability to dope a semiconductor n- or p-type depending on the chosen dopant, is a highly beneficial trait, unipolar devices can still be fabricated if ambipolar doping is unavailable. Moreover, if another suitable candidate with complementary polarity is available, heterojunctions could compensate for the lacking ambipolar doping, albeit at the cost of higher device complexity.

2.1 Polymorphism

Multiple crystal structures may exist for a single chemical composition. Each of the crystal structures is then referred to as a polymorph [20]. Polymorphism is a well-known phenomenon, first discovered by Mitscherlich in 1822, and the different polymorphs can have different physical properties [20]. At given conditions, e.g. temperature and pressure, one of the available polymorphs minimizes the free energy of the system and is the stable polymorph at the given conditions [20]. The other available polymorphs are metastable, and their formation is not thermodynamically favorable with respect to the stable polymorph.

Although a transition from any of the metastable polymorphs to the stable polymorph would be energetically favorable, whether or not the transition is observed depends on the transition rate. If the transition rate is sufficiently small, the metastable polymorph may in practice be stable indefinitely. The polymorphs of carbon present a well-known example. A transition from metastable diamond to stable graphite is not observed at ambient pressure and room temperature [20]. It is important to note that this stabilization is not thermodynamic in origin, and that thermodynamics therefore do not give a complete description of all aspects of polymorphism. The importance of kinetics in understanding transitions between polymorphs is also evident from the appearance of metastable phases during crystallization [32]. The polymorphism of Ga_2O_3 is relevant for this thesis, and will be discussed further in the next section.

2.2 Gallium oxide

Gallium sesquioxide, Ga_2O_3 , is an ultra wide band gap semiconductor which has received extensive research interest in recent years. The recent increase in interest is clearly illustrated by the number of Ga_2O_3 -related publications per year presented by Higashiwaki, exceeding 400 publications per year after 2019 [4]. It is commonly referred to simply as gallium oxide. Ga_2O_3 has

several distinct polymorphs [16, 33] including monoclinic β - Ga_2O_3 , corundum α - Ga_2O_3 , orthorhombic κ - Ga_2O_3 , spinel γ - Ga_2O_3 [34, 35, 36], and bixbyite δ - Ga_2O_3 [37]. ε - Ga_2O_3 was previously identified as a distinct hexagonal phase, but an article by Cora *et al.* revealed that ε - Ga_2O_3 is a structured version of κ - Ga_2O_3 [38]. The existence of δ - Ga_2O_3 is still under some debate, as some authors have suggested that it is composed of a mixture of β - and κ - Ga_2O_3 [16].

Corundum α - Ga_2O_3 can be synthesized with heteroepitaxy [35, 39] and is the stable polymorph at high pressure [40]. κ - Ga_2O_3 displays spontaneous polarization, which may enable formation of two-dimensional electron gases at its interfaces [41]. Cubic γ - Ga_2O_3 is predicted by first-principles calculations to have the highest formation energy of the Ga_2O_3 polymorphs at low temperatures [42]. β - Ga_2O_3 and γ - Ga_2O_3 are of the greatest importance for the results presented herein, and the other polymorphs will not be discussed in detail.

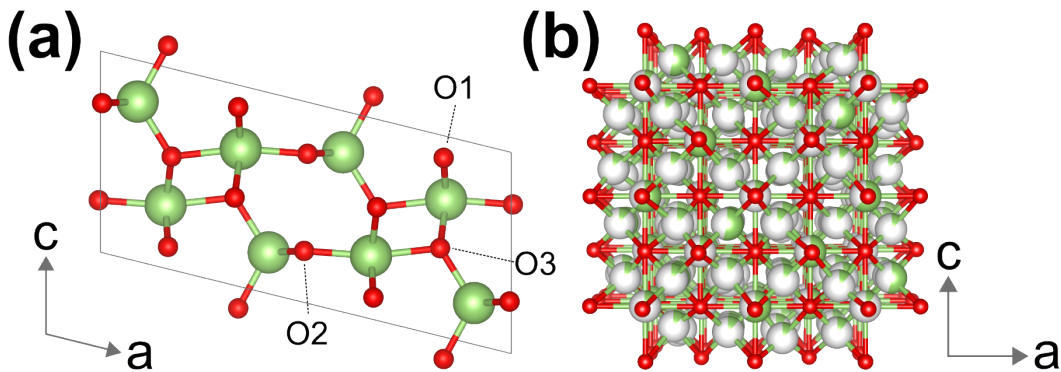


Figure 2.3: (a) The conventional unit cell of β - Ga_2O_3 , viewed along $[010]$. The labeling of inequivalent oxygen sites has been indicated. (b) The unit cell of γ - Ga_2O_3 , viewed along $[010]$. The green coloration of cations shows the partial occupancy of the various crystallographic sites. Anions are shown in red. The β - Ga_2O_3 structure is based on ICSD collection code 83645, while the γ - Ga_2O_3 structure is based on ICSD collection code 194506.

γ - Ga_2O_3 has spinel crystal structure, with systematic vacancies on the cation sites [36]. Figure 2.3(b) shows the crystal structure of γ - Ga_2O_3 . The systematic vacancies result from the difference in cation-to-anion ratio between Ga_2O_3 and the spinel composition AB_2O_4 where A and B denote metal cations. The ratio is $2/3$ for Ga_2O_3 and $3/4$ for the nominal spinel composition [43], resulting in systematic cation vacancies in γ - Ga_2O_3 . In previous work, it has been determined that cations occupy so-called "ideal spinel" sites, $8a$ (T_d) and $16d$ (O_h), and nonspinel sites, $48f$ (T_d) and $16c$ (O_h) [36]. The structural disorder in γ - Ga_2O_3 presents a challenge for first-principles calculations on this polymorph, but a recent article by Ratcliff *et al.* has demonstrated that a combination of density functional theory and machine learning techniques can be used to overcome this challenge [34]. γ - Ga_2O_3 has previously been observed as an interfacial layer in heteroepitaxial growth [44, 45]. γ - Ga_2O_3 nanoparticles have attracted attention in catalysis for anomalously high photocatalytic

activity [46], and for size-tunable phosphorescence [47].

Monoclinic β -Ga₂O₃ is the stable polymorph at ambient pressure and room temperature. The band gap of β -Ga₂O₃ has been reported in the range from 4.4 to 4.9 eV [13, 14, 15]. Literature results have demonstrated that the optical absorption edge is polarization-dependent [14, 15]. Figure 2.3(a) shows the conventional unit cell for β -Ga₂O₃, containing two crystallographically inequivalent Ga-sites, tetrahedrally coordinated Ga1 and octahedrally coordinated Ga2, and three inequivalent O-sites, two threefold-coordinated sites and one fourfold-coordinated site [48]. The low symmetry crystal structure of β -Ga₂O₃ results in anisotropic optical constants [49, 50], mechanical properties [50, 51], thermal conductivity [52], and diffusion rates [53].

N-type doping of β -Ga₂O₃ is readily achieved by introduction of group 14 elements [54, 55], while p-type doping has not been reliably and reproducibly demonstrated [4, 56], which is typical for ultra wide band gap semiconductors as discussed above, and is caused by low valence band dispersion [4, 57, 58], self-trapping of holes on oxygen atoms in the crystal lattice [48, 59], and compensating defects [30, 31]. In β -Ga₂O₃, self trapping at O1 and O2 sites is stable, while self-trapping at O3 sites is metastable [48]. It should be noted that recent reports of p-type conductivity in β -Ga₂O₃ exist in the literature [60], but independent reproduction of the results and further studies will be required to demonstrate that the difficulties listed above have been solved successfully. Since n-type doping of β -Ga₂O₃ is easily achievable, and since it is optically transparent in the visible range, β -Ga₂O₃ can be used as a transparent conducting oxide (TCO).

β -Ga₂O₃ has a high breakdown field, where fields up to 7 MV/cm have been reported [61], and it has a high Baliga's figure of merit value of 1570-1900 compared to 870 for GaN [4]. Therefore, β -Ga₂O₃ is expected to be well suited for power switching applications. The band gap value also makes β -Ga₂O₃ suitable for solar-blind UV photodetectors, as stated above [7]. The band gap of β -Ga₂O₃ is technically indirect, since the transition between the valence band maximum and the conduction band minimum involves momentum transfer, but the direct transition lies only about 50 meV above that of the lowest indirect transition [14].

Another large advantage of β -Ga₂O₃ is that relatively large single crystals can be fabricated easily by melt-growth methods, rendering wafers of β -Ga₂O₃ inexpensive compared to other wide band gap materials such as SiC and GaN [4]. Samples can be produced by floating zone [62], Czochralski [63], vertical Bridgman [64] or edge-defined film-fed growth [65, 66]. In edge-defined film-fed growth, a melt of source powder is transported up through a slit in a die [66]. At the top of the slit, crystal growth is initiated with a seed crystal. Dopants can be introduced by adding powders of appropriate oxides to the source powder [66]. This enables growth of n-type sample by addition of Si or Sn [66], and growth of semi-insulating samples by addition of Fe or Mg [4]. Epitaxial β -Ga₂O₃ can be grown, e.g. on bulk β -Ga₂O₃ substrates, by molecular beam epitaxy, halide vapor phase epitaxy, or metalorganic chemical vapor deposition [4].

The thermal conductivity of β -Ga₂O₃ is low, being 27.0 ± 2.0 W/mK along the [010] direction and 10.9 ± 1.0 W/mK along the [100] direction [52]. This presents a challenge to device fabrication, as it can limit performance and affect device reliability [4]. Thermal management is therefore essential in β -Ga₂O₃-based devices.

2.2.1 Polymorph transformation in ion-irradiated β -Ga₂O₃

When exposed to sufficiently high implantation fluences, initially crystalline samples tend to be amorphized. This occurs, for instance, for silicon [67, p. 66]. Over the last few years, it has become apparent that β -Ga₂O₃ does not follow this trend. Instead, exposure of β -Ga₂O₃ to high-fluence ion implantation results in the implanted layer undergoing a polymorphic phase transformation. This effect was first suspected by Wendler *et al.* [68], although they did not unambiguously demonstrate the effect. In the following years, reports first from Anber *et al.* [69], and subsequently from Azarov *et al.* [70] confirmed a polymorphic transformation in the ion-irradiated layer. In these two initial publications, X-ray diffraction and transmission electron microscopy was used to investigate the crystallographic structure in the implanted layer, and based on the available data it was concluded that the transformed layer could be identified as κ -Ga₂O₃. Petkov *et al.* have claimed that the β -phase was retained for 400 keV Ar-implantation up to 8×10^{15} Ar/cm². Notably, this work relied on *in situ* implantations into TEM samples, which have very low volume-to-surface ratio, and may therefore not be representative for similar implantation into bulk samples. The identification given also required high strain values, and did not provide conclusive indexing for a set of relatively bright spots in electron diffraction patterns along the proposed β -[207] zone axis [71].

Following these initial reports, there has been continued research into the polymorph transformation. More detailed structural characterization including indexing of electron diffraction patterns acquired from different zone axes reveal that it is the γ -Ga₂O₃ polymorph which is formed after high-fluence ion implantation, rather than κ -Ga₂O₃ or highly strained β -Ga₂O₃ as had initially been suggested [17, 18]. Subsequent results have corroborated this finding [19, 72]. Structural characterization of the polymorph transformation is presented in Papers I and II, and discussed further in Section 4.1 and 4.2. A schematic illustration of the transformation in ion-implanted β -Ga₂O₃ is shown in Figure 2.4.

Azarov *et al.* have demonstrated that the disorder accumulation in β -Ga₂O₃ is superlinear in the collision cascade density by performing shallow cluster ion implantations, and co-implantation with Ni [73], where detailed investigation of the disorder depth-profile for single implantations and co-implantations were also performed. It has been shown that diffusion of ion-implanted Si is suppressed for annealing in air up to 1000 °C if the implanted layer was transformed by additional implantation of Ni [74]. This work focused on explaining diffusion towards the sample bulk by a diffusion model of transport involving neutral and

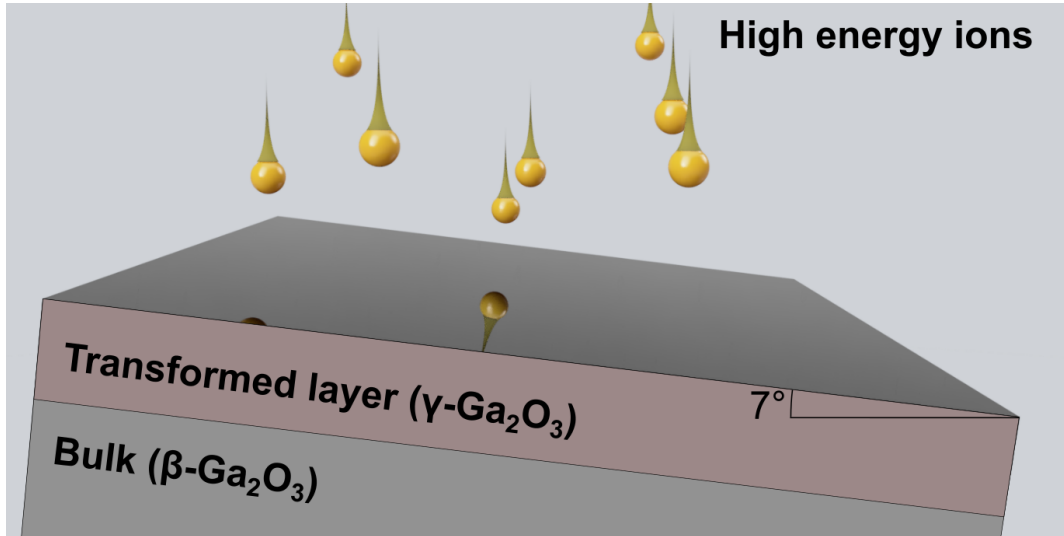


Figure 2.4: Schematic representation of high fluence ion implantation into $\beta\text{-Ga}_2\text{O}_3$, in which the top layer of the sample is transformed to $\gamma\text{-Ga}_2\text{O}_3$. The size of the implanted ions is not to scale. The sample is shown tilted 7° from the surface normal, which is a regular practice to reduce channeling effects.

singly negatively charged defects. Accumulation of Si at the sample surface was also observed, but was not the focus of the work and was not explained by the selected diffusion model.

It is important to understand the mechanism of the polymorph transformation for at least two reasons. First, a detailed understanding of the mechanism may explain why a polymorph transformation is observed instead of the typical amorphization. Second, it could explain why the polymorph transformation yields the $\gamma\text{-Ga}_2\text{O}_3$ polymorph, which has high formation energy [42], rather than another, lower energy polymorph. An important finding is that the chemistry of the implanted species appears to be largely inconsequential, as the polymorph transformation has been observed for implantation of many different species [17, 18, 68, 69, 70, 75]. Although far from all possible implanted species have been investigated, the available data concerns species with sufficiently dissimilar chemistry that chemical effects appear unlikely to be important drivers of the transformation. Defect production and strain accumulation in the implanted layer are plausible candidate causes for the observed polymorph transformation [76, 77]. Several aspects of the polymorph transformation were addressed in Paper II and will be discussed further below.

A full explanation of the transformation mechanism remains a topic of active research. In fact, key results on this topic have been reported very recently. A publication by Huang *et al.* is of particular note in this context. There, the authors provide scanning transmission electron microscopy images demonstrating formation of interstitial-divacancy complexes in ion-implanted $\beta\text{-Ga}_2\text{O}_3$ [77]. Importantly, these defects were found to cause a local change in the structure of $\beta\text{-Ga}_2\text{O}_3$, causing it to resemble $\gamma\text{-Ga}_2\text{O}_3$ crystallographically, thus providing a plausible transformation pathway between the two polymorphs via accumu-

lation of point defects [77]. The structural relation between the two phases was extended by Wouters *et al.* [78], by considering a "common" lattice between β - and γ -Ga₂O₃ with a shared oxygen sublattice, and a difference in cation population at the various sites, ordered in the case of β -Ga₂O₃ and disordered in the case of γ -Ga₂O₃. These approaches give a compelling explanation for the preferred formation of γ -Ga₂O₃ over other polymorphs after ion implantation. However, they do not fully explain why the polymorph transformation is preferred over amorphization in implanted β -Ga₂O₃.

Another recent publication from Azarov *et al.* has demonstrated that once the γ -Ga₂O₃ layer is formed, samples are remarkably resistant to further radiation damage from ion implantation, preventing amorphization up to very high implantation fluences [19]. Conservation of the oxygen sublattice was reported by Azarov *et al.* to be important for the high radiation tolerance, and to be due to strong recrystallization of the oxygen sublattice. This finding is consistent with approximate conservation of the oxygen sublattice in the β -to- γ transformation, which was, to the best of the author's knowledge, first pointed out in Paper II [18] in the specific context of the implantation-induced polymorph transformation. General reports of this structural relationship between the two phases were given in earlier work, e.g. by Playford *et al.* [16]. The publications from Huang *et al.* and Azarov *et al.* clearly show important advances in the understanding of implantation-induced polymorph transformations in Ga₂O₃.

When exposed to high temperature annealing, the transformed layer can be transformed back to β -Ga₂O₃ [72, 75]. This is unsurprising, as β -Ga₂O₃ is the stable polymorph. The transformation back to β -Ga₂O₃ during annealing will henceforth be referred to as the back-transformation. However, the crystallographic evolution in the layer as a function of temperature is non-trivial, showing a difference in the lattice matching between β -Ga₂O₃ and γ -Ga₂O₃ during recrystallization of β -Ga₂O₃ in the back-transformation compared with the lattice matching observed between β -Ga₂O₃ and γ -Ga₂O₃ in as-implanted samples. Contributions from the author of this thesis to crystallographic investigation of the back-transformation is contained in Papers I and III.

The functional properties of the implantation-induced γ -Ga₂O₃ layers, such as electrical or optical properties, remain scarcely investigated in the literature. Some initial characterization of electrical properties were undertaken by Polyakov *et al.* [79], providing numerous electrical measurements on samples implanted first with Ga to form a polymorph-transformed layer extending 1 μ m into the sample, followed by comparatively shallow Si-implantations to achieve n-type doping of the surface layer. However, the limitation of annealing temperatures imposed by the thermal stability of the transformed layer prevented the success of this method in forming samples with sufficiently good electrical properties. Instead, the authors had some success with treating the implanted samples with hydrogen plasma, which resulted in n-type films. An important issue exemplified by this publication is the difficulty in synthesizing samples with high conductivity without need for annealing at high temperatures around 1000 $^{\circ}$ C, for which back-transformation of the implanted layer occurs.

For some applications, suppression of the polymorph transformation may be

desired, as the back-transformation tends to yield β -Ga₂O₃ of relatively poor crystal quality [18, 75]. Another recent report from Sardar *et al.* has indicated that it is possible to suppress the transformation for Si-implantation by keeping the sample heated to 600 °C during implantation [80]. The authors were also able to demonstrate high levels of dopant activation in such samples, for implantation fluences above the polymorph transformation threshold. Heating of the sample during implantation is also effective in minimizing implantation damage for implantations below the polymorph transformation threshold, requiring lower temperatures than post-implantation annealing to yield similar results [81]. These findings may be important for fabrication of high crystal-quality β -Ga₂O₃ with high carrier concentrations by ion implantation.

2.2.2 Polymorph transformation from irradiation in other materials

Examples of polymorphic transformation in ion-irradiated materials, besides β -Ga₂O₃, have been reported in the literature previously, for ZrO₂ [82, 83], Y₂O₃ [84], HfO₂ [85], several lanthanide sesquioxides [86], and GaN nanowires [87]. This list has been limited to cases where transition from a stable initial polymorph to a metastable final polymorph has been reported. It is clear that implantation-induced polymorph transformations are not *unique* to β -Ga₂O₃, although they still appear to be relatively rare. The origin of the transformation in β -Ga₂O₃ could be similar to the origin of the transformation in one or more of the examples listed above, although there is no clear demonstration of such similarities to date, to the best of the author's knowledge. It is noted that the references for HfO₂ and lanthanide sesquioxides studied implantation energies in the MeV range, while the remaining references studied energies in the keV range, or in both energy ranges. As the experimental investigations of these effects in β -Ga₂O₃ have focused on the keV implantation energy range, literature references from the same range are likely to be of the greatest relevance.

The previous publication by Sickafus *et al.* concerning ZrO₂ is of particular importance [82]. Here, a transformation from a monoclinic stable phase to a higher-symmetry cubic or tetragonal phase was induced by ion implantation. More recent results have indicated that the final state is the tetragonal phase [88]. The transformation from a monoclinic stable state to a tetragonal phase is similar to what is observed in β -Ga₂O₃, where the transformation proceeds from a monoclinic to a cubic phase. Moreover, the authors suggested that the transformation in ZrO₂ may be caused by irradiation-induced point defects [82]. The transformation mechanism in β -Ga₂O₃ suggested by Huang *et al.* indicates that implantation-induced defects, particularly cation vacancies, may be important drivers of the observed transformation [77]. Finally, Sickafus *et al.* also reported that after the polymorphic transformation, the resulting phase was retained to very high peak displacement damage levels of 680 dpa, indicating high radiation tolerance [82]. This behavior has recently also been demonstrated in layers of implantation-induced γ -Ga₂O₃ by Azarov *et al.*, where the transformed layers were reported to remain stable up to 265

dpa [19]. Thus, several important features of the polymorph transformation are similar between ZrO_2 and Ga_2O_3 , supporting the hypothesis that the origins of the transformation may be shared across different materials. Furthermore, it appears likely that an improved understanding of the effect in $\beta\text{-Ga}_2\text{O}_3$ may be relevant to research concerning other materials.

Comparative studies of implantation-induced polymorph transformations across materials have not been undertaken as a part of the work presented in this thesis, where the focus has instead been to improve understanding of the effect in $\beta\text{-Ga}_2\text{O}_3$. Hopefully, the results obtained herein and in other recent literature can facilitate such comparisons in the future.

2.2.3 Defects

Intrinsic defects in $\beta\text{-Ga}_2\text{O}_3$ include the gallium and oxygen vacancies, V_{Ga} and V_{O} , and the gallium and oxygen interstitials, Ga_i and O_i . V_{Ga} acts as a polaronic triple acceptor [48]. Although it was previously believed that the unintentional n-type doping in $\beta\text{-Ga}_2\text{O}_3$ could be attributed to V_{O} , it has since been determined that this intrinsic defect is a deep donor with an ionization energy of more than 1 eV, and it therefore does not act as a shallow donor [55]. *Ab initio* calculations have revealed that gallium interstitials and vacancies can also exist in split interstitial and split vacancy configurations, in which displacement of adjacent gallium atoms lead to stabilization of the defect [89, 90]. It is noted that the formation energy of the various intrinsic defects depend on sample processing conditions. As an example, the formation energy of V_{Ga} is lower under oxygen-rich conditions than under gallium-rich conditions, and a greater concentration of V_{Ga} is therefore expected to form under oxygen-rich conditions [91]. Electronically, the most important extrinsic defects in $\beta\text{-Ga}_2\text{O}_3$ are the group 14 elements Si, Ge and Sn, which act as shallow donors when substituting on gallium sites [54, 55], and Mg and Fe, which are deep acceptors in $\beta\text{-Ga}_2\text{O}_3$ [54].

Bulk-grown $\beta\text{-Ga}_2\text{O}_3$ samples contain multiple impurity species, including Al, Si, Fe and Cr [66]. Cr in $\beta\text{-Ga}_2\text{O}_3$ has been reported to have charge state 3+ and to substitute on octahedral Ga sites [92, 93]. Cr in $\beta\text{-Ga}_2\text{O}_3$ exhibits strong luminescence, which will be discussed further in the next section. Two absorption bands at 425-440 nm and 585-620 nm have been attributed to ${}^4\text{A}_2 \rightarrow {}^4\text{T}_2$ and ${}^4\text{A}_2 \rightarrow {}^4\text{T}_1$ transitions of Cr, respectively [9, 93].

2.2.4 Luminescence

Despite having a direct transition lying close to the lowest-energy, indirect transition across the band gap, $\beta\text{-Ga}_2\text{O}_3$ does not typically display near-band-edge (NBE) luminescence, i.e. luminescence from recombination of an electron near the conduction band edge with a hole near the valence band edge. The author is aware of a report of NBE luminescence from $\beta\text{-Ga}_2\text{O}_3$ nanowires [94]. The normally observed luminescence of $\beta\text{-Ga}_2\text{O}_3$ is red-shifted with respect to the optical absorption, with the highest energy luminescence band appearing

at approximately 3.6 eV [59, 95]. This luminescence has been attributed to recombination of an electron near the conduction band edge with a self-trapped hole (STH) [59].

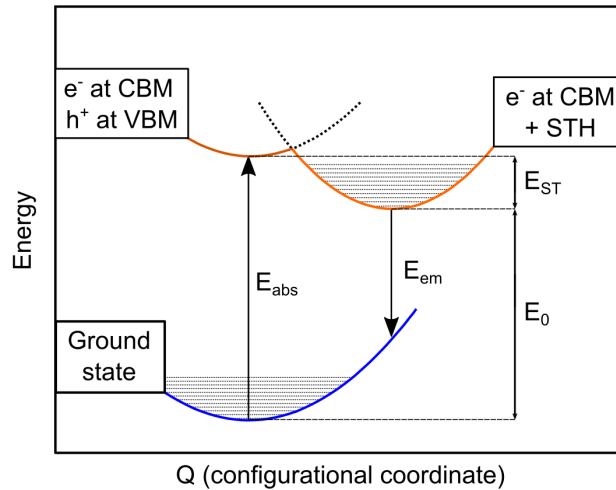


Figure 2.5: Configurational coordinate model for self-trapped holes in β -Ga₂O₃.

The emission due to self-trapped holes can be modeled using the configurational coordinate model. Absorption and emission processes in this model are shown in Figure 2.5. First, absorption of a photon moves the system into an excited electronic state with an electron at the CBM and a hole at the VBM, placing the system at the bottom of the upper left parabola in the figure [96]. Then, the hole localizes at an oxygen ion in the lattice. The resulting change in charge distribution yields a relaxation of the surrounding lattice, leaving the system at the bottom of the upper right parabola. The relaxation reduces the energy of the hole by E_{ST} . Due to the relaxation, the maximum energy released in radiative recombination of the electron at the CBM and the self-trapped hole is E_0 , corresponding to the zero-phonon line (ZPL). However, radiative recombination may also proceed via processes involving phonons, for which the energy of the luminescence will be less than E_0 with the remaining energy transferred to phonons. Thus, the emission is red-shifted with respect to the absorption [96, 97]. An expression for the emission line shape can be obtained by applying a semi-classical approximation [97, 98]. Importantly, the configurational coordinate model assumes that the configuration of lattice ions can be accurately represented by a single coordinate, an approximation which is frequently useful, but not universally applicable [99].

In β -Ga₂O₃, first principles calculations have revealed that localization of the hole is favorable at two of the three crystallographically inequivalent oxygen sites, yielding two luminescence contributions related to self-trapped holes [48]. Polarization-dependent photoluminescence measurements have provided experimental evidence for two distinct self-trapping sites being relevant for self-trapped hole luminescence in β -Ga₂O₃ [100].

In addition to the intrinsic STH luminescence, β -Ga₂O₃ exhibits several luminescence bands between 2.4 and 3.0 eV [95, 101, 102], commonly referred

to as the green and blue luminescence bands. The blue luminescence band has been attributed to defects, specifically to donor-acceptor-pair (DAP) recombination [103] involving intrinsic defects in β -Ga₂O₃ where V_O and Ga_i are reported candidate donors and V_{Ga} and V_O-V_{Ga} are reported candidate acceptors [101, 104]. Based on detailed cathodoluminescence measurements, Huynh *et al.* also reported that V_O is likely responsible for the blue luminescence [105]. Intensity enhancement of the green luminescence band has been observed for crystal growth under oxygen-rich atmosphere [102, 106]. Although not conclusively demonstrated, the green luminescence is also likely linked with defects, possibly donor-acceptor pair recombination [101] or isolated gallium vacancies [107]. The green luminescence is enhanced in presence of specific impurities including Ge and Sn [101, 106].

Cr³⁺ ions substituting at octahedral Ga-sites in β -Ga₂O₃ give strong luminescence in the red part of the visible spectrum [8, 9, 108]. The luminescence originates from transitions between the energy levels of Cr³⁺, split by the crystal field of the preferred substitutional site [92, 109]. Two narrow luminescence lines typically observed at around 689 and 697 nm wavelength have been demonstrated to be due to ²E→⁴A₂ transitions and are referred to as R₂ and R₁, respectively [9, 92]. A broad luminescence band centered at around 720-730 nm at temperatures of 150 K and above has been attributed to ⁴T₂→⁴A₂ transitions [9]. At cryogenic temperatures, a luminescence band is observed at wavelengths longer than R₁, consisting of multiple sharp luminescence lines. Temperature-dependent luminescence measurements have suggested that this band has the same origin as R₁ and it is therefore likely to be a side band to the ²E→⁴A₂ luminescence [9]. It is also noted here that both R₁ and R₂ red shift for increasing temperatures [9]. Thermal equilibrium between populations in the various excited states related to the luminescence lines and bands enable the use of luminescence from Cr in β -Ga₂O₃ for thermometry, and it has been demonstrated that this effect can successfully be used to probe in operando temperatures in catalysis [109]. Cr in β -Ga₂O₃ has also been suggested for use as a saturable absorber for passively Q-switched lasers [110] and pressure sensors [111]. The Cr-luminescence is strongly increased after high-temperature annealing in oxygen-rich atmosphere [112], and such annealing has also been reported to cause accumulation of Cr near the sample surface [106, 113]. Ion implantation with H- and He-ions has been demonstrated to increase the Cr-luminescence, which may be attributable to implantation-induced defects acting as sensitizers for luminescence from Cr-ions in β -Ga₂O₃ [114]. Similarly, Fe may sensitize Cr luminescence in Fe-doped samples [108]. Overall, Cr is an interesting emitter in β -Ga₂O₃, and an example case where the ultra wide band gap of β -Ga₂O₃ precludes optical absorption in the visible and infrared spectral ranges, and by which it can therefore act as a host for luminescence centers emitting in these spectral ranges.

2.3 Zinc oxide, zinc ferrite and Fe-decorated inversion domain boundaries

2.3.1 Zinc oxide

Zinc oxide, ZnO, is a wide band gap semiconductor with a direct band gap of 3.4 eV [115, 116], and a wurtzite crystal structure [117] with zinc atoms tetrahedrally coordinated by oxygen and vice versa. The ZnO C-axis ([0001]) is polar [117, 118].

N-type ZnO can be formed by incorporation of substitutional group-III dopants on Zn sites, as summarized by Janotti *et al.* [116]. In contrast, reliable and reproducible p-type doping of ZnO has remained elusive [117]. ZnO also exhibits large exciton binding energy [115, 116], and displays characteristic NBE luminescence where multiple exciton lines can be observed [115, 117]. In addition, various contributions from defects are frequently observed in the luminescence from ZnO. Specifically, intrinsic defects such as V_O , V_{Zn} and O_i and extrinsic defects likely contribute to the numerous luminescence bands of ZnO in the visible range of the electromagnetic spectrum, between approximately 1.75 and 2.6 eV [119, 120].

Previous work in our research group has demonstrated that ion implantation in ZnO followed by high temperature annealing can yield formation of nanoparticles embedded in ZnO. Specifically, both elemental Ge nanoparticles [121] and Zn_2GeO_4 nanoparticles [122] have been formed with this methodology, where the chemical composition of the nanoparticles depended on the annealing temperature. Paper V in this thesis investigates, among other topics, the incorporation of spinel $ZnFe_2O_4$ nanoparticles in ZnO, using a powder synthesis route.

2.3.2 Inversion domain boundaries in zinc oxide

Inversion domain boundaries (IDBs) are extended defects where the wurtzite crystallites located at opposite sides of the boundary have anti-parallel C-axis orientation [118]. Some trivalent metal ion species can promote formation of IDBs in ZnO, if they are incorporated in sufficiently high concentrations. In the resulting structure, accumulation of trivalent metal ions at IDBs is observed. Importantly for this thesis, the effect is observed for incorporation of Fe in ZnO [118, 123, 124].

The microstructure of ZnO containing such IDBs displays two types of IDBs. Basal IDBs (b-IDBs) are oriented parallel to (0001)-planes in ZnO, and feature crystallographic sites octahedrally coordinated by oxygen [118, 125]. Accumulation of Fe at b-IDBs has been reported to result in a close-packed monolayer of Fe^{3+} [118, 123]. Pyramidal IDBs (p-IDBs) are oriented parallel to $\{211\bar{l}\}$ - or $\{\bar{2}11l\}$ -planes in ZnO [118]. Fe also accumulates at p-IDBs. Based on the existing literature, Fe^{3+} at p-IDBs is probably located at trigonal bipyramidal sites [118, 124]. The orientation of the C-axes in the adjacent wurtzite crystallites is different for the two types of IDBs. For b-IDBs, the

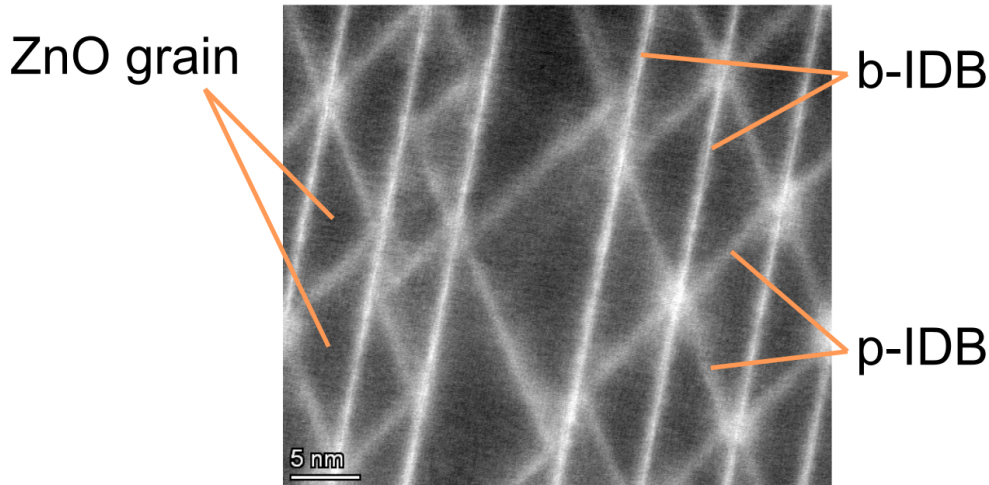


Figure 2.6: Scanning transmission electron microscopy image of a sample containing Fe-decorated IDBs, viewed along the ZnO- $[1\bar{1}00]$ zone axis. ZnO grains appear as dark triangles, and b-IDBs and p-IDBs appear as bright lines. Adapted from Paper V [126].

C-axes are oriented towards the IDB (head-to-head orientation [118]) while for p-IDBs the C-axes are oriented away from the IDB (tail-to-tail orientation [118]). The preferential occupation of sites at the IDBs by Fe is henceforth referred to as Fe-decoration of the IDBs.

When viewed along the $[1\bar{1}00]$ direction, referenced to the ZnO crystallites, both types of IDBs are visible [118, 124, 125]. The Fe-decorated b-IDBs appear as a series of parallel lines when viewing along this direction. The separation between adjacent pairs of b-IDBs is variable. Fe-decorated p-IDBs are seen as zigzag lines between b-IDBs, further dividing the ZnO grains, which appear as triangles. Figure 2.6 shows an example scanning transmission electron microscopy image of Fe-decorated b-IDBs and p-IDBs in ZnO.

The existing literature on Fe-decorated IDBs in ZnO has predominantly focused on detailed structural characterization. In contrast, little research has been dedicated to revealing the effects of such a defect network on functional properties of the sample, e.g. optical absorption. Although the networks of Fe-decorated b-IDBs and p-IDBs described above are not entirely regular, high-resolution electron microscopy images in the literature show that the orientations of the defects are retained over distances much larger than the separation between neighboring b-IDBs [124, 125, 127], and as such they form a quasi-regular network of extended defects with enriched Fe-concentrations. The effect of such structures on sample properties is of scientific interest and warrants further study.

2.3.3 Zinc ferrite

Zinc ferrite, ZnFe_2O_4 , has a cubic spinel crystal structure and a band gap of around 2.0 eV [128, 129]. The trivalent Fe-ions and the divalent Zn-ions are situated on octahedral and tetrahedral sites in a pseudo-cubic close-packed

lattice of oxygen ions [130]. Nanoparticles of ZnFe_2O_4 embedded in ZnO have received research attention for applications in photocatalysis, and for their magnetic properties [131, 132, 133].

Spinel has a degree of freedom associated with distribution of bivalent and trivalent metal ions across octahedral and tetrahedral sites, conventionally referred to as the degree of inversion or the inversion parameter x . When the inversion parameter is included, the spinel structure of ZnFe_2O_4 can be expressed as $[\text{Zn}_{1-x}\text{Fe}_x]_{\text{tet}}[\text{Zn}_x\text{Fe}_{2-x}]_{\text{oct}}\text{O}_4$, where subscripts "tet" and "oct" denote tetrahedral and octahedral cation sites respectively [134]. For $x = 0$, the divalent Zn-ions exclusively occupy tetrahedral sites, and the trivalent Fe-ions exclusively occupy octahedral sites. This is referred to as *normal* spinel. For $x = 1$ half of the octahedral sites are occupied by divalent Zn-ions, while trivalent Fe-ions occupy the remaining octahedral sites and all the tetrahedral sites. This is referred to as *inverse* spinel [129, 130].

Ambiguous literature reports exist concerning the impact of the inversion parameter on the properties of ZnFe_2O_4 . Specifically, some authors have reported a dependence of the band gap on the inversion parameter [129], while others have observed little or no variation of the band gap with the inversion parameter [128].

Chapter 3

Sample fabrication and characterization

In this chapter the main fabrication technique used in this work, namely ion implantation, is first introduced and discussed in Section 3.1. Then, the various characterization methods which have been used in the presented work are introduced in Section 3.2.

3.1 Sample processing

3.1.1 Ion implantation

Introduction of impurities with controlled concentration and spatial distribution is an essential step in fabrication of many semiconductor devices. Ion implantation provides excellent control over both the concentration and the spatial distribution of dopants, and is therefore a widely used and very important processing technique [67, p. 63]. A challenge with ion implantation is that it is intrinsically linked to generation of defects in the implanted sample. Alternative methods to introduce dopants exist, one notable example being in-diffusion. However, the dopant profiles generated by in-diffusion are governed by thermodynamic driving forces and kinetics which are highly temperature dependent and difficult to control. In contrast, ion implantation provides easily controlled dopant profiles [67].

Since fabrication of many devices requires ion implantation, a detailed understanding of the effects of ion implantation in novel semiconductors is a necessary condition for their technological maturity. In Ga_2O_3 , the effects of ion implantation is a rich topic, including polymorphic transformations for high fluence implantations, which was introduced above and will be discussed further below. From a technological point of view, introduction of defects in the implanted layer is typically undesirable, as it alters and potentially degrades the electronic properties of the sample [67, p. 171-175]. From a semiconductor physics point of view, this feature enables controlled introduction of defects, which can be used to study defects in semiconductors.

Historical technological developments have resulted in a wide variety of in-

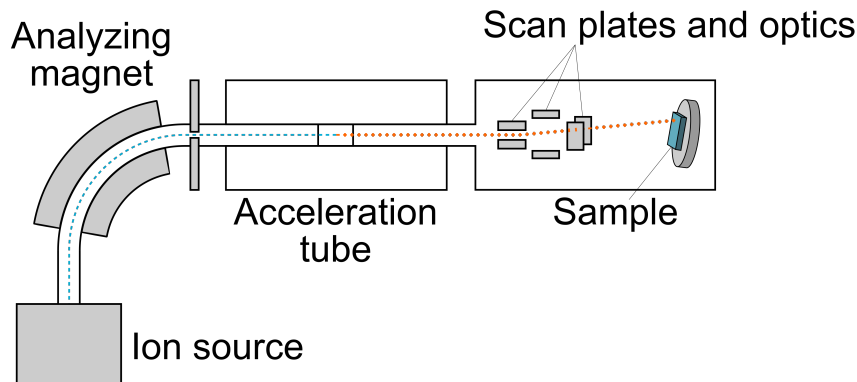


Figure 3.1: Simple schematic representation of an ion implanter. Ions of the desired species and charge are selected by an analyzing magnet and selection slit, after which the negative ions are accelerated by electric fields in the acceleration tube. Charge exchange converts the ions from negative to positive polarity (visualized as change in color and symbol of the beam), providing a doubling of the ion energy. The ions are finally focused into a beam and scanned across the sample to provide uniform implantation, either by scanning the ion beam or by scanning the sample.

strumentation for ion implantation. In general, the key parts of ion implanters include the ion source, from which ions with the desired charge state are extracted by ionization of a precursor, an analyzing magnet and mass defining aperture, through which only ions with the selected mass and charge are transmitted, an acceleration tube, where the ions are accelerated to the selected energy using electric fields, electromagnetic optics, which provide beam shaping, and scanning of either the beam or the sample holder [67, p. 311]. In tandem accelerators, which is the type of accelerator used in the present thesis, initially negative ions undergo charge exchange in the acceleration tube, yielding positive ions [67, 135]. For a given positive acceleration bias in the acceleration tube, the effect is a doubling of the ion energy [135]. A schematic representation of the main components in a tandem accelerator is shown in Figure 3.1.

For convenience, ions in the ion beam will be referred to as primary ions to distinguish them from ions in the sample. After entering the sample, a primary ion loses energy to electronic stopping, caused by interaction with sample electrons, and collisions with sample nuclei. The energy losses eventually cause the primary ions to come to rest at a certain depth in the sample. Both electronic stopping and collisions with sample nuclei contribute to the implantation damage, although it is primarily the latter that generates target atom displacements [67, p. 63-67]. First, collisions with a sufficiently large energy transfer, i.e. larger than the displacement energy, can directly displace sample nuclei from their lattice sites, thus creating a Frenkel pair consisting of a vacancy and an interstitial. If the kinetic energy of the displaced ion is sufficiently large, it may undergo secondary collisions with other sample nuclei, and the ion beam thereby creates collision cascades in the implanted sample. Moreover, propa-

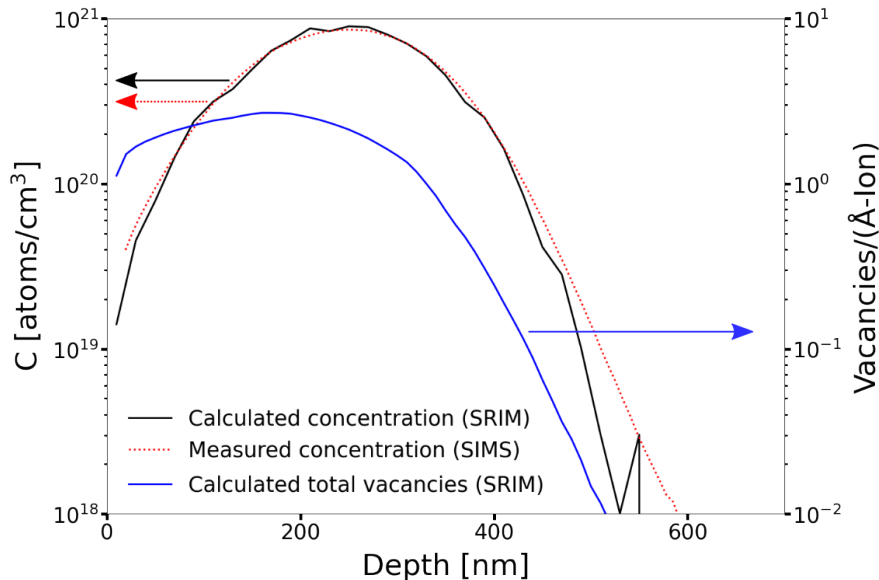


Figure 3.2: Example plot of SRIM-calculated concentration of the implanted species and total vacancy production as a function of depth for 650 keV Ge-implantation into β -Ga₂O₃. The concentration profile has been calculated for an implantation fluence of 2×10^{16} Ge/cm², and the concentration profile of Ge in a sample implanted to the same fluence was measured using secondary ion-mass spectrometry. Colored arrows indicate the y-axis for the different graphs.

gation of displaced nuclei combined with thermal diffusion in the sample from ion-induced heating contribute to migration and agglomeration of point defects [67, p. 66]. The accumulation of defects from ion implantation also often gives rise to strain in the implanted layer [76, 136].

In implantation of single crystal samples, the orientation of the sample during implantation is important. Primary ions are channelled if the angle between the ion beam and some high-symmetry axis of the single crystal sample is smaller than the critical angle, which is typically between 2° and 5° [67, p. 167-168]. When channelled, the ion is steered between atomic rows or planes in the crystal, referred to as axial and planar channelling respectively, by multiple correlated small angle scattering events. This effect is important in ion implantation, since a channelled ion has a drastically reduced probability to undergo collisions with sample nuclei, and can therefore penetrate the sample to greater depths than an unchannelled ion. When reproducible dopant depth profiles are required, it is therefore necessary to suppress channelling. To achieve this, one typically tilts the sample to a small angle, e.g. 7°, prior to implantation, although it should be noted that this procedure is not expected to fully suppress channeling [67, 137].

In ion implantations where channeling effects are relatively unimportant, the depth-distribution of implanted ions can be estimated using Monte Carlo methods. A software that is often used for such calculations is "The Stopping and Range of Ions in Matter" (SRIM) [138]. The calculations give the expected depth distribution of implanted ions given the composition and density

of the sample as well as the implanted species, implantation energy and sample tilt. The results typically show good agreement with experimental data, as can be verified for the SRIM-calculated and measured concentration profiles in Figure 3.2. The projected range R_p , defined as the depth where peak concentration of the implanted species is observed [135], is often used to quantify the implantation depth. In Figure 3.2, there is a minor divergence of calculated and measured concentration profiles below R_p , which can in part be attributed to a tail due to channeling effects [139].

SRIM can also be used to estimate the defect concentrations generated during implantation if the displacement energies of each constituent atomic species in the sample is known. The defect profile is shown in Figure 3.2, demonstrating that the vacancy concentration induced by ion implantation is peaked at depths somewhat shallower than R_p . The induced damage can be quantified by the number of displacements per atom (DPA). The peak DPA value can be calculated from SRIM-calculated vacancy profiles such as the one shown in Figure 3.2 by

$$\text{DPA} = \frac{N_{vac}^{max} \cdot f}{n_{at}} \quad (3.1)$$

where N_{vac}^{max} is the maximum value of the vacancy profile, f is the implantation fluence, and n_{at} is the atomic density of the sample, following the formalism described in the supplementary of Azarov *et al.* [19]. Conveniently for the case of calculating implantation damage in Ga_2O_3 with implantation-induced polymorph transformations, the densities of $\beta\text{-Ga}_2\text{O}_3$ and $\gamma\text{-Ga}_2\text{O}_3$ are similar, and only a minor error is introduced by using the atomic density of $\beta\text{-Ga}_2\text{O}_3$ to estimate DPA, even for implantation fluences above the polymorph transformation threshold, as was pointed out by Azarov *et al.* [19]. It should be noted that the Ga and O displacement energies could in principle differ between the two phases. It is noted that the numerical accuracy of SRIM-calculated DPA values has been discussed in the recent literature [140, 141], although this should not be an important problem when DPA values calculated with the same methodology are used to compare implantation damage between studies. Moreover, as stated explicitly in SRIM Tutorial #4, which is provided along with the software, SRIM damage calculations already neglect "self-annealing" or dynamic annealing of implantation-induced damage, being effectively calculations of the damage expected for an implantation temperature of 0 K [138]. At common implantation temperatures, e.g. room temperature, sample atoms have sufficient thermal energy to allow partial recombination of the implantation-induced defects, and thus the real defect concentrations are expected to be lower than those calculated using SRIM. As an example, previous literature has stated that around 5% of implantation-induced vacancies survive dynamic annealing in Si [142], and that around 3% of implantation-induced vacancies survive dynamic annealing and a 300 °C post-implantation annealing in SiC [143]. However, SRIM-calculated defect concentrations should still enable comparisons between different implantation parameters.

Ion implantation is inherently a non-equilibrium technique, enabling im-

plantation of ions to concentrations exceeding the solid solubility of the implanted species in the sample [121]. The concentration of the species after implantation can be controlled by varying the implantation fluence, i.e. the number of ions implanted per unit surface area. The depth distribution can also be controlled, by selecting the implantation energy, i.e. the energy of the implanted ions, and optionally by performing multiple implantations at different energies, e.g. to create a depth range in the sample with approximately constant concentration of the implanted species known as a box profile [69, 79].

The rate at which ions are implanted into the sample, i.e. the ion beam current or flux, and the temperature of the sample during implantation both have an effect on the production of defects in the implanted sample. More specifically, the average time between neighboring ion impacts is determined by the ion beam flux, while the sample temperature affects defect migration and defect annihilation rates [76]. Thus, for sufficiently high ion flux or sufficiently low temperature, the time between neighboring impacts is lower than the time required for annihilation or stabilization of defects created in a single cascade, leading to an overlap of the regions containing defects produced in the two cascades. This overlap is expected to increase the number of defects produced by the implantation, for a fixed implantation fluence, which was recently demonstrated for implantation in β -Ga₂O₃ by Azarov *et al.*, who varied both the ion beam flux and the sample temperature [76].

During implantation, the implanted sample is heated as a result of energy transfer from the ion beam. Parry *et al.* have demonstrated that this heating can be modeled. The authors considered the heating from the ion beam as well as conductive and radiative cooling, which revealed that significant heating can result for implantation in silicon [144].

Post-implantation annealing is frequently applied to ion-implanted samples. This process can reduce the damage in the implanted layer by assisting annihilation of implantation-induced defects [67, p. 171-175]. Similarly, for electrically or optically active implanted species, annealing assists in their incorporation in the semiconductor crystal lattice and thus provides activation of the implanted species [67, p. 171-175]. Annealing also promotes increased diffusion rates, which can yield transport of implanted species towards the surface or the bulk of the sample, yielding implantation profile broadening. If extrinsic species are implanted to sufficiently high concentrations, the implanted species may agglomerate and form secondary phases during annealing [121, 122]. Annealing can also produce defects in the sample, particularly close to the sample surface. As a specific example, annealing of Ga₂O₃ in oxygen-rich atmosphere was reported to produce gallium vacancies [145].

3.2 Characterization methods

This section introduces the main characterization methods used in this work. This includes structural characterization by X-ray or electron diffraction, secondary-ion mass spectrometry and ion backscattering, as well as absorption measurements by optical and electron microscope based methods, and luminescence measurements.

3.2.1 X-ray diffraction

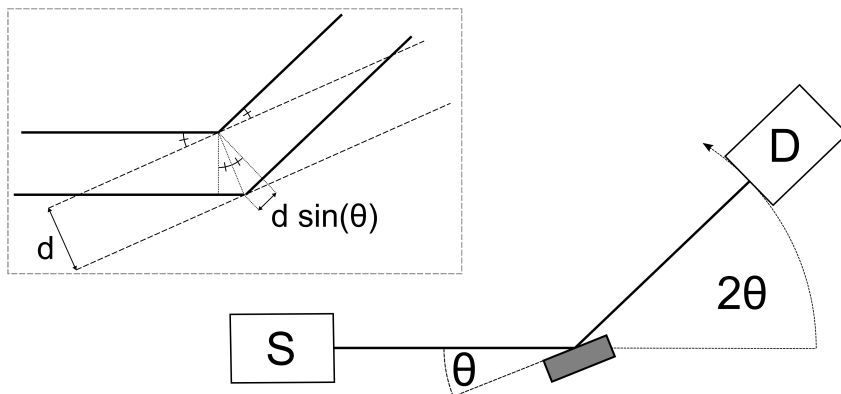


Figure 3.3: θ - 2θ X-ray diffraction configuration. X-rays are emitted from the source (S) and collected at the detector (D). The inset shows the geometric construction which yields the Bragg condition, where angles of size θ have been marked. For values of θ satisfying the Bragg condition, constructive interference gives high intensities at the detector.

X-ray diffraction (XRD), is a convenient non-destructive method for structural characterization of crystalline samples. When monochromatic X-rays impinge on a crystalline sample, they undergo diffraction due to elastic scattering from sample electrons [146]. X-rays are used since their wavelengths are comparable to the atomic spacings in the crystal [21, p. 3-25].

The inset in Figure 3.3 shows a schematic illustration of diffraction from a single crystal sample. Here, the crystal is assumed to consist of lattice planes, separated by a distance d . If X-rays scattered from neighboring planes have the same phase, constructive interference yields a diffracted beam of X-rays. Constructive interference then occurs for angle θ and X-ray wavelength λ when

$$2d \sin(\theta) = n\lambda, n \in \mathbb{N} \quad (3.2)$$

which is the Bragg condition [21]. The plane spacings in the crystal can be determined by observing the angles θ for which the Bragg condition is satisfied, yielding constructive interference at the detector, referred to as a diffraction peak. Thus, by observing the angles for which the intensity at the detector displays peaks, the plane spacings in the crystalline sample can be determined.

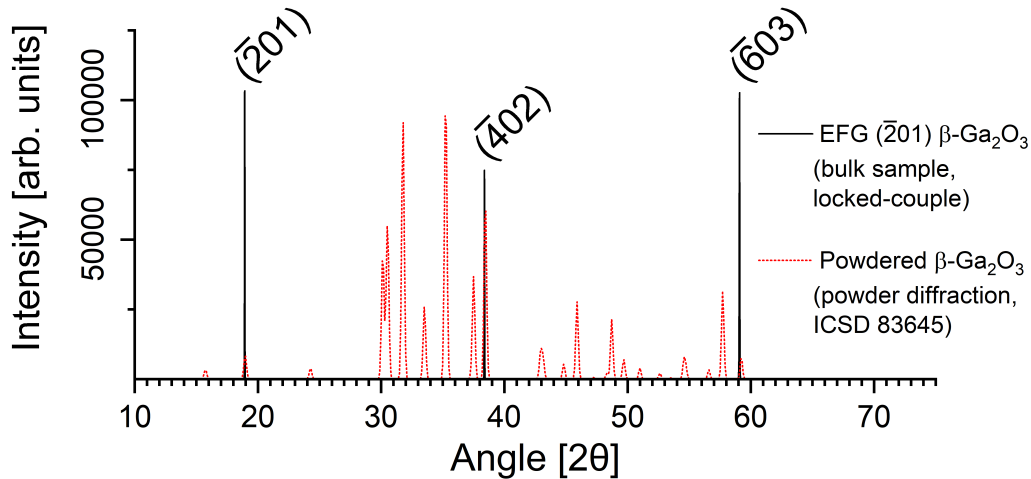


Figure 3.4: Example locked-couple diffractogram from an as-received edge-defined film-fed grown bulk $(\bar{2}01)$ -oriented β -Ga₂O₃ sample, and a powder diffraction pattern of β -Ga₂O₃ from the literature [147] exported from ICSD (collection code 83645). Only diffraction peaks present in from the former have been indexed. The intensity of the powder diffraction pattern has been scaled by a factor 15.

More generally, diffraction is observed when the scattering vector $\Delta\mathbf{k}$, the difference between the wavevector of the outgoing beam \mathbf{k} and the ingoing beam \mathbf{k}_0 , equals a reciprocal lattice vector \mathbf{G} of the crystal, i.e. $\Delta\mathbf{k} = \mathbf{G}$ [21].

Figure 3.3 shows the geometry of an XRD scan in which the X-ray source is kept stationary, the sample is rotated through an angle θ , and the detector is displaced an angle 2θ along a circular path centered at the sample. Then, the incident and diffracted beams form equal angles with the sample surface and the scattering vector remains parallel to the sample surface normal for all θ . Only diffraction from lattice planes oriented parallel to the sample surface give rise to constructive interference at the detector in such an XRD measurement [146]. This is observed in Figure 3.4, where diffraction is only observed from $(\bar{2}01)$ -planes in an as-received edge-defined film-fed grown $(\bar{2}01)$ -oriented β -Ga₂O₃ sample, whereas the powder diffraction pattern from the literature [147], ICSD collection code 83645, displays diffraction from several additional crystallographic planes. It is noted that by adding an offset to the rotation of the sample in Figure 3.3, it is possible to observe diffraction from planes which are not oriented parallel to the sample surface. This corresponds to changing the sample rotation from θ to ω . This is, for instance, useful to measure diffraction from single crystal samples or thin films in which the lattice planes are not perfectly aligned with the sample surface, e.g. where there is a miscut.

3.2.2 Optical absorption and diffuse reflectance measurements

The optical absorption of samples can be measured in transmittance spectroscopy, where the absorption of light transmitted through the sample is measured as a function of wavelength. However, transmittance spectroscopy measurements are not applicable in the case of strongly scattering samples or non-transparent substrates. Fortunately, the optical absorption properties of such samples can instead be probed by the alternative method of diffuse reflectance spectroscopy (DRS).

In DRS, the diffuse reflectance from a mat surface layer is measured as a function of wavelength. The absorption coefficient is obtained through the Kubelka-Munk equation

$$\frac{(1 - R_\infty)^2}{2R_\infty} = \frac{k}{s} \quad (3.3)$$

where R_∞ is the ratio of diffuse reflectance from the layer of interest, referred to a non-absorbing standard, $R_\infty = \Phi_{sample}/\Phi_{standard}$, k is the absorption coefficient, and s is the scattering coefficient. The scattering coefficient is typically assumed to be independent of wavelength, for which the left hand side in the equation is proportional to the absorption coefficient [148, p. 46-67].

The fundamental band gap of semiconductors can be assessed from the onset of optical inter-band absorption, which occurs for photon energies larger than the band gap. Hence, by determining the photon energy at which optical absorption begins, E_g can be determined. In practice, there is often an exponentially decaying absorption tail below the band gap, known as the Urbach tail [149, 150], which complicates determination of the band gap from optical absorption measurements. However, for both direct and indirect band gaps, the expected functional shape of the absorption onset is known, specifically

$$(\alpha h\nu)^{1/n} = A(h\nu - E_g) \quad (3.4)$$

where α is the absorption coefficient, h is Planck's constant, ν is the photon frequency, and A is a proportionality constant [149, 151]. n takes the value 1/2 for direct allowed transitions and 2 for indirect allowed transitions. The values of n become 3/2 and 3 for the corresponding forbidden transitions. Therefore, when plotting $(\alpha h\nu)^{1/n}$ on the ordinate and $h\nu$, the photon energy, on the abscissa, a region of linearity should be observed near the absorption onset for the correct transition type. The band gap E_g is then determined by extrapolating a linear fit in this region to its intersection with the abscissa. Plots generated with this procedure are referred to as Tauc plots. In principle, the transition type can be determined by evaluating the value of n that gives the best fit in the Tauc plot, i.e. a clear linear region [149]. In practice, such regions of linearity are sometimes present for more than one transition type. In this case, determination of the band gap is still possible if the correct transition type is known. It is important to note that the procedure outlined determines the optical band gap, which may be different from the fundamental band gap, e.g.

in the case of highly doped semiconductors where a Burstein-Moss shift may be present [152].

An additional complication arises in composites where two phases with different band gaps are present. The narrowest band gap can be determined using the Tauc plot technique described above. Near the absorption onset for the wider band gap, there may be contributions from absorption in the other phase. Then, extrapolation of the linear fit to the abscissa may yield erroneously low band gap values.

3.2.3 Scanning electron microscopy

In scanning electron microscopy (SEM), a focused electron beam impinges on the sample of interest under vacuum conditions. Electrons in the beam are referred to as primary electrons, and typically have energies below 30 keV. The width of the beam determines the achievable resolution, which is typically between 1 and 10 nm depending on the electron source [153, p. 16]. The beam is scanned stepwise across the sample using scanning coils with some dwell time at each step. One of several possible signals is acquired for each position of the beam on the sample. The intensity of the selected signal can then be correlated with the known position of the electron beam on the sample at the given time, from which an image of the sample is formed. The different available signals arise from different physical processes, and therefore provide information about different properties of the sample [153].

Primary electrons entering the solid sample undergo elastic and inelastic scattering. Due to the associated energy losses, the primary electrons penetrate the sample only to some maximum depth called the penetration depth. One also typically refers to the interaction volume as the part of the sample containing the scattered electrons [153].

A small fraction of the primary electrons are scattered elastically to angles greater than 90° . During such large-angle scattering, the energy loss of the electron is relatively small. Since the backscattered electron retains high kinetic energy, it has a reasonable probability to be reemitted through the sample surface, where it can be collected by a detector placed at high scattering angle with respect to the primary electron beam. The cross-section for high-angle scattering is strongly dependent on the mass of the sample atoms, and the contrast in backscatter electron images therefore carries information about variations in the chemical composition of the sample. [153]

The primary electrons also undergo inelastic scattering from sample electrons, in which the energy lost by the primary electron is transferred to the sample electron. For sample electrons in the valence or conduction bands, a part of this energy transfer causes release of the sample electron to an unbound state, and the remainder provides the kinetic energy of the unbound electron. Electrons produced in this way are referred to as secondary electrons, and typically have initial kinetic energies below 100 eV. Due to their comparatively low kinetic energies, secondary electrons have short mean free paths in the sample, typically on the order of a few nanometers [153]. Consequently, only secondary

electrons generated at most a few nanometers from the sample surface can be emitted from the sample and reach the detector. Therefore, the secondary electron signal is highly surface sensitive, and can be used to study sample topography [153].

In inelastic scattering of a primary electron from an inner-shell electron in the sample, the inner-shell electron may be excited to a higher-lying vacant state, leaving behind an inner-shell electron vacancy. After a short time, an electron relaxes into the now vacant inner-shell electron state, and may release the excess energy as an X-ray photon. These characteristic X-ray photons are measured in energy-dispersive X-ray spectroscopy (EDS). As the photons are characteristic for the respective element, the spectra of X-ray photons emitted by the sample during electron beam irradiation can be used to characterize the sample composition. For light elements, the excess energy is more likely to produce an Auger electron than an X-ray photon, and the EDS intensity from light elements is therefore weak [153].

Recombination of electron hole pairs generated in the interaction volume during electron beam irradiation of the sample can also yield emission of photons in the ultraviolet, visible and infrared ranges of the electromagnetic spectrum, which will be discussed separately in Section 3.2.4.

3.2.4 Cathodoluminescence

When a primary electron from an electron beam is scattered inelastically by a semiconductor sample, transferring a few eV to an outer-shell electron, an electron from the valence band may be excited into the conduction band, creating an electron hole pair [153]. Radiative recombination of the electron hole pair yields luminescence. In cathodoluminescence (CL) an electron beam incident on the sample of interest is used to generate electron hole pairs, and the resulting luminescence is detected. CL is often performed in a scanning electron microscope, where the luminescence can be recorded as a function of the position of the electron beam on the sample. In comparison to other luminescence techniques, the excitation provided in CL is highly localized, which can permit probing of the luminescence properties of the sample with excellent spatial resolution. The description of CL given here is restricted to incoherent luminescence [154]. Coherent transition radiation can also be excited in CL [154], but discussion of such effects is omitted here as they are not important for the purposes of this thesis. Figure 3.5 shows a schematic of a CL measurement setup with a spectrograph. CL instruments are commonly integrated in a scanning electron microscope, where a concave parabolic mirror positioned above the sample is used to collimate the luminescence emitted from the sample [154]. The electron beam is focused onto the sample through a small hole in the parabolic mirror. The collimated luminescence from the parabolic mirror can be passed to a spectrograph for analysis.

Luminescence measurements are often performed at cryogenic temperatures. The advantages are twofold. First, at low temperatures, sharp features such as excitonic lines can sometimes be resolved, and the observed lu-

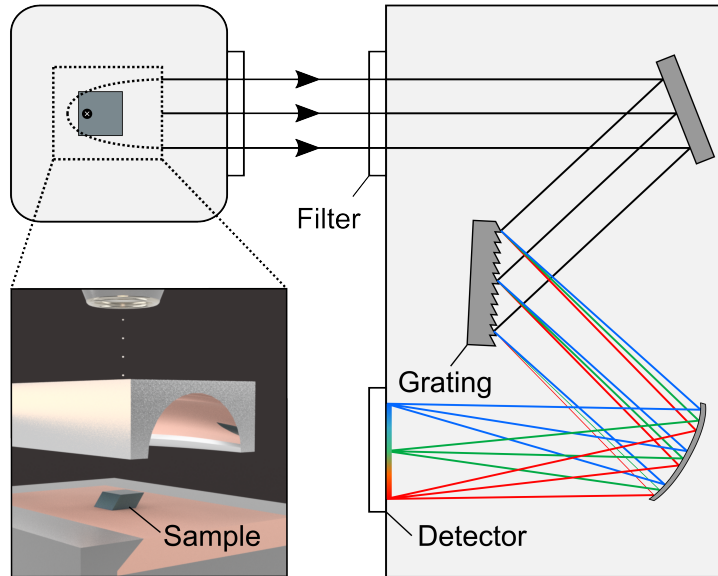


Figure 3.5: Top-view schematic of cathodoluminescence measurement setup. In the inset (lower left), an electron beam transmitted through a hole in the parabolic CL mirror impinges on the sample surface, generating electron hole pairs within the generation volume. Radiative recombination of the electron hole pairs causes light emission, and the light which is emitted through the sample surface is collimated by the parabolic mirror. The collimated light is transported to a spectrograph (top view schematic), where an optical grating disperses the light by wavelength. The dispersed light is directed onto a CCD detector, where spectra are recorded as a function of wavelength.

minescence generally tends to be sharper at low temperatures than at high temperatures since thermal broadening effects are minimized [155]. Second, the luminescence intensity tends to increase, since the rates of non-radiative recombination are lowered at cryogenic temperatures [154, 155, 156].

The primary electrons in the electron beam typically have energies ranging from 1 to 30 keV, and electron hole pairs are generated in the interaction volume. For this reason, the interaction volume is also referred to as the generation volume in the context of CL [154]. On average the energy required to produce an electron hole pair is approximately $3E_g$ [157], so a large number of electron hole pairs are generated per primary electron. As an example, a primary electron with energy 10 kV may then produce up to approximately 700 electron hole pairs in $\beta\text{-Ga}_2\text{O}_3$.

The size of the CL generation volume at a given acceleration voltage can be estimated by Monte Carlo calculations if the composition and the density of the sample are known [158]. Analytical approximations also exist for the depth of the interaction volume [153, p. 125]. An increase in the acceleration voltage yields an increase in the size of the generation volume, both in the lateral direction and in the depth direction. By varying the acceleration voltage, it is therefore possible to probe the depth-dependence of the luminescence in a technique normally referred to as depth-resolved CL (DR-CL) [159].

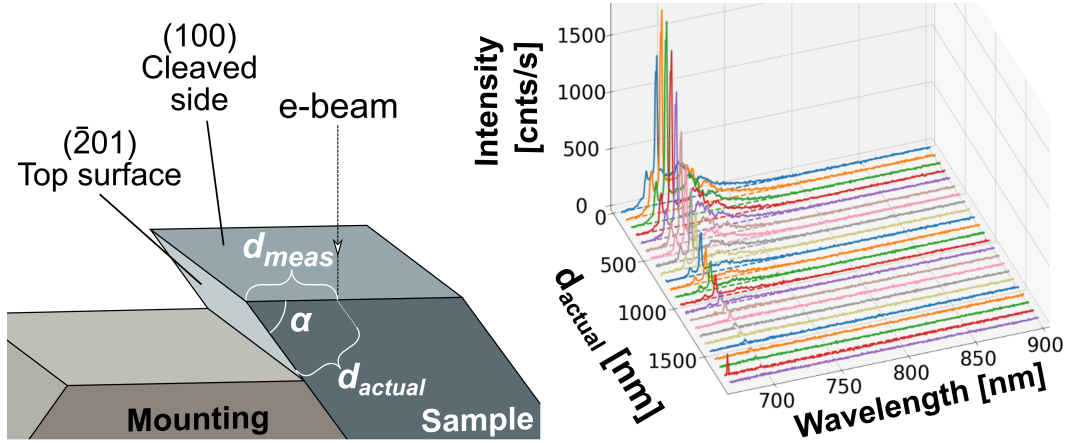


Figure 3.6: Schematic illustration of cross-sectional CL measured on (100)-cleave planes on $(\bar{2}01)$ -oriented bulk β - Ga_2O_3 samples. The depth-dependence of Cr-luminescence after background subtraction from a sample annealed at 1100 °C in air is included as an example.

This technique can be used to observe luminescence from features below the sample surface without the need for sample preparation, but it is restricted to relatively shallow depths, dictated by the depth of the generation volume for the maximum acceleration voltage. If a cross-section of the sample can be prepared, then the luminescence as a function of depth can be probed by scanning the electron beam along the cross-section, permitting depth-resolved measurements across the entire sample with electron beam parameters kept constant, as has e.g. been demonstrated in β - Ga_2O_3 by Sugie *et al.* [160]. In β - Ga_2O_3 , such a cross-section can be prepared by cleaving $(\bar{2}01)$ -oriented bulk samples along the (100) planes. This produces a cross-sectional surface which is inclined with respect to the top surface, but the actual depth, with respect to the top surface, can be calculated with trigonometry. Figure 3.6 shows schematically how the depth-dependent luminescence from such samples can be measured in CL, where the depth dependence of Cr-luminescence from a sample annealed at 1100 °C in air has been included as an example.

If carrier transport is neglected, the CL signal originates entirely from the generation volume, which has a larger lateral size than the beam spot on the sample surface due to scattering of the primary and secondary electrons. However, the generated electron hole pair may diffuse prior to recombination, yielding recombination from a volume larger than the generation volume [154]. The parabolic mirror collects luminescence emitted from a relatively large area on the sample surface, of approximate dimensions of 30-50 μm . [154]. Therefore, an enlargement of the recombination volume through charge carrier transport gives a decrease in the spatial resolution in CL measurements.

Since the excitation in CL is highly localized [154], the energy density in the generation volume can be very high, especially for high electron beam currents, which may cause unwanted heating of the sample or induce damage. Therefore, low electron beam currents are preferred for measurements on beam-sensitive samples. However, higher electron beam currents normally yield a

stronger luminescence signal. By varying the electron current from low to high and monitoring for spectral changes in the luminescence, it can be determined whether such effects are important, and a suitable current value can be found.

Various other luminescence characterization techniques exist. The most notable example for this thesis is photoluminescence (PL), in which the sample is excited by light, typically a laser. In PL, the wavelength of the excitation can be varied, enabling selective interrogation of specific transitions. This is not possible in CL, where the energetic primary electrons provide excitation over a large energy range [154]. However, this also makes CL suitable for measuring luminescence in materials with very wide band gaps, where it can be difficult to find suitable excitation sources for PL measurements. A common limitation of both techniques is that only radiative transitions can be observed directly.

3.2.5 Transmission electron microscopy and scanning transmission electron microscopy

In transmission electron microscopy (TEM), a beam of high energy electrons is directed onto a thin sample, with typical thickness 100 nm or less [153, p. 83][161, p. 29]. The high energy electrons are transmitted through the thin sample, undergoing at most a few interactions while traversing the sample [161]. Electrons in the electron beam will here be referred to as primary electrons. In conventional TEM, the electron beam is usually semi-parallel and illuminates an area of the sample typically between a few tens of nanometers to several micrometers in diameter. At the far end of the sample, a real-space image of the sample or an electron diffraction pattern can be formed using the imaging and projection lenses of the microscope.

In the related technique of scanning transmission electron microscopy (STEM), the electron beam is focused onto a small spot on the sample, often in the sub-angstrom to nanometer range, and the image is formed by raster scanning the electron beam across the sample, in a manner analogous to that described above for SEM, but with much higher spatial resolutions achievable. Many transmission electron microscopes are capable of operating in both TEM and STEM modes [153]. Both TEM and STEM can provide excellent spatial resolution. When referring jointly to TEM and STEM, or a combination of the two techniques, the abbreviation (S)TEM will be used.

If a single crystal sample is oriented such that the electron beam is incident along a high-symmetry direction of the crystal, typically referred to as a zone axis, atoms in consecutive layers of the sample overlap laterally, and atomic columns can be observed [161]. With TEM or STEM, these atomic columns can be imaged directly. An important feature of typical TEM and STEM real-space images is that they are two-dimensional projections of the three-dimensional sample [161, p. 9]. Similar to the discussion of SEM above, a number of signals can be used to form images in STEM, by correlating the signal at the appropriate detector with the position of the electron beam at the corresponding time. The signals typically used in STEM are different from those used in SEM, with the exception of X-ray emission since EDS measure-

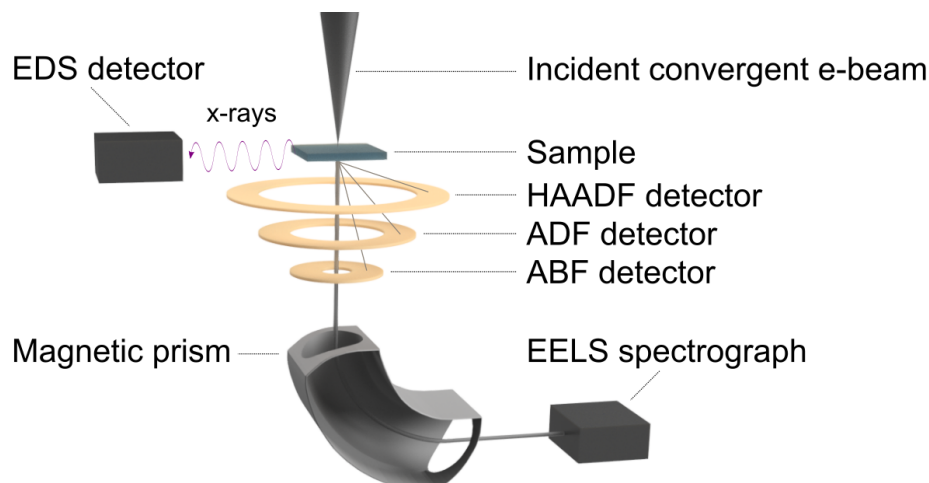


Figure 3.7: Schematic illustration of HAADF, ADF, ABF, EDS and EELS detectors in scanning transmission electron microscopy. The focusing in the magnetic prism is not shown. This figure was inspired by illustrations in the textbook by Williams and Carter [161].

ments are often performed both in SEM and STEM.

Primary electrons incident on a crystalline sample are diffracted in a manner analogous to X-ray diffraction, which was discussed above. Since the electron beam in TEM and STEM contains primary electrons with a distribution of incident angles determined by the experimental parameters, both techniques can be used to form electron diffraction patterns. In TEM, the beam convergence angle at the sample is small, and diffraction from a single crystal therefore yields sharp diffraction spots [161, p. 197-208]. When a single crystal sample is oriented with a zone axis parallel to the electron beam, an array of diffraction spots results, referred to as a diffraction pattern. By acquiring diffraction patterns along various zone axes, the crystal structure of the sample and the lattice parameters can be determined. In polycrystalline samples with grain sizes smaller than the width of the electron beam at the sample, rotational smearing of the diffraction spots due to random orientation of the individual crystallites yields diffraction rings. TEM-based electron diffraction measurements provide vastly superior spatial resolution compared to alternative techniques such as XRD. A typical measurement is selected-area electron diffraction (SAED), in which an aperture is used to limit the area of the sample contributing to the diffraction pattern [161, p. 152].

A number of STEM signals have been utilized for sample characterization in this thesis. The first group of signals of relevance are related to measurement of primary electrons scattered to specific angular ranges, collected by high-angle annular dark field (HAADF), annular dark field (ADF), and annular bright field (ABF) detectors. HAADF detectors record primary electrons scattered to comparatively large angles, typically greater than 50 mrad [161, p. 380]. The large scattering angle ensures incoherent scattering so that phase contrast and diffraction effects are not important in interpretation of HAADF images [161, p. 379]. The contrast is dominantly influenced by sample density, sample

thickness, and the average atomic weight of the constituent atoms [161, p. 379]. For fixed sample thickness, dark contrast in the HAADF image corresponds to low densities or low atomic weights, while bright contrast corresponds to high densities or high atomic weights. ADF detectors record electrons scattered to smaller angles, typically from 10 to 50 mrad [161, p. 380], where the scattering is no longer fully incoherent. Diffraction effects can therefore be important in interpretation of ADF images, where they can for example yield large contrast between crystal grains [161, p. 379]. Annular bright field (ABF) detectors record electrons scattered to small non-zero angles, e.g. 11-22 mrad [162]. ABF detectors can enable imaging of light atoms in the sample, e.g. oxygen anions in metal oxides [162]. However, as the scattering is coherent, image simulation may be required for detailed interpretation of ABF images. Other detectors are also available in STEM. EDS detectors measure X-ray emission from the sample during electron beam exposure, in which the intensity of characteristic X-rays can be analyzed to study the chemical composition of the sample. Finally, primary electrons can lose energy through inelastic scattering, which may for instance excite sample electrons either from inner shells or from the valence band into the conduction band in semiconductors. These energy losses can be analyzed in electron energy-loss spectroscopy (EELS), which is discussed in detail in the next section. An illustration of the relevant detectors in STEM is shown in Figure 3.7.

3.2.6 Electron energy-loss spectroscopy

Energy lost by a primary electron in an inelastic scattering event must, by energy conservation, be transferred to the sample. If the initial energy of the primary electron is known, the observed energy losses therefore carry information about the sample, where the type of information obtained depends on the scattering process in question [161, p. 679-757]. In EELS, electrons transmitted through a thin sample are passed to a spectrometer, where they are dispersed by their kinetic energy to produce an energy loss spectrum. A monochromated electron beam is preferred in EELS measurements, as it provides a smaller spread in the energies of the primary electrons prior to transmission through the sample, and thus higher spectral resolution in the EELS spectra [161, p. 693]. EELS spectra are often acquired in a transmission electron microscope, which should ideally be equipped with a monochromator, using an EELS spectrometer mounted after the sample to acquire the spectrum [161, p. 681]. The EELS spectrometer utilizes magnetic fields to disperse the transmitted electron beam by energy, enabling measurement of the energy-loss spectrum.

In thin samples, the most intense contribution to the EELS spectrum is the zero-loss peak, representing the energy-distribution of electrons transmitted through the sample without energy loss, or with energy losses below the energy resolution. For non-zero energy losses, many different interactions between the sample and the transmitted electron contribute to the EELS spectrum. For convenience, one often separates the EELS spectrum into two energy loss ranges: low-loss EELS below 50 eV energy loss and high-loss EELS above 50 eV

energy loss [161, p. 680]. EELS samples should ideally be thin enough that each primary electron may undergo at most one scattering event while traversing the sample, i.e. single scattering, with preferred EELS sample thicknesses typically stated to be below 100 nm [163, p. 1].

In low-loss EELS, the dominant feature is due to the excitation of plasmons. A comparison of the intensity of the zero-loss and the bulk plasmon peak can be used to estimate the thickness of the sample if the mean free path for plasmon excitation is known [161, p. 706]. In thick samples, a series of plasmon peaks appear since primary electrons can undergo multiple scattering events while traversing the sample [163]. Typical values of the plasmon mean free path are about 100 nm [161, p. 706]. Importantly, for materials with sufficiently large band gaps, it is also possible to measure the band gap in low-loss EELS, since the excitation of electrons across the band gap requires sufficiently high energies to be distinguishable from the zero-loss peak [161, p. 710]. At low energy losses, such as those associated with excitation of electrons across the band gap, the spatial resolution of EELS is diminished by the long-range electrostatic interactions that mediate the electron energy losses. The delocalization is typically on the order of a few nanometers at low energy losses, and limits the spatial resolution available in such measurements [163]. Simple approximations for the delocalization width have been given e.g. by Egerton [163, p. 339]

The high-loss range of the EELS spectrum comprises energy losses above 50 eV. In this range, the energy losses are due to excitation of electrons in the inner orbitals of the constituent atoms of the sample. Through interactions with primary electrons, a core electron can be excited to empty states above the Fermi level [163], resulting in an energy loss which is characteristic of the atomic species from which the core electron was excited. In the EELS spectrum, contributions from such energy losses appear as a series of ionization edges in the high-loss spectrum. The high-loss EELS spectrum therefore provides information about sample composition, and by appropriate integration over the various ionization edges quantitative compositional analysis is possible [161, p. 715-737][163, p. 6].

3.2.7 Secondary-ion mass spectrometry

In dynamic secondary ion mass spectrometry (SIMS), a beam of incident primary ions, e.g. Cs^+ , O^- or O_2^+ , are directed onto a sample of interest in the solid state. On impact, the ions sputter particles from the sample surface. A small percentage of the sputtered particles are electrically charged, and are referred to as secondary ions. The secondary ions are collected, focused and directed to a mass spectrometer, which separates the ionic species according to their mass-to-charge ratio [164, p. 1-18]. Thus, SIMS enables measurement of a mass spectrum, from which the concentration of various impurities in the sample can be determined with excellent sensitivity and with low detection limits. Therefore, SIMS is frequently used to measure impurity or dopant concentrations in semiconductors. For fixed position of the ion beam, sputtering

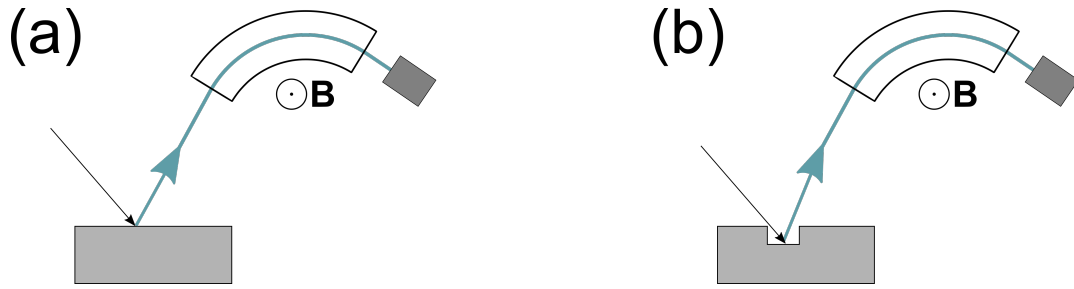


Figure 3.8: Schematic representation of concentration depth profile measurement with SIMS. (a) The ion beam is directed onto the sample, and secondary ions sputtered from the sample surface are directed onto the analyzer, which is adjusted such that the species of interest reaches the detector. (b) At a later time, the primary ion beam has sputtered the sample, and the secondary ions originate from a greater depth in the sample, enabling depth profiling.

of the sample material enables measurement of concentrations as a function of depth, if the signal at the mass spectrometer is recorded as a function of time. Figure 3.8 demonstrates the process by which the concentration of a single species can be measured as a function of depth in SIMS.

To obtain quantitative concentration profiles as a function of depth, two additional steps are required. First, the signal measured at the mass spectrometer at a certain time can be related to the corresponding depth in the sample by assuming a constant sputtering rate and measuring the depth of the crater at the end of the measurement. Second, the yield of secondary ions of a given species depends on the composition of the sample, referred to as the matrix effect. To obtain absolute concentrations, it is therefore necessary to acquire an additional SIMS measurement from a matrix-matched sample with known concentration of the species of interest [164]. For the purposes of this thesis, non-channeling ion implantation is a convenient way to make such reference samples, since the fluence is known from the implantation process.

The dependence of ion yield on sample composition causes complications when using SIMS to analyze samples containing secondary phases, e.g. embedded nanoparticles, if the species of interest is present in both the matrix and the secondary phase. It is assumed that the reference sample, used to calibrate the ion yield of the species of interest, contains only the matrix material, without secondary phases. If the ion yield of the species of interest in the secondary phase is, for instance, higher than that of the matrix material, the calculated concentration of the species of interest will be higher than the real concentration wherever the secondary phase is present. Indeed, such effects have been observed previously for Ge nanoparticles embedded in ZnO formed by ion implantation and annealing [121]. Similar arguments about a variation in the ion yield can be made for concentration gradients.

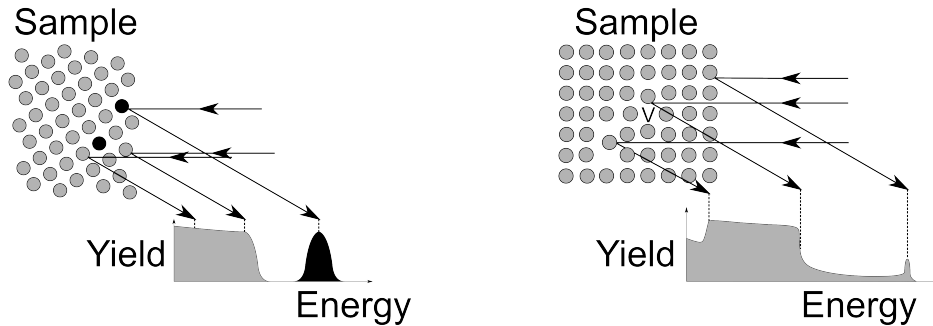


Figure 3.9: Schematic representation of random-orientation (left) and channeling (right) Rutherford backscattering spectrometry. In random orientation measurements, backscattering from different species is observed at different energies in the resulting spectrum, while direct backscattering and dechanneling by defects give rise to the signal in channeling measurements. A backscattering peak from the surface is also present in the spectrum from the channeling measurement.

3.2.8 Rutherford backscattering spectrometry

In Rutherford backscattering spectrometry (RBS) a beam of monoenergetic light ions, e.g. ${}^4\text{He}^+$, with energy typically in the MeV range, is directed onto a sample [165, p. 191-201]. The ions propagate through the sample where they may undergo backscattering from sample nuclei and subsequently be reemitted through the sample surface. A detector placed at a high angle relative to the incident beam, e.g. 165° , detects the backscattered ions. Using binary collision theory, the ratio of ion kinetic energies before scattering E_0 and the kinetic energy after scattering E_1 is given by

$$\frac{E_1}{E_0} = \left[\frac{(M_2^2 - M_1^2 \sin^2 \theta)^{1/2} + M_1 \cos \theta}{M_2 + M_1} \right]^2 \quad (3.5)$$

where M_1 is the mass of the ion, M_2 is the mass of the sample atom involved in the scattering, and θ is the scattering angle [165, p. 191-201][166, p. 22-26]. Backscattering from heavier sample nuclei yield a higher energy of the backscattered ions. In addition to backscattering from sample nuclei, the ions lose energy to excitation and ionization of sample electrons while propagating through the sample. This continuous energy loss is quantified by the stopping power, which is defined as the energy loss per unit path length. Hence, ions which are backscattered at a larger depth in the sample have reduced energies at the detector due to the sample stopping power, and it is possible to use these energy losses to relate the signal at a given energy to a specific depth in the sample [165].

In crystalline samples, by tilting the sample such that the incident beam of ions is oriented along a high-symmetry direction of the crystal, it is possible to achieve channeling of the ion beam [165]. This case is similar to channeling for ion implantation, in which ions are steered between planes or columns of atoms

in the sample by correlated small-angle scattering events. RBS measurements made under channeling conditions are referred to as channeling-mode RBS (RBS/c) measurements. Since channeled ions are prevented from approaching close to sample nuclei, they cannot undergo large-angle Rutherford scattering, and their scattering is thus reduced significantly compared to non-channeled ions, by a factor of approximately 100 [166, p. 224].

As channeled ions barely undergo backscattering from atoms located at lattice sites, RBS/c measurements are highly sensitive to defects, which perturb the local crystal structure and can thus give either direct backscattering or scatter the ions out of the channels, referred to as dechanneling. RBS/c can thus be used to study the depth distribution of defects, or disorder, in samples [166, p. 223-264]. For such studies, one also often records spectra from the sample under non-channeling conditions, typically referred to as random spectra, and channeling spectra from a crystal of the same phase with low defect concentrations, which may be referred to as a virgin, perfect or unimplanted spectrum etc., depending on the specific application. The acquisition of these additional spectra permit qualitative information about defect profiles to be gained. In some cases, quantitative results can also be obtained [166, p. 258-261]. An illustration of random (non-channeling) and channeling RBS measurements is given in Figure 3.9.

For the work presented herein, a consequence of the various aspects of RBS discussed above is that only damage in the Ga sublattice of ion-implanted Ga_2O_3 can be easily characterized by RBS/c, since O atoms are lighter than Ga atoms. Thus backscattering from oxygen atoms occurs at lower energies and is superimposed on scattering from gallium atoms deeper in the sample.

3.2.9 Photoelectron spectroscopy

In photoelectron spectroscopy, photons incident on a sample of interest cause release of electrons from the sample via the photoelectric effect. The process can be analyzed using a three-step model [167, p. 14]. In the first step, a photon is absorbed by the sample, exciting an electron. Subsequently, in the second step, the excited electron moves to the surface of the sample. In the third step, the electron is emitted from the surface of the sample. If the kinetic energy E_{kin} of the resulting photoelectron is measured with an analyzer of known work function ϕ_A , the binding energy of the initial state of the electron E_B relative to the Fermi level ε_F of the sample can be obtained from the relation

$$E_{kin} = h\nu - \phi_A - |E_b| \quad (3.6)$$

where $h\nu$ is the energy of the incident photon [167, p. 4]. The mean-free path of the excited electrons in the sample is normally a few Angstrom. Photoelectron spectroscopy therefore probes a narrow layer below the sample surface and it is a surface-sensitive technique. [167, p. 9]

If the incident photons are X-rays, core electrons can be excited, and the technique is referred to as X-ray photoelectron spectroscopy (XPS). Core electron energy levels are characteristic of the element [168], and XPS can thus

be used to determine the types of atomic species present in the sample and their concentrations [168]. However, small shifts in the same core energy level, referred to as chemical shifts, result from changes in the local surroundings of the atomic species of interest. Therefore, chemical shifts observed in XPS can, for instance, be used to distinguish between presence of a metal or the corresponding metal oxide in a sample [167, p. 66-70]. In addition to core levels, it is possible to excite electrons in the valence band in photoelectron spectroscopy, from which the energy difference between the valence band maximum and the Fermi level can be determined [168].

Chapter 4

Results

In this chapter, the main results of this thesis, presented in detail in the appended papers, are summarized and discussed. The first two papers concern studies of the structure of ion-implanted $\beta\text{-Ga}_2\text{O}_3$, starting with its dependence on key implantation parameters, namely fluence, the crystallographic orientation of the sample, and post-implantation annealing temperature, followed by unambiguous identification of the crystal structure in the polymorph-transformed layer as $\gamma\text{-Ga}_2\text{O}_3$. The results indicate that the transformation is insensitive to the implanted species. Paper III contains detailed structural characterization of the transformation of the implanted layer back to $\beta\text{-Ga}_2\text{O}_3$ using *in situ* annealing experiments. In Paper IV, a study of the luminescence properties of high fluence implanted $\beta\text{-Ga}_2\text{O}_3$ samples was undertaken, going beyond the structure of the implanted layer to investigate its effect on functional properties of the samples. Unexpectedly, the cross-sectional cathodoluminescence measurements revealed only minor changes in luminescence from the implanted layers with respect to the underlying bulk $\beta\text{-Ga}_2\text{O}_3$. However, the luminescence data revealed important changes in the chromium luminescence as a function of both implantation and annealing, with relevance to recently published literature. In addition, annealing of the Ge-implanted samples studied in Paper IV successfully produced Ge nanoparticles embedded in $\beta\text{-Ga}_2\text{O}_3$, showing the feasibility of using ion implantation to form nanoparticles embedded in $\beta\text{-Ga}_2\text{O}_3$, consistent with the finding in Paper I, in which SiO_2 nanoparticles were formed. Note that the demonstration of formation of Ge nanoparticles is given in Section 4.5 only, and is not present in the appended papers, as this work is not yet fully concluded. Formation of embedded nanoparticles in $\beta\text{-Ga}_2\text{O}_3$ extends previous results from our group showing that such embedded nanoparticles can successfully be formed in ZnO following a similar synthesis route [121, 122]. Paper V demonstrates formation of Fe-rich nanoparticles in ZnO fabricated through a powder synthesis route, and discusses their influence on functional properties compared to samples containing Fe-decorated inversion domain boundaries. This study complements the previous results from our research group on nanoparticles embedded in ZnO, as well as the existing literature on inversion domain boundaries in ZnO.

As is readily seen from the reference list of this thesis, multiple collab-

orators and colleagues of the author have made important contributions to the study of polymorphic transformations in ion-implanted β -Ga₂O₃ in recent years. In practice, these activities have been organized under two separate projects within the research group of which the author is part. Some publications have included authors from both projects, while other publications have been undertaken by one or the other project exclusively, since the two projects have followed different research paths. Because the contributions from within the research group constitute a significant portion of the recent research on this topic, discussion of publications from both projects is unavoidable. To the best of the author's ability, all publications where the author was not a contributor have been treated as if they had been reported by a different research group. In view of the partial overlap in the author lists in publications from the two projects, it is likely that this choice will appear artificial in some places. However, the distinction has been useful in giving a balanced and objective discussion of the available data, and in elucidating how the results presented in this thesis relate to the broader literature on the subject.

4.1 Initial investigations of the polymorphic transformation in ion-implanted β -Ga₂O₃

The initial investigations of ion implantation in β -Ga₂O₃ presented in Paper I focused on characterizing the effects of sample orientation, implantation fluence and annealing temperature on the structure of implanted layers in β -Ga₂O₃. This study was undertaken for implantation of silicon, which is an efficient n-type dopant in β -Ga₂O₃ and therefore of technological relevance [80, 152, 169]. Varying the fluence over more than two orders of magnitude, polymorphic transformation for Si-implantation was demonstrated for ($\bar{2}01$)- and (010)-oriented samples, consistent with previous reports [69, 70]. The transformation was not detected for (001)-oriented samples. This was very likely due to the limitations of the XRD characterization methodology, which only detects diffraction from crystal planes aligned with the sample surface. Indeed, previous results had shown polymorphic transformation in (001)-oriented samples by TEM characterization [69].

In the (010)- and ($\bar{2}01$)-oriented samples, the transformation was detected for a fluence of 2×10^{16} Si/cm². Since determination of the threshold fluence for transformation is important, ($\bar{2}01$)-oriented samples were subsequently implanted to fluences of 1×10^{14} Si/cm², 1×10^{15} Si/cm², and 2×10^{16} Si/cm². This revealed that the transformation threshold fluence for Si-implantation lies between 1×10^{14} Si/cm² and 1×10^{15} Si/cm² for implantation energy 300 keV, since the transformation was observed for 1×10^{15} Si/cm², but not for 1×10^{14} Si/cm². This can be seen from Figure 4 in Paper I which is reproduced here in Figure 4.1. Post-implantation annealing demonstrated thermal stability of the transformed layer up to 500 or 700 °C in air, depending on the implantation fluence. For higher annealing temperatures, the diffraction peaks related to the polymorph-transformed layer disappeared, attributed to

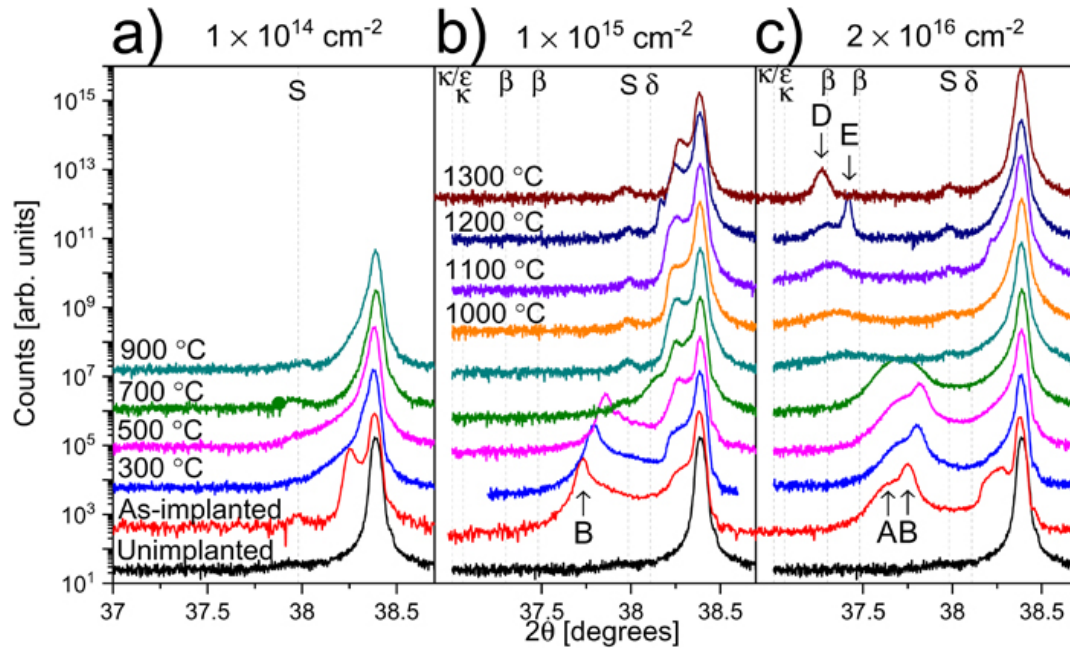


Figure 4.1: X-ray diffractograms from $(\bar{2}01)$ -oriented β - Ga_2O_3 samples implanted to fluence (a) 1×10^{14} Si/cm^2 , (b) 1×10^{15} Si/cm^2 , and (c) 2×10^{16} Si/cm^2 . Uppercase letters A, B, D, and E denote additional diffraction peaks that appeared after implantation or during the following annealing series. Vertical dashed lines represent positions of expected diffraction peaks from various Ga_2O_3 phases as they appeared in the original paper. Vertical dashed lines marked with "S" are from the sample stage. Note that indications of diffraction peaks from γ - Ga_2O_3 have not been included, as they were not labeled in the published paper. Figure reproduced from Paper I (S. B. Kjeldby et al., *Journal of Applied Physics* **131**, 125701 (2022)), with the permission of AIP publishing. The caption has been adapted from the same paper.

a back-transformation to the stable β - Ga_2O_3 . For anneals below the temperature required to trigger this back-transformation, a shift was observed for the diffraction peaks from the polymorph-transformed layer. RBS/c data revealed that after back-transformation, significant defect concentrations remained in the implanted layer, even after high-temperature annealing at 1200 °C, while post-implantation annealing successfully produced defect concentrations close to those of an unimplanted sample for an implantation fluence of 1×10^{14} Si/cm^2 , i.e. below the polymorph transformation threshold. A detailed study of the structural evolution as a function of annealing temperature was undertaken in Paper III. This is discussed below in Section 4.3, where identification of the peak labeled "B" in Figure 4.1 will also be given.

The XRD measurements used for the initial characterization were insufficient to conclusively determine the crystal structure of the transformed layer. Consequently, a sample implanted to 2×10^{16} Si/cm^2 was prepared for (S)TEM characterization. Electron diffraction patterns from the transformed layer and the underlying bulk β - Ga_2O_3 clearly corroborated a change in crystal struc-

ture, and were consistent with previous reports [69, 70], indicating that the transformation observed for Si-implantation yielded the same crystal structure as implantation of other species. However, it was found that the observed electron diffraction patterns could not be consistently indexed as κ -Ga₂O₃, in disagreement with the previous reports, and notably also differed from previous reports on electron diffraction patterns from κ -Ga₂O₃ such as those reported by Cora *et al.* [38]. Therefore, a detailed (S)TEM-based study was planned to unambiguously determine the crystal structure of the implanted layer, aiming also to investigate the dependence of the transformation on the implanted species. The result of this study is presented in Paper II. In Paper I, a conclusive determination of the crystal structure in the transformed layer was not given.

After annealing at 1100 °C, electron diffraction confirmed back-transformation to β -Ga₂O₃ for a sample implanted to 2×10^{16} Si/cm², consistent with the XRD results, and consistent with the expectation of return to the stable polymorph after high-temperature annealing. EDS measurements further revealed segregation of Si, with complementary EELS measurements being consistent with identification of Si-aggregates in the implanted layer as SiO₂, demonstrating the feasibility of using ion implantation and post-implantation annealing to form nanoparticles embedded in β -Ga₂O₃. The data also confirmed presence of voids in the same sample.

The methodology adopted in Paper I enabled investigation of a fairly wide range of implantation and annealing parameters, and their effects on the structure of ion-implanted β -Ga₂O₃. The XRD and RBS/c methods used have limitations, and do not capture all features of interest. This motivated the application of (S)TEM measurements to reveal additional details, both in the latter part of Paper I and in the two following papers. (S)TEM measurements were highly suitable here, as they provide excellent spatial resolution, enable chemical characterization using EDS and EELS, and provide structural characterization using electron diffraction along multiple zone axes.

4.2 Structural identification of the polymorph-transformed layer

Identification of the crystal structure in the transformed layer was left open in Paper I. In Paper II, a dedicated (S)TEM study was undertaken to provide unambiguous identification. Simultaneously, the effect of the implanted species on the transformation was studied. Specifically, implantations above the expected transformation threshold fluence were performed for Ni, Si, and a stoichiometric implantation. The Ni-implantation enabled comparison to previous work by Azarov *et al.* [70], and the Si-implantation enabled comparison to the results presented in Paper I. The stoichiometric implantation was designed to give similar projected range and defect production to the Si-implantation, as calculated with SRIM, while minimizing the changes to the chemical composition in the implanted layer.

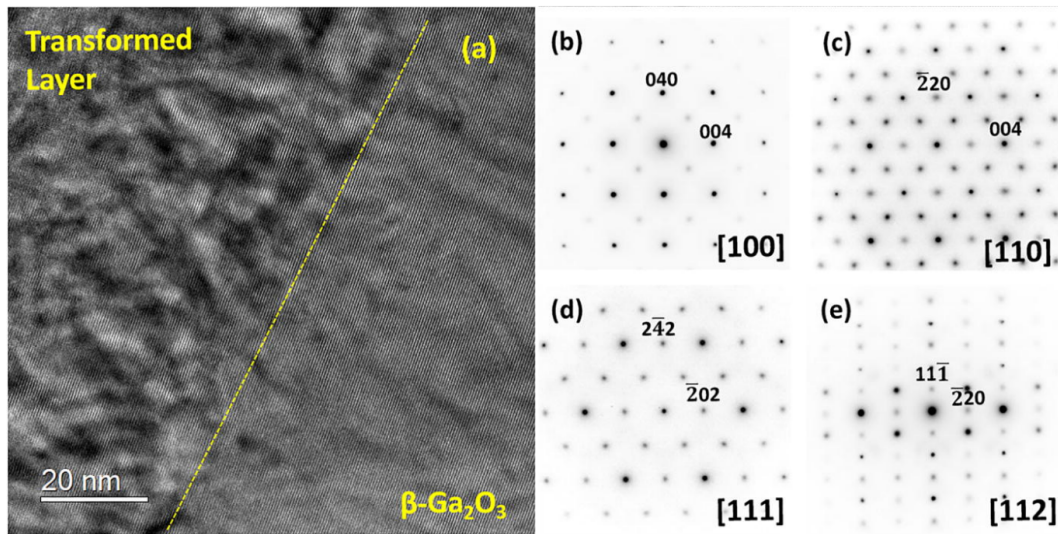


Figure 4.2: (a) Cross-sectional TEM image of the interface between the transformed layer and the underlying β -Ga₂O₃ in a $(\bar{2}01)$ -oriented β -Ga₂O₃ sample implanted to fluence 1×10^{15} Si/cm². SAED patterns from the transformed layer indexed as γ -Ga₂O₃ along different zone axes are given in (b-e). Figure reproduced from Paper II [18] (J. García-Fernández et al., *Appl. Phys. Lett.* **121**, 191601 (2022)), with the permission of AIP publishing. The caption has been adapted from the same paper.

SAED patterns were obtained from the transformed layer along multiple zone axes, which is necessary to provide unambiguous structural identification. For all implantations, the SAED patterns could be indexed as γ -Ga₂O₃, providing unambiguous structural identification of the implanted layer. As an example, Figure 2 from Paper II, which demonstrates this indexing for the transformed layer in samples implanted to fluence 1×10^{15} Si/cm², has been reproduced here in Figure 4.2. The assignment of the structure of the implanted layer as γ -Ga₂O₃ was confirmed by high-resolution HAADF- and ABF-STEM images. Importantly, the identification was in disagreement with the previous reports in the literature identifying the transformed layer as κ -Ga₂O₃ [69, 70], demonstrating that the initial suggestion for phase identification in the literature had been erroneous. Structural identification in agreement with that given in Paper II was also given by Yoo *et al.* in an article published shortly after Paper II was submitted [17]. As a note, it was observed that adjustment of the contrast of electron diffraction patterns acquired from the zone axis [111] of γ -Ga₂O₃ could reproduce diffraction patterns very similar to those observed previously [69, 70], strengthening the hypothesis that all authors were in fact observing the same polymorph transformation to γ -Ga₂O₃ for high-fluence ion implantation.

The data presented in Paper II suggested that the transformation was independent of the chemistry of the implanted species. In addition, the data suggested that all authors were in fact observing the same polymorphic transformation, and thus that the transformation had been observed for implanta-

tion of: Ni, Ga, and Au (Azarov *et al.*)[70]; Ge (Anber *et al.*)[69]; Sn (Yoo *et al.*)[17]; and Si, and stoichiometric implantation (Paper II). Previous work by Wendler *et al.* had also given initial indications for such a transformation for implantation of even more elements [68]. The available data was thus consistent with a β -to- γ transformation which was independent of the implanted species, indicating that the chemistry of the implanted ion was not essential in the transformation, for which the stoichiometric implantation provided the strongest evidence. Thus, the transformation appeared to be caused by intrinsic features of ion implantation, specifically implantation-induced defects or strain in the implanted layer.

Identification of the implanted layer as γ -Ga₂O₃ provided a challenge to explain the origin of the transformation, since γ -Ga₂O₃ has high formation energy [42]. However, structural similarities between β -Ga₂O₃ and γ -Ga₂O₃ could facilitate the transformation, making it preferred over transformation to other polymorphs. A qualitative assessment of the published crystal structures of β -Ga₂O₃, κ -Ga₂O₃ and γ -Ga₂O₃ revealed similarity in the oxygen sublattices in β -Ga₂O₃ and γ -Ga₂O₃ which was not present between β -Ga₂O₃ and κ -Ga₂O₃. This could plausibly facilitate transformation from β -Ga₂O₃ to γ -Ga₂O₃ by lowering the energetic barrier for this transformation compared to a hypothetical transformation to κ -Ga₂O₃. The full argument is given in Paper II and its supplementary materials. However, no detailed mechanism for the implantation-induced polymorph transformation was given in Paper II.

It is noted that recent publications have reported findings consistent with a largely unperturbed oxygen sublattice after the transformation [19]. Huang *et al.* have also suggested that the transformation may be driven by local transformation towards γ -Ga₂O₃ via formation of cation interstitial-divacancy complexes from implantation-induced cation vacancies [77]. These later works show progress towards an improved understanding of the polymorphic transformation.

4.3 In situ characterization of back-transformation of the implanted layer

In addition to the β -to- γ implantation-induced transformation, Paper I also revealed the back-transformation to β -Ga₂O₃ for annealing at or below 700 °C. This motivated a dedicated *in situ* (S)TEM study of the back-transformation, which was undertaken in Paper III, in which samples were sequentially annealed at increasing temperatures under vacuum conditions.

First, in Paper III, the lattice matching between β -Ga₂O₃ and the implantation induced γ -Ga₂O₃ layer was found to be $[100] \gamma\text{-Ga}_2\text{O}_3 \parallel [201] \beta\text{-Ga}_2\text{O}_3$ and $[110] \gamma\text{-Ga}_2\text{O}_3 \parallel [132] \beta\text{-Ga}_2\text{O}_3$. From crystallographic considerations, it is then expected that the diffraction from (222) planes in γ -Ga₂O₃ should be observed in the X-ray diffractograms from the ($\bar{2}01$)-oriented β -Ga₂O₃ studied in Paper I (see Figure 4.1). A comparison to published structures in the ICSD database then demonstrates that the diffraction peak labeled "B" in Paper I

and Figure 4.1 can be attributed to diffraction from (222) planes in γ -Ga₂O₃, which is expected at 37.8-37.9 °2 θ in the XRD data (ICSD collection codes 194506 [36] and 152085). This demonstrates consistency between the initial XRD characterization and the detailed characterization by (S)TEM methods prior to heat treatments.

The results in Paper III revealed that the back-transformation commenced already after annealing at 300 °C, and a prominent mixture of β -Ga₂O₃ and γ -Ga₂O₃ was observed after annealing at 500 °C. Recrystallization of β -Ga₂O₃ from γ -Ga₂O₃ occurred throughout the transformed layer, where [100] γ -Ga₂O₃ || [021] β -Ga₂O₃ and [110] γ -Ga₂O₃ || [010] β -Ga₂O₃ characterizes the crystallographic relationship between the γ -Ga₂O₃ and the recrystallized β -Ga₂O₃ grains. Notably, the crystallographic relationship between γ -Ga₂O₃ and recrystallized β -Ga₂O₃ grains was different from the crystallographic relationship between γ -Ga₂O₃ and the original β -Ga₂O₃. Moreover, electron diffraction revealed diffraction spots corresponding to different grains of β -Ga₂O₃ with orientations related by a 90° rotation. This observation is likely due to the symmetry of the cubic crystal structure of γ -Ga₂O₃, directing the orientation of recrystallized β -Ga₂O₃ grains.

The observed alignment between recrystallized β -Ga₂O₃ and γ -Ga₂O₃ persisted for increased annealing temperatures, with a continuous decrease in the volumetric ratio of γ -Ga₂O₃ at increasing annealing temperatures. For annealing temperatures above 900 °C, β -Ga₂O₃ recrystallized without preferred orientation, indicating that the high thermal energy available in this temperature range was sufficient to overcome energy barriers to recrystallization which caused preferred orientation in regrowth at lower temperatures. For annealing at 900-1100 °C, the transformed layer back-transformed completely to β -Ga₂O₃.

It is noted here that the difference in annealing atmosphere between Paper I and Paper III may affect the transformation process, e.g. the temperature required for regrowth of β -Ga₂O₃ to commence. In addition, sample dimensions were different for *in situ* and *ex situ* annealing, with thin TEM lamella used in the former and bulk samples used in the latter. Hence, the surface-to-volume ratio was much larger for the *in situ* samples, which would enhance the impact of any surface effects on the back-transformation.

The influence of implanted species on the back-transformation was also investigated, revealing that the regrowth of β -Ga₂O₃ was similar for annealing of Si- and Au-implanted samples. Notably, both the RBS/c results in Paper I and the structural characterization reported in Paper III indicate that for the parameters investigated here, high quality, single-crystal β -Ga₂O₃ was not regained after high-temperature annealing of samples where the implantation fluence was above the threshold for the β -to- γ transformation. Hence, to produce high crystal quality samples with high carrier concentration through ion implantation, it is likely necessary to suppress the implantation-induced β -to- γ polymorph transformation. Recent results in the literature have indicated that suppression of the polymorph transformation can be achieved by keeping the sample at an elevated temperature of 600 °C during implantation [80].

4.4 Luminescence from ion-implanted and annealed β -Ga₂O₃

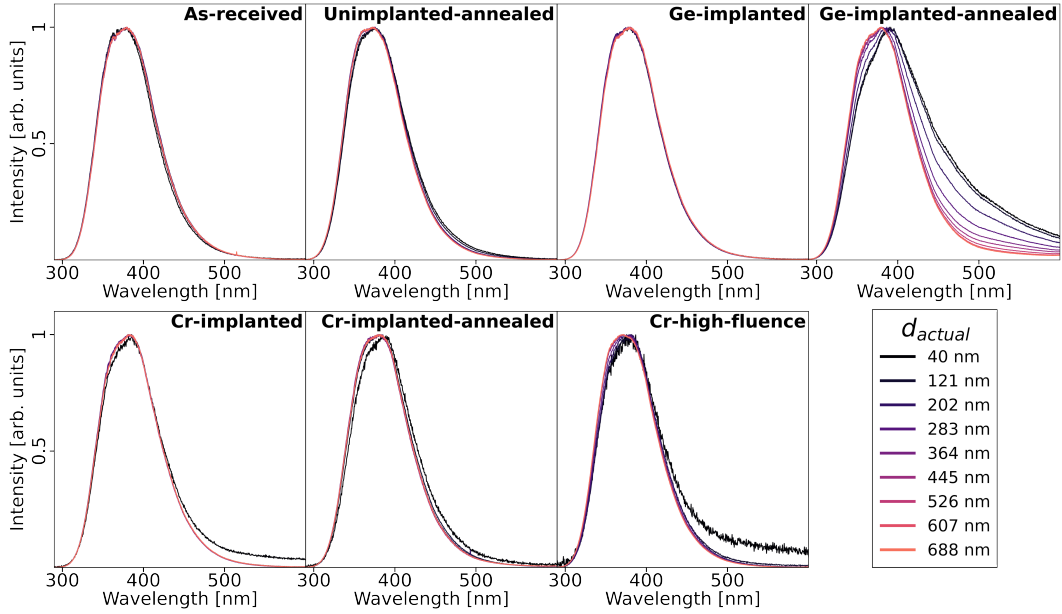


Figure 4.3: Normalized CL spectra in the spectral range 300-600 nm at different depths in the samples studied in Paper IV. The y-axis is shared across plots on the same row. The legend given on the bottom right is shared across all plots. Briefly, Ge-implanted samples were implanted to 2×10^{16} Ge/cm², Cr-implanted and Cr-implanted-annealed samples were implanted to 1.8×10^{14} Cr/cm², and the Cr-high-fluence sample was implanted to 5×10^{15} Cr/cm². All anneals were performed in air at 1100 °C. All samples were $(\bar{2}01)$ -oriented β -Ga₂O₃, except the Cr-high-fluence sample which was (001)-oriented with a HVPE top layer. Full sample preparation details can be found in Paper IV. This figure has been adapted from Figure S2 in Paper IV.

After the detailed characterization of the polymorph-transformed layer and related features presented in Papers I-III, Paper IV proceeded to study the luminescence properties of similarly prepared samples. Cross-sectional cathodoluminescence measurements at 80 K were applied to measure the depth-dependence of luminescence from such samples. Initially, the influence of ion implantation on the luminescence in the UV, blue and green bands was investigated for samples implanted with Ge to high fluence. As-implanted samples revealed only minor changes in the intrinsic luminescence compared to as-received samples. Since the implantation fluence was above the fluence for which polymorph transformation has been observed in Ge-implanted samples previously [69], the data suggested similar luminescence from β -Ga₂O₃ and γ -Ga₂O₃. Thus, the inherently disordered γ -Ga₂O₃ appears not to exhibit high luminescence intensities in the blue and green luminescence bands associated with defects in β -Ga₂O₃, retaining instead a luminescence line shape similar to that of β -

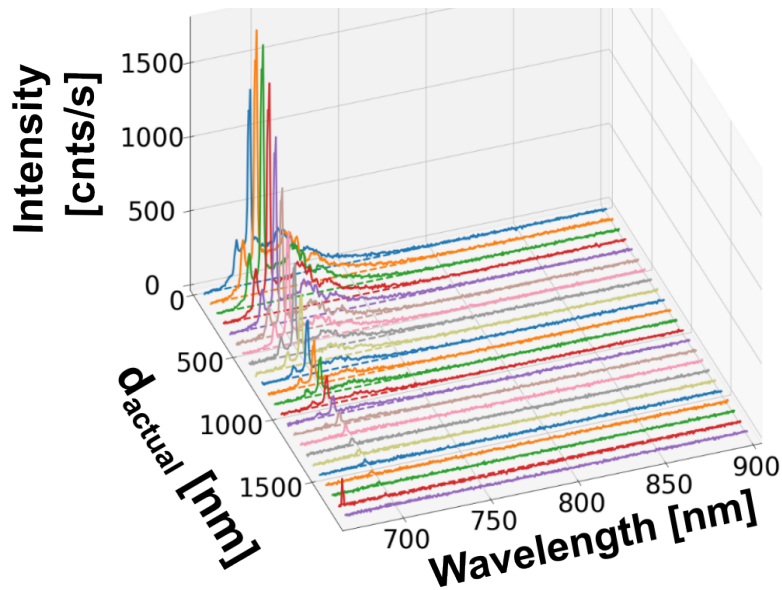


Figure 4.4: Cross-sectional cathodoluminescence measurement of the depth-dependence of Cr-luminescence in a $(\bar{2}01)$ -oriented β -Ga₂O₃ sample after annealing at 1100 °C in air for 30 minutes. Measured at 80 K, acceleration voltage 10 kV, and electron beam current 80 pA. A 3D plot is used to simultaneously show the spectral line shapes and the depth-dependence.

Ga₂O₃, as can be seen from Figure 4.3 (reproduced from Figure S2 in Paper IV). Cross-sectional CL measurements revealed that the integrated emission intensity between 300 and 600 nm wavelength was peaked near the surface in most samples, including the as-received sample. This effect could be explained by a decrease in the effective doping, i.e. a decrease in $N_d - N_a$, near the sample surface [104]. These results are presented in the supplementary of Paper IV in Figure S3.

A sample implanted with Ge to high fluence (2×10^{16} Ge/cm²) and annealed at high temperature (1100 °C) in air was an exception from the trend of minor changes in the intrinsic luminescence, showing significant intensity increases in the blue and green luminescence bands in the implanted layer. For this sample, SIMS measurements revealed significant diffusion of Ge out of the implanted layer during annealing. Blue luminescence in β -Ga₂O₃ has previously been linked with intrinsic defects [101, 103], and green luminescence is also likely to be defect-related [101, 107], as noted above. The diffusion of Ge in Ga₂O₃ has been reported to be related to point defects, likely V_{Ga} [170]. Thus, the observed diffusion of Ge and increased blue and green luminescence were likely related.

Interestingly, it was found in Paper IV that simple annealing in oxygen rich atmosphere gave a large increase in the Cr-luminescence near the sample surface. This is demonstrated in Figure 2 in Paper IV, a part of which is reproduced here as Figure 4.4. The figure shows the depth-dependent Cr-luminescence in a $(\bar{2}01)$ -oriented β -Ga₂O₃ sample after annealing at 1100 °C in air, demonstrating a clear intensity increase near the sample surface. SIMS

data confirmed that this effect was correlated with a substantial increase in the Cr-concentration near the sample surface compared to the bulk. This finding is consistent with a recent article from Wu *et al.* [113], who suggested that the accumulation of Cr was caused by diffusion of Cr during annealing and trapping of Cr at gallium vacancies near the sample surface. Notably, the cross-sectional CL measurements presented in Paper IV demonstrate directly that the increased Cr concentration near the sample surface is related to increased Cr-luminescence intensity.

The model for Cr-accumulation suggests that controlled introduction of additional V_{Ga} should result in even higher concentrations of Cr near the surface after annealing. SIMS depth profiles of the Cr-concentration from samples implanted with Ge to high fluences prior to annealing demonstrated that further enhancement of the Cr-concentration can be achieved by introduction of vacancies through ion implantation. This supports the model proposed by Wu *et al.* However, the Cr-luminescence line shape in this sample differed significantly from the typical line shape, e.g. displaying higher intensity for R_2 than for R_1 . This difference in luminescence line shape is likely related to influence of intrinsic or Ge-related defects on the Cr-luminescence. Indeed, the previous papers presented here demonstrated that high defect concentrations remain in back-transformed layers, supporting this conclusion. Notably, the direct demonstration of increased luminescence intensity near the sample surface in a sample annealed at 1100 °C in air demonstrated that simple annealing in oxygen-rich atmosphere provides strongly enhanced Cr-luminescence, which may be relevant as a fabrication strategy for devices based on Cr-luminescence from $\beta\text{-Ga}_2\text{O}_3$.

4.5 Formation of Ge-rich nanoparticles in ion-implanted $\beta\text{-Ga}_2\text{O}_3$

In addition to the luminescence study undertaken in Paper IV, detailed (S)TEM characterization of Ge-implanted samples annealed at various temperatures revealed formation of Ge-rich nanoparticles after annealing at 700 °C in air for an implantation fluence of 2×10^{16} Ge/cm². In high-resolution TEM images, Moiré fringes were observed in several regions in the samples, consistent with overlapping crystallites of different phases. An example is shown in Figure 4.5(a), where FFTs from the areas marked in blue and red are given in (b) and (c), respectively. The FFT in (b) could be consistently indexed as $\beta\text{-Ga}_2\text{O}_3$. In (c), the same spots from $\beta\text{-Ga}_2\text{O}_3$ are observed, but additional spots also appear in the FFT. One of these spots has been circled in red. It was found that this spot could be indexed as Ge-(001) in cubic Ge (Fd3m), based on the ICSD entry with collection code 121532. Although a reasonable assignment, further work is required to conclusively demonstrate its veracity.

EDS and EELS measurements were conducted on another particle, also identified by Moiré fringes in the high-resolution TEM image. The results are given in Figure 4.6. Here, the particle was located next to a dark spot in the

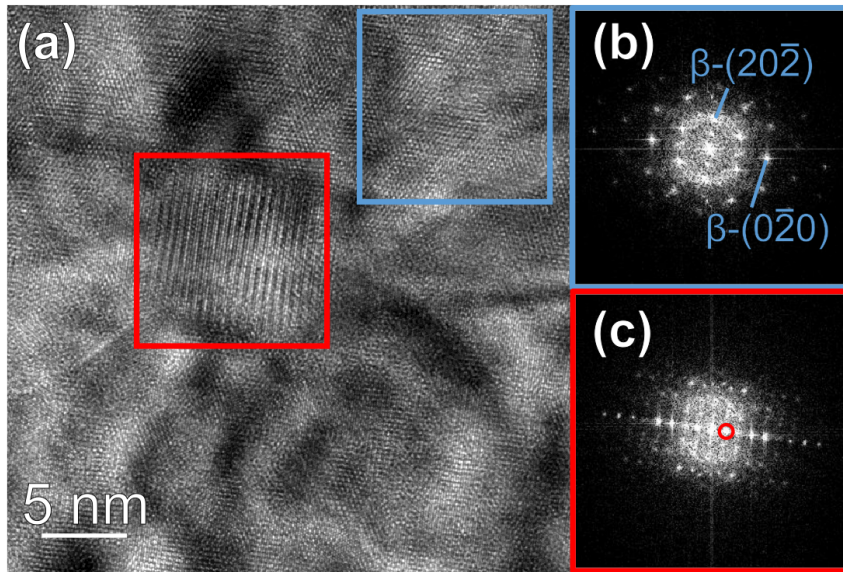


Figure 4.5: (a) High-resolution TEM data from a Ge nanoparticle embedded in the implanted layer of a sample implanted to fluence 2×10^{16} Ge/cm² after annealing at 700 °C. FFTs from the blue and red squares in (a) are given in (b) and (c), respectively. Indexing of the FFT according to β -Ga₂O₃ is shown in (b). In (c) additional spots appear in the FFT, one of these spots have been marked by a red circle. Javier García-Fernández is credited with acquisition of the data presented in this figure.

TEM image, which EDS maps and linescans revealed to be a void. The area containing Moiré fringes showed an increase in Ge content and a reduction in Ga and O content relative to the surrounding Ga₂O₃ matrix.

High-loss EELS spectra acquired from the red and green spots in Figure 4.6(a) revealed an edge onset at around 1120 eV in both spectra after background subtraction. This is consistent with the L₂ and L₃ edges of Ga at 1142 and 1115 eV energy loss, as listed in the EELS Atlas [171], which both have a gradual onset, accounting for the observed spectral shape. The energy of this Ga edge is also consistent with previous reports [172]. Fine structure was observed with peaks at around 1140 eV and 1155-1160 eV. In the spectrum acquired from the nanoparticle, an increase is observed at around 1230 eV, consistent with the L₂ and L₃ edges of Ge at 1248 and 1217 eV energy loss, which have a gradual onset, as listed in the EELS Atlas [171]. The onset value is also consistent with the onset value previously reported in the literature [173]. For comparison, the spectrum acquired from the Ga₂O₃ matrix was flat in this energy loss range, decreasing at higher losses. Thus, the secondary onset must be attributed to the particle, consistent with identification as a Ge nanoparticle. Low-loss spectra from the same areas were also acquired, see Figure 4.6. Using the $L_{50} \approx 17 \text{ nm}/E^{(3/4)}$ estimate given by Egerton [163, p. 339], the delocalization was found to be around 2.2 nm at 15 eV energy loss, and hence the low-loss spectra acquired from the bulk region should contain minimal contributions from the particle. Conversely, the spectrum acquired

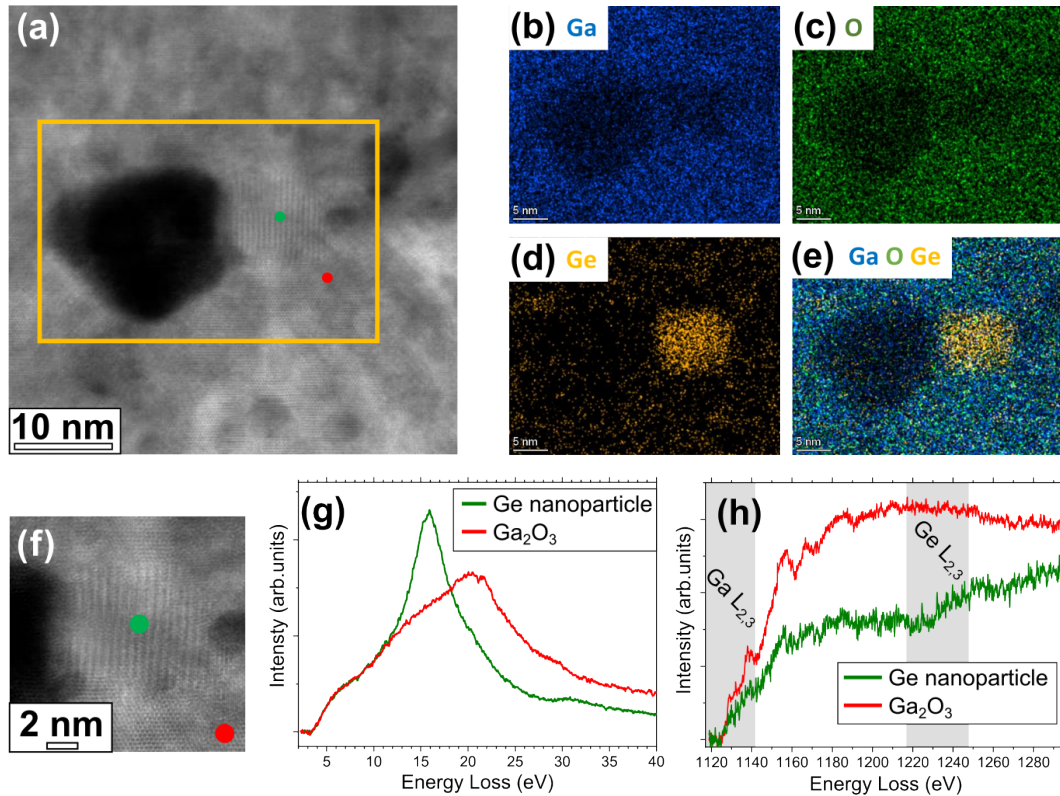


Figure 4.6: High-resolution TEM, EDS and EELS data from a Ge nanoparticle embedded in a 2×10^{16} Ge/cm² implanted Ga₂O₃ sample after annealing at 700 °C. (a) High-resolution TEM image showing lattice fringes at the particle, yellow boundary indicates region of interest for EDS analysis. (b)-(d), EDS maps of Ga, O, and Ge. (e) joint EDS image of Ga, O and Ge. (f) higher magnification high-resolution TEM image of the region around the particle. (g) low-loss EELS spectra and (h) high-loss EELS spectra in the spectral range of Ga-L_{2,3} and Ge-L_{2,3} edges from the Ge nanoparticle and the surrounding Ga₂O₃ matrix. Line color of spectra correspond to the colored dots in (a) and (f), which give the positions for acquisition of the EELS spectra. In (h), the positions where Ga-L_{2,3} and Ge-L_{2,3} edges are expected have been marked with gray bands. Javier García-Fernández is credited with acquisition of the data presented in this figure.

from the nanoparticle is expected to contain contributions from the Ga₂O₃ matrix, since the Moiré patterns in TEM images demonstrate overlap between the matrix and the particles, showing that the particles do not extend through the TEM sample. The low-loss spectra reveal a clear shift in the major peak, attributed to plasmons, consistent with a different phase for the particle than for the surrounding Ga₂O₃ matrix. The shape of the major peak is also different between the two spectra. Additionally, the spectrum from the nanoparticle displays a minor onset at 28-29 eV, which may be due to the M_{4,5} edge of Ge at 29 eV energy loss as listed in the EELS Atlas, which has a gradual onset and low intensity. The onset energy of Ge M_{4,5} is also in good agreement with

a previous literature report [174].

The formation of elemental Ge nanoparticles for annealing at 700 °C is consistent with the previous results in our group, which demonstrated similar effects for Ge-implantation in ZnO, at a fluence of 1×10^{16} Ge/cm² [121]. Other previous results on ZnO revealed that ternary oxide nanoparticles embedded in the sample could be formed by annealing at 1000 °C [122], for the same implantation fluence. Ge-implanted β -Ga₂O₃ samples annealed at 1100 °C were investigated in relation to Paper IV, but in this case no nanoparticles were observed. From SIMS data, it was found that Ge diffuses readily in Ga₂O₃ during annealing at 1100 °C, both in Paper IV and in the literature [170]. This diffusion causes decreased Ge concentration in the implanted layer, which may inhibit formation of nanoparticles.

Taking into account the formation of SiO₂ nanoparticles embedded in β -Ga₂O₃, which was demonstrated in Paper I, as well as the formation of the Ge-nanoparticles discussed above, it is clear that nanoparticles embedded in Ga₂O₃ can be synthesized through ion implantation followed by annealing.

4.6 Optical properties of ZnO containing ZnFe₂O₄ nanoparticles or Fe-decorated IDBs

Finally, Paper V concerns Fe-decorated IDBs and spinel ZnFe₂O₄ nanoparticles embedded in ZnO. Here, samples were fabricated through a powder synthesis route, introducing high Fe-concentrations in ZnO at elevated temperatures followed by cooling to room temperature. Despite being a very different fabrication strategy from that employed in the preceding papers, it nonetheless enables strong structural perturbation of a wide band gap semiconductor. Moreover, it extends on previous work from other authors in our group concerning nanoparticles embedded in ZnO [121, 122], and complements the existing literature concerning Fe-decorated IDBs in ZnO which has focused mostly on structural characterization of such samples.

The structural characterization of samples containing Fe-decorated IDBs in Paper V is consistent with the literature, where the crystallographic structure of such samples has been studied extensively in the past as was summarized above [118, 123, 124, 125]. By varying the thermal treatment during sample synthesis, it was possible to form either Fe-decorated IDBs, or alternatively spinel ZnFe₂O₄ nanoparticles embedded in ZnO [126]. The optical absorption of both types of samples was investigated. DRS results gave an initial indication that both sample types showed absorption below the band gap of ZnO, starting at around 2.0 eV, which is consistent with the reported band gap of ZnFe₂O₄ [134]. To ensure that this similarity was not due to e.g. presence of small grains of ZnFe₂O₄ in the samples containing Fe-decorated IDBs, additional low-loss EELS measurements were performed. The low-loss EELS spectra confirmed optical absorption at around 2.0 eV in ZnFe₂O₄ nanoparticles, and also confirmed optical absorption at 2.0 eV in ZnO containing Fe-decorated

IDBs, in a region of the sample where no ZnFe_2O_4 nanoparticles were observed. Therefore, ZnFe_2O_4 nanoparticles and Fe-decorated IDBs were found to give similar contributions to optical absorption. The effect was attributed to local structural similarity around Fe-ions at basal IDBs and in the spinel crystal structure of ZnFe_2O_4 . Importantly, the results revealed that the network of extended planar defects present in the samples containing Fe-decorated IDBs had important consequences for the optical absorption of the sample. The DRS and low-loss EELS data are presented in Figures 6 and 7 in Paper V, which have been combined and reproduced here in Figure 4.7. Luminescence measurements revealed significant differences between the samples, with samples containing spinel ZnFe_2O_4 nanoparticles exhibiting possible contributions from luminescence near the band edge of spinel ZnFe_2O_4 .

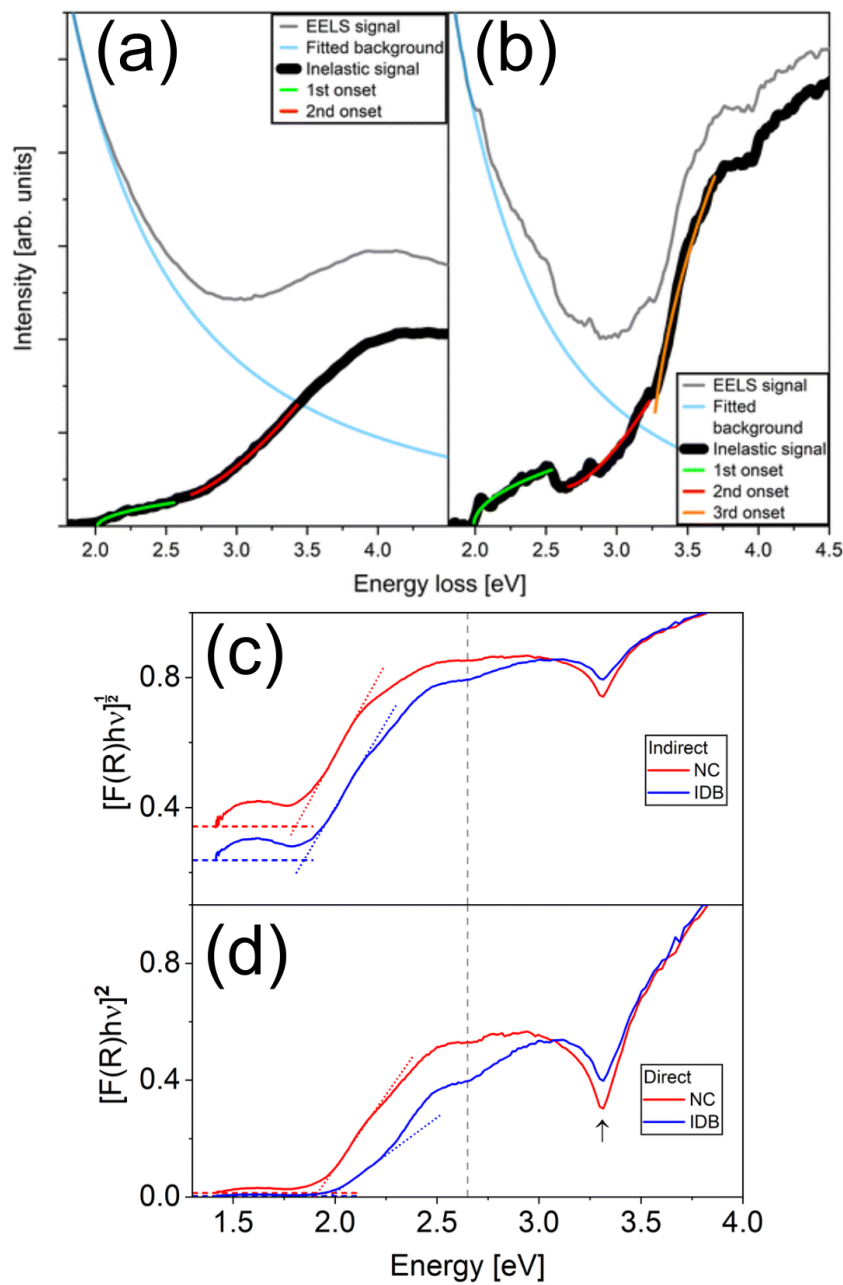


Figure 4.7: Low-loss EELS spectra from a sample containing ZnFe₂O₄ nanoparticles embedded in ZnO (a), and a sample containing Fe-decorated IDBs (b), showing determination of the inelastic signal by background subtraction and fitting of absorption onsets to the inelastic signal. Tauc plots of diffuse reflectance assuming indirect and direct transitions for the same two samples are given in (c) and (d), respectively. In (c) and (d), data from a sample containing ZnFe₂O₄ nanoparticles is shown in red, and data from a sample containing Fe-decorated IDBs is shown in blue. Linear fits around the first optical absorption onset are given in dotted lines. The transition at 3.3 eV is attributed to ZnO and is indicated by an arrow in (d). The figure was adapted from Paper V (S. B. Kjeldby et al., *Nanoscale Advances* **5**, 2102 (2023)) with permission from the Royal Society of Chemistry

Chapter 5

Concluding remarks

In this work, progress has been made towards an improved understanding of ion implantation in β -Ga₂O₃, particularly for high implantation fluences. Notably, transformation of the implanted layer to γ -Ga₂O₃ has been conclusively demonstrated. The available data suggest that the transformation occurs independently of the sample orientation of the initial β -Ga₂O₃. Importantly, the implantation has also been demonstrated to be independent of the implanted species, demonstrating that the transformation is driven by intrinsic features of ion implantation, e.g. defect production or induced strain in the implanted layer. An approximate conservation of the anion sublattice in the β -to- γ transformation reveals a structural similarity between the initial and final phases, which could be an important part in understanding the preference to form γ -Ga₂O₃.

The thermal stability of the γ -Ga₂O₃ layer has been investigated, first for *ex situ* annealing in air, followed by a detailed (S)TEM study for *in situ* annealing in vacuum. The back-transformation to β -Ga₂O₃ produced β -Ga₂O₃ with high defect concentrations for the implantation and annealing parameters investigated here. Electron diffraction patterns from the implanted layer revealed regrowth of β -Ga₂O₃ adhering to specific lattice matching relations with the γ -phase up to annealing at 850 °C. Notably, the lattice matching between γ -Ga₂O₃ and regrown β -Ga₂O₃ was different from the lattice matching between γ -Ga₂O₃ and the original β -Ga₂O₃. At temperatures above 850 °C, the annealing produced randomly oriented grains of β -Ga₂O₃, eventually giving full recrystallization of the γ -Ga₂O₃ layer to β -Ga₂O₃.

It has been demonstrated that high-fluence implantation of Si or Ge in β -Ga₂O₃ followed by annealing could successfully produce SiO₂ nanoparticles and Ge nanoparticles embedded in β -Ga₂O₃ respectively, extending the previous work from our group demonstrating that this fabrication route can be used to form nanoparticles embedded in ZnO. In Ga₂O₃, the formation of such particles was accompanied by formation of voids in the samples studied herein.

Cross-sectional CL studies revealed only minor variations in the characteristic Ga₂O₃ luminescence between a γ -Ga₂O₃ layer formed by ion implantation and underlying β -Ga₂O₃, suggesting similar luminescence from these two polymorphs. An increase in the luminescence intensity between 300 and 600 nm

wavelength was observed near the sample surface in as-received samples, possibly related to a lowered effective n-type doping in this region of the samples. Moreover, the CL measurements enabled direct demonstration of increased Cr luminescence in samples annealed in air, which was correlated with an increase in the Cr-concentration, consistent with recent literature reports from Wu *et al.* The model for Cr-concentration increase given by Wu *et al.* was supported by additional experiments on ion-implanted and annealed samples. Overall, annealing in air was found to be an efficient way of locally increasing the Cr luminescence.

Finally, characterization of optical absorption of ZnFe_2O_4 nanoparticles embedded in ZnO and Fe-decorated IDBs in ZnO revealed optical absorption at around 2.0 eV in both types of samples, consistent with the band gap of ZnFe_2O_4 . The similarity in optical absorption was attributed to the local structural similarity around Fe-ions at basal IDBs and in spinel ZnFe_2O_4 . Notably, this demonstrates that the presence of a quasi-regular network of Fe-decorated IDBs has important effects on the functional properties of the sample.

5.1 Suggestions for further work

A recent report by Azarov *et al.* has demonstrated that the $\gamma\text{-Ga}_2\text{O}_3$ layer formed after high-fluence ion implantation of $\beta\text{-Ga}_2\text{O}_3$ is highly radiation tolerant [19]. This demonstrates that the interaction of Ga_2O_3 with high-energy particles is highly atypical, and well worth further study. Based on the results from Azarov *et al.*, an interesting possibility is to use such $\gamma\text{-Ga}_2\text{O}_3$ layers for radiation tolerant semiconductor devices. To enable fabrication of such devices, electrical control of the $\gamma\text{-Ga}_2\text{O}_3$ layers is required. The author is aware that research efforts on this topic are already underway [176].

As was noted above, a careful review of the literature reveals that Ga_2O_3 is not unique in displaying polymorphic transformation from high-fluence ion implantation. It seems likely that a comparative study of the effect across different materials could further extend the understanding of the physical mechanisms underlying implantation-induced polymorph transformations. As was discussed above, ZrO_2 exhibits similar behavior to Ga_2O_3 in this regard, and a suitable research path may be a comparative study of the effect in these two materials, either by experimental methods, computational methods, or a combination thereof.

For $\beta\text{-Ga}_2\text{O}_3$ -based devices, controlled suppression of the polymorph transformation should be beneficial to forming devices with high carrier concentrations and good crystal quality. The results from Sardar *et al.*, which were introduced above, give initial indication that this may be achieved by performing implantation into a heated sample. Further research to corroborate this finding and determine optimal parameters for suppression could be beneficial for fabrication of $\beta\text{-Ga}_2\text{O}_3$ -based devices.

To verify the similar luminescence from $\beta\text{-Ga}_2\text{O}_3$ and $\gamma\text{-Ga}_2\text{O}_3$ in the UV and visible spectral ranges in the CL data in Paper IV, similar measurements should be performed on $\gamma\text{-Ga}_2\text{O}_3$ films synthesized by other means, e.g. thin

film deposition methods. Cross-sectional CL measurements revealed increased luminescence intensity in the UV and visible ranges near the sample surface, and it was suggested based on data from previous literature that the effect could be due to reduced effective doping in this part of the sample. This hypothesis should be tested by electrical characterization. The changes in Cr-luminescence line shape in ion-implanted samples with respect to unimplanted samples is likely related to implantation-induced defects, but has not been fully explained and is subject to further investigation. Similarly, the increased number of luminescence lines and lateral variation observed in Cr-implanted samples after annealing has not been explained here and should be investigated further. Both points are of relevance for use of Cr in Ga_2O_3 for technological applications if ion implantation is used in the sample processing.

Paper V demonstrates that Fe-decorated IDBs in ZnO have an important influence on the optical absorption of the sample. Electrical characterization of these extended defects would provide complementary information about the effects of the quasi-regular network on sample properties. This likely requires the use of a different fabrication technique, e.g. thin film deposition on an appropriate substrate. Moreover, such a study requires an electrical characterization technique with excellent spatial resolution.

Bibliography

- [1] W. Shockley and H. J. Queisser. *Journal of Applied Physics* **32** (1961), p. 510.
- [2] I. Almansouri et al. *IEEE Journal of Photovoltaics* **5** (2015), p. 968.
- [3] J. Lutz et al. *Semiconductor Power Devices*. 2nd Ed. Springer, 2018.
- [4] M. Higashiwaki. *AAPPS Bulletin* **32** (2022), p. 3.
- [5] J. Ballestín-Fuertes et al. *Electronics* **10** (2021), p. 677.
- [6] M. Higashiwaki et al. *Japanese Journal of Applied Physics* **55** (2016), 1202A1.
- [7] X. Hou et al. *Journal of Physics D: Applied Physics* **54** (2021), p. 043001.
- [8] H. H. Tippins. *Physical Review* **137** (1965), A865.
- [9] Y. Tokida and S. Adachi. *Journal of Applied Physics* **112** (2012), p. 063522.
- [10] T. Miyata, T. Nakatani, and T. Minami. *Journal of Luminescence* **87** (2000), p. 1183.
- [11] C. Janowitz et al. *New Journal of Physics* **13** (2011), p. 085014.
- [12] J. Shi et al. *Advanced Materials* **33** (2021), p. 2006230.
- [13] H. H. Tippins. *Physical Review* **140** (1965), A316.
- [14] T. Onuma et al. *Japanese Journal of Applied Physics* **54** (2015), p. 112601.
- [15] T. Matsumoto et al. *Japanese Journal of Applied Physics* **13** (1974), p. 1578.
- [16] H. Y. Playford et al. *Chemistry - A European Journal* **19** (2013), p. 2803.
- [17] T. Yoo et al. *Applied Physics Letters* **121** (2022), p. 072111.
- [18] J. García-Fernández et al. *Applied Physics Letters* **121** (2022), p. 191601.
- [19] A. Azarov et al. *Nature Communications* **14** (2023), p. 4855.
- [20] B. K. Vainshtein, V. M. Fridkin, and V. L. Indenbom. *Modern crystallography II: Structure of Crystals*. 3rd Ed. Berlin Heidelberg New York: Springer, 2000.
- [21] C. Kittel. *Introduction to Solid State Physics*. 8th Ed. John Wiley & Sons, 2005.
- [22] B. G. Streetman and S. K. Banerjee. *Solid State Electronic Devices*. 7th Ed. Harlow: Pearson, 2016.

- [23] O. Slobodyan et al. *Journal of Materials Research* **37** (2022), p. 849.
- [24] B. J. Baliga. *Journal of Applied Physics* **53** (1982), p. 1759.
- [25] B. J. Baliga. *IEEE Electron Device Letters* **10** (1989), p. 455.
- [26] H. M. Jeon et al. *APL Materials* **9** (2021), p. 101105.
- [27] M.-A. Pinault et al. *Physica B* **401** (2007), p. 51.
- [28] K. H. L. Zhang et al. *Journal of Physics: Condensed Matter* **28** (2016), p. 383002.
- [29] J. Li et al. *Physical Review B* **74** (2006), p. 081201.
- [30] J. Robertson and S. J. Clark. *Physical Review B* **83** (2011), p. 075205.
- [31] J. Robertson and Z. Zhang. *MRS Bulletin* **46** (2021), p. 1037.
- [32] S.-Y. Chung et al. *Nature Physics* **5** (2009), p. 68.
- [33] R. Roy, V. G. Hill, and E. F. Osborn. *Journal of the American Chemical Society* **74** (1952), p. 719.
- [34] L. E. Ratcliff et al. *Advanced Materials* **34** (2022), p. 2204217.
- [35] T. Oshima et al. *Journal of Crystal Growth* **359** (2012), p. 60.
- [36] H. Y. Playford et al. *The Journal of Physical Chemistry C* **118** (2014), p. 16188.
- [37] T. Kato et al. *ACS Applied Electronic Materials* **5** (2023), p. 1715.
- [38] I. Cora et al. *CrystEngComm* **19** (2017), p. 1509.
- [39] D. Shinohara and S. Fujita. *Japanese Journal of Applied Physics* **47** (2008), p. 7311.
- [40] D. Machon et al. *Physical Review B* **73** (2006), p. 094125.
- [41] M. B. Maccioni and V. Fiorentini. *Applied Physics Express* **9** (2016), p. 041102.
- [42] S. Yoshioka et al. *Journal of Physics: Condensed Matter* **19** (2007), p. 346211.
- [43] M. Mitome et al. *Crystal Growth & Design* **13** (2013), p. 3577.
- [44] S. Nakagomi and Y. Kokubun. *Journal of Crystal Growth* **479** (2017), p. 67.
- [45] S. Nakagomi, S. Kubo, and Y. Kokubun. *Journal of Crystal Growth* **445** (2016), p. 73.
- [46] V. Ghodsi et al. *The Journal of Physical Chemistry C* **121** (2017), p. 9433.
- [47] T. Wang et al. *Journal of the American Chemical Society* **132** (2010), p. 9250.
- [48] Y. K. Frodason et al. *Journal of Applied Physics* **127** (2020), p. 075701.
- [49] M. Zhao et al. *Optical Materials* **102** (2020), p. 109807.

-
- [50] W. Mu et al. *Journal of Alloys and Compounds* **714** (2017), p. 453.
- [51] T. Hou et al. *Materials Science in Semiconductor Processing* **158** (2023), p. 107357.
- [52] Z. Guo et al. *Applied Physics Letters* **106** (2015), p. 111909.
- [53] V. M. Reinertsen et al. *Applied Physics Letters* **117** (2020), p. 232106.
- [54] A. T. Neal et al. *Applied Physics Letters* **113** (2018), p. 062101.
- [55] J. B. Varley et al. *Applied Physics Letters* **97** (2010), p. 142106.
- [56] A. Kyrtsov, M. Matsubara, and E. Bellotti. *Applied Physics Letters* **112** (2018), p. 032108.
- [57] H. He et al. *Physical Review B* **74** (2006), p. 195123.
- [58] H. Peelaers and C. G. Van de Walle. *Physica Status Solidi B* **252** (2015), p. 828.
- [59] T. Harwig, F. Kellendonk, and S. Slappendel. *Journal of Physics and Chemistry of Solids* **39** (1978), p. 675.
- [60] M. M. Islam et al. *Scientific Reports* **10** (2020), p. 6134.
- [61] Z. Xia et al. *Applied Physics Letters* **115** (2019), p. 252104.
- [62] E. G. Víllora et al. *Journal of Crystal Growth* **270** (2004), p. 420.
- [63] Z. Galazka et al. *Journal of Crystal Growth* **404** (2014), p. 184.
- [64] K. Hoshikawa et al. *Journal of Crystal Growth* **546** (2020), p. 125778.
- [65] H. Aida et al. *Japanese Journal of Applied Physics* **47** (2008), p. 8506.
- [66] A. Kuramata et al. *Japanese Journal of Applied Physics* **55** (2016), 1202A2.
- [67] J. F. Ziegler. *Ion Implantation: Science and Technology*. Ed. by J. F. Ziegler. 2nd Ed. San Diego: Academic Press, Inc., 1988.
- [68] E. Wendler et al. *Nuclear Instruments and Methods in Physics Research B* **379** (2016), p. 85.
- [69] E. A. Anber et al. *Applied Physics Letters* **117** (2020), p. 152101.
- [70] A. Azarov et al. *Physical Review Letters* **128** (2022), p. 015704.
- [71] A. Petkov et al. *Applied Physics Letters* **121** (2022), p. 171903.
- [72] H.-L. Huang et al. *APL Materials* **11** (2023), p. 061113.
- [73] A. Azarov et al. *Scientific Reports* **12** (2022), p. 15366.
- [74] A. Azarov et al. *Applied Physics Letters* **119** (2021), p. 182103.
- [75] S. B. Kjeldby et al. *Journal of Applied Physics* **131** (2022), p. 125701.
- [76] A. Azarov et al. *Applied Physics Letters* **118** (2021), p. 232101.
- [77] H.-L. Huang et al. *Applied Physics Letters* **122** (2023), p. 251602.
- [78] C. Wouters et al. *APL Materials* **12** (2024), p. 011110.
- [79] A. Y. Polyakov et al. *Journal of Applied Physics* **133** (2023), p. 095701.

- [80] A. Sardar et al. *Applied Physics Letters* **121** (2022), p. 262101.
- [81] A. Azarov et al. *Journal of Vacuum Science & Technology A* **41** (2023), p. 023101.
- [82] K.E. Sickafus et al. *Journal of Nuclear Materials* **274** (1999), p. 66.
- [83] G. Sattonnay and L. Thomé. *Journal of Nuclear Materials* **348** (2006), p. 223.
- [84] B. Lacroix, R. J. Gaboriaud, and F. Paumier. *Acta Materialia* **153** (2018), p. 303.
- [85] A. Benyagoub. *Nuclear Instruments and Methods in Physics Research B* **218** (2004), p. 451.
- [86] C. L. Tracy et al. *Physical Review B* **92** (2015), p. 174101.
- [87] S. Dhara et al. *Applied Physics Letters* **84** (2004), p. 5473.
- [88] J. A. Valdez, Z. Chi, and K. E. Sickafus. *Journal of Nuclear Materials* **381** (2008), p. 259.
- [89] Y. K. Frodason et al. *Physical Review B* **107** (2023), p. 024109.
- [90] J. B. Varley et al. *Journal of Physics: Condensed Matter* **23** (2011), p. 334212.
- [91] Y. Huang et al. *Materials Today Communications* **35** (2023), p. 105898.
- [92] J. E. Stehr et al. *Applied Physics Letters* **119** (2021), p. 052101.
- [93] A. Luchechko et al. *Journal of Physics D: Applied Physics* **53** (2020), p. 354001.
- [94] Y. Li et al. *Advanced Functional Materials* **20** (2010), p. 3972.
- [95] T. Onuma et al. *Applied Physics Letters* **103** (2013), p. 041910.
- [96] J. B. Varley et al. *Physical Review B* **85** (2012), p. 081109.
- [97] M. A. Reshchikov. *Journal of Applied Physics* **129** (2021), p. 121101.
- [98] M. A. Reshchikov et al. *Physical Review B* **90** (2014), p. 035207.
- [99] A. Alkauskas, M. D. McCluskey, and C. G. Van De Walle. *Journal of Applied Physics* **119** (2016), p. 181101.
- [100] Y. Wang et al. *Scientific Reports* **8** (2018), p. 18075.
- [101] T. Harwig and F. Kellendonk. *Journal of Solid State Chemistry* **24** (1978), p. 255.
- [102] E. G. Vllora et al. *Solid State Communications* **120** (2001), p. 455.
- [103] L. Binet and D. Gourier. *Journal of Physics and Chemistry of Solids* **59** (1998), p. 1241.
- [104] T. Onuma et al. *Journal of Applied Physics* **124** (2018), p. 075103.
- [105] T. T. Huynh et al. *Physical Review Materials* **2** (2018), p. 105203.
- [106] R. Sun et al. *Journal of Physics D: Applied Physics* **54** (2021), p. 174004.

-
- [107] Y. Nie et al. *Journal of Alloys and Compounds* **900** (2022), p. 163431.
- [108] R. Sun et al. *Applied Physics Letters* **117** (2020), p. 052101.
- [109] M. Back et al. *Advanced Optical Materials* **9** (2021), p. 2100033.
- [110] W. Mu et al. *RSC Advances* **7** (2017), p. 21815.
- [111] T. P. Beales, C. H. L. Goodman, and K. Scarrott. *Solid State Communications* **73** (1990), p. 1.
- [112] A. Lucheckko et al. *ECS Journal of Solid State Science and Technology* **9** (2020), p. 045008.
- [113] S. Wu et al. *Crystals* **13** (2023), p. 1045.
- [114] D. M. Esteves et al. *Scientific Reports* **13** (2023), p. 4882.
- [115] A. Mang, K. Reimann, and S. Rübenacke. *Solid State Communications* **94** (1995), p. 251.
- [116] A. Janotti and C. G. Van De Walle. *Reports on Progress in Physics* **72** (2009), p. 126501.
- [117] Ü. Özgür et al. *Journal of Applied Physics* **98** (2005), p. 041301.
- [118] O. Köster-Scherger et al. *Journal of the American Ceramic Society* **90** (2007), p. 3984.
- [119] M. A. Reshchikov et al. *Physica B* **401-402** (2007), p. 358.
- [120] J. Lv, C. Li, and Z. Chai. *Journal of Luminescence* **208** (2019), p. 225.
- [121] B. L. Aarseth et al. *Nanotechnology* **32** (2021), p. 505707.
- [122] C. S. Granerød et al. *Nanotechnology* **30** (2019), p. 225702.
- [123] H. Schmid et al. *Micron* **43** (2012), p. 49.
- [124] T. Hörlin, G. Svensson, and E. Olsson. *Journal of Materials Chemistry* **8** (1998), p. 2465.
- [125] F. Wolf, B. H. Freitag, and W. Mader. *Micron* **38** (2007), p. 549.
- [126] S. B. Kjeldby et al. *Nanoscale Advances* **5** (2023), p. 2102.
- [127] H. Schmid, E. Okunishi, and W. Mader. *Ultramicroscopy* **127** (2013), p. 76.
- [128] L. I. Granone et al. *Physical Chemistry Chemical Physics* **20** (2018), p. 28267.
- [129] Y. Li et al. *Chemical Geology* **504** (2019), p. 276.
- [130] K. E. Sickafus, J. M. Wills, and N. W. Grimes. *Journal of the American Ceramic Society* **82** (1999), p. 3279.
- [131] S. Zhou et al. *Journal of Physics D: Applied Physics* **40** (2007), p. 964.
- [132] R. Bayat et al. *Solid State Sciences* **89** (2019), p. 167.
- [133] S. D. Kulkarni et al. *Materials Research Bulletin* **77** (2016), p. 70.
- [134] L. I. Granone et al. *Catalysts* **9** (2019), p. 434.

- [135] M. Nastasi and J. W. Mayer. *Ion Implantation and Synthesis of Materials*. Berlin Heidelberg: Springer, 2006.
- [136] B. M. Paine, N. N. Hurvitz, and V. S. Speriosu. *Journal of Applied Physics* **61** (1987), p. 1335.
- [137] D. C. Ingram et al. *Nuclear Instruments and Methods in Physics Research B* **21** (1987), p. 460.
- [138] J. F. Ziegler, M. D. Ziegler, and J. P. Biersack. *Nuclear Instruments and Methods in Physics Research B* **268** (2010), p. 1818.
- [139] A. E. Michel et al. *Applied Physics Letters* **44** (1984), p. 404.
- [140] R. E. Stoller et al. *Nuclear Instruments and Methods in Physics Research B* **310** (2013), p. 75.
- [141] Y. Sun et al. *Annals of Nuclear Energy* **183** (2023), p. 109667.
- [142] A. Hallén et al. *Materials Science and Engineering B* **61** (1999), p. 378.
- [143] M. E. Bathen et al. *npj Quantum Information* **5** (2019), p. 111.
- [144] P. D. Parry. *Journal of Vacuum Science and Technology* **13** (1976), p. 622.
- [145] J. Jesenovec et al. *Journal of Applied Physics* **129** (2021), p. 245701.
- [146] M. Birkholz. *Thin Film Analysis by X-Ray Scattering*. Weinheim: WILEY-VCH, 2006.
- [147] J. Åhman, G. Svensson, and J. Albertsson. *Acta Crystallographica Section C* **52** (1996), p. 1336.
- [148] W. W. Wendlandt and H. G. Hecht. *Reflectance Spectroscopy, Vol. 21 in Chemical Analysis - A series of Monographs on Analytical Chemistry and its Applications*. Ed. by P. J. Elving and I. M. Kolthoff. 1st Ed. New York/London/Sydney: Interscience Publishers, 1966.
- [149] B. D. Viezbicke et al. *Physica Status Solidi B* **252** (2015), p. 1700.
- [150] F. Urbach. *Physical Review* **92** (1953), p. 1324.
- [151] N. F. Mott and E. A. Davis. *Electronic Processes in Non-Crystalline Materials*. Ed. by W Marshall and D. H. Wilkinson. 2nd Ed. Oxford: Clarendon Press, 1979.
- [152] T. Zheng et al. *Computational Materials Science* **174** (2020), p. 109505.
- [153] R. F. Egerton. *Physical Principles of Electron Microscopy - An Introduction to TEM, SEM and AEM*. 2nd Ed. Springer, 2016.
- [154] T. Coenen and N. M. Haegel. *Applied Physics Reviews* **4** (2017), p. 031103.
- [155] B. G. Yacobi and D. B. Holt. *Journal of Applied Physics* **59** (1986), R1.
- [156] R. Pässler. *Physica Status Solidi B* **85** (1978), p. 203.
- [157] J. Fang et al. *IEEE Transactions on Nuclear Science* **66** (2019), p. 444.
- [158] D. Drouin et al. *Scanning* **29** (2007), p. 92.

-
- [159] L. J. Brillson. *Journal of Physics D: Applied Physics* **45** (2012), p. 183001.
- [160] R. Sugie et al. *Applied Physics Express* **13** (2020), p. 126502.
- [161] D. B. Williams and C. B. Carter. *Transmission Electron Microscopy*. 2nd Ed. New York: Springer, 2009.
- [162] R. Ishikawa et al. *Nature Materials* **10** (2011), p. 278.
- [163] R.F. Egerton. *Electron Energy-Loss Spectroscopy in the Electron Microscope*. 3rd Ed. Springer Science & Business Media, 2011.
- [164] P. Van der Heide. *Secondary Ion Mass Spectrometry - An Introduction To Principles and Practices*. 1st Ed. Hoboken, New Jersey: John Wiley & Sons, Inc., 2014.
- [165] G. Friedbacher and H. Bubert. *Surface and Thin Film Analysis*. Ed. by Gernot Friedbacher and Henning Bubert. 2nd Ed. Weinheim: WILEY-VCH, 2011.
- [166] W.-K. Chu, J. W. Mayer, and M.-A. Nicolet. *Backscattering spectrometry*. San Diego: Academic Press, Inc., 1978.
- [167] S. Hüfner. *Photoelectron Spectroscopy: Principles and Applications*. 3rd Ed. Berlin, Heidelberg: Springer, 2003.
- [168] F. A. Stevie and C. L. Donley. *Journal of Vacuum Science & Technology A* **38** (2020), p. 063204.
- [169] E. G. Víllora et al. *Applied Physics Letters* **92** (2008), p. 202120.
- [170] R. Sharma et al. *Journal of Vacuum Science & Technology B* **37** (2019), p. 051204.
- [171] C. C. Ahn and O. L. Krivanek. *EELS Atlas: A reference guide of electron energy loss spectra covering all stable elements*. Warrendale: Gatan, 1983.
- [172] M.-M. Soumelidou et al. *Physica Status Solidi C* **10** (2013), p. 105.
- [173] M. Floyd et al. *Applied Physics Letters* **82** (2003), p. 1473.
- [174] R. Pantel, M. C. Cheynet, and F. D. Tichelaar. *Micron* **37** (2006), p. 657.
- [175] C. S. Granerød et al. *Physical Review B* **98** (2018), p. 115301.
- [176] A. Y. Polyakov et al. *Journal of Materials Chemistry C* **12** (2024), p. 1020.

Papers

Paper I

Radiation-induced defect accumulation and annealing in Si-implanted gallium oxide

S. B. Kjeldby, A. Azarov, P. D. Nguyen,
V. Venkatachalapathy, R. Mikšová, A. Macková, A.
Kuznetsov, Ø. Prytz and L. Vines

Published in *Journal of Applied Physics*, March 2022, Volume 131

DOI:10.1063/5.008385

Reproduced from S. B. Kjeldby *et al.*, *Journal of Applied Physics* **131**,
125701 (2022), with the permission of AIP Publishing.









Radiation-induced defect accumulation and annealing in Si-implanted gallium oxide

Cite as: J. Appl. Phys. **131**, 125701 (2022); doi: [10.1063/5.0083858](https://doi.org/10.1063/5.0083858)

Submitted: 30 December 2021 · Accepted: 7 March 2022 ·

Published Online: 22 March 2022



S. B. Kjeldby,^{1,a)}  A. Azarov,¹  P. D. Nguyen,¹  V. Venkatachalapathy,^{1,2}  R. Mikšová,³  A. Macková,^{3,4} 
A. Kuznetsov,¹  Ø. Prytz,¹  and L. Vines¹ 

AFFILIATIONS

¹Department of Physics and Center for Materials Science and Nanotechnology, University of Oslo, Oslo, Norway

²Department of Materials Science, National Research Nuclear University, "MEPhI," Moscow, Russian Federation

³Nuclear Physics Institute of the Czech Academy of Sciences, Řež, Czech Republic

⁴Department of Physics, Faculty of Science, J.E. Purkyně University, Ústí nad Labem, Czech Republic

Note: This paper is part of the Special Topic on Defects in Semiconductors.

a) Author to whom correspondence should be addressed: s.b.kjeldby@smn.uio.no

ABSTRACT

Defect accumulation and annealing phenomena in Si-implanted monoclinic gallium oxide (β -Ga₂O₃) wafers, having ($\bar{2}01$), (010), and (001) orientations, were studied by Rutherford backscattering spectrometry in channeling mode (RBS/c), x-ray diffraction (XRD), and (scanning) transmission electron microscopy [(S)TEM]. Initially, the samples with different surface orientations were implanted with 300 keV ²⁸Si⁺-ions, applying fluences in the range of 1×10^{14} – 2×10^{16} Si/cm², unveiling interesting disorder accumulation kinetics. In particular, the RBS/c, XRD, and (S)TEM combined data suggested that the radiation disorder buildup in Si-implanted β -Ga₂O₃ is accompanied by significant strain accumulation, assisting crystalline-to-crystalline phase transitions instead of amorphization. Selected samples having ($\bar{2}01$) orientation were subjected to isochronal (30 min) anneals in the range of 300–1300 °C in air. Systematic RBS/c and XRD characterization of these samples suggested complex structural transformations, which occurred as a function of the fluence and the temperature. Moreover, a detailed (S)TEM analysis of the sample implanted with 2×10^{16} Si/cm² and annealed at 1100 °C was enhanced by applying dispersive x-ray and electron energy-loss spectroscopies. The analysis revealed silicon agglomerations in the form of silicon dioxide particles. Signal from silicon was also detected outside of the agglomerates, likely occurring as substitutional Si on Ga sites.

Published under an exclusive license by AIP Publishing. <https://doi.org/10.1063/5.0083858>

I. INTRODUCTION

Gallium oxide (Ga₂O₃) is a modern ultra-wide bandgap semiconductor of both academic and technological interest. On the technological side, Ga₂O₃ may provide unique opportunities to realize high-voltage tolerating devices as well as deep UV-operating optoelectronic devices. On the academic side, Ga₂O₃ shows rich variations in crystal structure through its polymorphism. In addition to the monoclinic β -phase (β -Ga₂O₃), which is the thermodynamically stable polymorph at room temperature and atmospheric pressure,¹ several other polymorphs including the orthorhombic κ -Ga₂O₃,^{2,3} the rhombohedral α -Ga₂O₃,⁴ the spinel-like γ -Ga₂O₃,⁵ and the bixbyite δ -Ga₂O₃^{6,7} were reported. The kinetics of annealing in gallium oxide and the related polymorph transformations have previously been investigated down to the atomic scale,

particularly for transformations between κ - and β -phases.^{8,9} The literature also contains atomic resolution studies of different Ga₂O₃ polymorphs grown by heteroepitaxy.^{10,11}

Among the electronic dopants in β -Ga₂O₃, silicon (Si) is highly technologically important because it creates an efficient donor state by Si substituting for Ga in the crystal lattice.^{12,13} Si occurs as an unintentional impurity in bulk β -Ga₂O₃ in concentrations up to 10^{16} – 10^{18} Si/cm³,¹⁴ but can also be incorporated via in-diffusion or ion implantation.¹⁵ Ion implantation is often technologically preferable as it typically permits higher dopant localization control. β -Ga₂O₃ MOSFETs already utilize Si-implanted channels, which has motivated studies of Si diffusion and redistribution in Si-implanted Ga₂O₃ with post-implantation anneals.¹⁶

15 February 2024 12:54:23

However, systematic studies of the Si ion-induced radiation disorder evolution during annealing are at least incomplete, even though the fundamentals of the radiation effects in $\beta\text{-Ga}_2\text{O}_3$ have attracted significant interest in the research community^{17–20} Very recently, Azarov *et al.*¹⁷ reported on phase transformation in $\beta\text{-Ga}_2\text{O}_3$ induced by Ni, Ga, and Au ion implantation. Ion-induced structural transformation in $\beta\text{-Ga}_2\text{O}_3$ has also been reported by Anber *et al.* for Ge-implantation.²¹ This structural transformation may open up possibilities to alter the properties of single crystal wafers in a layer or be used as a template for the growth of other gallium oxide polymorphs.

Certainly, disorder accumulation and annealing phenomena must also be understood for Si-implanted $\beta\text{-Ga}_2\text{O}_3$ since Si-implantation is used in device fabrication. In the present work, we undertook a systematic investigation of the radiation-induced defect evolution in Si-implanted $\beta\text{-Ga}_2\text{O}_3$ wafers exhibiting different crystallographic orientations, in particular studying the effects of the implantation fluence and post-implantation anneals. Our results reveal a structural transformation for the highest fluences and that significant disorder remains even after annealing at 1100 °C. Moreover, annealing at 1100 °C revealed a significant amount of Si precipitates, likely in the form of SiO_2 , which may reduce the doping efficiency when used in devices.

II. EXPERIMENTAL PROCEDURES

Three types of $\beta\text{-Ga}_2\text{O}_3$ wafers with different surface orientations were used in this study: a bulk edge-defined film-fed grown (EFG) crystal wafer having (201) surface orientation, a bulk EFG wafer having (010) surface orientation, and a halide vapor phase epitaxy (HVPE) film with (001) orientation grown on a doped EFG substrate. All samples were obtained from Novel Crystal Technology Inc., with donor concentrations of 2.9×10^{17} , 2.2×10^{17} , and $2.3 \times 10^{16} \text{ cm}^{-3}$ for the (201), (010), and (001) wafers, respectively. Samples with a size of approximately $5 \times 5 \text{ mm}$ were cut from the wafers, and one sample from each orientation was left as an unimplanted reference without further processing. The samples were implanted with 300 keV $^{28}\text{Si}^+$ -ions applying a fluence range from 1×10^{14} to $2 \times 10^{16} \text{ Si/cm}^2$. The current density was kept constant at $1.7 \times 10^{13} \text{ ions/s cm}^2$ ($2.8 \mu\text{A/cm}^2$) for all implants to avoid dose-rate effects.²⁰ All implants were performed at room temperature. Note that samples in the as-implanted state were too resistive for both electrical measurements and chemical profiling using, e.g., secondary ion mass spectrometry. Hence, the ion depth profiles and the corresponding defect production were simulated using the SRIM code,²² applying the density reported by Åhman *et al.* for $\beta\text{-Ga}_2\text{O}_3$.²³ The (201)-oriented samples were selected for a sequential 30-min isochronal annealing series, at 300, 500, 700, 900, 1000, 1100, 1200, and 1300 °C in air.

Rutherford backscattering spectrometry in channeling mode (RBS/c) measurements were carried out using either 1.6 or 2.0 MeV $^4\text{He}^+$ -ions in 165° and 170° backscattering geometry, respectively. Non-channeling (unaligned) RBS spectra were recorded for all samples. For these measurements, the sample was tilted away from channeling conditions. Under unaligned measurement conditions, the signal from crystalline and amorphous samples should be equivalent if the samples are otherwise identical.

Therefore, unaligned RBS measurements represent an upper limit to the damage that the sample can accumulate during ion implantation, namely, amorphization. Such RBS measurements are labeled as “random” below. Additionally, RBS/c spectra from as-received, unimplanted samples were recorded, which represent the limit of minimal sample damage. X-ray diffraction (XRD) characterization was performed using a Bruker AXS D8 Discover diffractometer with a monochromated $\text{Cu K}\alpha$ x-ray source in locked couple mode.

Two (201)-oriented samples implanted with $2 \times 10^{16} \text{ Si/cm}^2$ were prepared for (scanning) transmission electron microscopy [(S)TEM]. One of the samples was annealed at 1100 °C for 30 min in air. The samples were prepared for cross-sectional observations by mechanical grinding and finished with Ar-ion milling in a Gatan Precision Ion Polishing System (PIPS II). (S)TEM imaging, selected area electron diffraction (SAD), energy dispersive x-ray spectroscopy (EDS), and electron energy-loss spectroscopy (EELS) measurements were done at 300 kV in a Cs-corrected Thermo Fisher Scientific Titan G2 60-300 kV microscope, equipped with a Gatan GIF Quantum 965 spectrometer, and Super-X EDS detectors.

III. RESULTS AND DISCUSSION

A. Role of the surface orientation

Figure 1 shows RBS/c spectra of as-implanted (201), (010), and (001) $\beta\text{-Ga}_2\text{O}_3$ samples in panels (a), (b), and (c), respectively, comparing the data from the lowest ($1 \times 10^{14} \text{ Si/cm}^2$) and highest ($2 \times 10^{16} \text{ Si/cm}^2$) fluences with channeling spectra from the unimplanted samples. The spectra from the randomly oriented samples are also included in Fig. 1. As described above, channeling measurements on unimplanted samples represent a lower limit to ion-induced damage accumulation, whereas “random” measurements represent the upper limit, namely, amorphization. Note that the horizontal channel-number scale in Fig. 1(a) is different from that of Figs. 1(b) and 1(c) because different He-ion energies were used. However, the calculated depth scales enable direct comparison of the spectra from the three different orientations. Additionally, calculated SRIM depth profiles²² of implanted atoms are plotted in Fig. 1, revealing the implantation peak $\sim 250 \text{ nm}$ below the sample surface. The corresponding calculated vacancy profiles peaked at $\sim 200 \text{ nm}$. Previous work in the literature has shown that SRIM calculations of the depth distribution for Si-implantation in $\beta\text{-Ga}_2\text{O}_3$ correspond well with experimental measurements.^{16,24}

Different channels are active in RBS/c measurements on the differently oriented samples, which is corroborated by χ_{min} -values of 4.1%, 3.8%, and 7.4% for (201)-, (010)-, and (001)-oriented samples, respectively, measured on the unimplanted samples. Although the former two orientations have similar χ_{min} -values, it is clear from the rapid increase in the scattering yield at increased depth for (201) that the probability of dechanneling is higher for this channel than for the active channel of (010)-oriented samples. The difference in He-ion energy is also partially responsible for the difference in dechanneling between (201)- and (010)-oriented samples.

Naturally, disorder accumulation is observed in all samples independent of the surface orientation. This is evident from the fact that damage levels are increased for samples with higher implantation fluence. However, there are also distinct trends in the

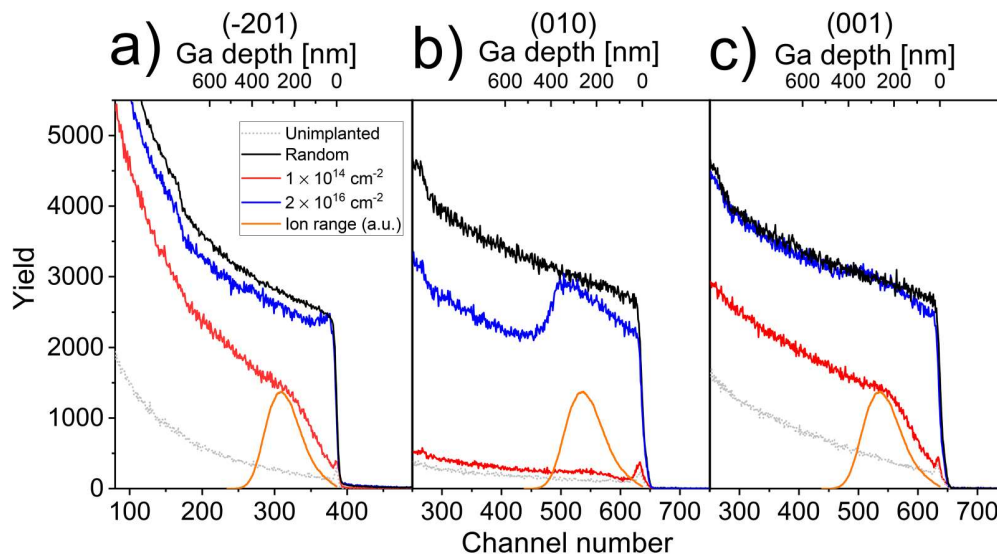


FIG. 1. RBS/c spectra for (a) $(\bar{2}01)$, (b) (010) , and (c) (001) samples showing the effect of the surface orientation on implantation-induced defect accumulation in β - Ga_2O_3 . (010) - and (001) -orientations were characterized with 2.0 MeV $^4\text{He}^+$ -ions, while the $(\bar{2}01)$ -orientation was characterized with 1.6 MeV $^4\text{He}^+$ -ions. Calculated depth scales for the Ga sublattice are given on top, and calculated Si-concentration profiles from SRIM have been included in orange (arbitrary units). The legend is shared across (a)–(c).

RBS/c spectra, which depend on the surface orientation. This is likely caused by different defect types dominating in the corresponding channels or by a difference in the defect density and nature. To start with, both $(\bar{2}01)$ - and (001) -oriented samples showed high disorder for the fluence of $1 \times 10^{14} \text{ Si/cm}^2$, whereas the (010) -oriented sample showed only slight deviation from the spectrum of the unimplanted sample. Moreover, a comparison between the dechanneling yields deeper in the samples indicates a significantly larger fraction of extended defects²⁵ for $(\bar{2}01)$ - and (001) -oriented samples compared with the (010) -oriented sample. Similar trends hold for samples implanted with $2 \times 10^{16} \text{ Si/cm}^2$, i.e., $(\bar{2}01)$ - and (001) -oriented samples again exhibiting higher dechanneling in the bulk than in the (010) -oriented sample. Importantly, a prominent disorder plateau with a gradually increasing RBS/c yield extending to $\sim 400 \text{ nm}$ from the sample surface is observed in Fig. 1(b) for (010) surface orientation.

The (001) -oriented HVPE film and the unimplanted (010) - and $(\bar{2}01)$ -oriented bulk samples may have had different defect concentrations prior to implantation. For implantation fluence $2 \times 10^{16} \text{ Si/cm}^2$, the RBS/c yield was far larger than for the unimplanted samples for all orientations. Hence, the signal was dominated by ion-induced defects, and small variations in preexisting defect concentrations can safely be ignored. However, for both the (010) - and (001) -oriented samples, the RBS/c yield for fluence $1 \times 10^{14} \text{ Si/cm}^2$ was much lower. Therefore, preexisting defects could contribute non-negligibly to the total defect concentration in these cases.

Figure 2 shows the XRD data from the same samples studied in Fig. 1. In the $(\bar{2}01)$ -oriented sample, $(\bar{2}01)$, $(\bar{4}02)$, $(\bar{6}03)$, and

$(\bar{8}04)$ diffraction peaks were present in the diffractograms. Importantly, the emergence of additional diffraction peaks was observed around the $(\bar{4}02)$ and $(\bar{8}04)$ peaks. To show the evolution of these peaks, we have chosen to focus on the (402) peak at 38.39° , corresponding to a plane spacing of 2.343 \AA . Calculated plane spacings from diffractograms are henceforth given in parenthesis. In the (010) - and (001) -oriented samples, the main diffraction peaks were attributed to the (020) -planes at 60.90° (1.520 \AA) and the (002) -planes at 31.71° (2.820 \AA), respectively. In addition, diffraction peaks from the sample holder at 38.00° (2.366 \AA) and 64.50° (1.444 \AA) were detected.

For the $1 \times 10^{14} \text{ Si/cm}^2$ implants, all samples showed an additional peak or shoulder on either the low-angle [(001) - and $(\bar{2}01)$ -oriented] or high-angle [(010) -oriented] side of the main diffraction peak. These side peaks were attributed to the implantation-induced strain.^{17,20} The fact that tensile strain is observed for some crystal orientations and compressive strain is observed for others reveals anisotropy in the induced strain in the samples.

The $2 \times 10^{16} \text{ Si/cm}^2$ implantation fluence was presumably high enough to reach the threshold reported by Azarov *et al.*¹⁷ and Anber *et al.*²¹ for structural transformation toward κ - Ga_2O_3 . Indeed, a broad additional diffraction peak, labeled as peak C, appeared around 63.5° (1.46 \AA) in the (010) -sample, and a double peak, labeled as peaks A and B, appeared around 37.5° (2.40 \AA) in the $(\bar{2}01)$ -sample for this fluence. In the (010) sample, the observed additional peak could be consistent with diffraction peaks from strained κ - Ga_2O_3 and is inconsistent with plane spacings in β - Ga_2O_3 from the literature.²³ In the $(\bar{2}01)$ -sample, the observed

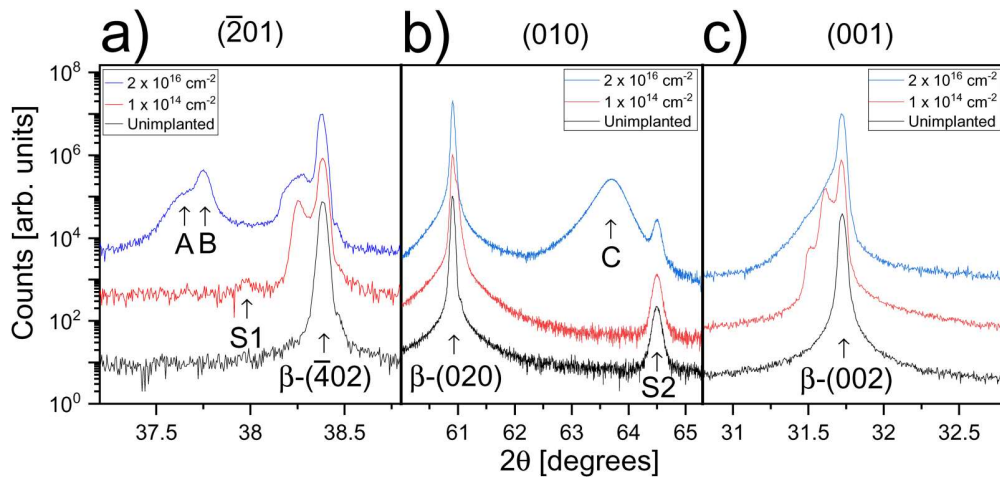


FIG. 2. XRD diffractograms from samples with surface orientation (a) $(\bar{2}01)$, (b) (010) , and (c) (001) , for different implantation fluences. Uppercase letters A–C indicate additional diffraction peaks that appeared after implantation. Labels S1 and S2 indicate the positions of known diffraction peaks from the sample stage.

double peak could be attributed to strained κ - Ga_2O_3 ,³ but could also be explained by strained β - Ga_2O_3 , although the reported intensity ratios for the β -phase are not in good agreement with the observed intensity ratio from the double peak.

For the $2 \times 10^{16} \text{ Si/cm}^2$ implants into the (001) -oriented sample, strain was observed as a broadening of the (002) -diffraction peak toward smaller angles. For this orientation, no additional diffraction peaks were observed. Note that our XRD measurements are only able to detect crystal planes lying parallel to the sample surface. Hence, it is possible that ion implantation causes additional diffraction peaks in this sample as well, but that these XRD peaks are invisible in our XRD geometry.

B. Defect annealing kinetics

To investigate the annealing behavior of Si-implanted β - Ga_2O_3 , a 30-min isochronal annealing study in air was undertaken for $(\bar{2}01)$ -oriented samples, using RBS/c and XRD for sample characterization after each annealing step. The main feature of interest revealed by XRD in the surface orientation study was the appearance of additional diffraction peaks. This feature was not observed for (001) -oriented samples. For this reason, (001) -oriented samples were not included in the annealing study. Furthermore, some previous work exists in the literature on the annealing behavior of (010) -oriented samples.¹⁷ Consequently, this orientation was also excluded from the annealing study. Finally, the significant technological interest in $(\bar{2}01)$ -oriented samples justifies focusing on this sample orientation.

Figure 3 shows the RBS/c spectra from the annealing series of $(\bar{2}01)$ -oriented samples implanted with 1×10^{14} , 1×10^{15} , and $2 \times 10^{16} \text{ Si/cm}^2$. The channeling spectrum from the unimplanted sample and the random spectrum are shown for comparison. Spectra with little change from the previous annealing step were excluded from Fig. 3(c).

Figure 3 reveals that the defect evolution exhibits prominent dependence on the fluence. Indeed, for the lowest implantation fluence ($1 \times 10^{14} \text{ Si/cm}^2$), significant defect reduction occurred after annealing at 300°C , with defect levels close to that of the unimplanted sample regained already at 700°C . For the intermediate implantation fluence ($1 \times 10^{15} \text{ Si/cm}^2$), a defect plateau was present within $\sim 300 \text{ nm}$ from the sample surface. Defect level reduction in this region started from the surface after annealing at 500°C , with the defect plateau disappearing after 900°C . However, high dechanneling yield behind the damage peak persisted and further heat treatments resulted in a minor backscattering yield reduction only. For the highest implantation fluence ($2 \times 10^{16} \text{ Si/cm}^2$), a slight defect reduction occurred to a depth of $\sim 100 \text{ nm}$ in the near-surface region after 500°C . Further annealing at higher temperatures led to a reduction in the damage plateau width, starting from the sample bulk. The latter effect could be attributed to the solid-phase regrowth of the β -phase from the bulk.¹⁷

Figure 4 shows diffractograms from the same samples at all stages in the annealing series. For the lowest implantation fluence, a shoulder peak appeared at 38.25° (2.35 \AA) after implantation. This peak was attributed to implantation-induced strain. For the intermediate fluence, similar strain effects were present in the diffractograms, in addition to the peak labeled as B, emerging around 37.7° (2.38 \AA). After annealing at 700°C , this peak disappeared, approximately coinciding with a reduction of the defect levels observed in RBS/c. For the highest implantation fluence, a double peak appeared around 37.7° (2.38 \AA), see peaks labeled A and B in the figure. Peak B disappeared after annealing at 700°C , and peak A underwent a minor shift toward smaller angles with increasing annealing temperature. For temperatures in excess of 700°C , a diffraction peak appeared around 37.3° (2.41 \AA), labeled D, with increasing peak intensity for increased annealing temperatures. This diffraction peak was attributed to regrowth of β - Ga_2O_3 , with the peak corresponding to diffraction from (310) -planes.²³ After

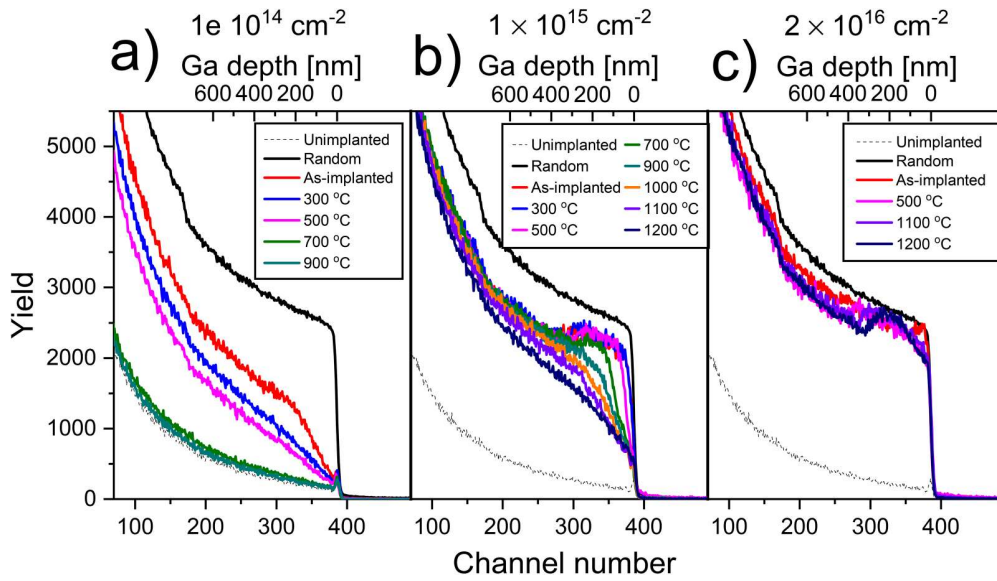


FIG. 3. RBS/c spectra of $(\bar{2}01)$ -oriented samples subjected to (a) 1×10^{14} , (b) 1×10^{15} , and (c) 2×10^{16} Si/cm^2 implants after implantation and after selected steps in the isochronal annealing series. The unimplanted (dotted gray line) and random (solid black line) spectra are shown for comparison. For the lowest fluence, the annealing series was terminated after 900 °C since defect levels had returned to those of the unimplanted sample.

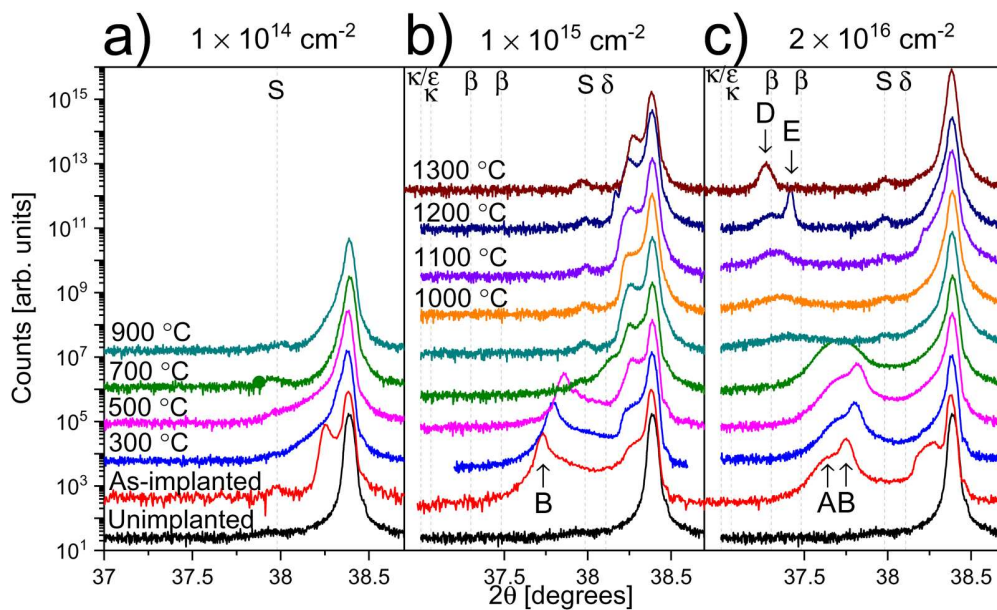


FIG. 4. X-ray diffractograms from $(\bar{2}01)$ -oriented samples implanted to fluence (a) 1×10^{14} , (b) 1×10^{15} , and (c) 2×10^{16} Si/cm^2 . Uppercase letters A, B, D, and E denote additional diffraction peaks that appeared after implantation or during the following annealing series. A and B refer to the same peaks as in Fig. 2(a). Indicated plane spacings for Ga_2O_3 polymorphs (vertical gray dashed lines marked by phase) are taken from Åhman *et al.*,²³ Cora *et al.*,³ and Roy *et al.*⁷ for β -, κ -, and δ -phases, respectively. Vertical gray dashed lines marked with "S" are from the sample stage.

15 February 2024 12:54:23

annealing at 1200 °C, an additional narrow diffraction peak, labeled as peak E, appeared at 37.4° (2.40 Å). This peak disappeared after annealing at 1300 °C.

Potentially, peaks B and A can be assigned to κ -(210) and κ -(131) planes, following the identification suggested previously.¹⁷ With this assignment, an isotropic compressive strain of 1.8% would be required to match the data from the as-implanted sample to literature references.³ Hence, if the additional diffraction peaks are due to κ -Ga₂O₃, then there is substantial strain in the samples after implantation. Similarly, it is possible to attribute peak A to the (310) diffraction peak of β -Ga₂O₃ and peak B to the (401) diffraction peak. This assignment gives a compressive strain of 0.92% and 0.68%, respectively, assuming isotropic strain and taking literature values from the work by Åhman *et al.*²³ However, literature results suggest a peak intensity ratio of 55 for the (401) and (310) peaks, while our diffractograms give an intensity ratio of 3 between peaks B and A. Thus, the XRD data in Figs. 2 and 4 were insufficient to unambiguously identify the origin of peaks A and B.

For the intermediate implantation fluence, another weak diffraction peak appeared at 38.16° (2.356 Å) after annealing at 1200 °C. For the highest implantation fluence, a straight shoulder appeared at 38.22° (2.353 Å) after annealing at 1100 °C. These features in the diffractogram appear near the (411) diffraction peak from δ -Ga₂O₃ at 38.2° (2.36 Å).⁷ Thus, the presence of a slightly strained δ -phase in our samples is possible. However, since we did not observe a consistent contribution from this diffraction peak, its origins were not investigated further. Similarly, the origins of peak E were not investigated, since it occurred in only one of the diffractograms.

C. Defect microstructure

To further investigate the microstructure of the samples, we proceeded to study (201)-oriented samples implanted to high fluence (2×10^{16} Si/cm²) both before and after annealing (1100 °C, 30 min) in more detail. Figure 5 shows STEM annular dark field (ADF) images of the near-surface region of the two samples in panels (a) and (b), respectively. SAD patterns from the implanted layer and the underlying bulk have been included as insets.

The ADF images in Fig. 5 reveal a contrast variation, with a bright-contrast region extending from the surface to the depth of ~400 and ~340 nm, in panels (a) and (b), respectively. The bright contrast is attributed to increased strain values. The colored arrows in Fig. 5 indicate three characteristic depths in the samples, with average values and uncertainties acquired from 10 measurements at different positions. In the as-implanted sample, the depth of the bright-contrast layer was measured to be 409 ± 2 nm (green arrow), while the corresponding depth in the annealed sample was found to be 344 ± 5 nm (blue arrow). Some residual streaks of bright contrast remained in the annealed sample and extended to a depth of 414 ± 7 nm (orange arrow) which was consistent with the observed depth of the damaged layer in the as-implanted sample. This indicated that the region in which these streaks were observed represents an area where crystal regrowth from the bulk had occurred. The width of the bright-contrast band was reduced from 409 to 344 nm after annealing at 1100 °C, a reduction of 65 nm. Inspection of the RBS/c spectra showed that both the absolute depth values and the changes are comparable with the evolution of the defect plateau for a sample with the same implantation fluence (2×10^{16} Si/cm²).

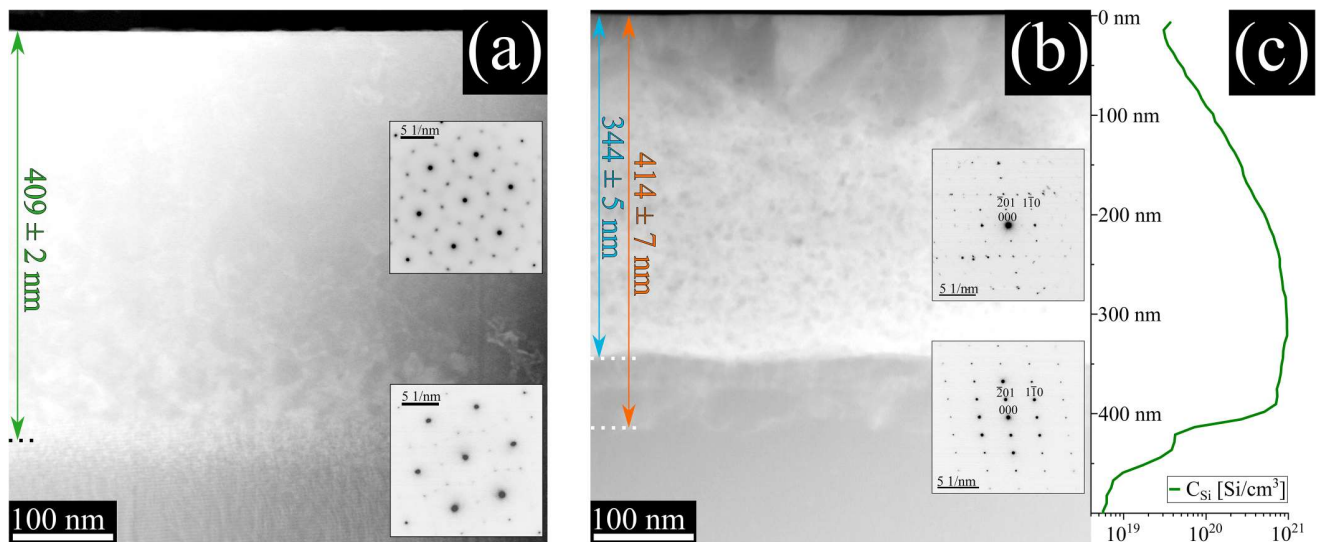


FIG. 5. STEM ADF images from (a) an as-implanted (201)-oriented sample with implantation fluence 2×10^{16} Si/cm² and (b) a (201)-oriented sample implanted to the same fluence and annealed at 1100 °C. Colored arrows and numbers mark relevant depth measurements from the samples. Insets show diffraction patterns from the implanted layer (upper inset) and bulk (lower inset). (c) Secondary ion mass spectrometry (SIMS) profile of the Si concentration in units of atoms/cm³, acquired from a circular area with a diameter of 33 μ m. The vertical length scale is shared between (b) and (c).

15 February 2024 12:54:23

Figure 5(b) features lateral contrast variations in the upper 100 nm of the sample. This contrast variation corresponded to the regrowth of β -Ga₂O₃. From the ADF contrast, which is sensitive to diffraction, the granular structure of the regrown β -phase is apparent. RBS/c spectra from the sample with the same fluence (2×10^{16} Si/cm²) also revealed reduced disorder near the sample surface after annealing. This damage reduction in the near-surface region occurred for the comparatively low annealing temperature of 500 °C, suggesting that regrowth of the β -phase near the sample surface started at comparatively low annealing temperatures. However, we did not observe continuation of the regrowth from the surface beyond the upper 100 nm of the sample even after annealing at 1100 °C.

The insets in Fig. 5 show SAD patterns from the implanted layer and the underlying bulk for as-implanted and annealed samples. The diffraction pattern from the implanted layer in the as-implanted sample displayed hexagonal symmetry, in accordance with that reported previously,^{17,21} with weak diffraction spots and low-intensity bands between the strongest reflections. The work by Cora *et al.* has also shown hexagonal symmetry for

diffraction measurements of κ -Ga₂O₃.³ However, the plane spacings in our SAD patterns deviated from the plane spacings in the relaxed κ -Ga₂O₃. Additionally, the low-intensity features in the diffraction patterns were not fully consistent with those reported by Cora *et al.*³ However, and importantly, the SAD pattern in Fig. 5(a) is obviously different from that of β -Ga₂O₃. First, it does not match the plane spacings reported in the literature.²³ Second, its structure does not match the SAD pattern from the unimplanted bulk in the same sample. Thus, it is clear that ion implantation leads to structural transformation in the implanted layer, consistent with the literature.^{17,21} This warrants a thorough investigation of the structure and its dependencies on the implanted species, sample orientation, and structural changes during thermal treatments, but is considered outside the scope of the present study.

The SAD pattern from the implanted layer in the annealed sample revealed diffraction spots corresponding to β -Ga₂O₃. It should be noted that as compared to the SAD pattern from the unimplanted bulk areas, composed of highly ordered single crystal β -Ga₂O₃, the SAD pattern from the implanted layer is more

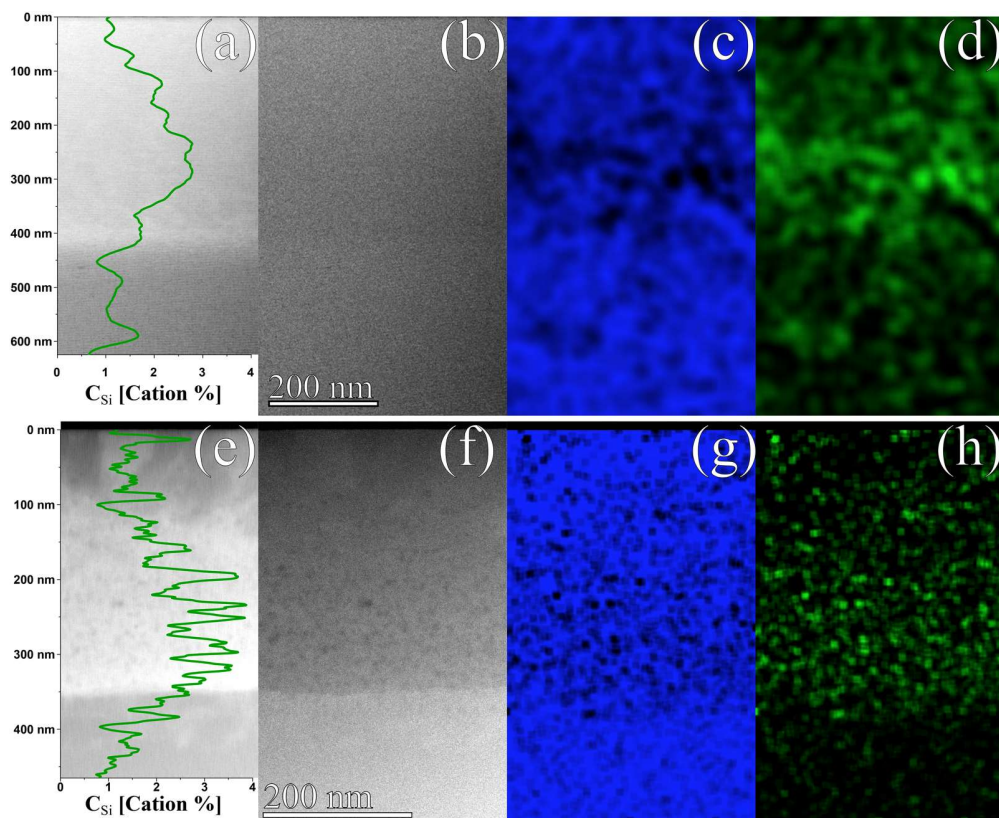


FIG. 6. (a) STEM ADF, (b) HAADF and EDS maps for (c) Ga and (d) Si for the as-implanted sample with fluence 2×10^{16} Si/cm². The Si-concentration profile, in units of cation (atomic) percent, is superposed on the ADF image. The scalebar is given in the HAADF image and is shared across all images. Corresponding datasets for a sample annealed at 1100 °C are shown in subfigures (e)–(h).

complex due to a granular crystal structure, tilted grains, defects, and Moiré fringes. However, we did not observe contributions from other phases or polymorphs. For the sample implanted to the same fluence (2×10^{16} Si/cm²) and annealed at the same temperature (1100 °C), RBS/c results also revealed high remaining disorder levels. Therefore, it was expected that the implanted layer should contain many defects even after annealing at 1100 °C.

The secondary ion mass spectrometry (SIMS) profile of the annealed sample in Fig. 5(c) reveals an abrupt Si-concentration decrease at ~400 nm. This value is close to the observed depth of the damaged layer in the as-implanted sample (409 nm). Consequently, the SIMS results indicate that diffusion of Si into the sample bulk is suppressed for annealing at 1100 °C.

Further, the chemical compositional variations in the sample implanted with 2×10^{16} Si/cm² were investigated using EDS in STEM. Figure 6 shows the EDS data from the as-implanted and annealed samples. The silicon concentration plots show a maximum Si-concentration around 250 nm below the sample surface for the as-implanted sample, consistent with expected values from SRIM calculations [see ion ranges in Fig. 1].

In the annealed sample, the concentration profile revealed the Gaussian-like implantation profile expected from SRIM [Fig. 6(e)], with a peak in the Si-concentration around 250–300 nm. In addition, there were oscillations in the Si-concentration over length scales of 10–20 nm. The corresponding EDS maps [Figs. 6(g) and 6(h)] showed areas with increased Si-concentration and decreased Ga-concentration. This accumulation of the implanted silicon atoms was not seen in the as-implanted sample, although there was a slight depletion of Ga near the implantation peak. The results show that

annealing of the sample leads to the formation of Si-rich particles. The corresponding high-angle annular dark field (HAADF) image revealed areas with dark contrast, which coincided with Si-accumulation for many of the areas. However, some of the dark areas in HAADF did not coincide with Si-accumulation. Consequently, some of the dark areas in the HAADF image were not caused by Si-rich particles. A plausible explanation for these additional dark-contrast areas in the HAADF image is formation of voids in the sample, which would lead to reduced mass-thickness contrast.

EELS measurements were performed to identify the composition of the Si-rich particles revealed by the EDS measurements on the annealed sample and additionally to reveal chemical changes in the surroundings of Si between samples. Figure 7 shows EELS data from the same samples as investigated in Figs. 5 and 6, i.e., (201)-oriented samples implanted with 2×10^{16} Si/cm², as-implanted and annealed at 1100 °C. In addition, reference spectra from crystalline Si and amorphous silicon dioxide are included.^{26,27} The spectra revealed a change in the Si L_{2,3}-edge line shape in one of the dark-contrast regions (area 6) in the ADF image from the annealed sample [Fig. 7(c)]. In the EELS spectrum from area 6, the L-edge line shape was consistent with previously reported results from silicon dioxide.^{26,28,29} Hence, EELS results indicate that the Si-accumulation observed in EDS was likely due to the formation of SiO₂ particles during annealing. The formation of such particles could contribute to the suppression of Si diffusion, which was observed in the SIMS profile from the same sample.

The EELS data from the different regions of both samples not showing signs of particle or void formation [Fig. 7(a),

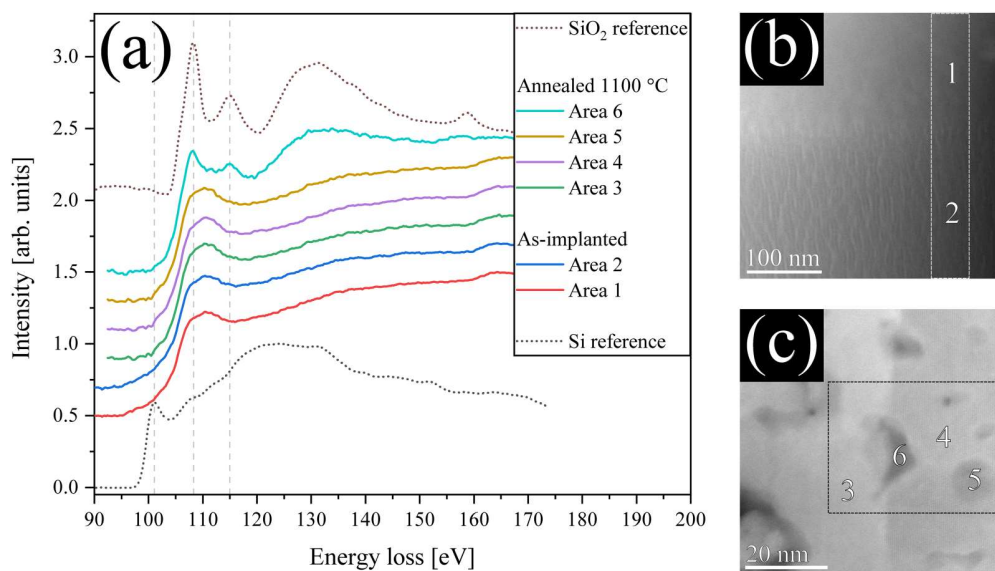


FIG. 7. (a) Core-loss EELS spectra of the Si L_{2,3} edge of the implanted layer and the bulk in an as-implanted sample (implantation fluence 2×10^{16} Si/cm²) and four selected areas in a sample annealed at 1100 °C (implantation fluence 2×10^{16} Si/cm²). Reference EELS spectra from Si and SiO₂ in dotted lines are included for comparison (see the text for references). The labeling corresponds to the regions of acquisition indicated by white numbers in ADF images from (b) the as-implanted sample and (c) the annealed sample. Dashed lines in images indicate the region of interest for EELS measurements.

spectra from areas 1–4] and one of the other dark areas in ADF images (spectrum from area 5) displayed a comparatively broad peak near the onset and did not show the secondary peak around 115 eV, which was clearly visible in the spectrum from area 6 and the SiO₂ reference spectrum. Therefore, EELS data did not show the presence of SiO₂ in areas 1–5. Instead, the origin of the EELS signal from these areas was interpreted in terms of substitutional Si on Ga sites (Si_{Ga}) or interstitial Si (Si_i) in β-Ga₂O₃. The latter option is unlikely to dominate due to the higher formation energy of Si_i compared with Si_{Ga} in β-Ga₂O₃¹² and the high density of vacancies produced during ion implantation into which Si could migrate to form Si_{Ga}. It has been previously reported that Si prefers the tetrahedral Ga(I) site in Ga₂O₃,³⁰ so it is likely that the major contributor to this signal was from Si_{Ga} situated on tetrahedral Ga(I) sites. Since the Si L_{2,3}-edge onset occurred at the same energy for all the spectra from areas 1–5, it is likely that the local surroundings of Si were similar in all of these areas.

In the present study, most attention has been paid to damage accumulation and annealing behavior in (2̄01)-oriented samples. Normally, generation of similar defects and defect concentrations should be expected for implantation into differently oriented samples, such as the (010)- and (001)-oriented samples which were investigated in the surface orientation study. However, since β-Ga₂O₃ is highly anisotropic, certain differences may exist. For instance, the crystal regrowth from the bulk which was observed in RBS/c and (S)TEM may occur at different rates for different crystallographic orientations.

IV. CONCLUSION

In conclusion, we have studied defect accumulation and annealing phenomena in Si-implanted β-Ga₂O₃ wafers, having (2̄01), (010), and (001) orientations, employing a combination of RBS/c, XRD, and (S)TEM. This systematic approach allowed us to investigate complex structural transformations occurring in Si-implanted β-Ga₂O₃ as a function of the sample orientation, accumulated fluence, and annealing temperature. In as-implanted samples, interesting disorder accumulation kinetics consistent with the literature was observed. In particular, the RBS/c, XRD, and (S)TEM combined data suggested that the radiation disorder buildup in Si-implanted β-Ga₂O₃ is accompanied by significant strain accumulation, which assists crystalline-to-crystalline structural transformations instead of amorphization. The analysis of the annealed samples suggested complex structural transformations, which occurred as a function of the fluence and temperature. Moreover, a detailed (S)TEM analysis of the sample implanted with 2×10^{16} Si/cm² and annealed at 1100 °C was enhanced by applying EDS and EELS. EDS analysis unveiled Si agglomerations of size 10–20 nm, and EELS revealed that the agglomerations were composed of silicon dioxide. The Si signal was also observed outside of the agglomerations, likely occurring as substitutional Si on Ga sites.

ACKNOWLEDGMENTS

The Research Council of Norway is acknowledged for the support to the Norwegian Micro- and Nano-Fabrication Facility, NorFab (Project No. 295864) and the Norwegian Center for

Transmission Electron Microscopy, NORTEM (Project No. 197405) and for support to the project Functionalization of Conducting Oxides by Ion beam and defect engineering (Project No. 287729). The INTPART Program at the Research Council of Norway (Project Nos. 261574 and 322382) enabled the international collaborations. Part of the experiments was realized at the CANAM (Centre of Accelerators and Nuclear Analytical Methods) infrastructure (No. LM 2015056) and under the project CANAM OP (No. CZ.02.1.01/0.0/0.0/16_013/0001812) supported by MEYS of the Czech Republic.

AUTHOR DECLARATIONS

Conflict of Interest

The authors have no conflicts to disclose.

Ethics Approval

Ethics approval is not required.

DATA AVAILABILITY

The data that support the findings of this study are available from the corresponding author upon reasonable request.

REFERENCES

- ¹M. Zinkevich and F. Aldinger, *J. Am. Ceram. Soc.* **87**, 683 (2004).
- ²H. Y. Playford, A. C. Hannon, E. R. Barney, and R. I. Walton, *Chem. - Eur. J.* **19**, 2803 (2013).
- ³I. Cora, F. Mezzadri, F. Boschi, M. Bosi, M. Čaplovičová, G. Calestani, I. Dódony, B. Pécz, and R. Fornari, *CrystEngComm* **19**, 1509 (2017).
- ⁴D. Shinohara and S. Fujita, *Jpn. J. Appl. Phys.* **47**, 7311 (2008).
- ⁵V. Gottschalch, S. Merker, S. Blaurock, M. Kneiß, U. Teschner, M. Grundmann, and H. Krautscheid, *J. Cryst. Growth* **510**, 76 (2019).
- ⁶S. Yoshioka, H. Hayashi, A. Kuwabara, F. Oba, K. Matsunaga, and I. Tanaka, *J. Phys. Condens. Matter* **19**, 346211 (2007).
- ⁷R. Roy, V. G. Hill, and E. F. Osborn, *J. Am. Chem. Soc.* **74**, 719 (1952).
- ⁸R. Fornari, M. Pavesi, V. Montedoro, D. Klimm, F. Mezzadri, I. Cora, B. Pécz, F. Boschi, A. Parisini, A. Baraldi, C. Ferrari, E. Gombia, and M. Bosi, *Acta Mater.* **140**, 411 (2017).
- ⁹I. Cora, Zs. Fogarassy, R. Fornari, M. Bosi, A. Rečnik, and B. Pécz, *Acta Mater.* **183**, 216 (2020).
- ¹⁰Y. Xu, J.-H. Park, Z. Yao, C. Wolverton, M. Razeghi, J. Wu, and V. P. Dravid, *ACS Appl. Mater. Interfaces* **11**, 5536 (2019).
- ¹¹H. Sun, K.-H. Li, C. G. T. Castanedo, S. Okur, G. S. Tompa, T. Salagaj, S. Lopatin, A. Genovese, and X. Li, *Cryst. Growth Des.* **18**, 2370 (2018).
- ¹²A. Bouzid and A. Pasquarello, *Phys. Status Solidi RRL* **13**, 1800633 (2019).
- ¹³T. Zheng, C. Wang, J. Dang, W. He, L. Wang, and S. Zheng, *Comput. Mater. Sci.* **174**, 109505 (2020).
- ¹⁴E. G. Villora, K. Shimamura, Y. Yoshikawa, T. Ujiie, and K. Aoki, *Appl. Phys. Lett.* **92**, 202120 (2008).
- ¹⁵K. Sasaki, M. Higashiwaki, A. Kuramata, T. Masui, and S. Yamakoshi, *Appl. Phys. Express* **6**, 086502 (2013).
- ¹⁶A. Azarov, V. Venkatachalapathy, L. Vines, E. Monakhov, I.-H. Lee, and A. Kuznetsov, *Appl. Phys. Lett.* **119**, 182103 (2021).
- ¹⁷A. Azarov, C. Baziotti, V. Venkatachalapathy, P. Vajeeston, E. Monakhov, and A. Kuznetsov, *Phys. Rev. Lett.* **128**, 015704 (2022).
- ¹⁸E. Wendler, E. Treiber, J. Baldauf, S. Wolf, and C. Ronning, *Nucl. Instrum. Methods Phys. Res., Sect. B* **379**, 85 (2016).

- ¹⁹M. Peres, K. Lorenz, E. Alves, E. Nogales, B. Méndez, X. Biquard, B. Daudin, E. G. Villora, and K. Shimamura, *J. Phys. D: Appl. Phys.* **50**, 325101 (2017).
- ²⁰A. Azarov, V. Venkatachalapathy, E. V. Monakhov, and A. Y. Kuznetsov, *Appl. Phys. Lett.* **118**, 232101 (2021).
- ²¹E. A. Anber, D. Foley, A. C. Lang, J. Nathaniel, J. L. Hart, M. J. Tadjer, K. D. Hobart, S. Pearton, and M. L. Taheri, *Appl. Phys. Lett.* **117**, 152101 (2020).
- ²²J. F. Ziegler, M. D. Ziegler, and J. P. Biersack, *Nucl. Instrum. Methods Phys. Res., Sect. B* **268**, 1818 (2010).
- ²³J. Åhman, G. Svensson, and J. Albertsson, *Acta Crystallogr., Sect. C: Cryst. Struct. Commun.* **52**, 1336 (1996).
- ²⁴R. Sugie, T. Uchida, A. Hashimoto, S. Akahori, K. Matsumura, and Y. Tanii, *Appl. Phys. Express* **13**, 126502 (2020).
- ²⁵A. Turos, P. Jóźwik, M. Wójcik, J. Gaca, R. Ratajczak, and A. Stonert, *Acta Mater.* **134**, 249 (2017).
- ²⁶P. E. Batson, *Microsc. Microanal. Microstruct.* **2**, 395 (1991).
- ²⁷P. Ewels, T. Sikora, V. Serin, C. P. Ewels, and L. Lajaunie, *Microsc. Microanal.* **22**, 717 (2016).
- ²⁸T. Zheleva, A. Lelis, G. Duscher, F. Liu, I. Levin, and M. Das, *Appl. Phys. Lett.* **93**, 022108 (2008).
- ²⁹G. Kissinger, M. A. Schubert, D. Kot, and T. Grabolla, *ECS J. Solid State Sci. Technol.* **6**, N54 (2017).
- ³⁰S. Lany, *APL Mater.* **6**, 046103 (2018).

Paper II

**Formation of γ -Ga₂O₃ by ion implantation:
Polymorphic phase transformation of β -
Ga₂O₃**

J. García-Fernández, S. B. Kjeldby, P. D. Nguyen,
O. B. Karlsen, L. Vines and Ø. Prytz

Published in *Applied Physics Letters*, November 2022, Volume 121

DOI:10.1063/5.0120103

Reproduced from J. García-Fernández *et al.*, *Applied Physics Letters*
121, 191601 (2022), with the permission of AIP Publishing.

II

Formation of γ -Ga₂O₃ by ion implantation: Polymorphic phase transformation of β -Ga₂O₃

Cite as: Appl. Phys. Lett. **121**, 191601 (2022); doi: 10.1063/5.0120103

Submitted: 11 August 2022 · Accepted: 20 October 2022 ·

Published Online: 7 November 2022



J. García-Fernández,^{a)} S. B. Kjeldby, P. D. Nguyen, O. B. Karlsen, L. Vines, and Ø. Prytz^{a)}

AFFILIATIONS

Department of Physics and Center for Materials Science and Nanotechnology, University of Oslo, Oslo 0315, Norway

^{a)}Authors to whom correspondence should be addressed: j.g.fernandez@smn.uio.no and oystein.prytz@fys.uio.no

ABSTRACT

Ion implantation induced phase transformation and the crystal structure of a series of ion implanted β -Ga₂O₃ samples were studied using electron diffraction, high resolution transmission electron microscopy, and scanning transmission electron microscopy. In contrast to previous reports suggesting an ion implantation induced transformation to the orthorhombic κ -phase, we show that for ²⁸Si⁺, ⁵⁸Ni⁺, and stoichiometric ⁶⁹Ga⁺/¹⁶O⁺-implantations, the monoclinic β -phase transforms to the cubic γ -phase. The γ -phase was confirmed for implantations over a range of fluences from 10¹⁴ to 10¹⁶ ions/cm², indicating that the transformation is a general phenomenon for β -Ga₂O₃ due to strain accumulation and/or γ -Ga₂O₃ being energetically preferred over highly defective β -Ga₂O₃.

Published under an exclusive license by AIP Publishing. <https://doi.org/10.1063/5.0120103>

Gallium sesquioxide, Ga₂O₃, which can exist in several polymorphic forms, has attracted considerable attention in the last few years due to its potential applications for power electronics and UV devices.^{1,2} The monoclinic β -phase (β -Ga₂O₃) is the thermodynamically stable polymorph at room temperature and atmospheric pressure in air,³ but other polymorphs also display attractive properties and can be stabilized using soft chemical synthesis methods,⁴ high temperature and high pressure solid state synthesis,⁵ strain engineering in thin films,⁶ or ion implantation.⁷ For example, the orthorhombic κ -phase may exhibit spontaneous polarization,⁸ while nanoparticles of the cubic defective spinel γ -phase can be suitable for catalyst uses.⁹ The other known polymorphs, the rhombohedral α -phase, and the cubic δ -phase also exhibit attractive features for solar-blind UV detection applications or MIS diodes with a high breakdown voltage.^{10,11}

Ion implantation produces complex changes in the microstructure of the exposed material. It can lead to disorder, formation of secondary phases in the form of nanoscale inclusions^{12,13} and, for sufficiently high fluences, amorphization commonly occurs.^{14,15} Recently, it was shown that ion implantation of bulk β -Ga₂O₃ samples could lead to a polymorphic transformation, forming a continuous, although defective layer.^{7,16} This intriguing observation may open up possibilities to stabilize metastable polymorphs on top of bulk β -Ga₂O₃, forming either an active layer or acting as a template for further growth. The polymorphic transformation is noteworthy, since high-fluence ion implantations normally yield amorphization in the implanted material. However, β -Ga₂O₃ is not unique in displaying such transformations.

In fact, similar effects occur in ZrO₂,^{17,18} HfO₂,^{19,20} Cu₂O/CuO,²¹ GaN nanowires,²² TiO₂,²³ and Co nanoparticles.²⁴

Anber *et al.*,⁷ and later Azarov *et al.*,¹⁶ reported on the formation of κ -phase after implantation with Ge, Ni, Ga, and Au ions in β -Ga₂O₃. The proposed assignment of the κ -phase was based on selected area electron diffraction (SAED) patterns obtained by transmission electron microscopy (TEM). However, no SAED or high-resolution TEM or scanning TEM (HRTEM/STEM) images could unambiguously confirm the κ -phase. Here, we propose an alternative assignment of the phase transformed layer by indexing it as the γ -phase. γ -Ga₂O₃ has a defective cubic spinel structure with the space group *Fd-3m* (227), a lattice parameter of $a = 8.23$ Å, with gallium being tetrahedrally and octahedrally coordinated to oxygen atoms.²⁵ This metastable γ -phase has attracted appreciable attention as its physical and chemical properties, such as wide band gap (~ 4.7 eV), are of interest for diverse applications including photonics (ultraviolet photo-detectors), solar devices, and photocatalysis.^{26–28} A detailed investigation of the γ -phase by STEM was conducted by Yoo *et al.*²⁹ discovering that Sn ion implantation induces the phase transformation from the β -phase to the γ -phase with high density of defects.

In the present work, we have carefully evaluated the structural evolution and phase transformations of ($\bar{2}01$) and (010) oriented β -Ga₂O₃ implanted with ²⁸Si⁺, ⁵⁸Ni⁺, and ⁶⁹Ga⁺/¹⁶O⁺ ions using SAED and HRTEM and STEM imaging. We have implanted with ²⁸Si⁺, since it is an effective donor dopant in Ga₂O₃,^{30,31} ⁶⁹Ga⁺/¹⁶O⁺ and ⁵⁸Ni⁺ implantations are used to evaluate the influence of the implanted ion

and to relate our work to previous reports.^{7,16} The SAED patterns combined with HRTEM and STEM images unambiguously show a phase transition from β -Ga₂O₃ to γ -Ga₂O₃ which is independent of the implanted species.

Ion implantations of $(\bar{2}01)$ oriented β -Ga₂O₃ single crystal wafers were performed in an NEC Tandem Accelerator. All samples were implanted at room temperature and at 7° from the surface normal. ²⁸Si-implantation was performed with a fluence of 1×10^{14} Si/cm² and 1×10^{15} Si/cm² at an energy of 300 keV. An additional ²⁸Si-implantation was performed in (010) oriented β -Ga₂O₃ single crystal wafers with a fluence of 2×10^{16} Si/cm² and at the same energy. Detailed characterizations by x-ray diffraction (XRD) and Rutherford backscattering spectrometry in the channeling mode on these samples were performed in our previous work.³² For the stoichiometric implantation, the energies of ⁶⁹Ga⁺ and ¹⁶O⁺ ions were selected to achieve the same projected range as for the Si-ions, yielding implantation energies of 715 keV for ⁶⁹Ga⁺ and 182 keV for ¹⁶O⁺. The ratio of ⁶⁹Ga⁺ and ¹⁶O⁺ fluences was fixed at 2/3, to match the stoichiometry of the sample. The total implantation fluency was selected to obtain the same number of defects at the defect peak for ²⁸Si⁺ and stoichiometric implantation, this means fluence values of 2.85×10^{14} Ga/cm² and 4.28×10^{14} O/cm². For ⁵⁸Ni⁺-implantation, we used an implantation energy of 400 keV and a fluence of 1×10^{15} Ni/cm² in order to correlate our work to previous reports on phase transformation in β -Ga₂O₃ after ion implantation.¹⁶

Electron transparent cross-sectional TEM samples were prepared by mechanical grinding, polishing, and final thinning by Ar ion milling in a Gatan PIPS II (Model 695). Plasma cleaning (Fishione Model 1020) was applied immediately prior to the TEM investigations. A JEOL JEM-2100F microscope operated at an acceleration voltage of 200 kV was used for initial sample investigations using SAED and HRTEM. Additionally, SAED and HRSTEM imaging were conducted using a Thermo Fisher Scientific Cs-corrected Titan G2 60–300 kV microscope operated at 300 kV. High angle annular dark field (HAADF) STEM images were recorded using a probe convergence semi-angle of 23 mrad, a nominal camera length of 60 mm, corresponding to an inner and outer collection semi-angle of 100 and 200 mrad, respectively. Annular bright field (ABF) STEM images were simultaneously acquired at the same camera length, with collection semi-angles of 10 and 20 mrad. SAED simulations were performed using the JEMS software package³³

Starting with the Ni-implantation, the implantation parameters were similar to those used in previous work by Azarov *et al.*,¹⁶ where

the κ -phase was reported. Contrary to the previous work, our results show that the transformed layer is γ -phase rather than κ -phase. We base this on the SAED patterns shown in Figs. 1(a)–1(c). These patterns are fully indexed as γ -phase (space group $Fd\bar{3}m$, lattice parameter $a = 8.36(2)$ Å) observed along the [110], [111], and [112] zone axes, respectively. The measured interplanar distances are shown in Table S1 of the supplementary material. Our lattice parameter is slightly higher than reported previously.²⁵ If this is a real feature of the sample, it may be a consequence of implantation-induced strain.

Looking closely at the SAED patterns reported by Anber *et al.*⁷ and Azarov *et al.*,¹⁶ we believe that the pattern indexed as [001] zone axis of κ -phase is actually the γ -phase along the [111] zone axis. These results shed a new light by confirming that the transformation that occurs is from the β -phase to the γ -phase, in good agreement with recent reports by Yoo *et al.*²⁹ In order to confirm this, we have performed simulations of κ -Ga₂O₃ along [001] zone axis, a superposition of 3 SAEDs of κ -Ga₂O₃ [001] rotated 120° as reported by Cora *et al.*³⁴ as a consequence of twinning resulting in a diffraction pattern with sixfold symmetry, and a simulated SAED of the γ -Ga₂O₃ phase along [111] zone axis. All these simulated SAEDs are shown in the supplementary material [Figs. S1(a)–S1(c)] together with the experimental SAED of γ -Ga₂O₃ phase along [111] zone axis in Fig. 1(b) [Fig. S1(d)] for better comparison. As can be seen, there is a close agreement between our experimental SAED and the simulated one for γ -Ga₂O₃.

For Si-implantation, XRD showed that for the samples implanted with 1×10^{14} Si/cm² only small peaks and shoulders attributed to the implantation-induced strain were observed, as reported previously.³² However, SAED pattern recorded at the top area of the sample [Fig. S2(a) in the supplementary material] along the [102] zone axis of β -phase shows the presence of an extra weak and diffuse contrast (indicated by blue arrows) where the $(\bar{2}20)$ plane of the γ -phase along the [112] zone axis should be [see Fig. 1(c) for a γ -phase SAED in this projection]. Figure S2(b) in the supplementary material shows an intensity profile along the line marked with yellow dashed dots in Fig. S2(a) for a better visualization. This intensity could indicate the presence of a very small fraction of γ -Ga₂O₃ (and, thus, the beginning of the transformation) in the sample, which was undetectable by XRD. For the fluences of 1×10^{15} Si/cm² and above, new XRD peaks were observed and HRTEM showed that the upper 400 nm of the sample had transformed. Here, we also find that the upper 400 nm of the samples has undergone a change in the crystal structure. Henceforth, we call this layer the transformed layer. Similar observations are made for all of the implanted samples in this work. Figure 2(a) shows a TEM

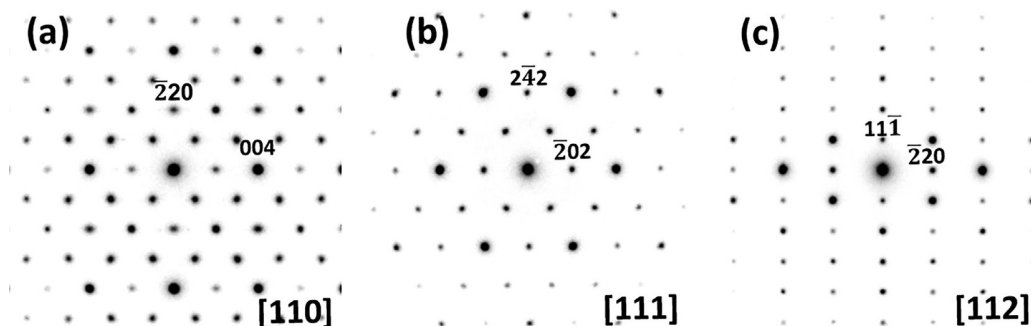


FIG. 1. SAED pattern from the transformed layer of the Ni implanted sample. The indexing is according to γ -Ga₂O₃ along the zone axes (a) [110], (b) [111], and (c) [112].

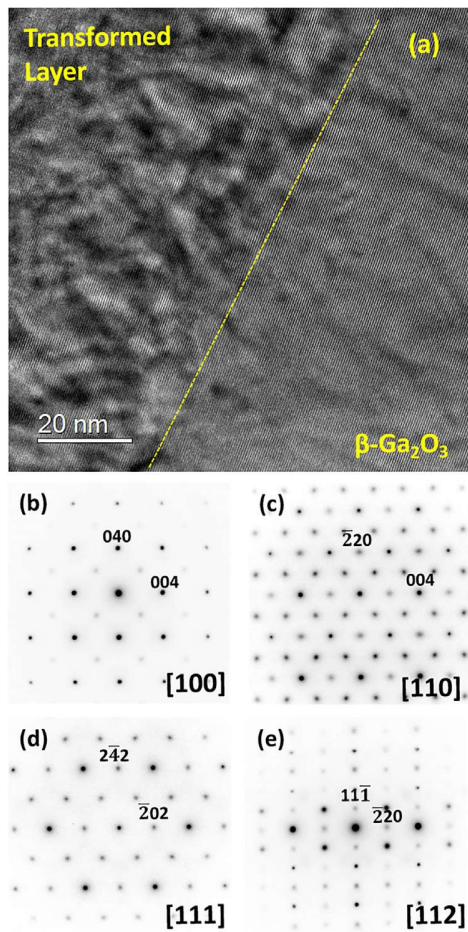


FIG. 2. (a) Cross-sectional TEM image of the interface between the transformed layer and the $(\bar{2}01)$ oriented β - Ga_2O_3 and the transformed layer in the sample implanted with 1×10^{15} Si/cm^2 . SAED pattern of the transformed layer indexed according to γ - Ga_2O_3 along the zone axes (b) $[100]$, (c) $[110]$, (d) $[111]$, and (e) $[112]$.

image of the interface between the $(\bar{2}01)$ oriented β - Ga_2O_3 and the transformed layer in the sample implanted with 1×10^{15} Si/cm^2 . The difference in contrast due to defects and strain in the transformed layer compared with the β - Ga_2O_3 below is clearly observed in the image. This corroborates that strain and defect formation are part of the structural transition mechanism. Figures 2(b)–2(e) show the SAED patterns from the transformed layer in various projections. The SAED pattern along $[100]$ zone axis [Fig. 2(b)] is acquired from the (010) oriented β - Ga_2O_3 sample, and the others are from the $(\bar{2}01)$ oriented β - Ga_2O_3 sample. All the SAED patterns from the two samples can be indexed unambiguously as γ - Ga_2O_3 , indicating that the orientation of the β - Ga_2O_3 does not have any influence on the phase transformation.

It is important to note that in the SAED patterns published by Anber *et al.*⁷ and Azarov *et al.*,¹⁶ some diffuse spots are observed. If we enhance the contrast of the SAED pattern in Fig. 2(d), similar diffuse spots become visible in our data, as shown in Fig. 3(a) and marked by orange arrows. For comparison, Fig. 3(b) is a SAED pattern taken at

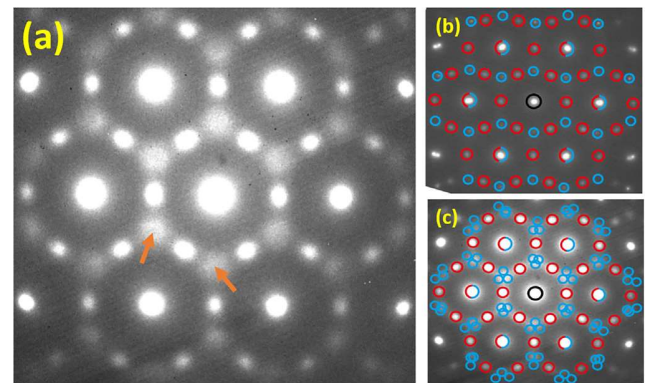


FIG. 3. (a) SAED pattern from the sample implanted with 1×10^{15} Si/cm^2 taken along the $[111]$ zone axis. This is the same pattern shown in Fig. 2(d) but has been digitally modified to reveal weak diffuse spots (two of them marked with orange arrows) that cannot be explained by the γ -phase. (b) SAED pattern from the interface, showing diffraction spots from both the β -phase (blue circles) and the γ -phase (red circles). (c) Superimposing three of the traced patterns, each rotated 120° , onto (a) shows that each diffuse spot is surrounded by three small, blue circles.

the interface, showing diffraction spots from both the transformed and untransformed layer. All spots have been marked with circles. The diffuse spots in Fig. 3(a) are indeed close to the position of the β -spots that are not overlapping with those from the γ -spots, but the arrangement has lower symmetry than the sixfold rotational symmetry of the $[111]$ projection of the γ -phase. If we superimpose three of the traced blue patterns in Fig. 3(b), each rotated 120° , the diffuse spots are closely surrounded by three of the spots from the β -phase [see Fig. 3(c)]. We, therefore, boldly propose that the diffuse spots originate from very small precipitates of the β -phase inside the γ -phase. The three orientations would be expected if the orientation of the β -phase is dictated by the threefold symmetry of the γ -phase. Although we have not observed these inclusions in the HRTEM or STEM imaging, such a reversion of γ -phase to β -phase should not be surprising. The β -phase is the thermodynamically stable polymorph at ambient conditions, and we have earlier shown that the γ -phase converts to β -phase during annealing.³²

The atomic structures of the polymorphs were also studied by atomic-resolution STEM imaging. Figure 4(a) shows an HAADF STEM image of the interface between the β - Ga_2O_3 (displayed along the $[102]$ zone axis) and the transformed layer (along the $[112]$ zone axis). Figures 4(b) and 4(c) show representative simultaneously acquired HAADF and ABF STEM images along the $[112]$ zone axis of the γ -phase, respectively. In the HAADF image, the brighter spots are associated with the arrangement of the heavy gallium cations in the γ -phase. In the ABF image, the locations of both gallium and oxygen atoms are identified as dark spots over a white background. The atomic arrangement of gallium (orange) and oxygen (blue) atoms are schematically represented. The gallium atoms in the positions corresponding to Wyckoff site $8a$ (T_d) and $16d$ (O_h) in the ideal spinel structure are clearly visible and marked in the insets of Figs. 4(b) and 4(c). However, according to the structure reported by Playford *et al.*²⁵ using neutron diffraction, two more gallium positions are needed to get a proper refinement of the diffractogram. These extra atomic positions are placed in $48f$ (T_d) and $16c$ (O_h). In our images, the contrast

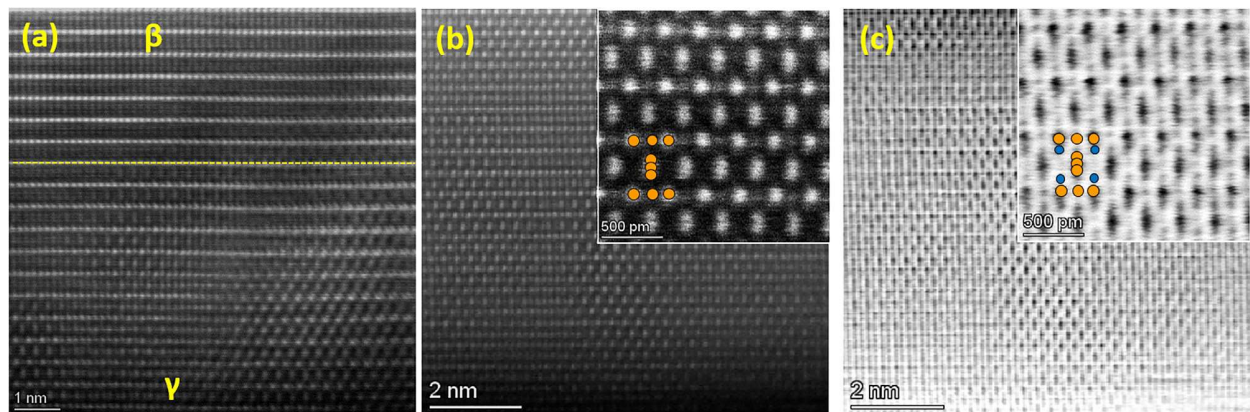


FIG. 4. (a) Atomic resolution HAADF STEM image of the interface between β -Ga₂O₃ (along [102] zone axis) and γ -Ga₂O₃ (along [112] zone axis) of the 1×10^{15} Si/cm² sample. (b) and (c) show HAADF and ABF STEM image of γ -Ga₂O₃ along [112] zone axis, respectively. The insets show areas at higher magnification. Gallium and oxygen atoms are schematically represented in orange and blue, respectively.

from these atomic columns is not resolved. This is as expected due to the low occupancy of both positions: 0.066 and 0.024, respectively. Our own experimental observations are in good agreement with the γ -phase structure analysis by electron microscopy reported by Cora *et al.*³⁵ and Castro-Fernandez *et al.*³⁶ when observed along the same zone axis.

In order to study the effect of chemical factors specific to the implanted ion on the phase transformation, a $(\bar{2}01)$ oriented β -Ga₂O₃ sample was implanted with $^{69}\text{Ga}^{+}/^{16}\text{O}^{+}$ in the stoichiometric ratio. Ion implantation parameters were selected to give projected range and defect generation similar to the Si-implantation. Figures 5(a) and 5(b) show the SAED patterns and representative HAADF STEM images of the transformed layer corresponding to the [112] and [111] zone axes of the γ -Ga₂O₃ phase, respectively. In both images, the positions of gallium atomic columns are marked in orange.

Diffraction patterns acquired for multiple zone axes and multiple implanted species clearly show that it is the γ -phase that is formed in this implantation-induced phase transformation. The formation of γ -Ga₂O₃ is also independent of the orientation of the implanted β -Ga₂O₃ wafers. This indicates that the transformation and stabilization by ion implantation is not driven by the chemistry of the implanted ions, and also not by factors such as the ionic size of the implanted species, since the transformation occurred even for stoichiometric implantation.

Azarov *et al.*¹⁶ have previously interpreted phase transitions in ion implanted β -Ga₂O₃ as a direct consequence of strain accumulation. Although the present work shows that it is the γ -phase rather than the κ -phase which is formed, we cannot rule out contributions from strain in the transformation mechanism. Another possible mechanism behind the transformation might be that defect-rich γ -Ga₂O₃ could be energetically preferred over defect-rich β -Ga₂O₃, even though the β -phase is preferred for low defect concentrations.³⁷ We note that the energy transferred to the sample during implantation is highly localized and that it could, therefore, be difficult to drive transformations which require long-range transport, such as precipitations of phases with different crystal structures. We further find that the anion sublattice stacking sequence is mostly conserved in the β -to- γ

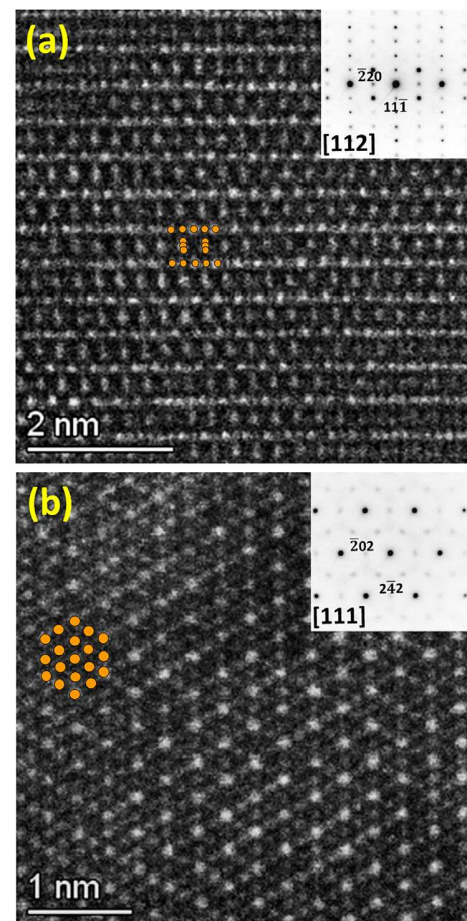


FIG. 5. SAED pattern and atomic resolution HAADF STEM images of the $^{69}\text{Ga}^{+}/^{16}\text{O}^{+}$ implanted sample along the zone axes (a) [112] and (b) [111]. Gallium is schematically represented in orange in both images.

transformation, while it would not be conserved in a β -to- κ transformation. To illustrate this, a schematic representation of the oxygen sublattice of β -Ga₂O₃ and γ -Ga₂O₃ at the interface is shown in Fig. S3 in the [supplementary material](#), along with a schematic representation of the potential interface between β -Ga₂O₃ and κ -Ga₂O₃ for comparison. This structural similarity of the initial and final crystal structures could lower the transition energy for transformation to the γ -phase, promoting transformation to this phase rather than the κ -phase. This warrants a thorough investigation of the structural stability and mechanism of why and how γ -Ga₂O₃ has been stabilized but this is considered outside the scope of the present study.

In summary, we have systematically investigated the structural evolution of β -Ga₂O₃ implanted with ²⁸Si⁺, ⁵⁸Ni⁺, and ⁶⁹Ga⁺/¹⁶O⁺ ions using SAED and HRTEM/STEM over a range of fluences from 10¹⁴ to 10¹⁶ ions/cm² in surface orientations ($\bar{2}01$) and (010). We demonstrate that the ion implantations resulted in β - to γ -polymorphic phase transformation. This process occurred independently of the investigated implanted species, which suggests that the transformation is an intrinsic feature of the implantation and is likely unrelated to chemical effects. This opens up the possibility of designing new devices and applications through customized “polymorph engineering” in thin films and interfaces.

See the [supplementary material](#) for some interplanar distances for the Ni implanted sample; SAED simulations of κ -Ga₂O₃ along [001] zone axis, a superposition of three SAEDs of κ -Ga₂O₃ along [001] zone axis rotated 120° as a consequence of twinning and γ -Ga₂O₃ along [111] zone axis; SAED analysis of the sample implanted with 1 × 10¹⁴ Si/cm²; and schematic representation of the oxygen sublattice of β -Ga₂O₃ and γ -Ga₂O₃ or κ -Ga₂O₃ along the interface.

The Research Council of Norway is acknowledged for the support to the Norwegian Center for Transmission Electron Microscopy (NORTEM, No. 197405/F50), the Norwegian Micro- and Nanofabrication Facility (NorFab, No. 295864), and the NANO2021 researcher project Functionalization of conducting oxides by ion beam and defect engineering (FUNCTION, No. 287729).

AUTHOR DECLARATIONS

Conflict of Interest

The authors have no conflicts to disclose.

Author Contributions

Javier García-Fernández: Conceptualization (equal); Data curation (equal); Formal analysis (equal); Investigation (equal); Methodology (equal); Writing – original draft (equal). **Snorre Braathen Kjeldby:** Conceptualization (equal); Data curation (equal); Formal analysis (equal); Investigation (equal); Methodology (equal); Visualization (equal); Writing – original draft (equal). **Phuong Dan Nguyen:** Conceptualization (equal); Formal analysis (equal); Methodology (equal); Supervision (equal); Validation (equal); Writing – original draft (equal); Writing – review & editing (equal). **Ole Bjørn Karlsten:** Conceptualization (equal); Formal analysis (equal); Investigation (equal); Project administration (equal); Supervision (equal); Writing – original draft (equal); Writing – review & editing (equal). **Lasse Vines:** Investigation (equal); Resources (equal); Supervision (equal);

Validation (equal); Visualization (equal); Writing – review & editing (equal). **Øystein Prytz:** Project administration (equal); Supervision (equal); Validation (equal); Writing – review & editing (equal).

DATA AVAILABILITY

The data that support the findings of this study are available from the corresponding authors upon reasonable request.

REFERENCES

- R. Singh, T. R. Lenka, D. K. Panda, R. T. Velpula, B. Jain, H. Q. T. Bui, and H. P. T. Nguyen, *Mater. Sci. Semicond. Process.* **119**, 105216 (2020).
- M. Zhong, Z. Wei, X. Meng, F. Wu, and J. Li, *J. Alloys Compd.* **619**, 572 (2015).
- M. Zinkevich and F. Aldinger, *J. Am. Ceram. Soc.* **87**, 683 (2004).
- T. Wang, S. S. Farvid, M. Abulikemu, and P. V. Radovanovic, *J. Am. Chem. Soc.* **132**(27), 9250 (2010).
- D. Machon, P. F. McMillan, B. Xu, and J. Dong, *Phys. Rev. B* **73**, 094125 (2006).
- Y. Xu, J. H. Park, Z. Yao, C. Wolverton, M. Razeghi, J. Wu, and V. P. Dravid, *ACS Appl. Mater. Interfaces* **11**, 5536 (2019).
- E. A. Anber, D. Foley, A. C. Lang, J. Nathaniel, J. L. Hart, M. J. Tadjer, K. D. Hobart, S. Pearton, and M. L. Taheri, *Appl. Phys. Lett.* **117**, 152101 (2020).
- F. Mezzadri, G. Calestani, F. Boschi, D. Delmonte, M. Bosi, and R. Fornari, *Inorg. Chem.* **55**, 12079 (2016).
- S. W. Kim, S. Iwamoto, and M. Inoue, *Ceram. Int.* **35**, 1603 (2009).
- J. Moloney, O. Tesh, M. Singh, J. W. Roberts, J. C. Jarman, L. C. Lee, T. N. Huq, J. Brister, S. Karboyan, M. Kuball, P. R. Chalker, R. A. Oliver, and F. C. P. Massabuau, *J. Phys. D* **52**, 475101 (2019).
- Y. S. Hsieh, C. Y. Li, C. M. Lin, N. F. Wang, J. V. Li, and M. P. Houg, *Thin Solid Films* **685**, 414 (2019).
- B. L. Aarseth, C. S. Granerød, A. Galeckas, A. Azarov, P. D. Nguyen, Ø. Prytz, and L. Vines, *Nanotechnology* **32**, 505707 (2021).
- A. Meldrum, R. F. Haglund, Jr., L. A. Boatner, and C. W. White, *Adv. Mater.* **13**, 1431 (2001).
- E. Wendler, E. Treiber, J. Baldauf, S. Wolf, and C. Ronning, *Nucl. Instrum. Methods Phys. Res., Sect. B* **379**, 85 (2016).
- A. Nikolskay, E. Okulich, D. Korolev, A. Stepanov, D. Nikolichiev, A. Mikhaylov, D. Tetelbaum, A. Almaev, C. A. Bolzan, A. Buaczik, Jr., R. Giulian, P. L. Grande, A. Kumar, M. Kumar, and D. Gogova, *J. Vac. Sci. Technol. A* **39**, 030802 (2021).
- A. Azarov, C. Bazioti, V. Venkatachalapathy, P. Vajeeston, E. Monakhov, and A. Kuznetsov, *Phys. Rev. Lett.* **128**, 015704 (2022).
- K. E. Sickafus, H. Matzke, T. Hartmann, K. Yasuda, J. A. Valdez, P. Chodak III, M. Nastasi, and R. A. Verrall, *J. Nucl. Mater.* **274**, 66 (1999).
- G. Sattonnay and L. Thomé, *J. Nucl. Mater.* **348**, 223 (2006).
- A. Benyagoub, *Phys. Rev. B* **72**(9), 094114 (2005).
- A. Benyagoub, *Nucl. Instrum. Methods Phys. Res., Sect. B* **218**, 451 (2004).
- U. C. Bind, R. K. Dutta, G. K. Sekhon, K. L. Yadav, J. B. M. Krishna, R. Menon, and P. Y. Nabhiraj, *Superlattices Microstruct.* **84**, 24 (2015).
- S. Dhara, A. Datta, C. T. Wu, Z. H. Lan, K. H. Chen, Y. L. Wang, C. W. Hsu, C. H. Shen, L. C. Chen, and C. C. Chen, *Appl. Phys. Lett.* **84**, 5473 (2004).
- A. Manna, A. Barman, S. R. Joshi, B. Satpati, P. Dash, A. Chattaraj, S. K. Srivastava, P. K. Sahoo, A. Kanjilal, D. Kanjilal, and S. Varma, *J. Appl. Phys.* **124**, 155303 (2018).
- D. J. Sprouster, R. Giulian, C. S. Schnohr, L. L. Araujo, P. Kluth, A. P. Byrne, G. J. Foran, B. Johannessen, and M. C. Ridgway, *Phys. Rev. B* **80**(11), 115438 (2009).
- H. Y. Playford, A. C. Hannon, E. R. Barney, and R. I. Walton, *Chem. Eur. J.* **19**, 2803 (2013).
- V. Vasanthi, M. Kottaisamy, and V. Ramakrishnan, *Ceram. Int.* **45**, 2079 (2019).
- X. Zhang, Z. Zhang, J. Liang, Y. Zhou, Y. Tong, Y. Wang, and X. Wang, *J. Mater. Chem. A* **5**, 9702 (2017).
- Y. Teng, L. X. Song, A. Ponchel, Z. K. Yang, and J. Xia, *Adv. Mater.* **26**, 6238 (2014).

- ²⁹T. Yoo, X. Xia, F. Ren, A. Jacobs, M. J. Tadjer, S. Pearton, and H. Kim, *Appl. Phys. Lett.* **121**, 072111 (2022).
- ³⁰T. Oshima, K. Matsuyama, K. Yoshimatsu, and A. Ohtomo, *J. Cryst. Growth* **421**, 23 (2015).
- ³¹H. M. Jeon, K. D. Leedy, D. C. Look, C. S. Chang, D. A. Muller, S. C. Badescu, V. Vasilyev, J. L. Brown, A. J. Green, and K. D. Chabak, *APL Mater.* **9**, 101105 (2021).
- ³²S. B. Kjeldby, A. Azarov, P. D. Nguyen, V. Venkatachalapathy, R. Mikšová, A. Macková, A. Kuznetsov, Ø. Prytz, and L. Vines, *J. Appl. Phys.* **131**, 125701 (2022).
- ³³P. A. Stadelmann, see <https://www.jems-swiss.ch/> for more information about the software used for SAED simulations.
- ³⁴I. Cora, F. Mezzadri, F. Boschi, M. Bosi, M. Čaplovičová, G. Calestani, I. Dódony, B. Pécz, and R. Fornari, *Cryst. Eng. Commun.* **19**, 1509 (2017).
- ³⁵I. Cora, Z. Fogarassy, R. Fornari, M. Bosi, A. Recnik, and B. Pécz, *Acta Mater.* **183**, 216 (2020).
- ³⁶P. Castro-Fernandez, M. V. Blanco, R. Verel, E. Willinger, A. Fedorov, P. M. Abdala, and C. R. Müller, *J. Phys. Chem. C* **124**(37), 20578 (2020).
- ³⁷P. Kalita, S. Saini, P. Rajput, S. N. Jha, D. Bhattacharyya, S. Ojha, D. K. Avasthi, S. Bhattacharya, and S. Ghosh, *Phys. Chem. Chem. Phys.* **21**, 22482 (2019).

Supplementary Material

Formation of γ -Ga₂O₃ by ion implantation: polymorphic phase transformation of β -Ga₂O₃

J. García-Fernández¹, S. B. Kjeldby¹, P. D. Nguyen¹, O. B. Karlsen¹, L. Vines¹, Ø. Prytz¹

¹ Department of Physics and Center for Materials Science and Nanotechnology, University of Oslo, PO Box 1048 Blindern, N-0316 Oslo, Norway

Table S1. Some interplanar distances from SAED patterns in Figure 1 and the corresponding values from Playford *et al.*²⁵.

Plane (<i>hkl</i>)	Distance (Å)	Ref. 25 (Å)
(111)	4.80 ± 0.03	4.75
(220)	2.96 ± 0.03	2.91
(400)	2.09 ± 0.02	2.06
(242)	1.71 ± 0.01	1.68

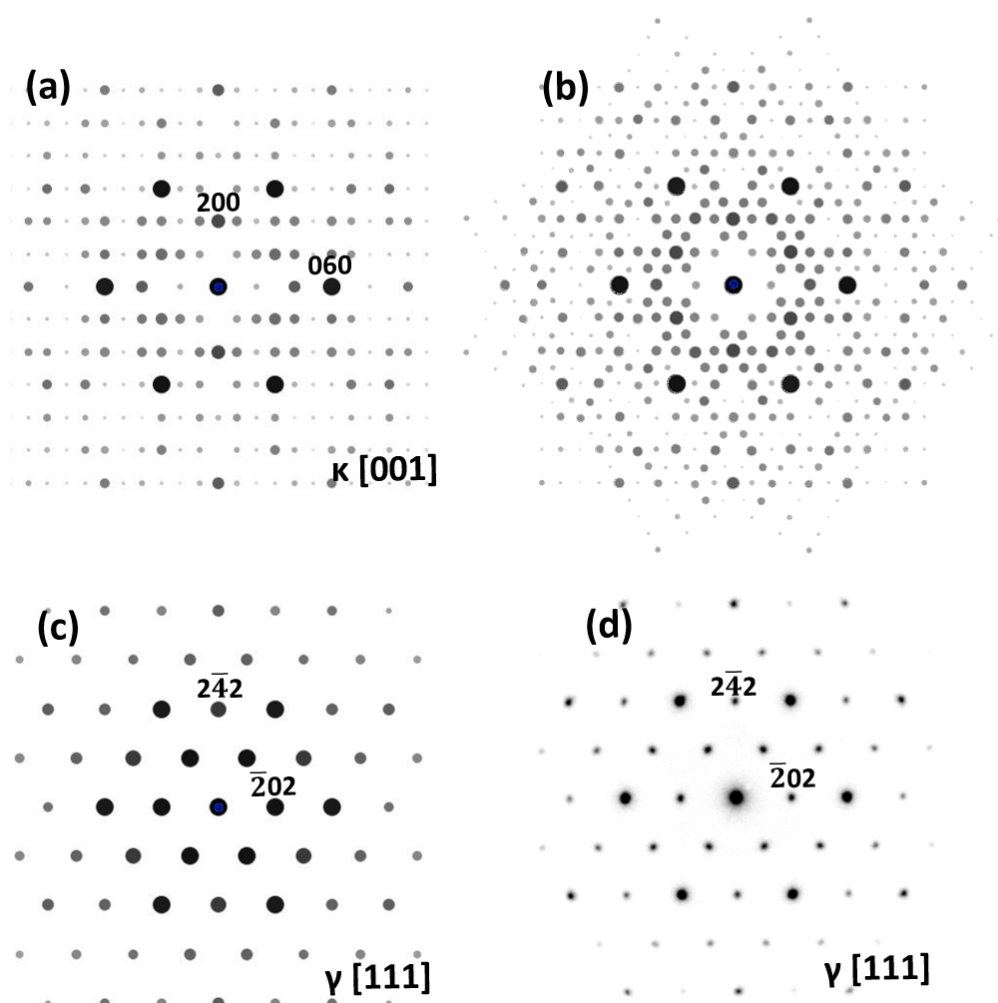


Figure S1. SAED simulations of: (a) κ -Ga₂O₃ along [001] zone axis. (b) Superposition of 3 SAEDs of κ -Ga₂O₃ along [001] zone axis rotated 120° as a consequence of twinning as in Ref. 34. (c) γ -Ga₂O₃ along [111] zone axis. (d) Experimental SAED of γ -Ga₂O₃ along [111] zone axis of the Ni implanted sample.

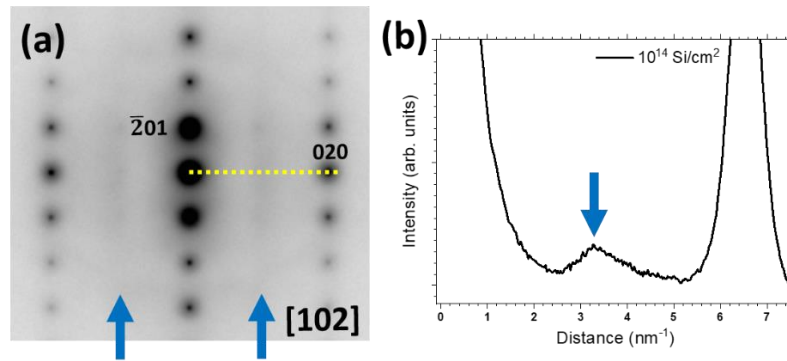


Figure S2. (a) SAED pattern from the sample implanted with 1×10^{14} Si/cm² taken along the [102] zone axis of β -Ga₂O₃. (b) Intensity profile along the yellow dashed line in (a).

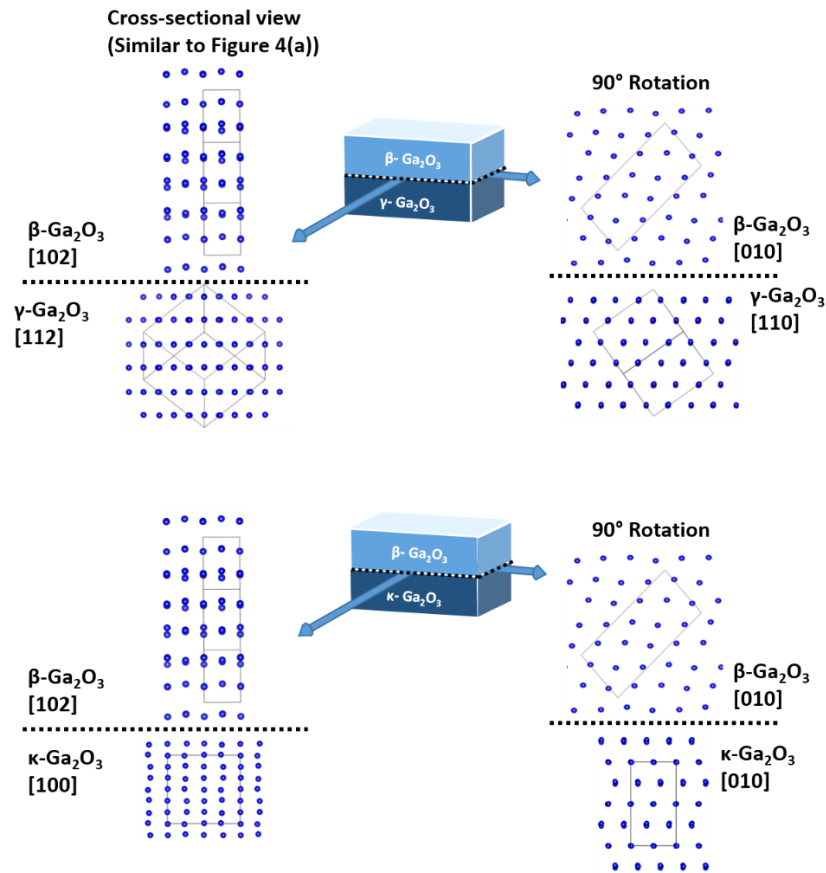


Figure S3. Schematic representation of the oxygen sublattice of β -Ga₂O₃ and γ -Ga₂O₃ along the interface (top) and β -Ga₂O₃ and κ -Ga₂O₃ (bottom). The oxygen atoms are represented in blue color. The solid black lines indicates the unit cell. The orientational relationship between β -Ga₂O₃ and γ -Ga₂O₃ is known from our STEM data, so there is no ambiguity about the projections shown for these two phases in Figure S3. For the κ -phase, the choice of projections is less straightforward, as we did not observe this phase in our study. To evaluate whether similarities in the anion sublattice of the initial and final phases could promote formation of γ -Ga₂O₃ over κ -Ga₂O₃, we searched for the orientation of the κ -phase where its anion sublattice is the most similar to the β -phase anion sublattice. This search was done by inspection, comparing projections of the β - and κ -phases while keeping track of the angle between different projections in the two crystal structures. This process yielded the projections of κ -Ga₂O₃ shown in Figure S3, for which the stacking sequence in the anion sublattice of the κ -phase is different from that of the β -phase. From the figure, it is clear that smaller changes in the anion sublattice are required for a β -to- γ transformation than for a β -to- κ transformation.

Paper III

**In-situ atomic-resolution study of
transformations in double polymorph γ/β -
 Ga_2O_3 structures**

J. García-Fernández, S. B. Kjeldby, L. J. Zeng, A. Azarov,
A. Pokle, P. D. Nguyen, E. Olsson, L. Vines,
A. Yu Kuznetsov, Ø. Prytz

Accepted in *Materials Advances*, March 2024

III

In-situ atomic-resolution study of transformations in double polymorph γ/β -Ga₂O₃ structures

Received 00th January 20xx,
Accepted 00th January 20xx

J. García-Fernández^{1,*}, S. B. Kjeldby¹, L. J. Zeng², A. Azarov¹, A. Pokle¹, P. D. Nguyen¹, E. Olsson², L. Vines¹, A. Yu Kuznetsov^{1,*} and Ø. Prytz^{1,*}

DOI: 10.1039/x0xx00000x

Disorder induced formation of metastable Ga₂O₃ polymorphs as well as their recovery to the stable state upon anneals attract attention both because of the fundamental novelty and rapidly increasing interest for the use of Ga₂O₃ in practical applications. In this study, double polymorph γ/β -Ga₂O₃ structures fabricated by the radiation induced disorder approach were used as a starting point for systematic in-situ annealing electron microscopy experiments. We show that, under conditions of the in-situ anneals, double γ/β -Ga₂O₃ polymorph structures remained stable up to 300°C, when onsets of the γ -to- β transformation become traceable, leading to a prominent γ - and β - mixture already at 500°C. Interestingly, the recrystallization of the β -Ga₂O₃ occurs throughout the whole γ -film and the preferential alignments at the newly emerging γ/β -interfaces are different from that of the initial γ/β -interface formed as a result of the disorder induced ordering. The alignments of the two polymorphs is maintained as a function of temperature – with a reduction in the volumetric ratio of γ -domains for increasing annealing temperature. Finally, at 1100°C, γ -Ga₂O₃ fully transforms into β -Ga₂O₃, without dominating crystallographic relationships or preferred orientations, indicating that energy barriers are not any longer implied limiting factors, because of sufficiently high thermal energy supply. Thus, these in-situ measurements enabled a new level of accuracy for assessing polymorphic transformations in Ga₂O₃

1. Introduction

Polymorphism contributes to a diversity of materials, so that even materials having the same chemical compositions exhibit variations in properties because of different crystal structures. Mechanistically, switching from one crystal structure to another depends on the ability of atoms to move out their sites, which can be achieved by changing temperature and/or pressure.¹ Moving atoms from their equilibrium positions by accelerated particle beams is another option; even though such polymorph transitions are rare due to a competing amorphization process. Nevertheless, irradiation disorder induced formation of metastable polymorphs have been observed in several materials,²⁻⁵ including gallium oxide (Ga₂O₃).⁶⁻¹¹ At present, the mechanisms of polymorph transitions in Ga₂O₃ are under intensive investigations, because of the rapidly increasing interest in Ga₂O₃ for its use in power electronics and UV photonics.^{12,13} Indeed, since ion beam processing is often an inevitable part of the device fabrication, it is essential to establish full control over the polymorphism of Ga₂O₃, in particular upon ion implantation and annealing. Concurrently, there is also a fundamental interest to study reconstruction of

the stable polymorph, since the rich polymorphism of Ga₂O₃ provides several potential reconstruction routes.

The present understanding is that upon the introduction of the lattice disorder by ion implantation, the thermodynamically stable β -Ga₂O₃ (monoclinic, C2/m^{14, 15}) transforms into a metastable spinel γ -Ga₂O₃ (cubic, Fd $\bar{3}$ m^{14, 15}), forming a continuous and homogeneous γ -Ga₂O₃ layer at the top of the β -Ga₂O₃ wafer; i.e. in the region containing highest disorder induced by implanted ions and recoils.⁵⁻¹⁰ In the rest of the paper, we refer to such structure as “double polymorph γ/β -Ga₂O₃ structure” and use it as a starting point for systematic in-situ annealing experiments in an electron microscope, which is currently missing in the literature. Notably, until the disorder-induced β -to- γ transformation in Ga₂O₃ was explained,⁶⁻¹⁰ the interpretations of the annealing experiments of ion implanted β -Ga₂O₃ samples were done in terms of the reduction of the “radiation disorder” in an unchanged lattice – as is conventionally done for other materials. Thus, on the top of missing in-situ studies, even ex-situ annealing experiments of the ion implanted β -Ga₂O₃ – until very recently – neglected the aspect of the polymorph reconstruction. Moreover, even though the most recent ex-situ studies revealed that γ -Ga₂O₃ eventually transforms back into thermodynamically stable β -Ga₂O₃ upon annealings,^{6,16-19} the kinetics of the process have not been clearly articulated. Indeed, apart from the transition temperature uncertainties, there are unresolved – and even previously unasked in literature – questions related e.g. to the nucleation sites of the “recrystallized” β -Ga₂O₃ as well as to its crystallographic alignment with the “initial” β -Ga₂O₃ matrix and

^a Department of Physics and Center for Materials Science and Nanotechnology, University of Oslo, Oslo 0315, Norway. Email: j.g.fernandez@smn.uio.no, andrei.kuznetsov@fys.uio.no, oystein.prytz@fys.uio.no

^b Department of Physics, Chalmers University of Technology, Gothenburg 41296, Sweden.

Electronic Supplementary Information (ESI) available: [details of any supplementary information available should be included here]. See DOI: 10.1039/x0xx00000x

eventually remaining γ -Ga₂O₃ inclusions. Another important question is whether the chemistry of the introduced ions affects the transformation upon annealing. The question is not trivial, since it has been shown that the γ -Ga₂O₃ formation as a result of the β -Ga₂O₃ disordering occurs independently of chemical nature of the implanted ions,^{9,10} because of the prime role of the Ga vacancies and punctual defects in the β -to- γ transformation instead of chemical effects, at least up to a certain impurity concentration.^{7,10} However, this may not necessarily hold for the transformations in double polymorph γ/β -Ga₂O₃ structures induced by temperature.

Thus, in the present work, we monitored structural transformations happening in double γ/β -Ga₂O₃ polymorph structures during anneals performed in-situ in an electron microscope using samples fabricated with either Si or Au ion implants. Si implants were selected because of their technological relevance for n-type doping in Ga₂O₃,²⁰ while Au implants were used for comparison, investigating possible chemical effects at the background of similar levels of the initial lattice disorder in both samples. We show that, under conditions of the in-situ electron microscope anneals, double γ/β -Ga₂O₃ polymorph structures remained stable up to 300°C, when onsets of the γ -to- β transformation become traceable, leading to a prominent γ - and β - mixture already at 500°C. Interestingly, the recrystallization of the β -Ga₂O₃ occurs throughout the whole γ -film and the preferential alignments of the newly emerging γ/β interfaces is different from that at the initial γ/β interface formed as a result of the disorder induced ordering. This transformation pattern is maintained as a function of temperature – with gradually reduced portion of the γ -domains. Finally, at 1100°C, γ -Ga₂O₃ fully transforms into β -Ga₂O₃, without dominating crystallographic relationships or preferred orientations, indicating that energy barriers are not any longer implied as limiting factors because of sufficiently high thermal energy supply. No apparent trends in the transformations were attributed to the chemical effects. The in-situ methodology enabled a new level of accuracy in the assessments of the transformations occurring in double polymorph γ/β -Ga₂O₃ structures.

2. Experimental Section

Double γ/β -Ga₂O₃ polymorph structures used in this work were fabricated by implantation of the (010)-oriented β -Ga₂O₃ single crystal wafers with either ²⁸Si⁺ or ¹⁹⁷Au⁺. Specifically, 300 keV ²⁸Si⁺ and 1.2 MeV ¹⁹⁷Au⁺ ions were implanted with fluences of 2×10^{16} Si/cm² and 3×10^{15} Au/cm², respectively. The implants were performed at room temperature and at 7° from the surface normal to minimize possible channeling effects. The Si and Au implant result in 31 and 40 displacements per atom (dpa) in the maximum of the disorder peaks, respectively (see Fig. S1 and S2 in Supp. Mat. I). Similar implantation conditions were used previously in literature for fabrication of double γ/β -Ga₂O₃ polymorph structures.^{10,16}

Subsequently, TEM lamellas were prepared by Focused Ion Beam (FIB) using a JEOL JIB 4500 and a FEI Versa 3D DualBeam

systems operating at 1-30 kV for the electron and Ga-ion beam. Final polishing of the TEM lamellas was done with low ion beam energy (2 kV) and current (~20 pA) to minimize the effect of Ga-ion beam. The crystal wafers were first sputter-coated by carbon (~20nm) using a Leica EM ACE600 sputter system. Further ~2 μ m protective layers of C/W were deposited using an e-beam (eW), followed by a Ga-ion beam (iW). High-resolution scanning transmission electron microscopy (HRTEM/STEM) and Selected Area Electron Diffraction (SAED) were conducted using a Thermo Fisher Scientific Cs-corrected Titan G2 60–300 kV microscope operated at 300 kV and equipped with a Gatan GIF Quantum 965 spectrometer. High angle annular dark field (HAADF) and bright field (BF) STEM images were recorded using a probe convergence semi-angle of 23 mrad, a nominal camera length of 60 mm, corresponding to an inner and outer collection semi-angle of 100 and 200 mrad for HAADF and 0–22 mrad for BF, respectively. In-situ heating experiments for the Si-implanted sample from RT to 850°C in steps of 50 °C were done using a Gatan double tilt heating holder (model 652), keeping the sample at the target temperature for 30 minutes in each step. Additionally, we used a Protochips Fusion holder to repeat the same experiments for the Au implanted sample but with improved temperature control, stability, and higher temperature range from RT to 1100 °C. As an example, Fig. S3 in Supp. Mat. II shows a low magnification BF STEM image of the prepared lamella. SAED patterns were acquired at each annealing temperature step during heating. Additional SAED patterns were acquired when cooling to RT to ensure that no crystal structure changes occurred during such cooling steps. All HAADF STEM images were recorded at RT. All the structural models for Ga₂O₃ polymorphs in this manuscript were displayed using VESTA software.²¹ In all lattice schematics used in the manuscript, gallium and oxygen atoms are represented in green and red, respectively. Higher color densities, darker green for gallium, is used for indicating higher atomic column density.

3. Results and discussion

3.1. As-fabricated double γ/β -Ga₂O₃ polymorph sample

Fig. 1 summarizes the TEM data collected from the as-fabricated samples. In particular Fig. 1(a) shows the low magnification BF STEM image and the corresponding SAED pattern of the Si-implanted sample, revealing a ~ 380 nm thick γ -Ga₂O₃ layer formed as a consequence of the radiation induced disorder. The γ -Ga₂O₃ layer formed as a result of Au-implants looks similar, see Fig. S3 in Supp. Mat. II, as expected because of the similar radiation disorder produced by both ions (see the explanation for the disorder calculations in the Supp. Mat. I). This is in accordance with literature data,^{9,10,16} reported the disorder induced β - to γ - polymorph transition. Notably, the newly formed γ -Ga₂O₃ is aligned with respect to the original β -Ga₂O₃ substrate following the crystallographic relationship: [100] γ -Ga₂O₃ // [201] β -Ga₂O₃ and [110] γ -Ga₂O₃ // [132] β -Ga₂O₃. This crystallographic orientation is probably due to the in-plane

matching (for planes vertical to the interface) between the newly formed γ -Ga₂O₃ and original β -Ga₂O₃.

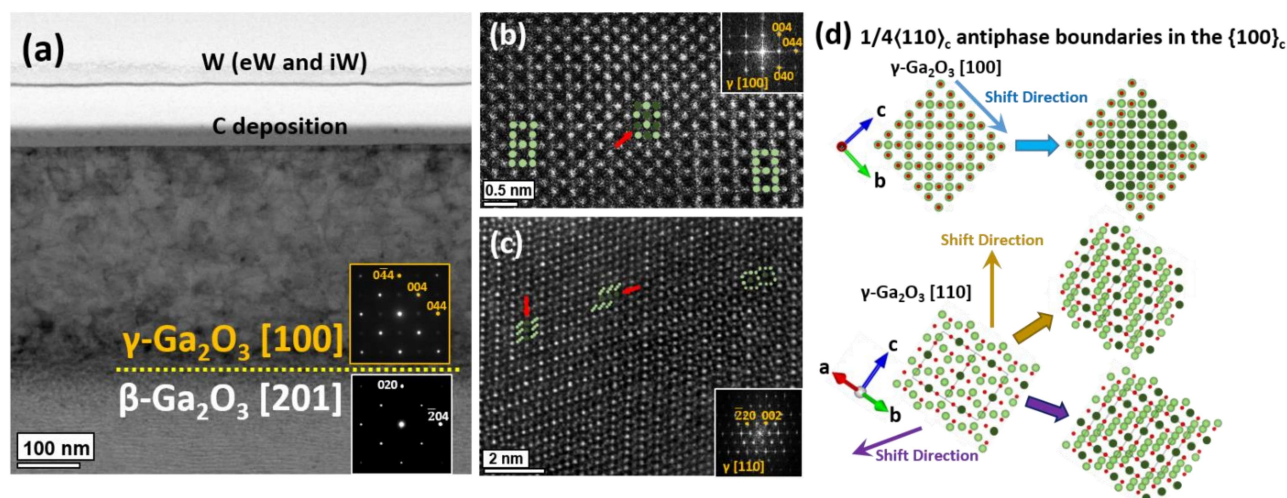


Fig. 1. Microscopy analysis of as-implanted samples. (a) Low magnification BF STEM image and SAED patterns of the Si-implanted sample showing the formation of the double γ/β -Ga₂O₃ polymorph structure. (b) HAADF STEM image and corresponding FFT of γ -Ga₂O₃ along the [100] zone axis for the Si-implanted sample. (c) HAADF STEM image and corresponding FFT of γ -Ga₂O₃ along the [110] zone axis for the Au-implanted sample. (d) Schematic representation of the lattices of γ -Ga₂O₃ along [100] and [110] zone axes, together with the projected model structures and the lattice shifts as a consequence of the APB. Color code: Ga green (dark green represents high density occupancy sites), O red.

There is a stacking similarity between the interplanar distances $d(044) = 1.48\text{\AA}$ and $d(-111) = 4.83\text{\AA}$ of γ -Ga₂O₃ with $d(-204) = 1.47\text{\AA}$ and $d(-201) = 4.82\text{\AA}$ of β -Ga₂O₃ phases, respectively. Further, Fig. 1(b-c) show HAADF STEM images and corresponding fast Fourier transforms (FFT) of γ -Ga₂O₃ along the [100] zone axis for the Si-implanted sample, and along the [110] zone axis for the Au-implanted sample. Both images show the presence of antiphase boundaries (APB), indicated by red arrows, that are characterized by the displacement vector $1/4(110)_c$ in the $\{100\}_c$ planes of the cubic spinel structure. Consequently, Fig. 1(d) shows two schematic representations of the γ -Ga₂O₃ lattice (viewed along the [100] and [110] directions) including the formation of APBs as a result of the atomic shifts. These schematics are in good agreement with the contrast observed in the HAADF STEM images in Fig. 1(b) and (c). Similar APBs in the γ -Ga₂O₃ spinel structure have been reported in literature.^{8, 22-24} Thus, in the initial stage, the samples used in this study are representative examples of the double γ/β -Ga₂O₃ polymorph structures. No apparent differences were detected in the quality of the γ -Ga₂O₃ produced either by Si or Au implants. We used both samples in the in-situ study to check for possible differences at the annealing stage.

3.2. In-situ monitoring of γ - to β - polymorph transition

Fig. 2(a-d) display the evolution in the SAED patterns for the Si-implanted sample, at RT and after in-situ anneals at 500°C, 700°C, and 850°C, respectively. The γ -Ga₂O₃ layer was initially tilted to [100] zone axis at RT, as shown in the indexed SAED pattern in Fig. 2(a). Notably, each SAED pattern is accompanied

by an inset showing the scaled features around the (022) spot of the γ -Ga₂O₃ to highlight the structural changes. We observed an onset γ - to β - polymorph transition already at $\approx 300^\circ\text{C}$ (see Fig. S4 in Supp. Mat. II) and prominently occurring at 500°C. The formation of the β -phase in the γ -Ga₂O₃ layer is confirmed by the emergence of new diffraction spots in the SAED pattern in Fig. 2(b). These new spots can be indexed as β -Ga₂O₃ phase domains (represented by red and blue colors) along the [021] and $[0\bar{2}1]$ zone axes, which are related by a 90° rotation. This could be induced by the four-fold symmetry of γ -Ga₂O₃ along the [100] direction, which may direct the formation of β -domains with 90° rotational relation. Subsequently, upon reaching 700°C, weaker spots surrounding the (022) become visible, as indicated by green dashed circles in the inset in Fig. 2(c). The number of these spots increases upon reaching 850°C, see the inset in Fig. 2(d). Additionally, the transformation from γ - to β -Ga₂O₃ is confirmed by EELS spectra in Fig. S5 in Supp. Mat. III. Fig. S5 shows the evolution of the O-K edge for as-implanted γ -Ga₂O₃ and after annealing at 500°C and 850°C, together with bulk β -Ga₂O₃, as reference. The O K-edge is characterized by two peaks at 537 eV and 543 eV,^{10,19} and the relative intensity between these peaks can be used as a fingerprint of the corresponding polymorph. Importantly, we did not observe any change in the sample while cooling the samples to room temperature, confirming the stability of the

transformation, and enabling accurate high resolution measurement

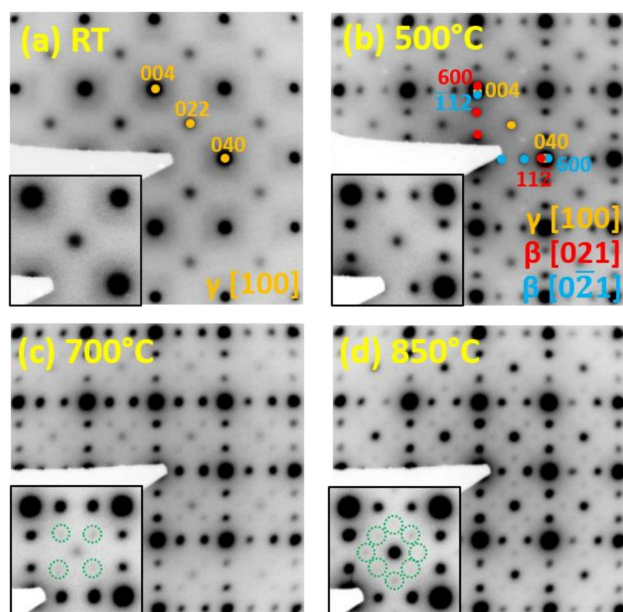


Fig. 2. Comparison of the SAED patterns from the Si-implanted sample in (a) as-fabricated state, with that upon in-situ anneals at (b) 500°C, (c) 700°C, and (d) 850°C. The insets show the scaled up features around the (022) spot. Color code: orange: γ -Ga₂O₃ along the [100] zone axis, red and blue: β -Ga₂O₃ along the [021] and [0 $\bar{2}$ 1] zone axes.

Indeed, Fig. 3 provides an example of such atomic-resolution measurements for samples annealed at 500°C and 850°C. Specifically, Fig. 3(a-b) depict low and high magnification HAADF STEM images of the Si-implanted sample after heating at 500°C. In both images, two types of domains β -Ga₂O₃ can be observed, oriented along the [021] and [0 $\bar{2}$ 1] directions and related to each other by a 90° rotation, marked in blue and red. Importantly, Fig. 3(b) is accompanied by two extra panels, showing the FFTs obtained from the areas marked by red and blue dashed rectangles. These FFTs confirm the remaining γ -Ga₂O₃ in the [100] orientation and reveal the presence of individual β -Ga₂O₃ domains exhibiting the [021]/[0 $\bar{2}$ 1] with a 90° rotational relationship described above. Fig. 3(c) displays a HAADF STEM image of the sample after heating at 850°C. On the left-hand side in Fig. 3(c), remaining γ -Ga₂O₃ is still visible, together with the presence of APBs, identified already in the as-fabricated sample. On the right-hand side of Fig. 3(c), the contrast associated with β -Ga₂O₃ along the [021] zone axis is clearly observed. Additionally, the presence of APBs between two β -phase regions is also visible in Fig. 3(c), as indicated with a red arrow. Thus, Fig. 3(c), in combination with the SAED pattern (Fig. 2(d)), confirms the presence of remaining γ -Ga₂O₃

upon 850°C anneals. For clarity, Fig. 3(d) provides a detailed view of the interface between the [100] γ -Ga₂O₃ (left) and [021] β -Ga₂O₃ (right) phases, taken from the region marked with a green rectangle in Fig. 3(c), accompanied by a schematic representation of both phases. As can be deduced from Fig. 3(d), the γ - to β - polymorph transition proceeds via the stacking of {400} γ to {600} β planes. We suggest that the newly formed strong spots observed in Fig. 2(b-d) correspond to the formation of new β -phase along the [021] direction, while the weaker spots marked with dashed green in Fig. 2(c-d) could be a consequence of the presence of domains and extended defects resulting from the recrystallization of the new β -Ga₂O₃ phase, consistently with literature.²⁵⁻²⁷ Recently, the presence of four rotational domains of β -Ga₂O₃ related by a 90° rotation has been reported for β -Ga₂O₃ grown on top of γ -Ga₂O₃.²⁸ Thus, in our samples, cubic γ -Ga₂O₃ may play a similar role, promoting the domains formation.

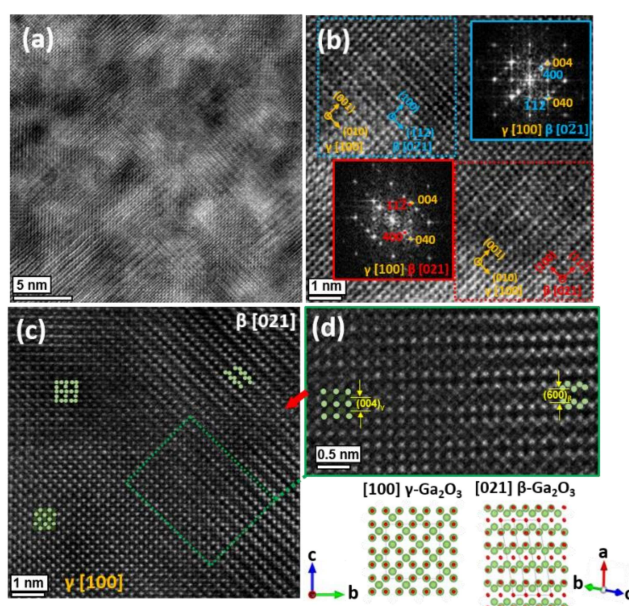


Fig. 3. Atomic-resolution measurements of Si-implanted sample upon anneals at 500°C and 850°C. (a) Low and (b) high magnification HAADF STEM images and corresponding FFTs of the Si-implanted sample after heating at 500°C. (c) Atomic resolution HAADF STEM images of the same sample after heating at 850°C showing the presence of [100] γ -Ga₂O₃ (left) and [021] β -Ga₂O₃ (right) with the presence of extensive defects such as APBs (red arrow). (d) HAADF STEM image at the interface between the two polymorphs. Schematic representation of [100] γ -Ga₂O₃ and [021] β -Ga₂O₃ polymorphs. Color code: Ga green (dark green represents high density occupancy sites), O red.

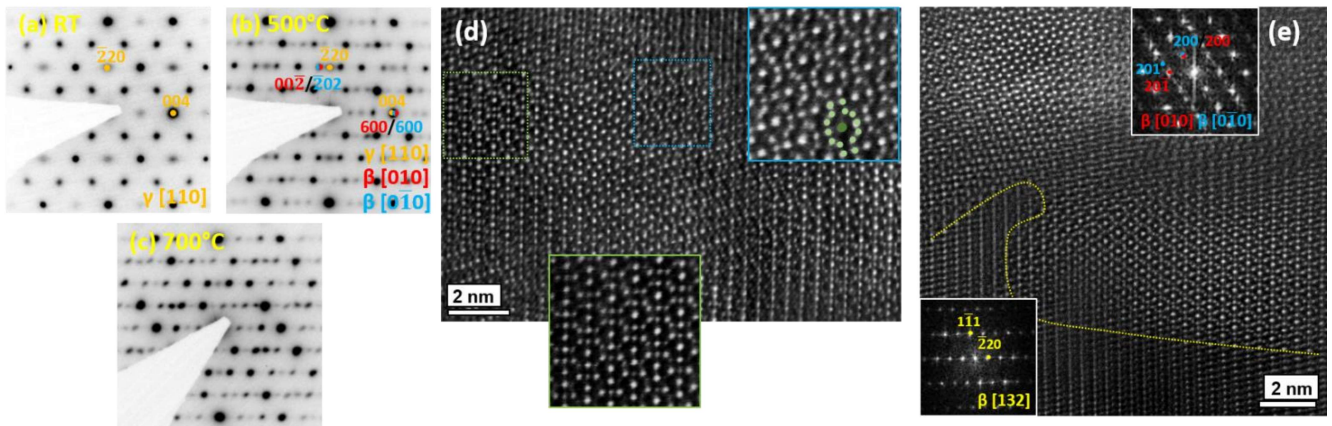


Fig. 4. Complementary microscopy data measured on the Au-implanted sample. SAED patterns for (a) as-fabricated state, with that upon in-situ anneals at (b) 500°C, (c) 700°C. Color code: Orange: γ -Ga₂O₃ along the [110] zone axis, red and blue: β -Ga₂O₃ along the [010] and [0 $\bar{1}$ 0] zone axes. (d-e) HAADF STEM images and corresponding FFT after heating at 500°C and 700°C, respectively. The green and blue boxes in figure (d) correspond to two domains of [010] β -phase. Color code: Ga green (dark green represents high density occupancy sites).

To control the generic character of the γ - to β - polymorph transition observed in Fig. 2 and 3, we repeated the experiment with the Au-implanted sample. This also allows us to explore different crystallographic orientation between γ -Ga₂O₃ and the newly formed β -Ga₂O₃. Firstly, Fig. S4 in the Supplementary Materials shows an HRTEM image and corresponding FFT from different areas after annealing at 300°C. Upon careful inspection in some of the FFTs, we observe the formation of additional weak spots assigned to β -Ga₂O₃ inclusions, confirming the γ - to β - polymorph transition starts already ~300°C. Furthermore, Fig. 4(a-c) display the SAED patterns of the Au-implanted sample acquired at RT as well as after heating at 500°C and 700°C. The SAED pattern acquired at RT can be indexed to the γ -Ga₂O₃ phase along the [110] zone axis (see orange indexing in Fig. 4(a)). After heating, additional spots emerge in the SAED pattern marked by red and blue spots in Fig. 4(b). Similar to the Si-implanted sample, these new spots can be indexed as two separate β -Ga₂O₃ domains, in this case, oriented along [010] and [0 $\bar{1}$ 0] zone axes. This observation is in full agreement and correlation with the data obtained for the Si-implanted sample acquired from a different zone axis. This is because the angle between [100] and [110] directions in the γ -phase (45°) is similar to that for [021] and [010] directions in the β -phase (43.68°). As can be seen in the SAED pattern, like in the previous case, there is a perfect overlapping between the (004) plane of γ -Ga₂O₃ with the (600) plane of β -Ga₂O₃. The HAADF STEM image recorded after heating at 500°C (Fig. 4(d)), displays remaining γ -Ga₂O₃ phase, as well as the newly formed [010] β -Ga₂O₃ domains with presence of the stacking faults which have been observed previously in literature.²⁸ The green and blue squares in Fig. 4(d) show details of the defect associated with the newly formed β -Ga₂O₃ phase. Finally, Fig. 4(e) shows a representative HAADF STEM image and corresponding FFTs taken at the interface, indicated by a dashed yellow line, between the newly formed β -phase along [010] zone axis and the original (untransformed) β -phase along the [132] zone axis after heating at 700°C, confirming their different relationships.

Thus, taking into account data in Fig. 2-4, we conclude that the γ - to β - polymorph transition in the double γ/β -polymorph structure fabricated via Si and Au ion implantation occurs in a generic and analogous manner, at least for the dose range and in-situ TEM conditions used in our experiment.

Furthermore, to investigate whether the β -matrix could be recovered with high temperature anneals, we tested in-situ heating of the Au-implanted sample up to 1100°C. Notably, after annealing at 1100°C, the γ -Ga₂O₃ has been completely transformed to β -Ga₂O₃ in other orientations. For example, Fig. 5(a) shows an area of the TEM lamella containing newly formed β -Ga₂O₃ viewed along the [010] direction. In addition, the corresponding FFT of two domains (blue and red) and the global FFT from the region marked in orange are included as insets. The FFTs obtained from the blue and red areas confirm the presence of two domains of [010] and [0 $\bar{1}$ 0] β -Ga₂O₃ separated by a twin boundary indicated by the pink dashed line. For clarity, Fig. 5(b) displays a schematic representation of [010] β -Ga₂O₃ resulting in the twin boundary observed in Fig. 5(a). Similar results were previously observed in β -Ga₂O₃ domains related by a twin boundary in the literature.³⁰⁻³²

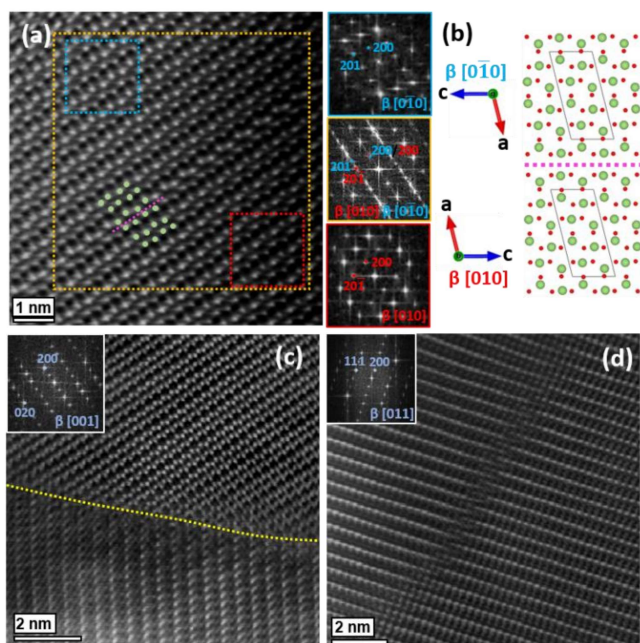


Fig. 5. HAADF STEM images of Au-implanted sample after heating at 1100°C. (a) β -Ga₂O₃ along the [010] direction with corresponding global FFT (orange) and local FFT taken from different areas (red and blue boxes) corresponding to two different domains. (b) Schematic representation of both domains and the twin boundary indicated by the pink dashed line. Ga atomic columns are represented in green and O in red. (c) Image recorded at the interface between newly formed [010] β -Ga₂O₃ and original (untransformed) [132] β -Ga₂O₃. (d) Image recorded from another area of the lamella corresponding to newly formed [011] β -Ga₂O₃ containing APB.

Nevertheless, we found that the crystallographic relationship deduced from the SAED patterns in Fig. 4(b-c) was no longer maintained. Fig. 5(c) shows a HAADF STEM image of the interface between the original and the newly formed β -Ga₂O₃, with the interface marked by the dashed yellow line. Here, the original (untransformed) β -Ga₂O₃ is viewed along the [132] zone axis, while the newly formed β -Ga₂O₃ is now viewed along the [001] zone axis instead. Additionally, Fig. 5(d) display a HAADF STEM image of the newly formed β -phase from another area of the lamella at the same tilting angle, oriented in the [011] direction, and revealing the presence of an APB. In both cases, this crystallographic relationship is different from that initially observed for lower annealing temperatures, as in Fig. 4(e) at 700°C.

3.3. Discussion

The data in Fig. 1-5 provide new insights on how the metastable γ -Ga₂O₃, formed by the disorder-induced transformation, converts back into β -Ga₂O₃ upon annealing. In our interpretation, under annealing conditions used in this work, β -Ga₂O₃ form domains exhibiting the crystallographic relationship of [021] β -Ga₂O₃//[100] γ -Ga₂O₃ and [010] β -Ga₂O₃//[110] γ -Ga₂O₃. Importantly, looking accurately into the SAED patterns, e.g. in Fig. 2(b) and 3(b), we observe that some of the interplanar distances in the γ - and β -polymorphs are rather

similar. Specifically, we see that the lattice spacing of 2.06 Å for (400) planes in the γ -Ga₂O₃ is close to that of 1.98 Å and 2.10 Å for (600) and (11 $\bar{2}$) planes in the β -Ga₂O₃, respectively. Such similarity in distances may contribute to the reduction of the strain barrier associated with the recrystallization of the β -Ga₂O₃ domains inside the γ -film. Moreover, J. Wang et al.³³ showed experimentally and by first-principles calculations that similar transitions occurs in Ga₂O₃ nanowires. From their results, the calculated surface energy of {600} β is smaller than that of {400} γ . Considering that a TEM-lamella has a higher surface area/volume ratio than a bulk sample, the observed transition in this work could be induced by the reduction of the surface energy. Our results also showed that the nucleation of β -Ga₂O₃ domains takes place all over the γ -epilayer, and not in a preferential location, such as at the γ/β -interface. Spectacularly, these newly formed β -Ga₂O₃ domains exhibit different preferential crystallographic stacking with the γ -lattice as compared to that in the initial γ/β -interface. For clarity, Fig. 6 illustrates the dominating orientation relationships observed in our samples.

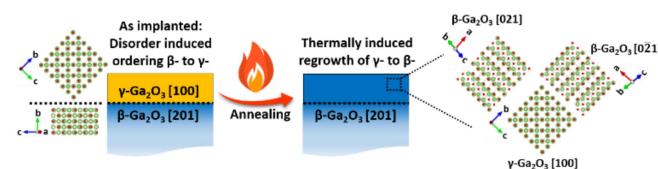


Fig. 6. Schematics of the dominating orientation relationships observed in our samples.

Notably, formation of the β -Ga₂O₃ domains inside the γ -matrix upon ex-situ anneals was proposed in the literature too, specifically suggesting that the defects available in the γ -matrix may induce the formation of such β -domains at temperatures below those require for a massive γ -to- β transition.¹⁸ This hypothesis is in agreement with our data, where high concentrations of APBs in the γ -Ga₂O₃ triggers the formation of β -Ga₂O₃ already at 300°C. Further on, for the anneals in the range of 900 - 1100°C, the remaining γ -Ga₂O₃ back-transforms to β -Ga₂O₃ without preferential orientations, indicating that energy barriers are not any longer implied as limiting factors because of a high enough thermal energy supplied.

Importantly, the parameters controlling the polymorphism from a macroscopic sample (typically used in the ex-situ annealing experiments in literature^{8, 16}) and a TEM-lamella sized sample (as used in this work) – may be different. Consequently, there could be potential discrepancies between the in-situ and ex-situ observations. Moreover, all in-situ anneals in the microscope were performed in vacuum, featuring quite different conditions as compared to that in air or gas flow frequently used in literature for ex situ annealing. In its turn, it is well-known that the differentiation between the oxygen rich or lean conditions may radically change properties of oxides.³⁴ Thus, this factor might be considered while comparing in-situ and ex-situ observations too. For example, in the present work we have not detected any signs of the implanted impurity

precipitation, while SiO_x nanoparticles and voids formation were observed upon the ex-situ air anneals of the double polymorph γ/β -Ga₂O₃ structures fabricated using similar Si ion implantation conditions.¹⁶ All-in-all, the results in Fig. 1–5, taken in the context of the literature data confirm the complexity of the processes occurring in the double polymorph γ/β -Ga₂O₃ structures upon anneals.

4. Conclusions

In conclusion, we performed in-situ heating studies of the double γ/β -Ga₂O₃ polymorph structures fabricated by the radiation induced disorder approach and revealed several new interesting trends for the γ -to- β polymorph transition. The in-situ TEM study reveals the emergence of β -Ga₂O₃ domains at temperatures around 300°C. The nucleation of these newly formed β -Ga₂O₃ domains take place according to the crystallographic relationship: [100] γ -Ga₂O₃//[021] β -Ga₂O₃ and [110] γ -Ga₂O₃//[010] β -Ga₂O₃, possibly explicable by the reduction of the surface energy and strain minimization due to very similar lattice planes spacing in the polymorphs. This was interpreted in terms of the reduction of the strain barrier associated with the formation of the β -Ga₂O₃ domains inside the γ -film. Importantly, these orientations are different from that established at the initial as-implanted γ/β -interface. However, at high temperatures (900–1100°C), γ -Ga₂O₃ fully recrystallizes into β -Ga₂O₃ in other orientations, indicating that energy barriers are not any longer implied as limiting factors because of sufficiently high thermal energy supply. Thus, the in-situ observation methodology enabled a novel unprecedented accuracy in the assessments of the γ -to- β polymorph transition.

Author Contributions

J.G.F and S.B.K: conceptualization, data curation, formal analysis, investigation, methodology, visualization, writing original draft, writing – review and editing. L. J. Z., A. Z., A. P., P. D. M: formal analysis, investigation, methodology, visualization, writing original draft, writing – review and editing. E. O, L. V., A. Y. K and Ø. P: formal analysis, funding acquisition, investigation, project administration, resources, supervision, validation, writing – review & editing

Conflicts of interest

There are no conflicts to declare.

Acknowledgements

The Research Council of Norway is acknowledged for support through the projects NANO2021 researcher project Functionalization of conducting oxides by ion beam and defect engineering (FUNCTION, no. 287729) and the M-ERA.NET Program via GOFIB project (no. 337627). We also acknowledge the Norwegian Center for Transmission Electron Microscopy (NORTEM, no 197405/F50), the Norwegian Micro- and Nanofabrication Facility (NorFab, no. 295864), NordForsk is

acknowledged for support to the NordTEMhub project no. 96971. Viktor Mihaly Bobal is acknowledge for performing ion implantation on the samples studied herein. This work was performed in part at the Chalmers Material Analysis Laboratory, CMAL. The acknowledgements come at the end of an article after the conclusions and before the notes and references.

References

- 1 A. W. Li, X. Qian and J. Li, *Nature Reviews Materials*, 2021, **6**, 829.
- 2 M. Ishimaru, I. V. Afanasyev-Charkin and K. E. Sickafus, *Appl. Phys. Lett.* 2000, **76**, 2556.
- 3 S. Dhara, A. Datta, C. T. Wu, Z. H. Lan, K. H. Chen, Y. L. Wang, C. W. Hsu, C. H. Shen, L. C. Chen and C. C. Chen, *Appl. Phys. Lett.* 2004, **84**, 5473.
- 4 A. Benyagoub, *Phys. Rev. B* 2005, **72**, 094114.
- 5 G. Sattonnay and L. Thomé, *J. Nucl. Mater.* 2006, **348**, 223.
- 6 F. Liu, X. Zhao, Y. Li and C. Liu, *J. Alloys Compd.* 2023, **946**, 169301.
- 7 H.-L. Huang, J. M. Johnson, C. Chae, A. Senckowski, M. H. Wong and J. Hwang, *Appl. Phys. Lett.* 2023, **122**, 251602.
- 8 T. Yoo, X. Xia, F. Ren, A. Jacobs, M. J. Tadjer, S. Pearton and H. Kim, *Appl. Phys. Lett.* 2022, **121**, 072111.
- 9 J. García-Fernández, S. B. Kjeldby, P. D. Nguyen, O. B. Karlsen, L. Vines and Ø. Prytz, *Appl. Phys. Lett.* 2022, **121**, 191601.
- 10 A. Azarov, J. García Fernández, J. Zhao, F. Djurabekova, H. He, R. He, Ø. Prytz, L. Vines, U. Bektas, P. Chekhonin, N. Klingner, G. Hlawacek and A. Kuznetsov, *Nat. Commun.* 2023, **14**, 4855.
- 11 A. Azarov, C. Bazioti, V. Venkatachalapathy, P. Vajeeston, E. Monakhov and A. Kuznetsov, *Phys. Rev. Lett.* 2022, **128**, 015704.
- 12 S. J. Pearton, Fan Ren, Marko Tadjer and Jihyun Kim, *J. Appl. Phys.* 2018, **124**, 220901.
- 13 M. J. Tadjer, *Science* 2022, **378**, 724.
- 14 J. Xu, W. Zheng and F. Huang, *J. Mater. Chem. C* 2019, **7**, 8753.
- 15 H. Y. Playford, A. C. Hannon, E. R. Barney and R. I. Walton, *Chem. Eur. J.* 2013, **19**, 2803.
- 16 S. B. Kjeldby, A. Azarov, P. D. Nguyen, V. Venkatachalapathy, R. Mikšová, A. Macková, A. Kuznetsov, Ø. Prytz and L. Vines, *J. Appl. Phys.* 2022, **131**, 125701.
- 17 H.-L. Huang, C. Chae, J. M. Johnson, A. Senckowski, S. Sharma, U. Singiseti, M. H. Wong and J. Hwang, *APL Mater.* 2023, **11**, 061113.
- 18 P. Castro-Fernández, M. V. Blanco, R. Verel, E. Willinger, A. Fedorov, P. M. Abdala and C. R. Müller, *J. Phys. Chem. C* 2020, **124**, 37, 20578.
- 19 A. Sharma, M. Varshney, H. J. Shin, K. H. Chae and S. O. Won, *RSC Adv.* 2017, **7**, 52543.
- 20 A. T. Neal, S. Mou, S. Rafique, H. Zhao, E. Ahmadi, J. S. Speck, K. T. Stevens, J. D. Blevins, D. B. Thomson, N. Moser, K. D. Chabak and G. H. Jessen, *Appl. Phys. Lett.* 2018, **113**, 062101.
- 21 K. Momma and F. Izumi, *J. Appl. Crystallogr.* 2011, **44**, 1272.
- 22 M. Mitome, S. Kohiki, T. Nagai, K. Kurashima, K. Kimoto and Y. Bando, *Cryst. Growth Des.* 2013, **13**, 8, 3577.
- 23 C. S. Chang, N. Tanen, V. Protasenko, T. J. Asel, S. Mou, H. G. Xing, D. Jena and D. A. Muller, *APL Mater.* 2021, **9**, 051119.
- 24 J. Tang, K. Jiang, S. D. House, C. Xu, K. Xiao, L. M. Porter and R. F. Davis, *Appl. Phys. Lett.* 2023, **123**, 012103 (2023).
- 25 P. Mazzolini, A. Falkenstein, C. Wouters, R. Schewski, T. Markurt, Z. Galazka, M. Martin, M. Albrecht and O. Bierwagen, *APL Mater.* 2020, **8**, 011107.
- 26 G. Wagner, M. Baldini, D. Gogova, M. Schmidbauer, R. Schewski, M. Albrecht, Z. Galazka, D. Klimm and R. Fornari, *Phys. Status Solidi A* 2014, **211**, 1, 27.

- 27 S. Gao, Y. Wu, R. Kang and H. Huang, *Mater. Sci. Semicond.* 2018, **79**, 165.
- 28 K. Jiang, J. Tang, C. Xu, K. Xiao, R. F. Davis and L. M. Porter, *J. Vac. Sci. Technol. A* 2023, **41**, 062702.
- 29 D. Gogova, G. Wagner, M. Baldini, M. Schmidbauer, K. Irmscher, R. Schewski, Z. Galazka, M. Albrecht and R. Fornari, *J. Cryst. Growth*. 2014, **401**, 665.
- 30 G. Wagner, M. Baldini, D. Gogova, M. Schmidbauer, R. Schewski, M. Albrecht, Z. Galazka, D. Klimm and R. Fornari, *Phys. Status Solidi A* 2014, **211**, 1, 27.
- 31 R. Schewski, K. Lion, A. Fiedler, C. Wouters, A. Popp, S. V. Levchenko, T. Schulz, M. Schmidbauer, S. Bin Anooz, R. Grüneberg, Z. Galazka, G. Wagner, K. Irmscher, M. Scheffler, C. Draxl and M. Albrecht, *APL Mater.* 2019, **7**, 022515.
- 32 S. Vura, U. Ul Muazzam, V. Kumar, S. C. Vanjari, R. Muralidharan, N. Digbijoy, P. Nukala and S. Raghavan, *ACS Appl. Electron. Mater.* 2022, **4**, 4, 1619.
- 33 J. Wang, X. Guan, H. Zheng, L. Zhao, R. Jiang, P. Zhao, Y. Zhang, J. Hu, P. Li, S. Jia and J. Wang, *Nano Lett.* 2023, **23**, 16, 7364.
- 34 T. Moe Børseth, B. G. Svensson, A. Yu. Kuznetsov, P. Klason, Q. X. Zhao and M. Willander, *Appl.Phys.Lett.* 2006, **89**, 262112.

SUPPLEMENTARY MATERIAL

In-situ atomic-resolution study of transformations in double polymorph γ/β -Ga₂O₃ structures

*J. García-Fernández**, *S. B. Kjeldby*, *L. J. Zeng*, *A. Azarov*, *A. Pokle*, *P. D. Nguyen*, *E. Olsson*, *L. Vines*,
*A. Yu Kuznetsov**, *Ø. Prytz**

I. Displacement per atom calculations and irradiation parameters

The implantation parameters for the Au and Si ions were chosen in such a way to produce nearly the same distribution and number of primary defects as can be seen from Fig. S1 and Table SI summarizing the implantation parameters. As seen from Fig. S1 that despite the displacement per atom (DPA) depth profile produced by Si ions is broader and has a lower maximum as compared to that of Au ions, the profiles of these ions are comparable.

Note that the DPA vs depth profiles were calculated using conventional methodology [Ref. S1] based on SRIM code [Ref. S2] simulations. Specifically, the SRIM vacancy generation profiles for a given fluence were normalized to an atomic density of β -Ga₂O₃ ($n_{at} = 9.45 \times 10^{22}$ at/cm³). The SRIM simulations were performed with 28 eV and 14 eV as the displacement energies for Ga and O atoms, respectively [Ref. S3].

Ion	Energy (keV)	Fluence			R_{pd} (nm)	R_p (nm)	Max conc. (at.%)
		(ions/cm ²)	1 dpa (ions/cm ²)	(max dpa)			
²⁸ Si ⁺	300	2×10^{16}	6.5×10^{14}	31	200	245	1
¹⁹⁷ Au ⁺	1200	3×10^{15}	7.5×10^{13}	40	115	160	0.3

Table SI. Implant parameters used in the present study, where the ion fluences are shown also for the 1 DPA as well as maximum values of DPA are indicated for both ions. The R_{pd} and R_p indicate the depth where the defect generation profile is maximal and the projected range of the implanted ions, respectively.

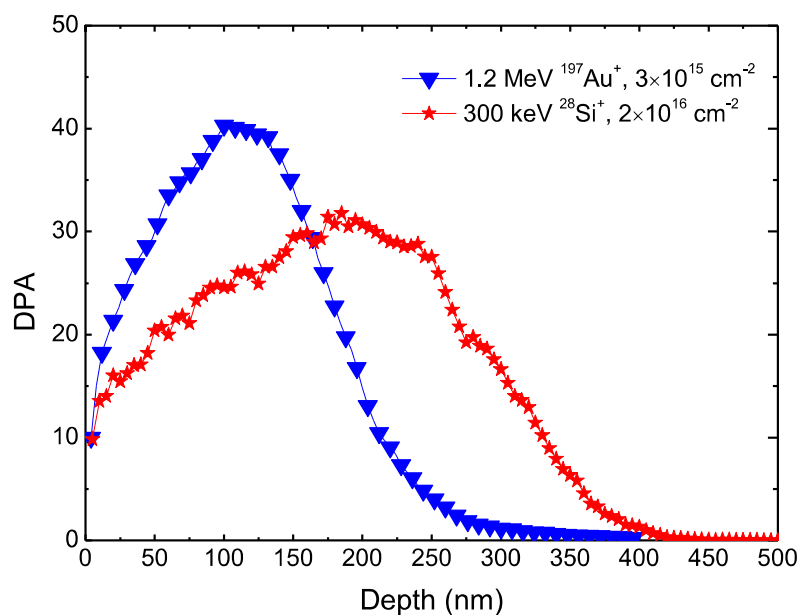


Fig. S1. DPA vs depth profiles in β -Ga₂O₃ for Si and Au implants as indicated in the legend.

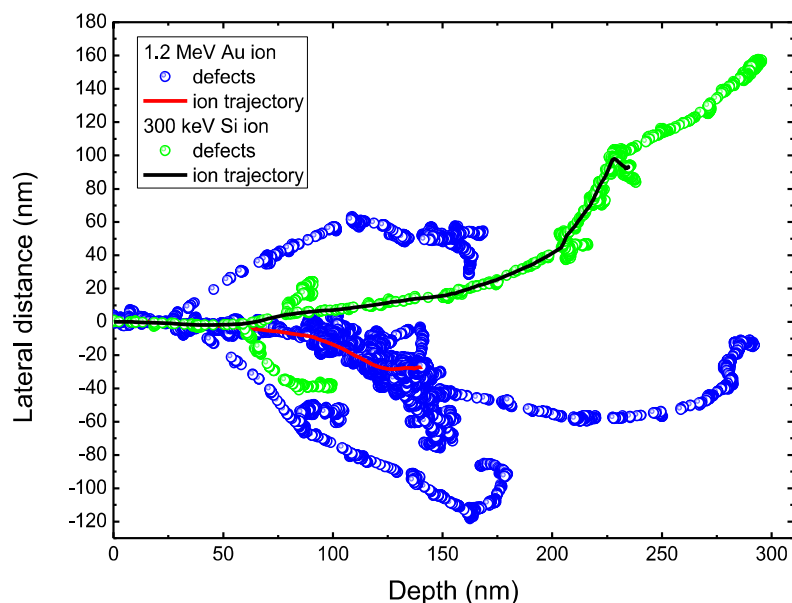


Fig. S2. Projections of individual collision cascades produced by 1.2 MeV Au and 300 keV Si ions in β -Ga₂O₃ simulated using the SRIM code [Ref. S2]. The lines correspond to the ion trajectories while the circles correspond to the point defects.

However, it should be mentioned that the collision cascade shape as well as number of primary defects generated by one individual ion are different for Au and Si due to large difference in atomic masses of these ions. Indeed, Fig. S2 illustrates the difference in the volumetric defect distribution in the β -Ga₂O₃ samples for the single Au and Si implants. It is clearly seen that in contrast to Si ions, heavy Au ions generate dense collision cascade involving many large sub-cascades. Such difference in volumetric defect distribution and, therefore, in the density of collision cascades can result in the disorder enhancement attributed to the nonlinear defect interaction within collision cascade volume [Ref. S4].

II. STEM analysis of the Au as-implanted and low-temperature annealed sample

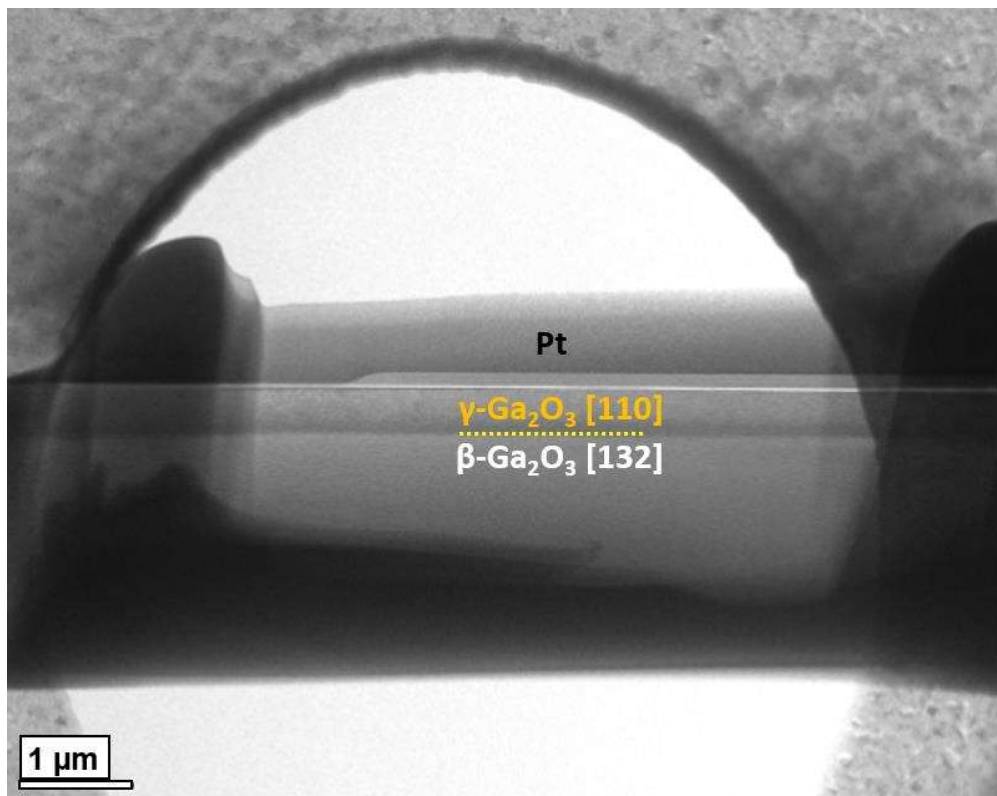


Fig. S3. Low magnification BF STEM image of the Au-implanted sample as fabricated in the heating E-chip showing the starting state of the double $\gamma/\beta\text{-Ga}_2\text{O}_3$ polymorph structure.

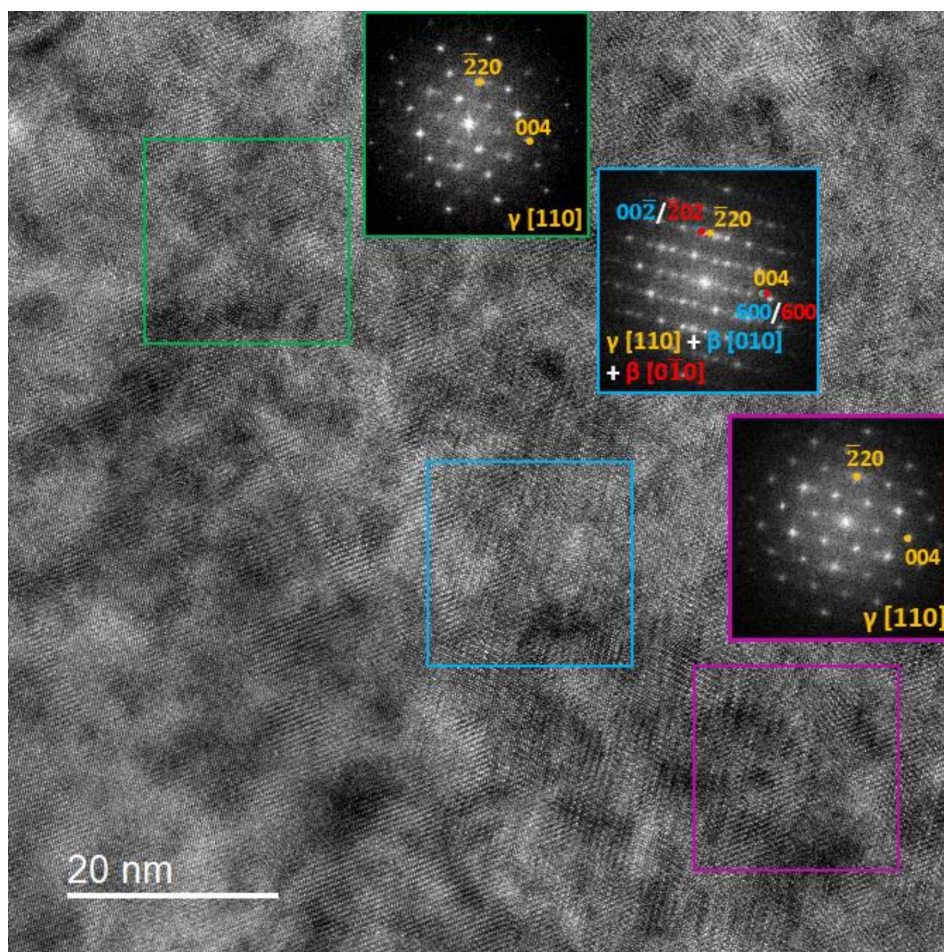


Fig. S4. HRTEM and corresponding FFT of different areas of the Au-implanted sample after annealing at 300°C. The formation of β -Ga₂O₃ domains can be detected in the sample.

III. Oxygen-K edge analysis by EELS on the Si as-implanted and annealed sample

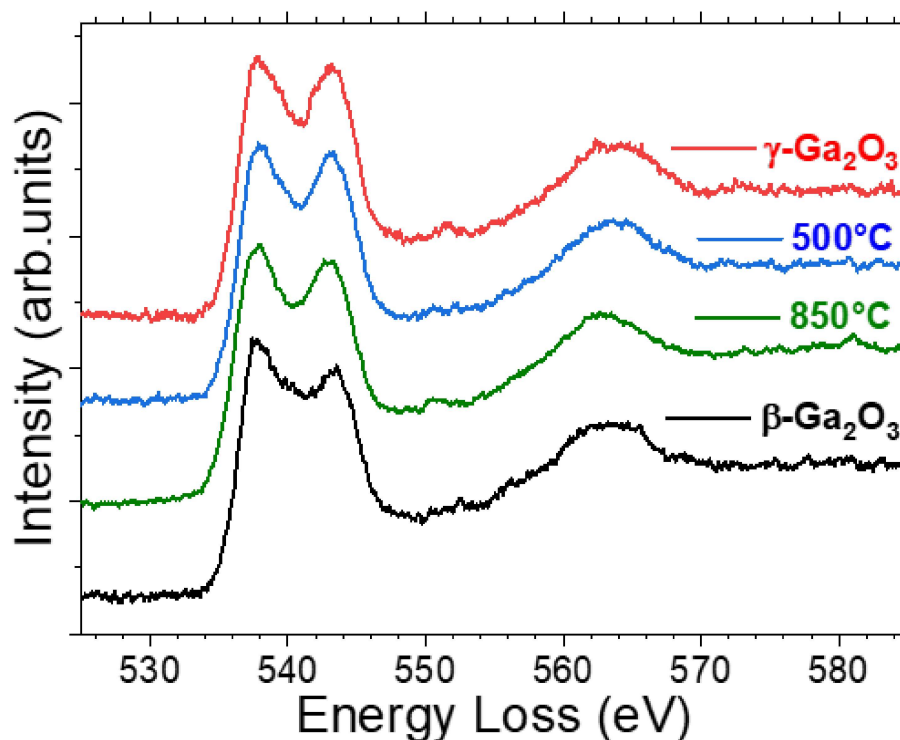


Fig. S5. ELS spectra of the oxygen-K edge, acquired from the as-implanted $\gamma\text{-Ga}_2\text{O}_3$ (red), and after annealing at 500°C (blue) and 850°C (green), together with bulk $\beta\text{-Ga}_2\text{O}_3$ (black). The obtained ratio between the two maxima centered at 537 and 543 eV is 1.02, 1.05, 1.14, and 1.21 for $\gamma\text{-Ga}_2\text{O}_3$, 500°C, 850°C, and $\beta\text{-Ga}_2\text{O}_3$ samples, respectively, confirming the gradual transformation from γ - to $\beta\text{-Ga}_2\text{O}_3$.

Ref. S1. A. I. Titov, A. Yu. Azarov, L. M. Nikulina, and S. O. Kucheyev, "Damage buildup and the molecular effect in Si bombarded with PFn cluster ions", *Nucl. Instrum. Methods Phys. Res. B* **256**, 207 (2007).

Ref. S2. J. F. Ziegler, M. D. Ziegler, and J. P. Biersack, "SRIM—the stopping and range of ions in matter (2010)", *Nucl. Instrum. Methods Phys. Res. B* **268**, 1818 (2010).

Ref. S3. B. R. Tuttle, N. J. Karom, A. O'Hara, R. D. Schrimpf, and S. T. Pantelides, "Atomic-displacement threshold energies and defect generation in irradiated $\beta\text{-Ga}_2\text{O}_3$: A first-principles investigation", *J. Appl. Phys.* **133**, 015703 (2023).

Ref. S4. A. Azarov, V. Venkatachalapathy, P. Karaseov, A. Titov, K. Karabeshkin, A. Struchkov, and A. Kuznetsov, "Interplay of the disorder and strain in gallium oxide" *Scientific Reports* **12**, 15366 (2022).

Paper IV

**Cross-sectional cathodoluminescence
measurements of Cr-luminescence in
implanted and annealed gallium oxide**

S. B. Kjeldby, J. García-Fernández, A. Galeckas,
I.J.T. Jensen, Ø. Prytz and L. Vines

Submitted to *Journal of Applied Physics*, February 2024

IV

Paper V

**Optical properties of ZnFe₂O₄
nanoparticles and Fe-decorated inversion
domain boundaries in ZnO**

S. B. Kjeldby, P. D. Nguyen, J. García-Fernández, K. Haug,
A. Galeckas, I. J. T. Jensen, A. Thøgersen, L. Vines
and Ø. Prytz

Published in *Nanoscale Advances*, March 2023, Volume 5

DOI: 10.1039/D2NA00849A

Reproduced from S. B. Kjeldby *et al.*, *Nanoscale Advances* **5**, 2102
(2023) with permission from the Royal Society of Chemistry

Cite this: *Nanoscale Adv.*, 2023, 5, 2102

Optical properties of ZnFe₂O₄ nanoparticles and Fe-decorated inversion domain boundaries in ZnO†

S. B. Kjeldby,^{ID}*^a P. D. Nguyen,^a J. García-Fernández,^{ID}^a K. Haug,^{ID}^a
A. Galeckas,^{ID}^a I. J. T. Jensen,^{ab} A. Thøgersen,^b L. Vines,^{ID}^a and Ø. Prytz,^{ID}^a

The maximum efficiency of solar cells utilizing a single layer for photovoltaic conversion is given by the single junction Shockley–Queisser limit. In tandem solar cells, a stack of materials with different band gaps contribute to the conversion, enabling tandem cells to exceed the single junction Shockley–Queisser limit. An intriguing variant of this approach is to embed semiconducting nanoparticles in a transparent conducting oxide (TCO) solar cell front contact. This alternative route would enhance the functionality of the TCO layer, allowing it to participate directly in photovoltaic conversion *via* photon absorption and charge carrier generation in the nanoparticles. Here, we demonstrate the functionalization of ZnO through incorporation of either ZnFe₂O₄ spinel nanoparticles (NPs) or inversion domain boundaries (IDBs) decorated by Fe. Diffuse reflectance spectroscopy and electron energy loss spectroscopy show that samples containing spinel particles and samples containing IDBs decorated by Fe both display enhanced absorption in the visible range at around 2.0 and 2.6 eV. This striking functional similarity was attributed to the local structural similarity around Fe-ions in spinel ZnFe₂O₄ and at Fe-decorated basal IDBs. Hence, functional properties of the ZnFe₂O₄ arise already for the two-dimensional basal IDBs, from which these planar defects behave like two-dimensional spinel-like inclusions in ZnO. Cathodoluminescence spectra reveal an increased luminescence around the band edge of spinel ZnFe₂O₄ when measuring on the spinel ZnFe₂O₄ NPs embedded in ZnO, whereas spectra from Fe-decorated IDBs could be deconvoluted into luminescence contributions from bulk ZnO and bulk ZnFe₂O₄.

Received 25th November 2022

Accepted 24th February 2023

DOI: 10.1039/d2na00849a

rsc.li/nanoscale-advances

1 Introduction

ZnO is a wide band gap (3.3 eV¹) semiconductor with a hexagonal wurtzite crystal structure which is used in a wide range of applications,^{2,3} including as a transparent conducting oxide (TCO).^{4,5} For photovoltaics, absorption in nanoparticles can permit efficient generation of multiple charge carriers for absorption of photons with energies higher than twice the band gap, a process which is typically inefficient in bulk materials.⁶ Nanoparticles embedded in a TCO are of particular interest, since this design could facilitate extraction of the optically generated charge carriers *via* the nanoparticle-TCO heterojunction.⁷ In addition, this design allows the TCO layer to actively participate in solar energy conversion, effectively turning the TCO layer into the top cell in a tandem-like solar cell. Previous research has demonstrated that it is possible to form Ge nanoparticles⁷ or Zn₂GeO₄ nanoparticles⁸ in ZnO by ion

implantation followed by annealing. The same synthesis method can also be used to form SiO₂ nanoparticles in Ga₂O₃.⁹ In the current work, we examine similar samples fabricated *via* a powder synthesis route.

The reported phase diagram of the Zn–Fe–O system indicates that for cation ratios in excess of ~2% it is possible to form spinel ZnFe₂O₄ nanoparticles (NPs) in ZnO,¹⁰ which has also been experimentally confirmed.¹¹ In normal spinel ZnFe₂O₄, *i.e.* with an inversion parameter of zero, Zn²⁺ occupies tetrahedral sites, and Fe³⁺ occupies octahedral sites sharing edges. ZnFe₂O₄ is a semiconductor with a bandgap of about 2.0 eV¹². In two junction tandem solar cells with a silicon bottom cell, the optimal top cell band gap is 1.7–1.8 eV, depending on device architecture.¹³ If the top cell is composed of a TCO functionalized with embedded semiconducting nanoparticles, the nanoparticles should consequently have a band gap of around 1.7–1.8 eV. Since ZnFe₂O₄ has a bandgap close to these values, ZnFe₂O₄ NPs could be appropriate for TCO functionalization. The optical properties of bulk ZnFe₂O₄ and ZnFe₂O₄ nanoparticles have been previously investigated by photoluminescence spectroscopy^{12,14,15} and diffuse reflectance spectroscopy (DRS).¹⁶ The stabilisation of heterostructures of ZnFe₂O₄ nanoparticles embedded in ZnO has attracted

^aCentre for Materials Science and Nanotechnology, University of Oslo, N-0318 Oslo, Norway. E-mail: s.b.kjeldby@smn.uio.no

^bSINTEF Industry, Sustainable Energy Technology, N-0314 Oslo, Norway

† Electronic supplementary information (ESI) available. See DOI: <https://doi.org/10.1039/d2na00849a>



attention, particularly for their magnetic properties and photocatalytic activity.^{11,17,18} The possibility of embedding nanoparticles of ZnFe₂O₄ in ZnO combined with the band gap value of ZnFe₂O₄ makes this phase a good candidate for functionalization of bulk and thin film ZnO.

Several transition metal impurities, like In or Fe, can promote formation of the inversion domain boundary (IDB) microstructure in ZnO.^{19–22} Inversion domains in ZnO are planar defects across which the wurtzite *c*-axis orientation is rotated 180°. Two different types of IDBs are found in the IDB microstructure. Basal IDBs (b-IDBs) lie parallel to the ZnO-(0001) planes and have a head-to-head configuration (*c*-axes in the bordering grains point toward each other).²¹ Pyramidal IDBs (p-IDBs) lie parallel to the ZnO- $\{2\bar{1}\bar{1}5\}$ or $\{2115\}$ planes and have tail-to-tail configuration (*c*-axes of neighboring grains point away from each other).²¹ For sufficiently high Fe-concentrations, iron tends to occupy octahedral sites on b-IDBs or trigonal bipyramidal sites on p-IDBs,^{21,23} referred to as Fe-decoration of the IDBs. On b-IDBs, it has been reported that the decoration can result in a completely filled close-packed iron monolayer embedded in the ZnO matrix.²¹ The structure of the ZnO IDBs has been studied extensively by microscopic techniques,^{20,24,25} and the elemental composition has been investigated with core-loss electron energy loss spectroscopy (EELS) and energy dispersive X-ray spectroscopy (EDS).^{21,23} However, little attention has been paid to the low-loss range of the EELS spectrum, which contains information about the dielectric response of the sample. Similarly, optical characterization of the structures remains scarce. The effect of such a regular defect structure on functional properties certainly warrants further investigation. Additionally, the local configuration of Fe-ions is similar at Fe-decorated b-IDBs and in normal spinel, including similar Fe–O bond lengths.²⁶ Functional similarities could arise from such structural similarities.

In the present work, we have studied the functional and structural properties of Fe-decorated IDBs in ZnO and spinel ZnFe₂O₄ NPs embedded in ZnO. This study complements previous structural characterization of the IDB microstructure, and explores similarities and differences in the functional behavior of the IDB microstructure and the embedded nanoparticles.

2 Experimental procedures

Samples were prepared by a powder synthesis route where powders of ZnO (Sigma Aldrich 99.99%) and α -Fe₂O₃ (Sigma Aldrich 99.5%) were mixed to arrive at a 10% cation ratio (Fe/(Zn + Fe)) for samples 1 and 2. The powders were ball milled in isopropanol using an agate jar and 10 mm agate balls for 2 hours at 300 rpm. The resulting mixtures were pressed into pellets measuring 13 mm in diameter, which were loaded into a furnace at 1400 °C and allowed to homogenize for between 4 and 17 hours. According to the phase diagrams,¹⁰ the iron is fully incorporated into the wurtzite matrix in a solid solution at this temperature. The pellets were left in the furnace to cool to room temperature over a 5 hour period. One of the pellets was subjected to a second heat treatment at 1000 °C for 36 hours

(sample 1). Samples were cut from the middle of the pellets. Two additional samples were prepared with nominal compositions ZnFe₂O₄ (sample 3) and ZnO (sample 4). An overview of the samples can be found in Table 1. For clarity, samples are henceforth referred to by the label given in the table.

The samples were characterized by X-ray diffraction (XRD) on the pellet samples, (scanning) transmission electron microscopy ((S)TEM) and optical measurements. XRD data were obtained in a Rigaku MiniFlex600 diffractometer with a Cu K_{α1} source. Electron transparent cross-sectional TEM samples were prepared by mechanical grinding, polishing, and final thinning by Ar ion milling in a Gatan PIPS II (Model 695). Structures were initially investigated using selected area electron diffraction (SAED) and STEM techniques in a JEOL JEM 2100F operated at 200 kV. Subsequently, atomic-resolution structural characterization and EDS studies were carried out using a Thermo Fisher Scientific Cs-corrected Titan G2 60–300 kV microscope equipped with a Wien-filter monochromator, Gatan GIF Quantum 965 EELS spectrometer and Super-X EDS detectors. The microscope was operated at 300 kV accelerating voltage, and the probe-forming optics were configured to form a ~0.8 Å probe with a convergence semi-angle of 22 mrad. The semi-angular ranges of the high-angle annular dark field (HAADF) and annular bright field (ABF) detectors were 100–200 and 10–20 mrad, respectively. Additionally low-loss EELS was performed at 60 kV using a collection semi-angle of 21 mrad. The acquisition at 60 kV acceleration voltage reduces the impact of retardation effects, which may otherwise complicate the determination of the bandgap. The energy dispersion was 0.01 eV per channel. The energy resolution measured using the full width at half maximum (FWHM) of the zero-loss peak was 0.18 eV. Principle component analysis (PCA)²⁷ with 20 components was used to reduce spectral noise.

In EELS, the energy loss of high-energy electrons transmitted through a sample is measured. This energy loss is caused by interactions between the electron and the sample and gives information about sample composition (core-loss EELS) or optical properties such as the band gap (low-loss EELS). Low-loss EELS measurements require a monochromated electron beam as good energy resolution is needed. Importantly, low-loss EELS permits characterization of band gap variations on length scales down to approximately 10 nm,^{28,29} providing vastly superior spatial resolution to conventional optical techniques. The high spatial resolution makes low-loss EELS an excellent

Table 1 Sample number, label, nominal composition and annealing. For sample 1, annealing steps were applied in the order given in the table

Sample	Sample label	Nominal composition	Annealing
1	Nanocomposite	Zn _{0.9} Fe _{0.1} O _{1.05}	1400 °C for 12 h +1000 °C for 36 h
2	IDB sample	Zn _{0.9} Fe _{0.1} O _{1.05}	1400 °C for 4 h
3	Bulk ZnFe ₂ O ₄	ZnFe ₂ O ₄	1400 °C for 17 h
4	Bulk ZnO	ZnO	1400 °C for 12 h



technique for characterizing optical properties of samples containing nanoparticles.

Sample absorption properties were characterized using DRS and low-loss EELS. Room temperature DRS data were collected using an EVO-600 (Thermo Fisher Scientific, Inc.) UV-Vis spectrophotometer. Sample emission properties were characterized with cathodoluminescence (CL) in a JEOL IT-300 SEM, equipped with an Andor SR 193i spectrograph and an Andor Newton CCD detector. CL spectra were acquired at 80 K, at accelerating voltages from 10 to 15 kV, and were averaged over the region of interest. A smoothing filter was applied to reduce noise. X-ray photoelectron spectroscopy (XPS) was used to study the compositional elements in the different samples. The XPS analysis was performed in a KRATOS AXIS ULTRA DLD instrument (Kratos Analytical Ltd, Manchester, UK) using monochromatic Al K α radiation ($h\nu = 1486.6$ eV).

3 Results

Fig. 1 displays locked-coupled X-ray diffractograms from the pellet samples between 28 and 52° for all samples. As expected, diffractograms from the nanocomposite, the IDB sample and the bulk ZnO sample revealed diffraction peaks from ZnO. The nanocomposite and the bulk ZnFe₂O₄ sample had diffraction peaks from ZnFe₂O₄. Interestingly, the IDB sample displayed a small shift toward lower angles for the ZnO-(10 $\bar{1}$ 1) peak, and a splitting of the ZnO-(0002) peak. The (0002) peak with low intensity (34.45°) is close to the ZnO-(0002) peak from the bulk ZnO sample. The higher intensity peak appears at a smaller angle (34.05°), indicating elongation of the ZnO *c*-axis in this sample, which will be discussed further later. Additionally, we observe additional peaks at around 35.5 and 47.1°. A diffraction peak similar to the former was previously observed in similarly prepared samples.³⁰ Potential candidates for the peak at 35.5°

are magnetite (Fe₃O₄) or maghemite (γ -Fe₂O₃), for which strong diffraction peaks have been observed around this angle (ICSD 77588 and ICSD 172906), although other diffraction peaks from these phases were not observed. Alternatively, this low-intensity diffraction peak could be due to a small volumetric portion of ZnFe₂O₄, with the (311) diffraction peak shifted by 0.3° relative to the bulk ZnFe₂O₄. At the surface of the IDB sample, a small portion of ZnFe₂O₄ might be expected, due to Zn evaporation during heat treatment. However, the ZnFe₂O₄ phase was not observed in the TEM data from the IDB sample.

SEM-EDS data confirmed that the composition of the nanocomposite and the IDB sample was spatially homogeneous, please see the ESI† for further details. Secondary electron and backscatter electron imaging in SEM also revealed the presence of voids in these samples.

To investigate the microscopic structure of the samples, STEM and EDS characterization was conducted. In Fig. 2(a), the bright field STEM image from the nanocomposite reveals bright rod-like particles embedded in a dark ZnO matrix. The crystal structure and chemical composition of the particles were determined through SAED and EDS mapping respectively, see Fig. 2(b)–(e). The data confirmed that the particles were composed of spinel ZnFe₂O₄. This identification is consistent with our XRD data, and is in line with what was expected from published phase diagrams,¹⁰ which indicate formation of the spinel phase at the annealing temperature and composition of the nanocomposite. The particles have undergone solid state growth, and are embedded in the ZnO matrix with their [111] axis parallel to the polar ZnO [0001] axis. The aspect ratios of the particles show a clear preferential growth in the [121] direction.

Fig. 3(a) and (b) show simultaneously acquired HAADF and ABF STEM images of an interface between ZnO and a spinel ZnFe₂O₄ nanoparticle in the nanocomposite. In Fig. 3(a), fast Fourier transforms (FFTs) for both phases and the projected atomic model of ZnFe₂O₄ superposed on the magnified HAADF STEM image from the spinel particle are shown in the insets. From the FFTs, we find the lattice matching relation ZnO [0001]||ZnFe₂O₄ [$\bar{1}\bar{1}\bar{1}$], which is in agreement with the SAED data. The interface appears slightly diffuse in both the ABF and HAADF images. This could be due to the presence of strain and misfit dislocations at the mismatched interfacial region, a situation which was recently reported for spinel ZnCr₂O₄ nanoparticles embedded in ZnO by geometric phase analysis.³¹

Fig. 4 shows a HAADF STEM image of the IDB sample along the ZnO-[2 $\bar{1}\bar{1}$ 0] zone axis. It is known from the literature that b-IDBs are visible in this zone axis, while p-IDBs are not resolved clearly.²² The overlaid EDS profile of Fe in cation atomic percent reveals increased Fe concentration at the b-IDBs. The EDS data also revealed decreased Zn concentration at the b-IDBs (not shown). In HAADF, the contrast is heavily influenced by the atomic number and density of the sample. This gives dark contrast at the Fe-decorated b-IDBs in the HAADF image, since they have higher concentrations of the lighter Fe atoms and lower concentrations of the heavier Zn atoms than the surrounding ZnO grains. Convergent beam electron diffraction from the same area (not shown) confirmed that the polarity of

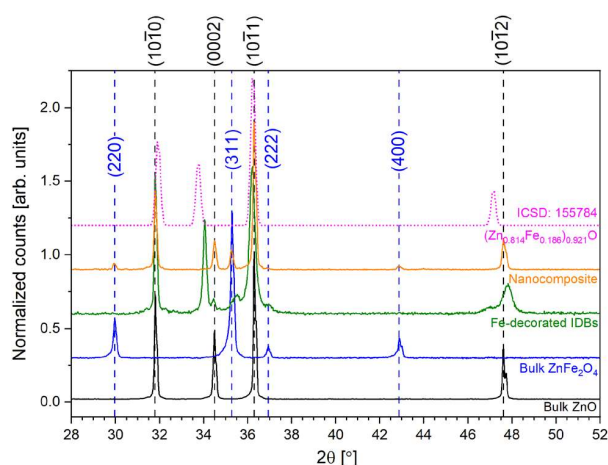


Fig. 1 Diffractograms from all samples in Table 1. A zero-point shift has been applied. Peak positions for ZnFe₂O₄ and ZnO have been indicated by dotted lines and indices (blue for ZnFe₂O₄, black for ZnO). The pink dotted line shows the diffractogram from an Fe-rich ZnO solid solution obtained from ICSD (ICSD: 155784).



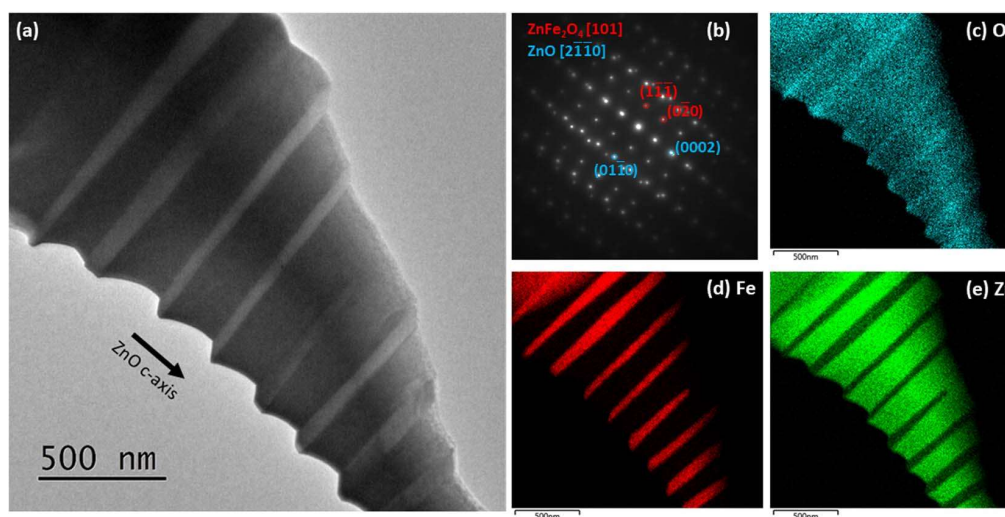


Fig. 2 (a) Bright field STEM image from the nanocomposite sample, taken along the ZnO-[2110]-projection. (b) Indexed SAED pattern from a large part of the area in (a), showing diffraction from both the ZnO matrix and the ZnFe₂O₄ NPs. (c)–(e) STEM EDS maps showing an accumulation of Fe and a depletion of Zn at the ZnFe₂O₄ NPs, compared to the ZnO matrix.

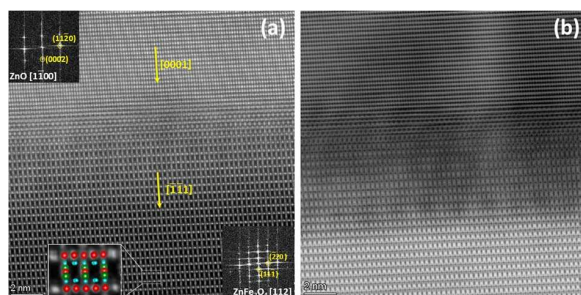


Fig. 3 High resolution (a) STEM-HAADF and (b) STEM-ABF images of the interface between a ZnFe₂O₄ NP and the ZnO matrix in the nanocomposite sample. Insets show FFTs from the corresponding areas and a schematic representation of the atomic structure of ZnFe₂O₄ overlaid on the magnified HAADF image from the ZnFe₂O₄ particle (Zn in green, Fe in red, and O in blue). Yellow arrows indicate the directions of the lattice matching.

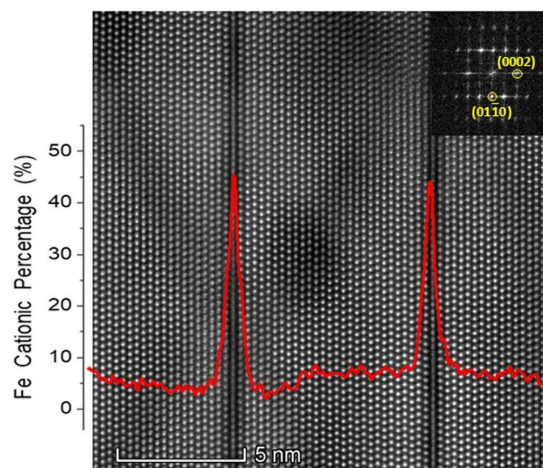


Fig. 4 STEM-HAADF image of the IDB sample along the ZnO-[2110] projection. The inset shows the corresponding FFT. The EDS profile of Fe in cationic percent is superimposed on the HAADF image. The EDS signal was collected from the entirety of the displayed area, and the Fe-signal was averaged vertically to produce the superposed line profile.

the ZnO grains was indeed inverted across the b-IDBs. These observations are in line with previous studies.^{22,23}

Fe cationic concentrations around 5 and 45% were observed in the ZnO grains and the b-IDBs respectively. The observed Fe-concentrations at the b-IDBs is relatively low compared to the literature, where a full Fe monolayer at b-IDBs has been reported.²¹ This is attributed to partial Zn-occupation at the b-IDBs, minor sample inhomogeneity, or scattering effects. Due to scattering, the electron beam spreads while passing through the sample. Hence, even when the electron beam is positioned directly on an IDB, some of the EDS signal originates from the neighboring ZnO grains. Consequently, scattering effects are expected to lower the observed Fe concentrations at the b-IDBs. Analogously, scattering effects would increase the observed Fe concentration in ZnO grains.

The b-IDBs are of primary interest in the current work, but observations of iron-decoration of p-IDBs can be found in the ESI (Fig. S3†). In normal spinel ZnFe₂O₄, Zn and Fe are tetrahedrally and octahedrally coordinated, respectively. XPS data (see the ESI, Fig. S4†), show some tetrahedrally coordinated Fe in the nanocomposite, revealing a small but non-zero inversion parameter in this sample. From the XPS data, we find that Fe is octahedrally coordinated in the IDB sample, similar to what is found for the bulk ZnFe₂O₄ sample.

As stated previously, the ZnO-(0002) peak was split in the IDB sample, with one low intensity peak at 34.45° and a high



intensity peak at 34.05° , see Fig. 1. For the high intensity peak, a qualitatively similar shift was observed in previous work by Yamashita *et al.* for Fe-rich ZnO.³² For a solid solution containing 18.6 cation atomic percent Fe (pink line in Fig. 1), the ZnO-(0002) and (10 $\bar{1}$ 2) diffraction peaks are shifted to around 33.8 and 47.1° in the data from Yamashita *et al.* Comparing with our data, we find that presence of Fe-rich ZnO can account for the XRD peaks at 34.05 and 47.1° . Since we observe smaller shifts than Yamashita *et al.*, particularly for the ZnO-(0002) peak, the solid solution is likely less Fe-rich in our case, which is reasonable since the IDB sample had a nominal composition of 10 cation atomic percent Fe. The low-intensity ZnO-(0002) peak is attributed to ZnO grains with low Fe concentration, where the reduced Fe concentration is caused by accumulation of Fe at the IDBs. The low intensity of this diffraction peak reveals that these grains are either small or make up a small volumetric fraction of the sample.

Spinel ZnFe₂O₄ features atomic layers of Fe octahedrally coordinated by O on {111} planes. Fe-decorated b-IDBs in ZnO consist of a single layer of Fe octahedrally coordinated by O on ZnO basal planes ((0001) planes). A schematic representation is given in Fig. 5. As can be seen from the figure, the two structures are similar up to the closest neighbors of the Fe-atoms, while there are differences in the second closest neighbors of the Fe-atoms. Based on this observation, it is interesting to investigate

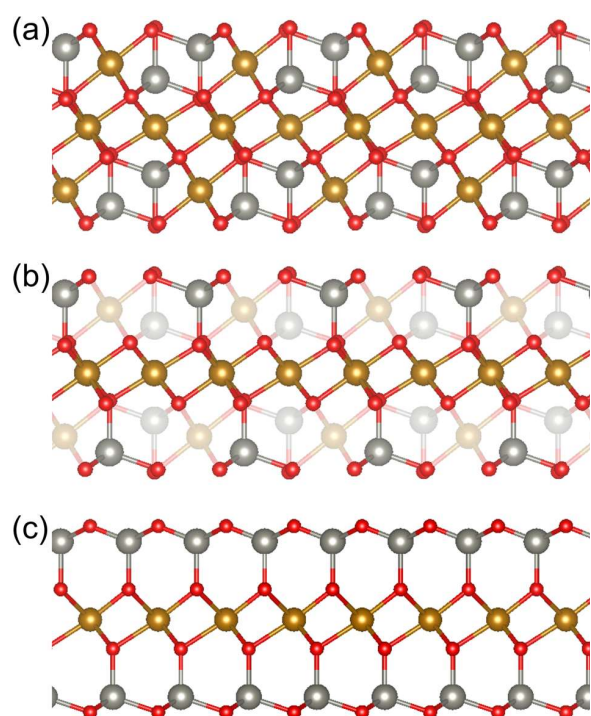


Fig. 5 Comparison of atomic structure of (a) a layer of Fe atoms octahedrally coordinated by O on a {111} plane in ZnFe₂O₄ (projection [101]), and (c) schematic representation of an Fe-decorated b-IDB in ZnO (projection [11 $\bar{2}$ 0]). In (b) the similarities in the two structures are highlighted by making some of the atoms in the ZnFe₂O₄ structure transparent. Atoms are shown in gray (Zn), red (O) and gold (Fe).

whether the structural similarity gives rise to functional similarities. We therefore focus on characterizing the optical properties of spinel ZnFe₂O₄ NPs and Fe-decorated IDBs in ZnO in the remainder of this work.

In Fig. 6, DRS Tauc plots assuming direct and indirect transition are shown for the nanocomposite and IDB sample. The plots reveal clear similarities between the two samples, with the absorption band edge slightly below 2 eV for both samples. At 3.2 eV, the spectra show a decrease, followed by a sharp increase from ~ 3.3 eV, which is attributed to the direct band transition in ZnO. At 2.6–2.7 eV, the spectra flatten out, followed by an increase which is more prominent in the IDB spectra than in the nanocomposite spectra. This behavior is similar to the behavior around the onset of the ZnO absorption edge, and indicates additional transitions at 2.6–2.7 eV.

For the first onset, DRS reveals an energy of 2.0 (direct) or 1.9 eV (indirect) for the IDB sample, and 1.9 (direct) or 1.8 eV (indirect) for the nanocomposite. The similarity in absorption onsets is attributed to the local structural similarity around Fe-ions at b-IDBs and Fe-ions in spinel ZnFe₂O₄, resulting in absorption at similar energies in the two samples. A minor shift of ~ 50 meV was observed between the absorption onset of the IDB sample and the nanocomposite, with higher onset energy for the IDB sample. As stated, XPS data revealed a small degree of inversion in the spinel nanoparticles. Some previous work has observed that the bandgap of ZnFe₂O₄ decreases with increasing degree of inversion,³³ and the magnitude of the

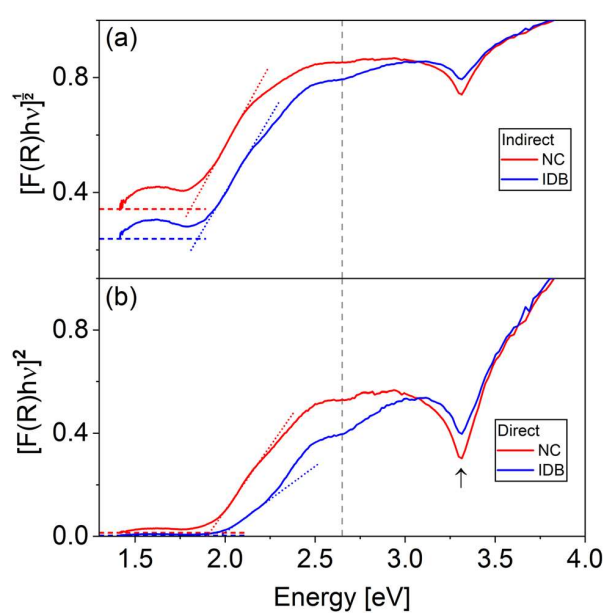


Fig. 6 Tauc plots of diffuse reflectance assuming (a) indirect and (b) direct transitions from the nanocomposite and IDB samples. Baselines are indicated with horizontal dashed lines in red (nanocomposite) and blue (IDB). Linear fits around the first optical absorption onset are given in dotted lines. The transition at 3.3 eV is attributed to ZnO and is indicated by the arrow in (b), as ZnO is known to have a direct bandgap. The dashed vertical gray line indicates the position of an additional onset in the data, see the text for further discussion.



reported bandgap lowering is similar to the difference in energy between the absorption onsets of the IDB sample and the nanocomposite. From this, the onset energy difference could be explained by bandgap lowering in the nanocomposite due to non-zero degree of inversion. Note that other authors have reported that the bandgap of ZnFe_2O_4 is independent of the degree of inversion.³⁴ An alternative explanation for the shift observed in the current work is quantum confinement of charge carriers at the IDBs, which would blue shift the absorption onset of the IDB sample.^{35,36}

Fig. 7 shows low-loss EELS spectra from the nanocomposite and IDB samples from 1.8 to 4.5 eV. For the nanocomposite, the data was collected directly from a ZnFe_2O_4 NP extending through the TEM sample. Signal from the ZnO grains nearby was consequently not observed in this spectrum. The spectrum from the IDB sample is a convolution of the signal from ZnO grains and IDBs, which was unavoidable due to inelastic delocalization.³⁷

The EELS results indicate two absorption onsets in the spinel ZnFe_2O_4 NPs. The first absorption onset occurred at 2.0 eV and represents the absorption band edge. This value is consistent with our DRS data. Another absorption onset was found around 2.6 eV. The two transitions were fitted to the lineshape of a direct and an indirect transition, respectively. The first transition corresponds well with the expected band gap of ZnFe_2O_4 .^{12,34} Interestingly, the energy of the second transition corresponds approximately with one of the electronic transitions observed in photoluminescence measurements on ZnFe_2O_4 which Granone *et al.*,¹² attributed to a transition involving Zn. Importantly, the data show that spinel ZnFe_2O_4

NPs embedded in ZnO have absorption onsets at energies similar to bulk ZnFe_2O_4 . Hence, embedding spinel ZnFe_2O_4 NPs in a ZnO TCO is a viable approach to enhance absorption in the yellow, green and blue bands of the visible spectrum, while leaving the composite transparent in the red band.

In the EELS spectrum from the IDB sample, we find that the line shape has three contributions: a direct transition at 2.0 eV, an indirect transition at 2.6–2.7 eV, and a direct transition at 3.2 eV. The transition at 3.2 eV is due to band-to-band transitions in ZnO, while the first transition at 2.0 eV is the absorption band edge of the sample. The absorption band edge position is consistent with our DRS data. Both EELS and DRS indicate another transition around 2.6–2.7 eV in the IDB sample.

Generally, for both the nanocomposite and the IDB sample, the onset energies from EELS and DRS are in good agreement. The data clearly reveals similar optical absorption in spinel ZnFe_2O_4 NPs and Fe-decorated IDBs. Previously, density functional theory (DFT) studies of the band structure of ZnFe_2O_4 have revealed that the valence band maximum (VBM) and the conduction band minimum (CBM) is mainly made up of Fe 3d and O 2p states,³⁸ so the size of the bandgap is largely determined by the bonding between these elements. As noted above, both the nanocomposite and the IDB sample contain layers of Fe octahedrally coordinated by O. We also found above that the majority of Fe is octahedrally coordinated by O in both samples. Since the DFT results from literature show that the size of the band gap is largely determined by the bonding between Fe and O, it is thus reasonable to conclude that the similar optical absorption in the two samples arises from the structural similarity. Crystallographically, Fe-decorated b-IDBs cannot be

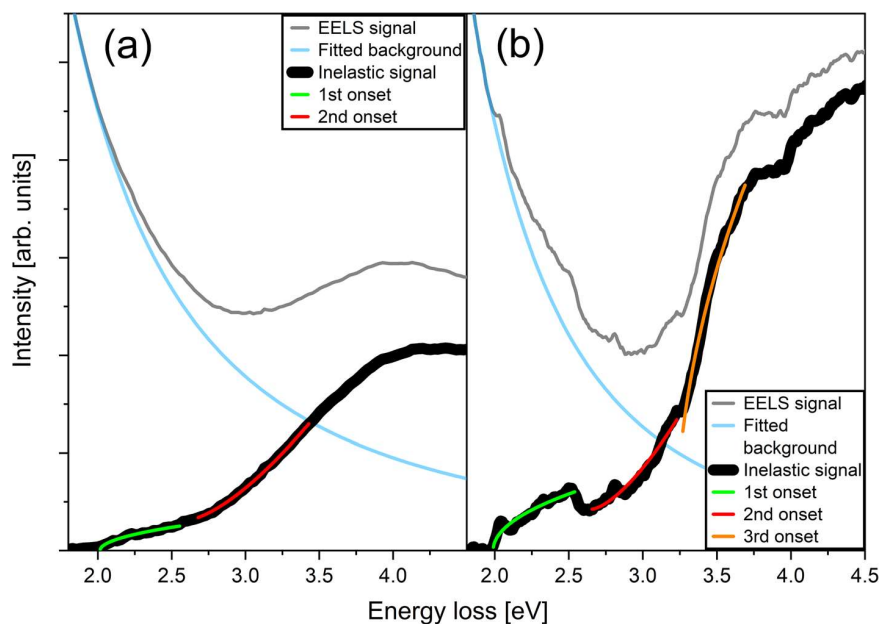


Fig. 7 Low-loss EELS spectra from the (a) nanocomposite and (b) IDB sample, showing the EELS signal, the fitted background, the inelastic signal (background subtracted signal) and fitting of the spectra to direct and indirect transitions. The IDB sample showed signal variation on nanometer scale, hence the spectrum was averaged over a smaller area than the nanocomposite spectrum, accounting for the difference in signal intensity, which is evident from the noise levels in the two spectra.



accurately described as spinel ZnFe_2O_4 inclusions in ZnO. However, motivated by the structural and functional similarities described above, we suggest that b-IDBs can be viewed as few-layer spinel-like inclusions in ZnO.

Valence band XPS spectra from all the samples are presented in the ESI†. The data show that the nanocomposite and the IDB sample have valence band maxima at approximately the same energy, and that the valence band XPS spectrum from the nanocomposite can be explained as a combination of ZnO and ZnFe_2O_4 . These observations are consistent with Fe-decorated b-IDBs behaving similarly to spinel ZnFe_2O_4 . Please see the ESI† for a full discussion of the valence band XPS spectra.

With the excellent spatial resolution provided by the low-loss EELS measurements, we have demonstrated that the absorption bands at ~ 2.0 and ~ 2.6 eV in the nanocomposite originate from the ZnFe_2O_4 nanoparticles. In the IDB sample, the data do not allow us to conclusively rule out contributions from defects in the ZnO grains to the optical absorption properties. Defects that may contribute include vacancies, intrinsic interstitials, and solute Fe. If the absorption properties of the IDB sample are attributed to defects in the ZnO grains, then the functional similarity between the nanocomposite and the IDB sample is coincidental. However, both samples had absorption onsets at 2.0 and 2.6 eV, so we find that such a coincidence is unlikely. Furthermore, contributions to absorption from defects tend to manifest as an Urbach tail. We have tried to suppress contributions from the Urbach tail to the absorption band edge analysis by applying Tauc plots. Finally, the valence band XPS spectra from the two samples are similar (see the ESI†). This is expected if Fe-decorated b-IDBs behave similarly to spinel ZnFe_2O_4 . From the presented data, the most probable interpretation is therefore that the structural similarity around Fe ions at b-IDBs and in spinel ZnFe_2O_4 causes the observed functional similarities.

The DRS data is, in principle, susceptible to contributions from the impurity phase detected in the diffractogram from the IDB sample. However, the superior spatial resolution of EELS, along with simultaneous access to structural data, revealed that the absorption onsets at 2.0 eV and 2.6–2.7 eV cannot be attributed to impurity phases.

CL spectra in the range from 1.6 to 3.8 eV were collected from all samples at 80 K, see Fig. 8 and 9 for the nanocomposite and IDB sample respectively. Measurements on the bulk ZnO sample revealed the characteristic near-band-edge (NBE) emission of ZnO and a separate broad defect band. The defect band was well described by fitting with 4 Gaussian emission components. Fitting of the bulk ZnFe_2O_4 emission required 7 Gaussian emission components, centered at 3.0 (B1), 2.6 (B2), 2.3 (B3), 2.2 (B4), 2.1 (B5), 2.0 (B6) and 1.9 (B7) eV. B6 and B7 are likely due to NBE and defects in ZnFe_2O_4 ,^{12,33} respectively. B2 and B3 are consistent with previous reports of luminescence from higher-lying bands in ZnFe_2O_4 .¹² See the ESI† for deconvolution of the luminescence from both bulk samples (Fig. S6†).

Fig. 8 shows CL data from the nanocomposite. To deconvolute the spectra, emission components from the bulk ZnO sample were included, and three further components had to be introduced, centered at 2.5, 2.1 and 2.0 eV. The additional peaks

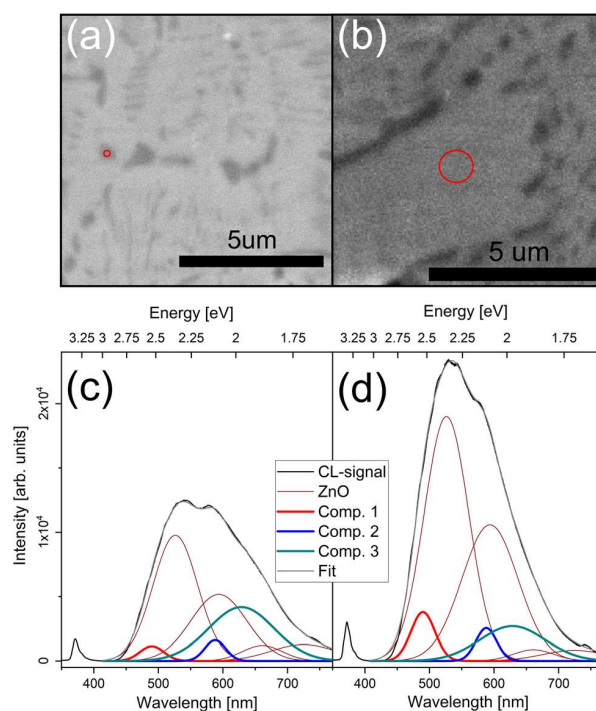


Fig. 8 Secondary electron micrographs and CL spectra acquired at 80 K from the nanocomposite. The spectrum in (c) was acquired on a ZnFe_2O_4 NP, with the region of acquisition indicated by the red circle in (a). The spectrum in (d) was acquired on the ZnO matrix, with the region of acquisition indicated by the red circle in (b). The spectral deconvolution is shown in (c) and (d) using emission components from the bulk ZnO sample ("ZnO" in legend) and three additional components (Comp. 1 (2.5 eV), 2 (2.1 eV) and 3 (2.0 eV)).

at 2.1 and 2.0 eV are close to components B5 and B6 from the bulk ZnFe_2O_4 sample, but have a different width than those of the bulk sample. In contrast, the peak at 2.5 eV does not match

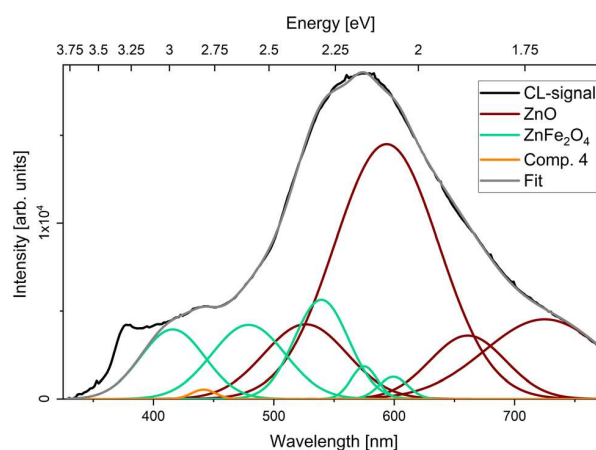


Fig. 9 CL spectrum acquired at 80 K from the IDB sample. The spectral deconvolution using emission components from bulk ZnO and bulk ZnFe_2O_4 is shown. A final component was added at 2.8 eV (orange line).



any emission component from the bulk ZnFe_2O_4 sample. Hence, the luminescence from the nanocomposite could not be deconvoluted as a simple combination of emission components from the ZnO and ZnFe_2O_4 bulk samples. There are several possible origins for the additional emission peaks. First, there could be luminescence contributions from the $\text{ZnO}/\text{ZnFe}_2\text{O}_4$ interfaces, which are not present in either of the bulk samples. Second, the XPS data revealed a non-zero inversion parameter for the nanocomposite. In the literature, some authors have observed a change in luminescence peak positions as a function of the inversion parameter,³³ while others have found only changes in peak intensities.¹² Finally, solute Fe in ZnO could contribute to the luminescence. This possibility will be discussed below. The intensity of the component at 2.0 eV increased when measuring directly on ZnFe_2O_4 NPs, and the energy of this emission component agrees with the band gap of ZnFe_2O_4 as determined from our EELS and DRS data as well as previous reports in the literature.^{12,34} Therefore, this emission component is likely related to NBE emission in the ZnFe_2O_4 NPs.

Note that secondary electron (SE) imaging is more surface sensitive than the CL measurements. Consequently, the underlying ZnO matrix can contribute to the CL signal, even when the signal is acquired from an area corresponding to a ZnFe_2O_4 NP as determined from the SE image.

CL measurements on the IDB sample (Fig. 9) featured an increase in luminescence between 2.6 and 3.1 eV compared to the spectra from the bulk ZnO sample. Spectral deconvolution was achieved using emission components from bulk ZnO and bulk ZnFe_2O_4 , keeping both the peak energy and width constant for all components. The spectrum from the IDB featured a final minor emission peak at 2.8 eV, which was accounted for by addition of a final fitting component. The ZnO NBE was not included in the fitting.

The optical properties of solid solutions of Fe in ZnO have not been explicitly studied here, and contributions from Fe dopants cannot be ruled out in the interpretation of our luminescence data. Previous work by Wang *et al.* has shown a broadening in photoluminescence from ZnO samples doped with Fe in the spectral region between 2.4 and 3.0 eV approximately.³⁹ Hence, solute Fe in ZnO could contribute to the observed luminescence in this range in our CL data. However, the absence of diffraction peaks from ZnO in the bulk ZnFe_2O_4 sample in the XRD data (see Fig. 1) indicates that if there are ZnO particles in this sample they are either small or make up a small volumetric ratio of the sample. Hence contributions from solute Fe in ZnO are considered unlikely to dominate the luminescence from the bulk ZnFe_2O_4 sample. Since luminescence components from the bulk ZnFe_2O_4 sample were used to deconvolute the luminescence from the IDB sample, we therefore argue that luminescence from Fe-decorated IDBs likely contributed to the CL data. It should be noted that alternative deconvolutions may be possible with the large number of luminescence components used for the IDB sample. The luminescence components at 2.5 and 2.1 eV in the nanocomposite could be due to luminescence from solute Fe in ZnO . However, we argue that the emission component at 2.0 eV in the

nanocomposite is likely due to NBE emission in the ZnFe_2O_4 NPs, since its energy matches the expected bandgap of ZnFe_2O_4 , and due to the variation in the intensity of this luminescence component as a function of position on the sample. Further studies are required to unambiguously determine the origin of all emission components.

4 Conclusion

The optical properties of ZnO were modified through incorporation of ZnFe_2O_4 spinel particles. We have shown that the optical properties are changed through the incorporation of the spinel particles, specifically that the absorption edge is lowered from 3.3 eV for pristine ZnO , to 2.0 eV in samples containing the ZnFe_2O_4 spinel particles. Furthermore, samples containing Fe-decorated IDBs and samples containing embedded spinel ZnFe_2O_4 particles displayed similar absorption properties. We suggest that the origin of this similarity is the layers of Fe octahedrally coordinated by O, which is present in both samples. We have demonstrated that by introducing iron into ZnO , the optical band gap of the system can be modified, making iron-containing ZnO a candidate as a modified TCO for improving solar cell efficiency. CL measurements suggest that luminescence from ZnO containing Fe-decorated IDBs is explained by a combination of ZnO and spinel ZnFe_2O_4 luminescence, whereas increased luminescence near the bandgap of spinel ZnFe_2O_4 was observed from spinel ZnFe_2O_4 nanoparticles embedded in ZnO .

Author contributions

S. B. Kjeldby: conceptualization; data curation; formal analysis; investigation; methodology; visualization; writing – original draft; writing – review & editing. P. D. Nguyen: conceptualization; data curation; formal analysis; investigation; methodology; supervision; validation; visualization; writing – original draft; writing – review & editing. J. García-Fernández: conceptualization; formal analysis; investigation; methodology; visualization; writing – original draft; writing – review & editing. K. Haug: conceptualization; investigation; methodology. A. Galeckas; formal analysis; investigation; supervision; visualization; writing – review & editing. I. J. T. Jensen; formal analysis; investigation; methodology; writing – review & editing. A. Thogersen; formal analysis; investigation; methodology; visualization; writing – review & editing. L. Vines: conceptualization; funding acquisition; methodology; project administration; resources; supervision; validation; writing – review & editing. Ø. Prytz: conceptualization; funding acquisition; methodology; project administration; resources; supervision; validation; writing – review & editing.

Conflicts of interest

The authors have no conflicts to disclose.



Acknowledgements

The Research Council of Norway is acknowledged for the support to the Norwegian Micro- and Nano-Fabrication Facility, NorFab (Project No. 295864) and the Norwegian Center for Transmission Electron Microscopy, NORTEM (Project No. 197405) and for support to the project Functionalization of Conducting Oxides by Ion beam and defect engineering (Project No. 287729). The authors would like to thank Ole Bjørn Karlsen for fruitful discussions.

References

- 1 V. Srikant and D. R. Clarke, *J. Appl. Phys.*, 1998, **83**, 5447.
- 2 M. A. Borysiewicz, *Crystals*, 2019, **9**, 505.
- 3 Ü. Özgür, *et al.*, *J. Appl. Phys.*, 2005, **98**, 041301.
- 4 P. Souletie, *et al.*, *J. Cryst. Growth*, 1988, **86**, 248.
- 5 W. W. Wenas, *et al.*, *Jpn. J. Appl. Phys.*, 1991, **30**, L441.
- 6 M. C. Beard, *et al.*, *Acc. Chem. Res.*, 2013, **46**, 1252.
- 7 B. L. Aarseth, *et al.*, *Nanotechnology*, 2021, **32**, 505707.
- 8 C. S. Granerød, *et al.*, *Nanotechnology*, 2019, **30**, 225702.
- 9 S. B. Kjeldby, *et al.*, *J. Appl. Phys.*, 2022, **131**, 125701.
- 10 S. A. Degterov, *et al.*, *Metall. Mater. Trans. B*, 2001, **32**, 643.
- 11 S. Zhou, *et al.*, *J. Phys. D: Appl. Phys.*, 2007, **40**, 964.
- 12 L. I. Granone, *et al.*, *Catalysts*, 2019, **9**, 434.
- 13 I. Almansouri, *et al.*, *IEEE J. Photovoltaics*, 2015, **5**, 968.
- 14 A. K. Srivastava, *et al.*, *Mater. Chem. Phys.*, 2009, **114**, 194.
- 15 M. Chandrika, *et al.*, *Mater. Chem. Phys.*, 2019, **230**, 107.
- 16 N. Kislov, *et al.*, *Mater. Sci. Eng. B*, 2008, **153**, 70.
- 17 R. Bayat, *et al.*, *Solid State Sci.*, 2019, **89**, 167.
- 18 S. D. Kulkarni, *et al.*, *Mater. Res. Bull.*, 2016, **77**, 70.
- 19 N. Daneu, S. Bernik and A. Rečnik, *J. Phys.: Conf. Ser.*, 2011, **326**, 012003.
- 20 T. Walther, *et al.*, *Int. J. Mater. Res.*, 2006, **97**, 934.
- 21 O. Köster-Scherger, *et al.*, *J. Am. Ceram. Soc.*, 2007, **90**, 3984.
- 22 H. Schmid, E. Okunishi and W. Mader, *Ultramicroscopy*, 2013, **127**, 76.
- 23 H. Schmid, *et al.*, *Micron*, 2012, **43**, 49.
- 24 J. Hoemke, *et al.*, *J. Am. Ceram. Soc.*, 2017, **100**, 4252.
- 25 J. Hoemke, *et al.*, *J. Am. Ceram. Soc.*, 2018, **101**, 2616.
- 26 F. Wolf, B. H. Freitag and W. Mader, *Micron*, 2007, **38**, 549.
- 27 M. Bosman, *et al.*, *Ultramicroscopy*, 2006, **106**, 1024.
- 28 M. Bosman, *et al.*, *Appl. Phys. Lett.*, 2009, **95**, 101110.
- 29 W. Zhan, *et al.*, *Nanotechnology*, 2017, **28**, 105703.
- 30 T. Hörlin, G. Svensson and E. Olsson, *J. Mater. Chem.*, 1998, **8**, 2465.
- 31 W. Zhan, *et al.*, *Materials*, 2019, **12**, 888.
- 32 T. Yamashita, R. Hansson and P. C. Hayes, *J. Mater. Sci.*, 2006, **41**, 5559.
- 33 Y. Li, *et al.*, *Chem. Geol.*, 2019, **504**, 276.
- 34 L. I. Granone, *et al.*, *Phys. Chem. Chem. Phys.*, 2018, **20**, 28267.
- 35 K. Ismail, *et al.*, *Appl. Phys. Lett.*, 1991, **58**, 1539.
- 36 M. Choi, *et al.*, *Appl. Phys. Lett.*, 2015, **106**, 192902.
- 37 R. F. Egerton, *Electron Energy-Loss Spectroscopy in the Electron Microscope*, Springer Science & Business Media, 3rd edn, 2011.
- 38 J. Yao, *et al.*, *Integr. Ferroelectr.*, 2013, **145**, 17.
- 39 Y. S. Wang, P. John Thomas and P. O'Brien, *J. Phys. Chem. B*, 2006, **110**, 21412.



Supplementary materials for Optical Properties of ZnFe_2O_4 Nanoparticles and Fe-Decorated Inversion Domain Boundaries in ZnO

S1 SEM-EDS investigation of the nanocomposite and the IDB sample

SEM-EDS data were acquired at 20 kV in a JEOL IT-300 SEM equipped with a Thermo Scientific Ultra Dry silicon drift X-ray detector, and the data was analyzed using the Pathfinder X-ray Microanalysis Software (ThermoFisher). The EDS signal was collected from an area of $1.2 \times 1.1 \text{ mm}^2$. The resulting secondary electron image and EDS maps for Fe, Zn and O are given for the nanocomposite in Figure S1 and for the IDB sample in Figure S2. No inhomogeneity is apparent from the EDS maps. To determine the average composition of the samples and its standard deviation, the composition was extracted from 94 non-overlapping areas of approximate size $100 \times 100 \text{ }\mu\text{m}^2$ in both samples. The resulting compositions are given in Table S1. We did not observe systematic variations of the composition over the measured area, and the relatively small standard deviation also indicates homogenous samples. We further extracted the Fe contents in units of cation atomic percent from each of the $100 \times 100 \text{ }\mu\text{m}^2$ areas, resulting in a value of 10.0 ± 0.4 in the nanocomposite and 10.0 ± 0.7 in the IDB sample. Notably, the average Fe content in cation atomic percent is equal in the two samples, and the measured Fe content is consistent with the nominal content of 10 cation atomic percent Fe. Analysis of the composition at the edge of the sample and in the middle of the sample indicated slightly decreased O-concentration and increased Zn-concentration near the edge in the nanocomposite, while the opposite was seen in the IDB sample. The observed variation in composition at the edges was within the standard deviation of the measurement and were therefore likely not significant. Overall, the standard deviations in composition were below 1 atomic percent, and the maps reveal uniform distribution of the EDS signal. This demonstrates the homogeneity of the samples. Please note that the oxygen concentration determined from SEM-EDS measurements at 20 kV are not expected to be very accurate due to x-ray absorption and scattering in the samples.

Table S1: Composition of the nanocomposite and the IDB sample as measured from 94 non-overlapping areas of approximate size $100 \times 100 \text{ }\mu\text{m}^2$ selected from the flat areas shown in Figure S1 and Figure S2

	Nanocomposite	IDB sample
Species	Concentration [atomic %]	Concentration [atomic %]
Fe	5.0 ± 0.2	5.0 ± 0.3
Zn	44.9 ± 0.7	44.7 ± 0.6
O	50.2 ± 0.7	50.3 ± 0.6

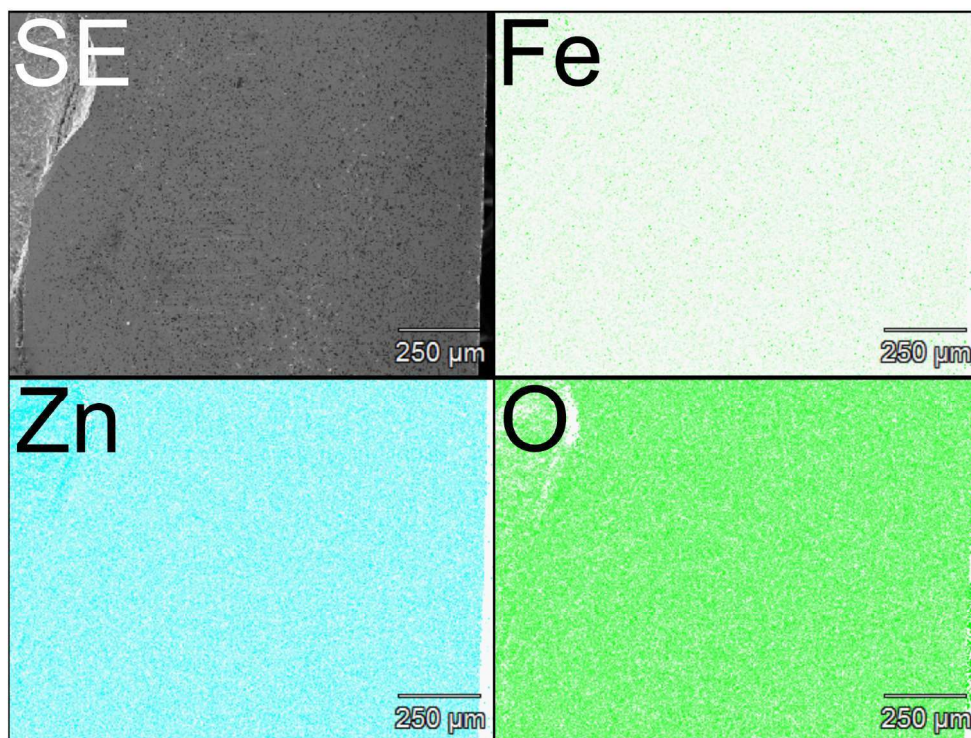


Figure S1: Secondary electron image, Fe, Zn and O SEM-EDS maps from the nanocomposite.

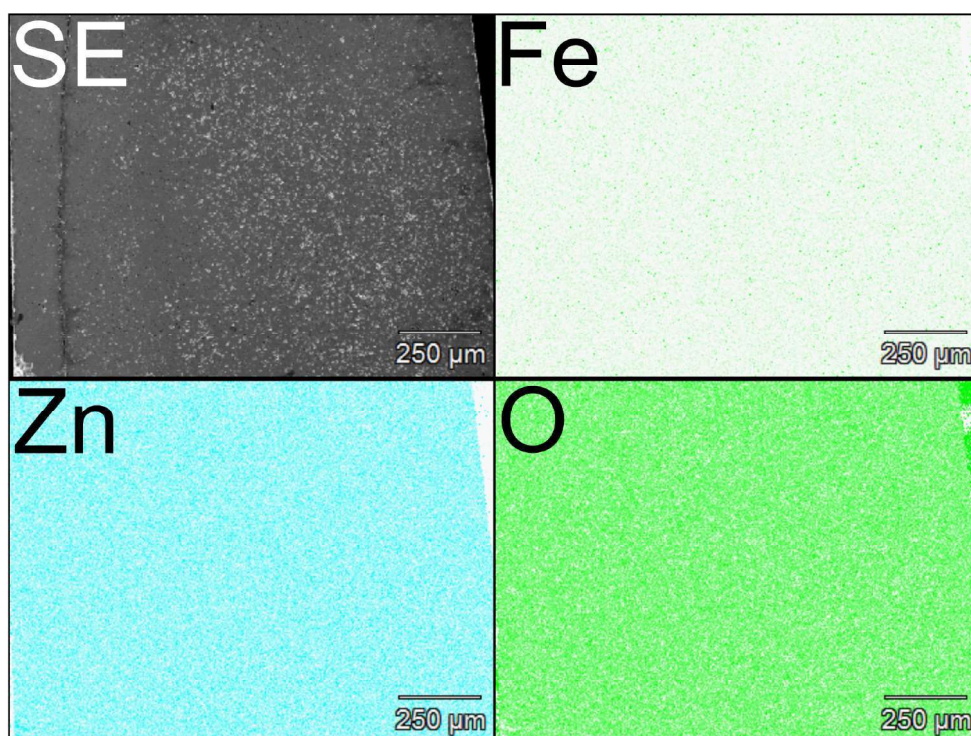


Figure S2: Secondary electron image, Fe, Zn and O SEM-EDS maps from the IDB sample.

S2 Pyramidal inversion domain boundaries

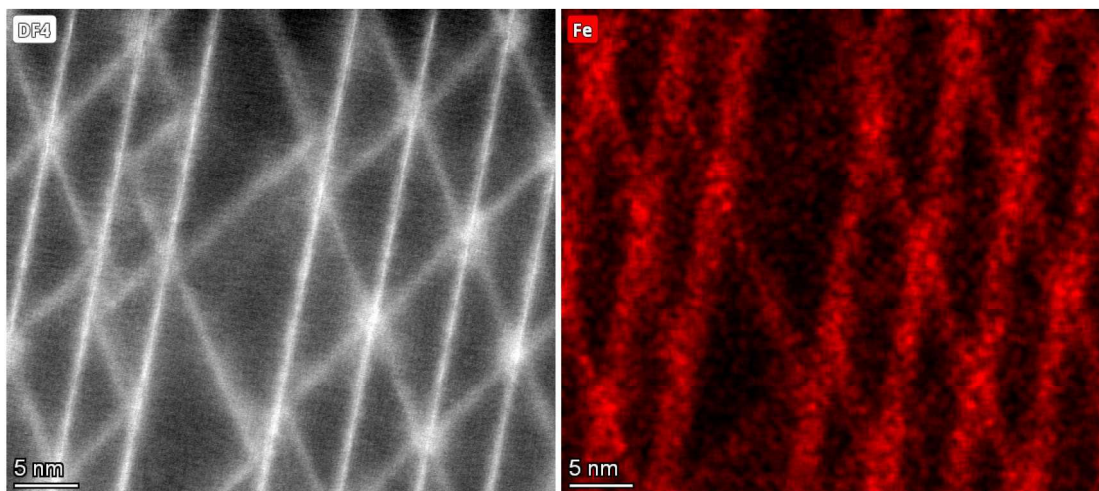


Figure S3: Medium angle annular dark field image and EDS map along ZnO- $[\bar{1}\bar{1}00]$ demonstrating the iron decoration of pyramidal IDBs in the IDB sample.

Figure S3 shows a medium angle annular dark field STEM image and corresponding EDS map of iron with zone axis ZnO- $[\bar{1}\bar{1}00]$, along which both basal and pyramidal IDBs can be seen. The figure clearly shows that pyramidal IDBs were present in the IDB sample, and that both the basal and pyramidal IDBs were Fe-decorated.

S3 X-ray photoelectron spectroscopy

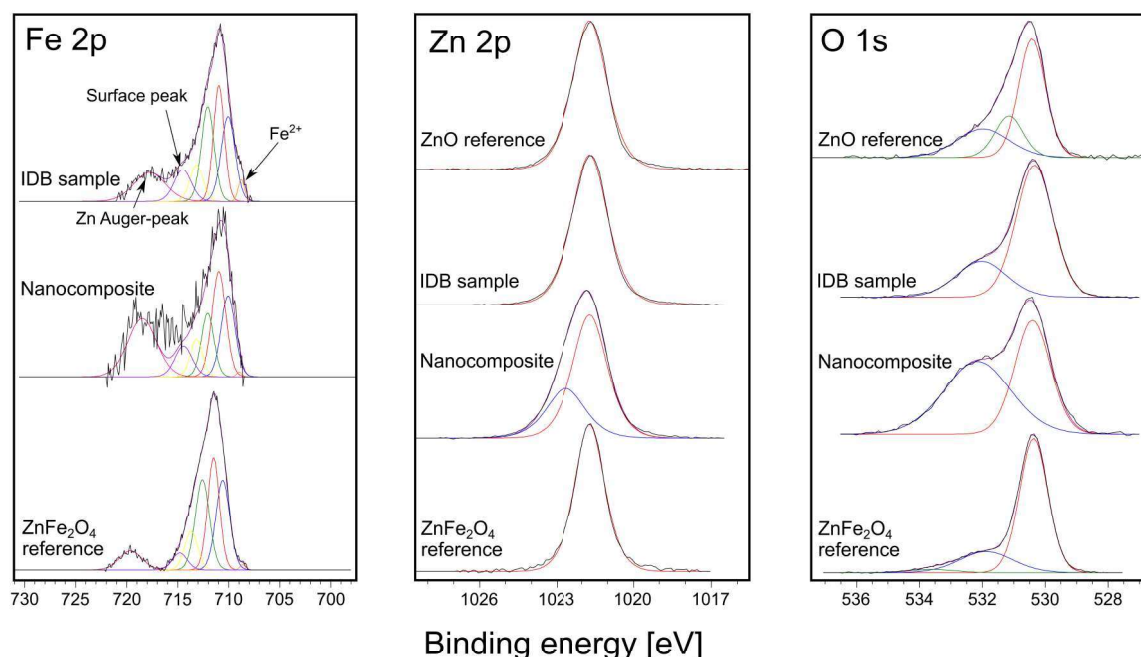


Figure S4: XPS spectra of the Fe 2p, Zn 2p, and O 1s peaks from the bulk ZnO reference, the bulk ZnFe₂O₄ reference, the nanocomposite, and the IDB sample. No Fe 2p spectrum is shown for the bulk ZnO reference, since this sample did not contain iron.

X-ray photoelectron spectroscopy was used to study the compositional elements in the different samples. The XPS analysis was performed in a KRATOS AXIS ULTRA DLD instrument (Kratos Analytical Ltd, Manchester, UK) using monochromatic Al K α radiation ($h\nu = 1486.6$ eV). A low energy electron flood gun was used to charge compensate the sample. The Zn 2p_{3/2} component corresponding to tetrahedrally coordinated Zn in ZnO was used as an internal energy reference and calibrated to 1021.7 eV in all samples^{S1}. The spectra were fitted using the CasaXPS software^{S2}.

The XPS spectra of the Fe 2p, Zn 2p, and O 1s peaks from bulk ZnO, bulk ZnFe₂O₄, the nanocomposite, and the IDB sample are shown in Figure S4. The main component of the Zn 2p spectra was used to calibrate the energy axis and is therefore well aligned in all the samples. In the nanocomposite, octahedrally coordinated Zn was found in the Zn 2p spectrum at about 1 eV above the binding energy of the tetrahedrally coordinated Zn^{S1}. The main components of the O 1s spectrum are also well aligned. For pure ZnO, the O 1s spectrum could be split into three peaks centered at 530.4, 531.2 and 532.0 eV, which were attributed to O²⁻ in the ZnO crystal structure, O²⁻ in oxygen deficient regions in the ZnO matrix (changes in this peak may be connected with the amount of oxygen vacancies in the ZnO), and loosely bound oxygen on the surface of ZnO (e.g., -CO₃, adsorbed H₂O or adsorbed O₂), respectively^{S3,S4}. The middle component connected to oxygen vacancies was not seen in the other samples.

The Zn 2p-based calibration of the energy gives good overlap in the peak position of Fe 2p for the nanocomposite and the IDB sample, but in the bulk ZnFe₂O₄ sample the Fe 2p peak is shifted to higher binding energy by about 0.5 eV. Notably, the shape of the Fe 2p peak is very similar across all three samples, and the data therefore indicates that the shift is caused by a difference in the Fermi level position in the nanocomposite and the IDB sample relative to the bulk ZnFe₂O₄ sample. The Fe 2p peak has a broad character, which has been reported to be due to inclusion of electrostatic interactions, spin-orbit coupling between the 2p core hole and unpaired 3d electrons of the photoionized Fe cation and crystal field interactions^{S5,S6,S7}.

The Fe^{3+} $2p_{3/2}$ peak has therefore been fitted with four Gaussian-Lorentzian (GL) Gupta and Sen (GS) multiplet^{S5,S6} peaks in addition to surface structures and a Zn Auger-peak. The binding energy of the four GS multiplets are 710.6 eV, 711.5 eV, 712.6 eV and 713.7 eV, modified slightly from work by Grosvenor et al.^{S7}. The multiplet area-intensities used are found from fitting the bulk ZnFe_2O_4 sample. This shows that the Fe is octahedrally coordinated in the IDB sample just as in bulk ZnFe_2O_4 . In addition, the XPS results show that about 3% of Fe in the IDB sample is present either as Fe^{2+} or in a coordination which is neither tetrahedral nor octahedral, e.g., the trigonal bipyramidal sites on Fe-decorated p-IDBs. In order to achieve a good fit for the nanocomposite we had to increase multiplet 2 with 8 % and decrease multiplet 3 with 8 %. Multiplet 2 has previously been correlated with tetrahedrally coordinated Fe^{S7}. An increase in multiplet 2 therefore indicates that more Fe is tetrahedrally coordinated in the nanocomposite.

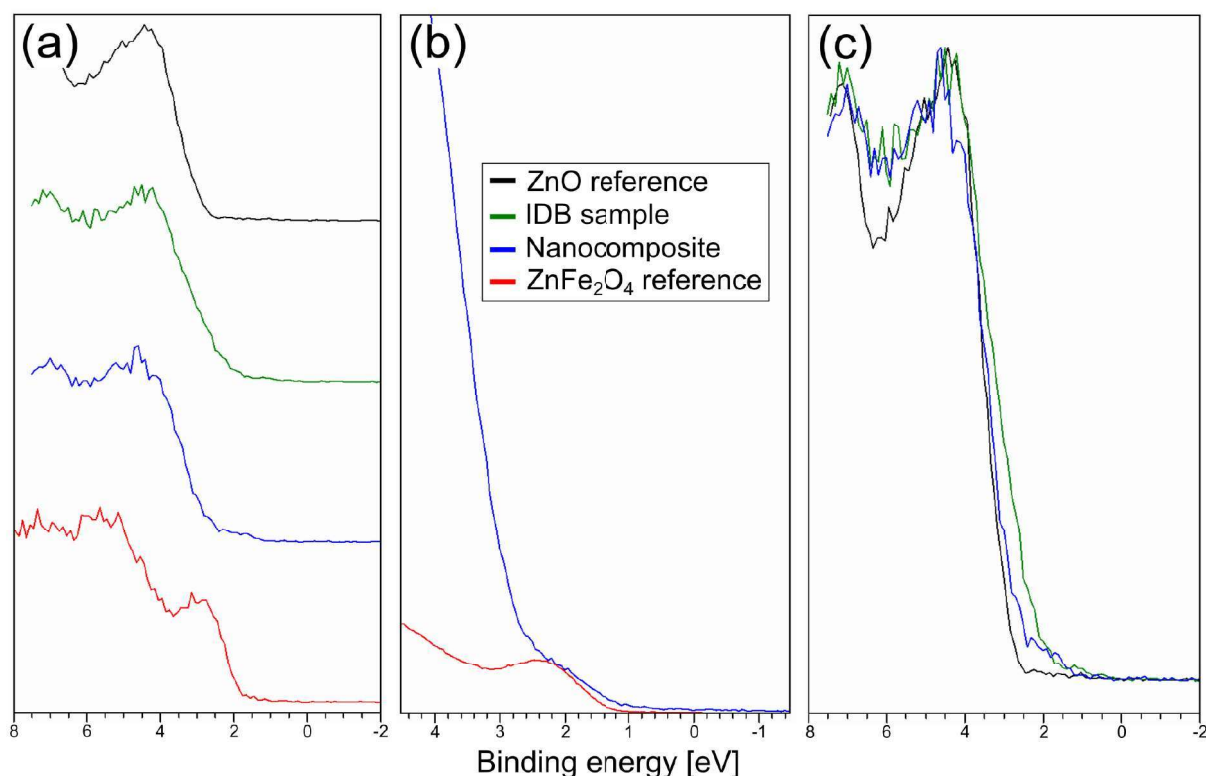


Figure S5: Valence band XPS data for all samples. The energy axis in (a) and (c) was calibrated by aligning the Zn 2p peaks. (b) Spectra from the nanocomposite and bulk ZnFe_2O_4 . Here the Fe 2p peaks of the two samples were aligned to account for differences in the Fermi level position of ZnFe_2O_4 in the two samples, in order to directly compare ZnFe_2O_4 -related features. (c) Overlaid spectra from bulk ZnO, the IDB sample and the nanocomposite, showing the change in valence band maximum caused by adding ZnFe_2O_4 nanoparticles or Fe-decorated IDBs to ZnO

XPS valence spectra from all the samples are shown in Figure S5 (a). The bulk ZnO sample, the nanocomposite and the IDB sample all contain ZnO and have similar valence spectra, while the bulk ZnFe_2O_4 sample has a strong feature at lower binding energy. Figure S5 (b) shows the valence spectra from the nanocomposite and bulk ZnFe_2O_4 sample in detail. Here, the bulk ZnFe_2O_4 spectrum has been shifted to align its Fe 2p peak with the Fe 2p peak of the nanocomposite and IDB sample, in order to compensate for the difference in Fermi level position described above. Hence, we find that the feature near the top of the valence band in the spectrum from the nanocomposite corresponds to the valence band edge of ZnFe_2O_4 . Figure S5 (c) shows that inclusion of Fe in ZnO as embedded ZnFe_2O_4 nanoparticles or Fe-decorated IDBs moves the valence band edge to lower binding energies. This results in a gradually decreasing slope of the band edge in the IDB sample, while it causes a distinct ZnFe_2O_4 -like feature in the nanocomposite. From (b) and (c),

we find that the spectrum of the nanocomposite can be explained as a combination of ZnO and ZnFe₂O₄, as expected. We note that at binding energies higher than that of the valence band edge, the XPS signal is stronger for the IDB sample than for the nanocomposite, suggesting a higher density of states (DOS). The origin of this difference has not been unambiguously determined. Two possible causes are contributions from p-IDBs, which have not been included in the analysis, or the difference in dimensionality between Fe-decorated b-IDBs (two-dimensional) and ZnFe₂O₄ nanoparticles (three-dimensional).

S4 Bulk ZnO and bulk ZnFe₂O₄ cathodoluminescence spectra

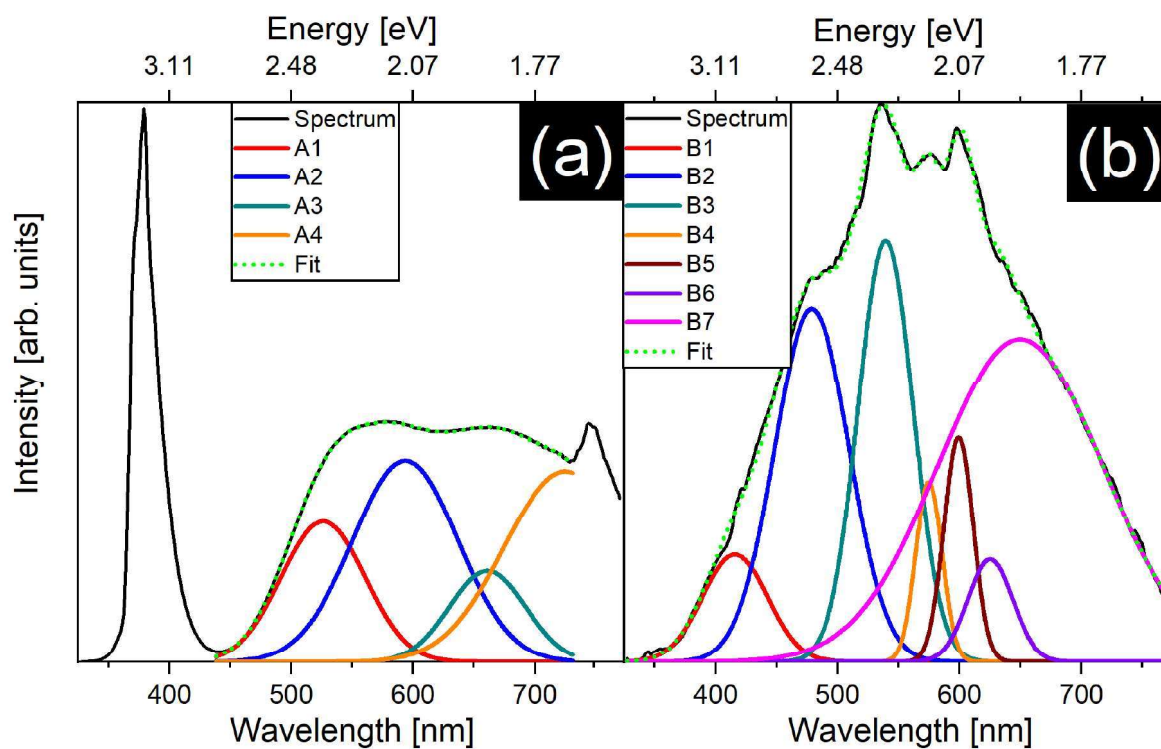


Figure S6: Cathodoluminescence spectra from the bulk ZnO (a) and bulk ZnFe₂O₄ (b) samples. Fitting of the spectra is shown for both samples, along with all of the Gaussian components which were used for the fitting. Components have been labeled according to phase (A for ZnO, B for ZnFe₂O₄). There is *no* correspondence between components plotted in the same color in the two subfigures.

Supplementary references

- [S1] S. Bera et al. *Journal of Materials Science* **36** (2001), p. 5379.
- [S2] Neal Fairley et al. *Applied Surface Science Advances* **5** (2021), p. 100112.
- [S3] Wenjuan Cheng and Xueming Ma. *Journal of Physics: Conference Series* **152** (2009), p. 012039.
- [S4] M. Chen et al. *Applied Surface Science* **158** (2000), p. 134.
- [S5] R. P. Gupta and S. K. Sen. *Physical Review B* **10** (1974), p. 71.
- [S6] R. P. Gupta and S. K. Sen. *Physical Review B* **12** (1975), p. 15.
- [S7] A. P. Grosvenor et al. *Surface and Interface Analysis* **36** (2004), p. 1564.

